Optical Study of the Electronic Structures of Molecular Conductors

(分子性伝導体の電子構造の光学的研究)

Thesis Submitted to the University of Tokyo
in Fulfillment of the Requirement
for the Degree of Doctor of Science

December, 1994

by Masafumi Tamura

学位論文

平成６年１２月　博士（理学）申請

田　村　　雅　史

Acknowledgment

The present work has been conducted under the guidance of Professor Haruo Kuroda, and has been completed under the supervision of Professor Minoru Kinoshita. The author would like to express sincere gratitude for their many valuable discussions, suggestions and encouragement.

The author is indebted to Professor Kyuya Yakushi (The Institute for Molecular Science) for useful discussions and encouragement. The author would like to acknowledge Dr. Hiroyuki Tajima for enlightening discussions and encouragement.

The author gratefully acknowledges Professor Hayao Kobayashi (Toho University), Professor Akiko Kobayashi, Professor Reizo Kato for providing him with many attractive samples, useful comments and encouragement.

The author is grateful to Dr. Madoka Tokumoto (Electrotechnical Laboratory) for helping the magnetic measurements, valuable discussions and encouragement. The author is also indebted to Professor James S. Brooks (Boston University), Dr. Alka G. Swanson (AT&T Bell Laboratories), Professor C. C. Agosta (Clark University), Dr. S. T. Hannahs (Massachusetts Institute of Technology). Their many experimental efforts have come to fruition of the first observation of the de Haas-van Alphen oscillations in θ-(BEDT-TTF)$_2$I$_3$. The author would like to thank Dr. Takehiko Mori (Tokyo Institute for Technology), Dr. Haruyoshi Aoki, Dr. Shinya Uji and Dr. Taichi Terashima (National Research Institute for Metals) for their excellent experiments and helpful discussions. The author acknowledge his debt to Professor Koichi Kikuchi (Tokyo Metropolitan University) for providing the author with the interesting samples of a salt of a non-symmetric donor, DMET.

Many thanks are given to all the members of the Laboratories of Professor Haruo Kuroda, Professor Minoru Kinoshita and Professor Reizo Kato.

Contents

Chapter 1.

General Introduction

1.1. Electronic structures of Molecular Conductors

Molecular conductors (organic conductors or synthetic metals) have afforded many research topics both in chemistry and physics for the last 40 years. The study originated from the pioneering work by Akamatu, Inokuchi and Matsunaga in 1954 [1]. The most memorable is the discovery of superconductivity in a series of quasi-one-dimensional conductors, TMTSF salts [2,3], and in a variety of two-dimensional conductors, BEDT-TTF salts [3]. Following them, some salts of non-symmetric organic donors such as DMET [4-6] and those of the metal complexes, $[Ni(dmit)_2]$ [7] and $[Pd(dmit)_2]$ [8], have been found to exhibit superconductivity. So far, various types of metallic systems have been identified. (For the chemical structures of TMTSF, BEDT-TTF, DMET and $[M(dmit)_2]$, see Fig. 1.1) The discovery of superconductivity in an alkaline metal salt of C_{60} [9] is also striking in this field.

Not only superconductivity but also several peculiar physical properties such as CDW (charge density wave) and SDW (spin density wave), which are closely related to their low dimensionality, have been revealed in molecular conductors. Such exotic features have activated many experimental and theoretical investigations on the electronic structures of these systems, both from chemical and physical sides. It has been widely accepted that the dimensionality of the electronic structures plays a key role in the physical properties of these materials.

In the recent several years, application of sophisticated experimental techniques at low temperatures, and sometimes under high magnetic fields, have provided much information about the electronic structures of these

conductors (see Sec. 1.3). This makes it clear that their electronic band structures can be basically understood within the framework of tight-binding band model based on the frontier molecular orbital, HOMO (the highest occupied molecular orbital) or LUMO (the lowest unoccupied molecular orbital). At the present time, this should be considered as the most significant characteristic of the electronic structures of the molecular conductors.

Prior to the direct experimental evidence for the formation of band structures, the tight-binding band model has been applied to elucidate the dimensionality of a molecular conductor from the structural viewpoint mainly by chemists [10,11]. The basis of this approach is that the separation of the intramolecular energy levels is sufficiently larger than the intermolecular charge transfer energy. The estimation of the intermolecular transfer integrals is the main part of the investigation in this framework. Usually, they are obtained as intermolecular overlap integrals multiplied by an energy factor, where the overlap integrals are calculated on the basis of the extended Hückel method [12] and only the nearest neighbor ones are considered. In this way, even rather involved features of the electronic properties become describable in terms of the chemical ideas based on the frontier orbitals and the transfer integrals between them. On the other hand, in order to improve this framework and to develop a new design of molecular conductors, it is desired to estimate the intermolecular interactions experimentally.

1.2. Tight-binding Band Model

The most basic theory of metals is the electronic band theory based on Bloch's theorem. In the theory, the one-electron states are described by the Bloch wavefunctions, which is delocalized over the crystal and has the periodicity in accord with that of the lattice. Fourier transformation of the Bloch function with respect to the lattice periodicity yields local function localized on each unit cell. This localized function is called Wannier function. The Bloch function is thus given as the linear combination of the Wannier functions.

The tight-binding band model is constructed by regarding the molecular orbitals (MOs) in the crystal as the Wannier functions. This means that the molecular identity still holds in the crystal. Diagonalization of the one-electron Hamiltonian in the space of the MOs taking account of the lattice periodicity yields the one-electron energy eigenvalues as functions of the wavevector, $\boldsymbol{k}$. This is the energy band structure in the tight-binding framework. This treatment of the electronic state of the crystal is analogous to the MO theory based on the linear combination of atomic orbitals. The only difference is the consideration of the lattice periodicity.

If only one MO on each molecule is taken into the basis set, the treatment is in a complete analogy to the primitive Hückel theory of π-MOs, in which only one 2p orbital is considered for each atom in a planar aromatic compound. For simplicity, it is assumed that all the MOs are equivalent in the following. The off-diagonal element of the one-electron Hamiltonian between the MOs, $|a\rangle$ and $|b\rangle$,

$$t_{a,b} = \langle a | H | b \rangle, \tag{1.2.1}$$

is called the transfer integral between $| a \rangle$ and $| b \rangle$. The role of t is essentially the same as that of the resonance integrals in the primitive Hückel MO theory. Similarly, only the nearest-neighbor ones are considered in the ordinary tight-binding band calculations. The transfer integrals are usually approximated as the overlap integrals multiplied by an energy factor, ε , that is,

$$t_{a,b} \approx \varepsilon \ S_{a,b} , \tag{1.2.2}$$

where,

$$S_{a,b} = \langle a | b \rangle , \tag{1.2.3}$$

and ε is given by the Mulliken approximation,

$$\varepsilon \ \langle a | a \rangle \approx \langle a | H | a \rangle = \langle b | H | b \rangle \approx \varepsilon \ \langle b | b \rangle. \tag{1.2.4}$$

The second equality comes from the equivalency of the MOs. With MOs normalized, ε agrees with the energy of the MOs.

The extended Hückel method is the standard way to calculate the MOs in the molecular conductors. The band calculations start from the estimation of the overlap integrals between the MOs in the crystal calculated by the extended Hückel method. Then, the transfer integrals are obtained by use of Eqs. (1.2.2) and (1.2.4).

Within this framework, the metallic properties of molecular crystals can be discussed in terms of the chemical intermolecular interactions. In Chapter 2, the procedure of band calculations starting from a set of transfer integrals is explained.

1.3. Experimental Approach to the Band Structure

Since most electronic properties of a metal are prescribed by the Fermi surface, the study of the Fermi surface can be compared to the study of the frontier orbitals, which dominates the chemical properties of a molecule. The band structure or the Fermi surface of a metallic material can be studied by various types of experiments.

The electronic specific heat and the static spin susceptibility afford the estimation of the density of states at the Fermi level. The coefficient of the T-linear term in specific heat, as well as the temperature independent Pauli-like susceptibility, is proportional to the density of states.

The transport properties, including the Hall effect, thermoelectric power and magnetoresistance give information on the band-filling, the curvatures of band near the Fermi level, or the topology of the Fermi surface. The electric resistivity, of course, provides significant information on the band structure. Magnetic resonances (NMR and ESR) and (photo)electron spectroscopy (e.g., XPS, UPS and energy-loss spectroscopy) are also known to work as useful tools to study the band structure, as well as some microscopic features.

The de Haas-van Alphen (dHvA) effect and the Shubnikov-de Haas

(SdH) effect, the magneto-quantum oscillations, are the direct probe to the Fermi surface [13]. These experiments are carried out under high magnetic field at low temperature. Periodic oscillation of magnetization (dHvA) or resistance (SdH) as a function of inverse magnetic field can be observed in such a condition. This is a result of the cyclotron motion of carriers along the Fermi surface. The frequency of the oscillation is proportional to the extremal cross-sectional area of the Fermi surface viewed along the field direction. From the temperature dependence of the oscillation amplitude, the cyclotron mass, a kind of effective mass of the carriers on the Fermi surface, is estimated. These techniques, which are sometimes called the fermiology, are based completely on the nature of the Fermi surface. In other words, the information provided by these measurements comprises purely of the features of the Fermi surface. These experiments cannot be applied to one-dimensional conductors without closed Fermi surface.

There is a special technique which has been advanced in the field of molecular conductors: the angle dependent magnetoresistance oscillation (ADMRO) [14-17]. This phenomenon is unique to the cylindrical Fermi surface with small warping, which is characteristic of the quasi-two-dimensional metals such as the BEDT-TTF salts [16,17]. The ADMRO is characterized by the periodic oscillation of magnetoresistance as a function of tan θ, where θ is the angle between the magnetic field and the axis normal to the two-dimensional plane. From the period, the Fermi wavenumber, i.e., the radius of the cylindrical Fermi surface can be derived [16].

Unlike the magneto-quantum oscillations and the ADMRO, the pre-

viously mentioned experiments may include information on other features related to phonons, defects, and so on. Sometimes, they may yield controversial results about the band structure. This caused the criticism on the applicability of the tight-binding band model. However, the situation has been changed by the observation of the SdH effect in κ-(BEDT-TTF)$_2$[Cu(NCS)$_2$] in 1988 [18], for the first time in molecular conductors. Since then, the SdH or the dHvA experiment has been applied to many two-dimensional molecular conductors [19]. This advance has greatly contributed in establishing the validity of the tight-binding model. It is also noteworthy that the observation of the magneto-quantum oscillations requires considerably high quality of the sample. Therefore, the appearance of the oscillations in a variety of molecular conductors indicates the high quality of the crystals of such molecular conductors.

1.4. Optical Study of the Band Structure

Except for the electron spectroscopy, the experimental methods mentioned in the preceding section are related to the ground state properties or to low-lying states just above the ground state. In contrast to them, the optical spectroscopy from the infrared to the visible range is the observation of the excitation of electrons by such photon energies. For this reason, the optical properties generally reflect the global structure of the band rather than the local structure near the Fermi surface. Consequently, the optical spectrum over the infrared to visible regions is insensitive to the phenomena characterized by a low energy below about 0.05 eV, such as

magnetism and superconductivity. In order to study such phenomena, experiments in the far-infrared or microwave region are required.

Practically, the study of optical spectra of metals has the following advantages.

(1) It is very easy to examine the dimensionality and anisotropy by the optical experiment using polarized light, while it is difficult to control the direction of current in a small single crystal in the measurement of transport properties.

(2) The optical properties are not sensitive to internal cracks in the crystal, while such cracks reduce the accuracy of the results of the transport measurements.

(3) The optical technique can be applied to a metal with many defects or a non-metallic material, whereas the methods sensitive to the Fermi surface cannot yield any information on such kind of materials.

(4) Materials with any dimensionality can be studied by the optical spectroscopy.

(5) Neither high magnetic field nor very low temperature is required in the optical experiments.

The optical transitions of the conduction electrons can be divided into two categories, intraband transitions and interband transitions. The intraband transitions have the character of the collective motion of charge carriers corresponding to the plasma oscillation, which is characteristic of a metal. The intraband transitions are described by the Drude model of dielectric function (complex ac dielectric constant),

$$\varepsilon(\omega) = \varepsilon_C - \omega_P^2 / (\omega^2 + i\,\omega\,\tau), \tag{1.4.1}$$

where $\hbar\omega$ is the photon energy, τ is the relaxation time of the carriers, and ω_P is the plasma frequency. The first term includes the constant contributions from the higher excitations. From the plasma frequency, the optical effective mass is estimated by the relation,

$$m^* = 4\,\pi\,n\,e^2 / \omega_P^2\,, \tag{1.4.2}$$

where n is the number density of the carriers per unit volume. This nature of the intraband transition has been widely used to estimate the optical effective mass, the number of the carriers and the relaxation time of a metal. In view of the relation,

$$\sigma_{dc} = \omega_P^2\tau / 4\pi = n\,e^2\tau / m^*, \tag{1.4.3}$$

it is clear that the intraband transitions are closely related to the dc conductivity. The integrated intensity of the intraband transitions, as well as the dc conductivity, is determined by the character of the Fermi surface.

It should be remarked here that the optical effective mass should be distinguished from the thermal effective mass related to the specific heat and from the cyclotron mass. These three masses agree with one another only in the free-electron model. Generally, the three masses take different values, particularly in a low-dimensional band described by the tight-binding model; only the orders of magnitudes are in agreement. These are defined as the averages of the Fermi velocities by different ways of

integrations [20]. In addition, the optical mass is a tensor; the principal values can be anisotropic with respect to the direction of light polarization. And the cyclotron mass is defined for each closed cyclotron orbit. Care must be taken, in comparing the "effective masses" obtained from different experiments.

Outstanding examples illustrating the relation of the Fermi surface and the intraband transitions can be found in recent literature. The one concerns the metal-insulator transition in $(DCNQI)_2Cu$ system, where DCNQI is *N,N′*-dicyanoquinonediimine [21]. In this system, the intraband transitions disappear abruptly at the phase transition accompanied by a drastic change in dimensionality. From this, it follows that the system changes from a three-dimensional metal into a one-dimensional insulator. Another one deals with the temperature dependence of the reflectance spectra of κ-$(BEDT\text{-}TTF)_2Ag(CN)_2 \cdot H_2O$ [22]. Disappearance of a part of the Fermi surface at low temperature was recognized as the suppression of the intraband transitions in this case.

On the other hand, the interband transitions, optical transitions across the band gaps, reflect the gap structure of the bands. By examining the fine structures of the spectral shape of interband transitions, the band structures of inorganic crystals including many semiconductors have been extensively investigated. However, the situation is somewhat different in the organic molecular conductors. Because of considerably narrow width of the conduction band, only a broad peak corresponding to the interband transitions can be observed in the infrared spectra of the molecular conductors. It seems that the interband transitions afford only coarse features of the band structure. However, the interband transitions can probe the

molecular packing mode in the crystal, which is very useful information in considering the band formation in view of the tight-binding model. This characteristic arises from the fact that the interband transitions have an origin similar to that of the intermolecular excitations of a charge-transfer complex, which is obvious in the framework of the tight-binding model. In this model, the origin of the band gaps is attributed to the difference between the transfer integrals, which are determined by the molecular packing.

In the determination of the basic optical properties of metals, the measurement of reflectivity is the most convenient and reliable technique. The absorption spectroscopy is difficult, because most metallic materials are not transparent. It is also difficult to measure the thickness of a small single crystal sample, which results in inaccurate estimation of the optical constants. On the other hand, the measurement of reflectivity or reflectance spectra requires only smooth surface of the sample. In this study, polarized reflectance spectra were measured by use of microspectrophotometers (spectrophotometers equipped with reflection microscopes and polarizers) arranged especially for small single crystals of molecular conductors. Cooling the sample down to low temperature is efficient to resolve different types of transitions. For this purpose, low temperature measurements were carried out.

1.5. The Purposes of This Study

This study mainly treats the determination of the band structures and

the Fermi surfaces of several two-dimensional conductors based on π-donor or π-acceptor molecules by use of the intensities of the intraband transitions obtained from the polarized reflectance spectra. The compounds picked up in this study possess considerably simple molecular arrangement, at least approximately. This has made it possible to relate the intraband transitions to the transfer integrals describing the band structure. The application of this method, developed in this study, is unique to the molecular conductors, which is describable by the simple tight-binding band model. Nevertheless, it is expected to extend the applicability of the optical spectroscopy in this field.

The obtained results are then compared with those from the other experiments such as the magneto-quantum oscillations or the ADMRO, in order to demonstrate the validity of the method. If both results are in agreement, it can be concluded that the band structure is well described by the simple tight-binding model over the energy range of about 1 eV, the highest excitation energy of conduction electrons within the band. This information cannot be obtained from the other experiments.

The interband transitions play only a secondary role in this study. In some cases, they are too weak to be treated quantitatively. Moreover, accurate theoretical calculations of the intensities of the interband transitions are considerably difficult, because they explicitly concern the excited states of a many-electron system. However, as mentioned in the preceding section, the interband transitions give useful information on the molecular arrangement. The interband transition thus helps the determination of the tight-binding band structures.

1.6. The Contents of the Present Thesis

In Chapter 2, theory of the optical transitions of the conduction electrons is treated in the framework of the tight-binding band model. Chapter 3 summarizes the experimental techniques and the procedures of analysis of the optical data.

From Chapters 4 to 7, experimental results and discussion of the electronic band structures and the shape of the Fermi surfaces of several two-dimensional molecular conductors are given. Chapter 4 is devoted to the study of the electronic structure of the θ-(BEDT-TTF)$_2$I$_3$. Since the molecular arrangement of this material has approximately high symmetry, θ-(BEDT-TTF)$_2$I$_3$ is considered to be suitable for the investigation from different points of view. Thereby, Chapter 4 includes not only the optical study but also the studies of the magnetic properties, thermoelectric power, the dHvA and SdH oscillations, and the ADMRO. Chapter 5 describes the study of the reflectance spectra of a dimeric BEDT-TTF salt, κ-(BEDT-TTF)$_2$I$_3$. Chapters 6 and 7 treat the studies of the reflectance spectra of two [Ni(dmit)$_2$] salts, Me$_4$N[Ni(dmit)$_2$]$_2$ and α-Et$_2$Me$_2$N[Ni(dmit)$_2$]$_2$, respectively. Chapter 8 deals with the study of reflectance spectra of a two-dimensional DMET salt, κ-(DMET)$_2$AuBr$_2$.

Concluding remarks for the present thesis are given in Chapter 9. Appendices describe some useful properties of the interband transitions in connection with the symmetry of the molecular arrangement.

References

1. H. Akamatu, H. Inokuchi and Y. Matsunaga: Nature **173** (1954) 168.
2. D. Jérome, A. Mazaud, M. Ribault and K. Bechgaard: J. Physique Lett. **41** (1980) L95-98; K. Bechgaard: Mol. Cryst. liq. Cryst. **79** (1982) 1.
3. See for example, *The Physics and Chemistry of Organic Superconductors*, Ed. by G. Saito and S. Kagoshima (Springer, Heidelberg, 1990); *Organic Superconductors: Synthesis, Structure, Properties and Theory*, Ed. by J. M. Williams, J. R. Ferraro, R. J. Thorn, K. D. Carlson, U. Geiser, H. H. Wang, A. M. Kini and M.-H. Whangbo (Prentice Hall, Englewood Cliffs, 1992).
4. K. Kikuchi, K. Murata, Y. Honda, T. Namiki, K. Saito, H. Anzai, K. Kobayashi, T. Ishiguro and I. Ikemoto: J. Phys. Soc. Jpn. **56** (1987) 4241.
5. K. Murata, K. Kikuchi, T. Takahashi, K. Kobayashi, Y. Honda, K. Saito, K. Kanoda, T. Tokiwa, H. Anzai, T. Ishiguro and I. Ikemoto: J. Mol. Elect. **4** (1988) 173.
6. G. C. Papavassiliou, G. A. Mousdis, J. S. Zambounis, A. Terzis, A. Hountas, B. Hilti, C. W. Mayer and J. Pfeiffer: Synth. Metals **27** (1988) B379.
7. A. Kobayashi, H. Kim, Y. Sasaki, R. Kato, H. Kobayashi, S. Moriyama, Y. Nishio, K. Kajita and W. Sasaki: Chem. Lett. 1819 (1987).
8. A. Kobayashi, H. Kobayashi, A. Miyamoto, R. Kato, R. A. Clark and A. E. Underhill: Chem. Lett. 2163 (1991).
9. A. F. Hebard, M. J. Rosseinsky, R. C. Haddon, D. W. Murphy, S. H. Glarum, T. T. M. Palstra, A. P. Ramirez and A. R. Kortan: Nature **350** (1991) 600.
10. T. Mori, A. Kobayashi, Y. Sasaki, H. Kobayashi, G. Saito and H. Inokuchi: Bull. Chem. Soc. Jpn. **57** (1984) 627.
11. For example, see: M.-H. Whangbo, J. M. Williams, P. C. W. Leung, M. A. Beno,

T. J. Emge, H. H. Wang, K. D. Carlson, G. W. Crabtree: J. Am. Chem. Soc. **107** (1985) 5815.

12. R. Hoffmann: J. Chem. Phys. **39** (1963) 1397.
13. D. Shoenberg: *Magnetic Oscillations in Metals* (Cambridge Univ. press, Cambridge, 1984).
14. M. V. Kartsovnik, P. A. Kononovich, V. N. Laukhin and I. F. Shchegolev: JETP Lett. **48** (1988) 542.
15. K. Kajita, Y. Nishio, T. Takahashi, W. Sasaki, R. Kato, H. Kobayashi, A. Kobayashi and Y. Iye: Solid State Commun. **70** (1989) 1189.
16. K. Yamaji: J. Phys. Soc. Jpn. **58** (1989) 1520.
17. R. Yagi, Y. Iye, T. Osada and S. Kagoshima: J. Phys. Soc. Jpn. **59** (1990) 3069.
18. K. Oshima, T. Mori, H. Inokuchi, H. Urayama, H. Yamochi and G. Saito: Phys. Rev. B **38** (1988) 938.
19. For a review, see: J. Wosnitza: Int. J. Modern Phys. B **7** (1993) 2707.
20. For example, see: J. M. Ziman: *Principles of the Theory of Solids* (Cambridge Univ. Press, Cambridge, 1972) 2nd Ed., Chaps. 8. and 9.
21. K. Yakushi, A. Ugawa, G. Ojima, T. Ida, H. Tajima, H. Kuroda, A. Kobayashi, R. Kato and H. Kobayashi: Mol. Cryst. Liq. Cryst. **181** (1990) 217.
22. R. Masuda, H. Tajima, H. Kuroda, H. Mori, S. Tanaka, T. Mori and H. Inokuchi: Synth. Metals **56** (1993) 2489.

Chapter 2.

Theoretical Aspects of the Optical Transitions of Conduction Electrons

2.1. Introduction

In this chapter, theoretical aspects of the optical transitions of the conduction electrons are described. The calculations of the tight-binding band are explained in Sec. 2.2. Section 2.3. deals with the intraband transitions on the basis of the relaxation time approximation of the Boltzmann equation. Finally, a brief treatment of the interband transitions is given in Sec. 2.4. It is recommended to refer to these descriptions to understand the analysis of the optical data in the following chapters.

2.2. The Band Structure

In the tight-binding framework, the band structure is calculated from the set of transfer integrals as follows. Using the second-quantization expression, the one-electron Hamiltonian is simply expressed as,

$$H = \sum_{l,l'} \sum_{m,m'} t_{lm,l'm'} a^{\dagger}_{lm} a_{l'm'} \quad , \tag{2.2.1}$$

where (l, m) specifies the m 'th MO in the l 'th unit cell. The summation is taken over the crystal. The Fourier transform of $a^{\dagger}_{lm}$ with respect to the lattice periodicity is given by,

$$a^{\dagger}_{lm} = N^{-1/2} \sum_{\boldsymbol{k}} a^{\dagger}_{m,\boldsymbol{k}} \exp(\mathrm{i}\boldsymbol{k}\cdot\boldsymbol{R}_l) \ , \tag{2.2.2}$$

where N is the number of the unit cells in the crystal, and $\boldsymbol{R}_l$ denotes the

position of the l 'th unit cell. Substitution with this converts Eq. (2.2.1) into,

$$H = N^{-1} \sum_{m,m'} \sum_{\boldsymbol{k},\boldsymbol{k}'} \sum_{l,l'} t_{l\,m,l'm'} \exp[\mathrm{i}(\boldsymbol{k}\cdot\boldsymbol{R}_l - \boldsymbol{k}'\cdot\boldsymbol{R}_{l'})]\, a^{\dagger}_{m,\boldsymbol{k}}\, a_{m',\boldsymbol{k}'} \,. \quad (2.2.3)$$

Taking account of the lattice periodicity, we have,

$$\begin{aligned} &\sum_{l,l'} t_{l\,m,l'm'} \exp[\mathrm{i}(\boldsymbol{k}\cdot\boldsymbol{R}_l - \boldsymbol{k}'\cdot\boldsymbol{R}_{l'})] \\ &= \sum_{l'} \exp[\mathrm{i}(\boldsymbol{k}-\boldsymbol{k}')\cdot\boldsymbol{R}_{l'}] \sum_{l-l'} t_{l\,m,l'm'} \exp[\mathrm{i}\boldsymbol{k}\cdot(\boldsymbol{R}_l - \boldsymbol{R}_{l'})] \\ &= \sum_{l'} \exp[\mathrm{i}(\boldsymbol{k}-\boldsymbol{k}')\cdot\boldsymbol{R}_{l'}] \sum_{l} t_{0\,m,l\,m'} \exp(\mathrm{i}\boldsymbol{k}\cdot\boldsymbol{R}_l) \,. \end{aligned} \quad (2.2.4)$$

The summation over l' results in

$$\sum_{l'} \exp[\mathrm{i}(\boldsymbol{k}-\boldsymbol{k}')\cdot\boldsymbol{R}_{l'}] = N\,\delta_{\boldsymbol{k},\boldsymbol{k}'} \,. \quad (2.2.5)$$

Thus Eq. (2.2.3) is reduced into,

$$\begin{aligned} H &= \sum_{m,m'} \sum_{\boldsymbol{k}} [\sum_{l} t_{0\,m,l\,m'} \exp(\mathrm{i}\boldsymbol{k}\cdot\boldsymbol{R}_l)\, a^{\dagger}_{m,\boldsymbol{k}}\, a_{m',\boldsymbol{k}}] \\ &= \sum_{m,m'} \sum_{\boldsymbol{k}} h_{m,m'}(\boldsymbol{k})\, a^{\dagger}_{m,\boldsymbol{k}}\, a_{m',\boldsymbol{k}} \,, \end{aligned} \quad (2.2.6)$$

where,

$$h_{m,m'}(\boldsymbol{k}) = \sum_{l} t_{0\,m,\,l\,m'} \exp(\mathrm{i}\boldsymbol{k}\cdot\boldsymbol{R}_l) \ . \qquad (2.2.7)$$

This is an $M \times M$ matrix, M being the number of MOs in the unit cell. Equation (2.2.6) has been already diagonalized with respect to $\boldsymbol{k}$. The major contribution in the summation over (l, m') in (2.2.6) comes from the nearest-neighbor sites of the (0,m) one. By diagonalizing $h_{m,m'}(\boldsymbol{k})$, Eq. (2.2.7), we obtain the eigenvalues, $\varepsilon_{\mu}(\boldsymbol{k})$ (μ = 1, 2, ...M) for each $\boldsymbol{k}$. That is,

$$H = \sum_{\mu,\,\boldsymbol{k}} \varepsilon_{\mu}(\boldsymbol{k})\, a^{\dagger}_{\mu,\,\boldsymbol{k}}\, a_{\mu,\,\boldsymbol{k}} \quad , \qquad (2.2.8)$$

with,

$$a_{\mu,\,\boldsymbol{k}} = \sum_{m} U_{\mu,m}(\boldsymbol{k})\, a_{m\boldsymbol{k}} \quad , \qquad (2.2.9)$$

where $U_{\mu,m}$ is the element of the unitary matrix to diagonalize $h_{m,m'}(\boldsymbol{k})$. The tight-binding band structure is thus given as $\varepsilon_{\mu}(\boldsymbol{k})$. From this, any electronic properties related to the conduction band can be given in terms of μ (the branch index), $\boldsymbol{k}$, and transfer integrals, as far as the one-electron band picture holds.

2.3. Intraband Transitions [1,2]

In the equilibrium state, the distribution of the electrons in a conduction band is given by the Fermi distribution function, $f_0(\varepsilon_k, T)$. Application of an external electric field, $\boldsymbol{E}(\boldsymbol{r}, t)$, perturbs the distribution into $f(\boldsymbol{r}, T) = f_0 + g(\boldsymbol{r}, T)$. The Boltzmann equation for $f(\boldsymbol{r},T)$ is given as,

$$\mathrm{d}f / \mathrm{d}t = \partial f / \partial t + (\boldsymbol{v}_k - e\boldsymbol{E}/\hbar) \cdot \mathrm{grad}_k f \ . \qquad (2.3.1)$$

Assuming that the relaxation of $g(\boldsymbol{r},T)$ to 0, as well as $f(\boldsymbol{r},T)$ to f_0, is a single exponent type with the relaxation time, τ, we obtain a differential equation for $g(\boldsymbol{r},T)$,

$$\partial g / \partial t + \boldsymbol{v}_k \cdot \mathrm{grad}_r g + g / \tau = -e\boldsymbol{E} \cdot \boldsymbol{v}_k (\partial f_0 / \partial \varepsilon_k) \ . \qquad (2.3.2)$$

Since we concern only the linear response to the field, only the term linear to $\boldsymbol{E}$ is retained. Suppose that both $\boldsymbol{E}$ and g are periodic in time and space, i.e.,

$$\boldsymbol{E} = \boldsymbol{E}_{q,\omega} \exp[\mathrm{i}(\boldsymbol{q} \cdot \boldsymbol{r} - \omega t)] \ , \qquad (2.3.3)$$

$$g = g_{q,\omega} \exp[\mathrm{i}(\boldsymbol{q} \cdot \boldsymbol{r} - \omega t)] \ . \qquad (2.3.4)$$

Then, the solution of Eq. (2.3.2) is given in terms of $g_{q,\omega}$,

$$g_{q,\omega}(\boldsymbol{k}) = -e\tau \boldsymbol{E}_{q,\omega} \cdot \boldsymbol{v}_k (-\partial f_0 / \partial \varepsilon_k) / [1 + \tau(\boldsymbol{q} \cdot \boldsymbol{v}_k - \mathrm{i}\omega)] \ . \qquad (2.3.5)$$

With this distribution function, any kind of the bulk collective response to the field can be calculated.

In what follows, the principal value of the conductivity tensor is calculated. The optical response can be expressed in terms of the complex conductivity with respect to the electric field of the radiation. The current density along the principal axis, x, is written in the form,

$$\boldsymbol{J}_{\mathrm{x}} = 2\,(1/8\pi^3) \int (-e\,\boldsymbol{v}_{\boldsymbol{k}})_{\mathrm{x}}\, g\ \mathrm{d}^3\boldsymbol{k}\ . \tag{2.3.6}$$

The factor 2 stems from the spin degrees of freedom. Substituting g in Eq. (2.3.6) with Eqs. (2.3.4) and (2.3.5), we obtain

$$(\boldsymbol{J}_{\mathrm{q},\,\omega})_{\mathrm{x}} = (e^2/4\pi^3)\,(\boldsymbol{E}_{\boldsymbol{q},\,\omega})_{\mathrm{x}} \int \tau\,|\boldsymbol{v}_{\boldsymbol{k}}|^2\,[1+\tau(\boldsymbol{q}\cdot\boldsymbol{v}_{\boldsymbol{k}} - \mathrm{i}\omega)]^{-1}\,(-\partial f_0 / \partial\varepsilon_{\boldsymbol{k}})\,\mathrm{d}^3\boldsymbol{k}\ . \tag{2.3.7}$$

Comparing this with the definition of the conductivity, σ,

$$\boldsymbol{J}_{\boldsymbol{q},\,\omega} = \sigma(\boldsymbol{q},\,\omega)\,\boldsymbol{E}_{\boldsymbol{q},\,\omega}\ , \tag{2.3.8}$$

we have,

$$\sigma_{\mathrm{x}}(\boldsymbol{q},\,\omega) = (e^2/4\pi^3) \int \tau\,|\boldsymbol{v}_{\boldsymbol{k}}|^2\,[1+\tau(\boldsymbol{q}\cdot\boldsymbol{v}_{\boldsymbol{k}} - \mathrm{i}\omega)]^{-1}\,(-\partial f_0 / \partial\varepsilon_{\boldsymbol{k}})\,\mathrm{d}^3\boldsymbol{k}\ . \tag{2.3.9}$$

This can be reduced into

$$\sigma_x(\omega) = (e^2/4\pi^3\hbar)\int_{F.S.} [(v_F)_x^2/|\boldsymbol{v}_F|]\,(1/\tau - i\,\omega)^{-1}\,dS\,, \qquad (2.3.10)$$

by use of the facts,

$$\omega = 2\pi c' |\boldsymbol{q}| \gg |\boldsymbol{q}\cdot\boldsymbol{v}_k|\,, \qquad (2.3.11)$$

$$-\partial f_0 / \partial \varepsilon_k \approx \delta(\varepsilon - \varepsilon_F), \qquad (2.3.12)$$

$$d^3\boldsymbol{k} = (d\,\varepsilon\ / |\,\mathrm{grad}_k\ \varepsilon_k|)\,dS\,, \qquad (2.3.13)$$

where c' is the light velocity in the material, and $k_B T \ll \varepsilon_F$ is assumed. The integration in Eq. (2.3.10) is taken over the Fermi surface. We assume here that τ in Eq. (2.3.10) is independent of $|\boldsymbol{k}|$ and ω. Only the anisotropy of τ is phenomenologically taken account of. Thus we have,

$$4\pi\,\sigma_x(\omega) = (1/\tau_x - i\omega)^{-1}\,(e^2/4\pi^2\hbar)\int_{F.S.} [(v_F)_x^2/|\boldsymbol{v}_F|]\ dS\,. \qquad (2.3.14)$$

The assumptions made for τ is not a trivial one; it should be checked by experiments in each case. Introduction of the plasma frequency, $(\omega_P)_x$, by

$$(\omega_P^2)_x = (e^2/\pi^2\hbar)\int_{F.S.} [(v_F)_x^2/|\boldsymbol{v}_F|]\ dS\ , \qquad (2.3.15)$$

leads to

$$4\pi\,\sigma_x(\omega) = (\omega_P^2)_x / (1/\tau - i\,\omega)\,, \qquad (2.3.16)$$

or, in terms of the dielectric function,

$$\varepsilon_x(\omega) - 1 = (4\pi i/\omega)\,\sigma_x(\omega) = -(\omega_P^2)_x / (\omega^2 - i\omega\tau) . \quad (2.3.17)$$

The final expression is equivalent to that of the Drude model. The intensity of the intraband transitions, ω_P^2, is thus related to the band structure near the Fermi surface. That is, the plasma frequency can be calculated from the band structure, $\varepsilon_\mu(k)$ in Eq. (2.2.8), using Eq. (2.3.15). Application of Gauss' theorem to Eq. (2.3.15) yields

$$(\omega_P^2)_x = (e^2/\pi^2\hbar)\int_{F.S.} (v_F)_x \boldsymbol{u}_x \cdot d\boldsymbol{S}$$

$$= (e^2/\pi^2\hbar)\int \mathrm{div}\,[(v_F)_x \boldsymbol{u}_x]\, f_0(\varepsilon_k)\, d^3\boldsymbol{k}$$

$$= (e^2/\pi^2\hbar^2)\int (\partial^2\varepsilon/\partial k_x^2) f_0(\varepsilon_k)\, d^3\boldsymbol{k} , \quad (2.3.18)$$

where $\boldsymbol{u}_x$ is the unit vector in the x-direction. For a parabolic band given as

$$\varepsilon = -\hbar^2[k_x^2/2m^*_x + k_y^2/2m^*_y + k_z^2/2m^*_z] , \quad (2.3.19)$$

Eq. (2.3.18) reduces into a simple form,

$$(\omega_P^2)_x = 4\pi n e^2/m^*_x , \quad (2.3.20)$$

where

$$n = (1 / 4\pi^2) \int f_0(\varepsilon_k)\, \mathrm{d}^3\boldsymbol{k} \quad , \tag{2.3.21}$$

is the number density of the electrons.

In the above discussion, the intraband transitions are regarded as the transverse collective motion of the conduction electrons. Such kind of treatment is based closely on the theory of random-phase approximation for the Fermi liquid. However, the assumption for τ to be independent of $|\boldsymbol{k}|$ and ω is a subtle problem. If there is a relaxation process important only at low frequencies, the relation between the optical properties and the Fermi surface, Eq. (2.3.15), may be modified. This can be detected as the discrepancy between the band structure deduced from the optical properties and that concluded from the transport properties. Such a "dynamical" effect implies the deviation of the band structure just near the Fermi surface from the global one over the range of the photon energy.

2.4. Interband Transitions [3-5]

In the framework of the one-electron band theory, the interband transitions can be regarded as one-electron excitations, which is in contrast to the case of the intraband transitions. For such a process, the probability of the optical transition can be readily obtained. Suppose the Hamiltonian for the tight-binding model, Eq. (2.2.1),

$$H = \sum_{l,l'} \sum_{m,m'} t_{lm,l'm'} a^{\dagger}_{lm}\, a_{l'm'} \quad , \tag{2.4.1}$$

And the x-component of the electric dipole moment operator is written in the form,

$$P_{\mathrm{x}} = e \sum_{l,\,m} (\boldsymbol{R}_{l,\,m})_{\mathrm{x}}\, a^{\dagger}_{l\,m}\, a_{l\,m} \ , \tag{2.4.2}$$

where $\boldsymbol{R}_{l,\,m}$ is the position of the m 'th molecular site in the l 'th unit cell. From the standard first-order perturbation theory with the dipole approximation, the transition probability per unit time interval is obtained as,

$$w = E_{\mathrm{x}}^{\,2} \sum_{\mathrm{i,\,f}} <\mathrm{i}\,|\,P_{\mathrm{x}}\,|\,\mathrm{f}><\mathrm{f}\,|\,P_{\mathrm{x}}\,|\,\mathrm{i}>\,(\pi / 2\hbar)\,\delta(\hbar\omega - \hbar\omega_{\mathrm{f,\,i}}) \ , \tag{2.4.3}$$

where i and f denotes the initial and final states, respectively. The energies of the initial and final states are ε_{i} and ε_{f}, respectively, and the transition energy is then, $\hbar\omega_{\mathrm{f,\,i}} = \varepsilon_{\mathrm{f}} - \varepsilon_{\mathrm{i}}$. The power loss of light due to the absorption can be expressed in terms of the transition probability, that is,

$$p = \hbar\,\omega\ w \ . \tag{2.4.4}$$

On the other hand, the power loss is related to conductivity as,

$$p = \sigma_{\mathrm{x}}\, E_{\mathrm{x}}^{\,2}\, V / 2 \ , \tag{2.4.5}$$

where V is the volume of the crystal. Comparison of Eq. (2.4.5) with Eq. (2.4.4) yields

$$\sigma_x = (2 / V E_x^{\,2})\, \hbar\omega\, w \quad . \tag{2.4.6}$$

Consequently, from Eqs. (2.4.3) and (2.4.6), we obtain,

$$\sigma_x(\omega) = (\pi / V\hbar) \sum_{i,f} \omega_{f,i} < i \mid P_x \mid f > < f \mid P_x \mid i > \delta(\omega - \omega_{f,i}), \tag{2.4.7}$$

When the δ-function is replaced by a Lorentzian line-shape function with the width of γ, Eq. (2.4.7) is rewritten in the form,

$$\sigma_x(\omega) = (2i / V\hbar) \sum_{i,f} \omega_{f,i} < i \mid P_x \mid f >< f \mid P_x \mid i > \omega\ /(\omega^{\,2} - \omega_{f,i} + i\,\gamma\omega)\ . \tag{2.4.8}$$

The commutator of H and P_x is,

$$[H\ , P_x] = e \sum_{l,l'} \sum_{m,m'} t_{\,lm,l'm'}\, a^{\dagger}_{\,lm}\, a_{l'm'}\, (\boldsymbol{R}_{l,m} - \boldsymbol{R}_{\,l',m'})_x\, (a^{\dagger}_{\,lm}\, a_{l'm'} - a^{\dagger}_{\,l'm'}, a_{lm}). \tag{2.4.9}$$

The matrix element of $[H, P_x]$ is,

$$< i \mid [H, P_x] \mid f > = (\varepsilon_i - \varepsilon_{\,f}) < i \mid P_x \mid f > . \tag{2.4.10}$$

Using this, Eq. (2.4.8) is converted into,

$$\sigma_x(\omega) = (2 / iV\hbar^{\,3}) \sum_{i,f} < i \mid [H, P_x] \mid f > < f \mid [H, P_x] \mid i >$$

$$(\omega / \omega_{f,i}) / (\omega^2 - \omega_{f,i} + i\gamma\omega) \ . \tag{2.4.11}$$

which is calculable in the framework of the tight-binding model by use of Eq. (2.4.9). In the actual calculations, the pair of states, (i, f), is specified by the pair, (μ, $\boldsymbol{k}$) and (μ', $\boldsymbol{k}$), the occupied and vacant one-electron states, respectively. The matrix element, then, reduces into that between the one-electron states (μ, $\boldsymbol{k}$) and (μ', $\boldsymbol{k}$) and the summation is taken over the pairs of the branch indices (μ, μ') and all $\boldsymbol{k}$ in the first Brillouin zone.

This formulation is based simply on the one-electron picture; highly excited one-electron states, in which the many-body effect may play an essential role even in the metallic state, are concerned. As regards the quantitative features, the result may be modified, even if the band picture holds for low-lying states. However, it is still useful in elucidating the basic origin and character of the transition.

References

1. J. M. Ziman: *Principles of the Theory of Solids* (Cambridge Univ. Press, Cambridge, 1972) 2nd Ed., Chaps. 7. and 8.
2. N. W. Ashcroft and N. D. Mermin: *Solid State Physics* (Saunders College, Philadelphia, 1976).
3. H. Tajima: Doctorate Thesis, The Univ. of Tokyo, 1986.
4. H. Tajima, K. Yakushi, H. Kuroda and G. Saito: Solid State Commun. **56** (1985)

159.

5. Useful discussions by Mr. T. Naito (Toho Univ.) on the derivation of Eq. (2.4.7) is gratefully appreciated.

Chapter 3.

Measurement of Polarized Reflectance Spectrum and Analysis of the Data

3.1. Measurement of Polarized Reflectance Spectrum

As mentioned in Sec. 1.4., the polarized reflectance spectroscopy is the most efficient tool to examine the basic optical properties of a metallic material. The standard experimental configuration used for a single crystal of conductors is the normal reflectance measurement, where the incident light is normal to the crystal face. The absolute value of reflectivity can be determined as a function of the wavenumber and polarization of light by comparing the intensity of the light reflected from the sample face with that from a standard mirror.

With regard to the application to the organic π-molecular conductors, the main difficulty lies in the smallness of their single crystals. The typical dimension of the most developed crystal face is about 1×1 mm^2 or less. This problem can be solved by combined use of a microscope and a spectrophotometer, the microspectrophotometry

A mid-infrared reflection microspectrophotometer made by Dr. H. Tajima (Univ. of Tokyo), JASCO MIR-300, has been used in this study. The main experimental techniques for the room temperature and low temperature measurements of the infrared reflectance spectra have been established by him, and the details are described in his thesis [1,2]. The spectrometer is originally equipped with a semiconductor detector of InSb (1800-5400 cm^{-1}) and HgCdTe (720-1800 cm^{-1}) by Infrared Associates Inc. The optical study in Chap. 4. was carried out with this combination. The performance of the apparatus has been improved by the introduction of a liquid helium cooled composite Ge bolometer by Infrared Laboratories Inc. This has extended the spectral to 450-6000 cm^{-1} and has shown to

afford better signal-to-noise ratio over the mid-infrared region, during this study. The experiments in Chaps. 5-8 were done with this improved version. For the low temperature measurements, a liquid helium flow type cryostat, CF 104A by Oxford Instruments Limited, was used.

In the near-infrared and visible regions (4200-25000 cm^{-1}), a modified version of a reflection microspectrophotometer, Olympus MMSP, has been used. The low temperature measurements in these regions were carried out by use of a closed cycle helium refrigerator, CTI SPECTRIM. Since the focal length of the objective lenses in the microscope varies with wavenumber, the height of the sample has to be adjusted at each wavenumber. This process has been automated by Dr. T. Ida (Himeji Institute of Technology). Since the optical system used for the mid-infrared region contains no lens, the adjustment of sample height is not required in the mid-infrared measurements.

The alternate measurement of the reflectance signals of a sample and a standard mirror at each wavenumber is employed in order to minimize the effects of drifting of the atmosphere (H_2O and CO_2 in air), the source light intensity and the detector sensitivity. This was done by use of computer-controlled movable sample stages. The light was chopped, monochromatized, polarized and then introduced in the microscopes equipped with half mirrors separating the incident and reflected rays. The light intensity data were collected by lock-in amplifiers and transferred to the computers. The reflectivity values were calculated from the ratio of the sample signal to the mirror signal. As the standard mirror, a silver mirror is used for the mid-infrared measurement, and a Si plate for the near-infrared and visible regions.

In every case in this study, the crystal face on which the spectra were measured has rather high symmetry; it includes at least one unique axis. In such a case, the principal directions of reflectance should agree with the crystal axes, because the reflectivity, as well as the conductivity, is a tensor quantity. This was checked in every measurement by comparing the X-ray photographs with the reflectance results obtained by rotating the polarizer.

In the low temperature measurements, a single crystal sample was mounted on a small Si plate placed on the rotating center of a goniometer head for each cryostat attached on the cold head of the cryostat. The attachment of the sample and the Si plate was made by Apiezon L grease. The crystal face was aligned so as to retain the normal incidence of light at room temperature. The goniometer head was covered with a radiation shield and a vacuum chamber. Both have windows of KBr (mid-infrared) or quartz (near-infrared and visible), through which the ray can pass. The window and the sample face were not kept in parallel, in order to avoid the light reflected from the window. Evacuation inside the vacuum chamber should be followed by readjustment of the position of the cryostat. In the cooling, the temperature of the goniometer head was monitored by Au(Fe)/Chromel thermocouple.

The alternate measurement was applied also to the low temperature case. In the mid-infrared apparatus, a movable mirror was installed above the cryostat to switch the ray focus from the sample in the cryostat to a standard mirror. The effect of the KBr windows was corrected by measuring the data for the standard Ag mirror placed in the cryostat instead of a sample at room temperature. In the near-infrared and visible measurements,

the position of the cryostat was automatically adjustable. Thereby, the alternate measurement was done by changing the ray focus from the sample on the cold head to a Si plate outside by moving the cryostat. The effect of the quartz windows was also corrected by measuring the room temperature reflectance of a Si plate or the sample.

3.2. Analysis of the Reflectance Spectrum

In this study, the most important thing is the estimation of the intensity of the intraband transitions. Since the observed spectra contain other spectral features such as the interband transitions, it is required to separate the intraband contribution from the other ones.

A curve-fitting method was applied to extract the intraband contributions from the reflectance spectra. As the model function, the Drude-Lorentz model [3] was used. It is written, in terms of the dielectric function, as

$$\varepsilon(\omega) = \varepsilon_C - \omega_P^2 / (\omega^2 + i\omega / \tau) + \sum_j f_j / [(\omega_j^2 - \omega^2) - i\gamma_j\omega] \ . \quad (3.2.1)$$

The reflectivity is related to the dielectric function by the equation,

$$R = [1 + |\varepsilon| - \sqrt{2(|\varepsilon| + \mathrm{Re}(\varepsilon))}] / [1 + |\varepsilon| + \sqrt{2(|\varepsilon| + \mathrm{Re}(\varepsilon))}] \ . \quad (3.2.2)$$

The first term in the right-hand side of Eq.(3.2.1), ε_C, stands for the constant contribution from the higher energy transitions outside the experimental spectral region. The second term, the Drude term, gives the contribution of the intraband transition. The square of the Drude plasma

frequency, ω_P^2, is the integrated intensity of the intraband transitions, and τ is the relaxation time of the charge carriers. The summation describes the contributions of other transitions: the interband transitions, the e-mv coupling modes. The intensity, position and spectral width of each term in the summation, are given as f_j, ω_j and γ_j, respectively. Strictly speaking, they do not follow the Lorentzian profile. However, it is found in every case in this study that these contributions are well approximated as a Lorentzian or as a superposition of a few Lorentzian profiles, at least at sufficiently low temperature. Thus, this Drude-Lorentz fitting afforded satisfactory results for the estimation of the intraband plasma frequencies.

As is clear from Eq. (3.2.2), the reflectance spectrum is not the superposition of different transitions. This makes it difficult to choose the Lorentzian terms suitable for the curve-fitting. In stead of the reflectance spectra, the conductivity spectra can be used for the choice. The conductivity spectra, in which the contributions of different transitions are more resolved and the superposition of them is visible, were obtained by the Kramers-Kronig transformation [4] of the reflectance spectra. The use of conductivity spectra enables us to find out a deviation from the Drude behavior easily.

3.3. Derivation of Band Structure and Fermi Surface

In Sec. 2.3., a general expression for the intensity of the intraband transitions is derived. That is,

$$(\omega_P^2)_x = (e^2/\pi^2\hbar)\int_{F.S.} [(v_F)_x^2 / |\boldsymbol{v}_F|]\ dS \ , \qquad (3.3.1)$$

In a two-dimensional case, this can be reduced into a very simple form. Let the *xy*-plane be the two-dimensional plane. It follows immediately that $(\omega_P^2)_z = 0$ because $(v_F)_z$ is zero at any $\boldsymbol{k}$. The transformations,

$$dS = |\boldsymbol{v}_F|\ dk_{Fy}\, dk_{Fz} / |(v_F)_x| = |\boldsymbol{v}_F|\ dk_{Fx}\, dk_{Fz} / |(v_F)_y| \ , \qquad (3.3.2)$$

yield the set of equations,

$$(\omega_P^2)_x = (e^2/\pi^2\hbar)\ (2\pi / z)\int_{F.S.} |(v_F)_x|\ dk_{Fy} \ , \qquad (3.3.3)$$

$$(\omega_P^2)_y = (e^2/\pi^2\hbar)\ (2\pi / z)\int_{F.S.} |(v_F)_y|\ dk_{Fx} \ , \qquad (3.3.4)$$

where z denotes the lattice period along the z-direction. These equations well describe the anisotropic shape of a two-dimensional Fermi surface and the anisotropy of the plasma frequency. Since the Fermi velocity vector is perpendicular to the Fermi surface at each $\boldsymbol{k}_F$, the major contribution comes from the portion of the Fermi surface nearly perpendicular to the light polarization.

If the band structure is describable only by two independent transfer integrals, t_1 and t_2, they can be directly determined form the plasma frequencies by Eqs. (3.3.3) and (3.3.4). In the actual calculations, the knowledge of the Fermi level is required to settle the Fermi surface. The Fermi energy can be determined from the band filling. That is, the

following equation should be satisfied,

$$F\, S_{BZ} = \int | k_{Fx} |\ \mathrm{d}k_{Fy} = \int | k_{Fy} |\ \mathrm{d}k_{Fx}\ , \qquad (3.3.5)$$

where F is the band filling expected from the stoichiometry. The integrals in (3.3.5) stand for the half of the area inside the Fermi surface. By solving Eqs. (3.3.3)-(3.3.5) simultaneously, the three band parameters t_1, t_2 and E_F can be derived from the three experimental data, ω_{Px}, ω_{Py} and the stoichiometry. The integrals in Eqs. (3.3.3)-(3.3.5) were numerically evaluated in a computational program to find out the optimal values of t_1, t_2 and E_F, which was developed in this study.

From the band structure and Fermi surface determined as above, the cross-sectional area of each cyclotron orbit and the extremal values of k_{Fx} and k_{Fy} can be readily calculated. These parameters are referred to in the comparison of the optical results with those of the magneto-quantum oscillations and the ADMRO. The cyclotron mass was also evaluated following the definition [5],

$$m^*_c = (\hbar^2 / 2\pi)\ (\mathrm{d}S\ / \mathrm{d}E)\ ;\ E = E_F, \qquad (3.3.6)$$

where S is the corresponding cross-sectional area. For a two-dimensional system, it is noteworthy that the evaluation of the cyclotron mass is the same as that of the density of states.

3.4. A Case Study of the Relation between the Optical Properties and Fermi Surface

In order to illustrate how the Fermi surface determines the optical properties and other physical properties, a case study was carried out for a model of a realistic two-dimensional molecular arrangement shown in Fig. 3.1. The plasma frequencies, the cross-sectional areas, the cyclotron masses and the extremal values of the Fermi wavenumbers were calculated as functions of the transfer integrals, assuming 1/2- or 3/4-filling of the conduction band. The computational method is outlined in the preceding section.

In the following, the lattice parameters normalized to unity are used. The band structure of the model is given by,

$$E(k_x, k_y) = 2t_x \cos k_x \pm 2\,(t_y^{\,2} + 2t_y\, t_y' \cos k_y + t_y'^{\,2})^{1/2} \cos\,(k_x / 2), \quad (3.4.1)$$

When $t_y = t_y'$, this reduces into

$$E(k_x, k_y) = 2t_x \cos k_x \pm 4\, t_y \cos(k_x / 2) \cos\,(k_y / 2)\,. \qquad (3.4.2)$$

There are the degeneracies between the two branches at the zone boundary ($k_x = \pi$ or $k_y = \pi$) in Eq. (3.4.2), while it is removed at the $k_y = \pi$ line in Eq. (3.4.1). As $t_y = t_y' = 0$ is approached, the system becomes one-dimensional, while the system remains two-dimensional even at $t_x = 0$.

The physical properties were calculated for the 1/2- or 3/4-filled band of Eq. (3.4.2), as functions of the ratio, t_x / t_y or t_y / t_x , where $t_x + t_y =$

1 eV. The results are displayed in Figs. 3.2-3.6. for the 1/2-filled case and in Figs. 3.7-3.11 for the 3/4-filled case.

In Figs. 3.2 and 3.7, the ratio of the plasma frequencies for the polarization $\boldsymbol{E} \parallel \boldsymbol{x}$ and $\boldsymbol{E} \parallel \boldsymbol{y}$ is plotted. The effect of the dimensionality is obvious. By use of these diagrams, we can determine the ratio of the transfer integrals from the observed anisotropy of the plasma frequency. Since the plasma frequency is proportional to $x/\sqrt{V}$ (for the $\boldsymbol{E} \parallel \boldsymbol{x}$ polarization) or to $y/\sqrt{V}$ (for $\boldsymbol{E} \parallel \boldsymbol{y}$), where V is the cell volume, the plasma frequency should be normalized with respect to these factors before use.

The absolute values of the transfer integrals in eV units can be obtained by comparing the observed values of the plasma frequency with the ones plotted in Figs. 3.3 and 3.8, which are normalized for the lattice parameters and for $t_T^{1/2} = (t_x + t_y)^{1/2}$ and are measured in $\text{Å}^{1/2}\,\text{eV}^{1/2}$ units. Suppose that $t_x + t_y = t_T$ eV in our case and that we have the value of the observed plasma frequency of ω_P^{obs} eV $\text{Å}^{1/2}$ normalized for the lattice parameters. Using the diagrams, we can find the value for $t_x + t_y =$ 1 eV, $\omega_P^{calc}\ \text{Å}^{1/2}\,\text{eV}^{1/2}$, from the relevant transfer integral ratio. Then, we obtain $t_T = (\omega_P^{obs}/\omega_P^{calc})^2$, because the plasma frequency is proportional to the square root of the transfer integrals. From the sum and ratio of the two, the value of each transfer integral can be determined.

The fractional value of the cross-sectional area for each cyclotron orbit is shown in Figs. 3.4 and 3.9, as a function of the transfer integral ratio. The topology of the Fermi surface varies with the ratio as schematically shown in Fig. 3.12, where the notation of the orbits is also shown. Since the β-orbit has the constant value (1.0 for the 1/2-filled case and

0.5 for 3/4-filled case), it is omitted in the diagrams. Strictly speaking, the cyclotron motion around the α-orbit should not be observed for this band structure. Therefore, the present results should be regarded as those with considerably small difference between t_y and t_y'.

Figures 3.5 and 3.10 show the cyclotron mass for each orbit for $t_x + t_y = 1$ eV. We can obtain the cyclotron mass values in our case, $t_x + t_y = t_T$ eV, by dividing those in the diagrams by $x\ y\ t_T$. In the 1/2-filled case, the mass for the β-orbit is about twice as large as that for the α-orbit over a wide range of the transfer integral ratio.

Figures 3.6 and 3.11 display the radii of the cyclotron orbits. These values are useful not only in drawing the approximate shape of the Fermi surface but also in predicting the ADMRO periods.

In order to see the effect of the removal of degeneracy, some quantities are calculated for the 1/2-filled band of Eq. (3.4.1) as functions of the relative difference, $2(t_y - t_y')/(t_y + t_y')$. The values of the transfer integrals, $t_x = 0.048$ eV and $t_y + t_y' = 0.104$ eV are used. Figure 3.13 shows the plasma frequencies. It is found that the intensity of intraband transitions for $\boldsymbol{E} \parallel \boldsymbol{y}$ decreases more rapidly than that for $\boldsymbol{E} \parallel \boldsymbol{x}$. The cyclotron masses are shown in Fig. 3.14, where the magnetic breakdown is assumed for the β-orbit. Compared with the plasma frequencies, they seem to be less sensitive to the removal of degeneracy in this model.

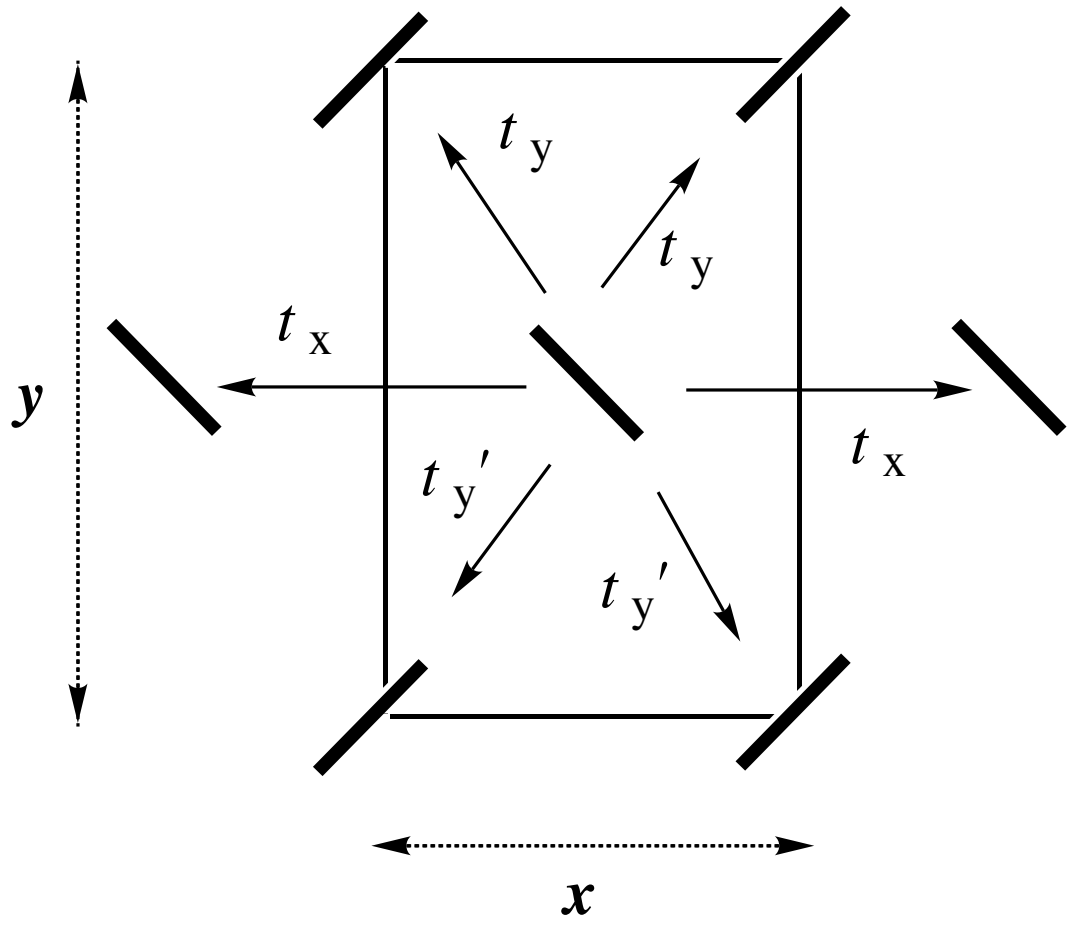

Fig. 3.1. A realistic model of the intermolecular interactions in two-dimensional molecular conductors. All the molecules are equivalent. Each molecule is surrounded by six nearest neighbor ones. Solid lines indicates the unit cell.

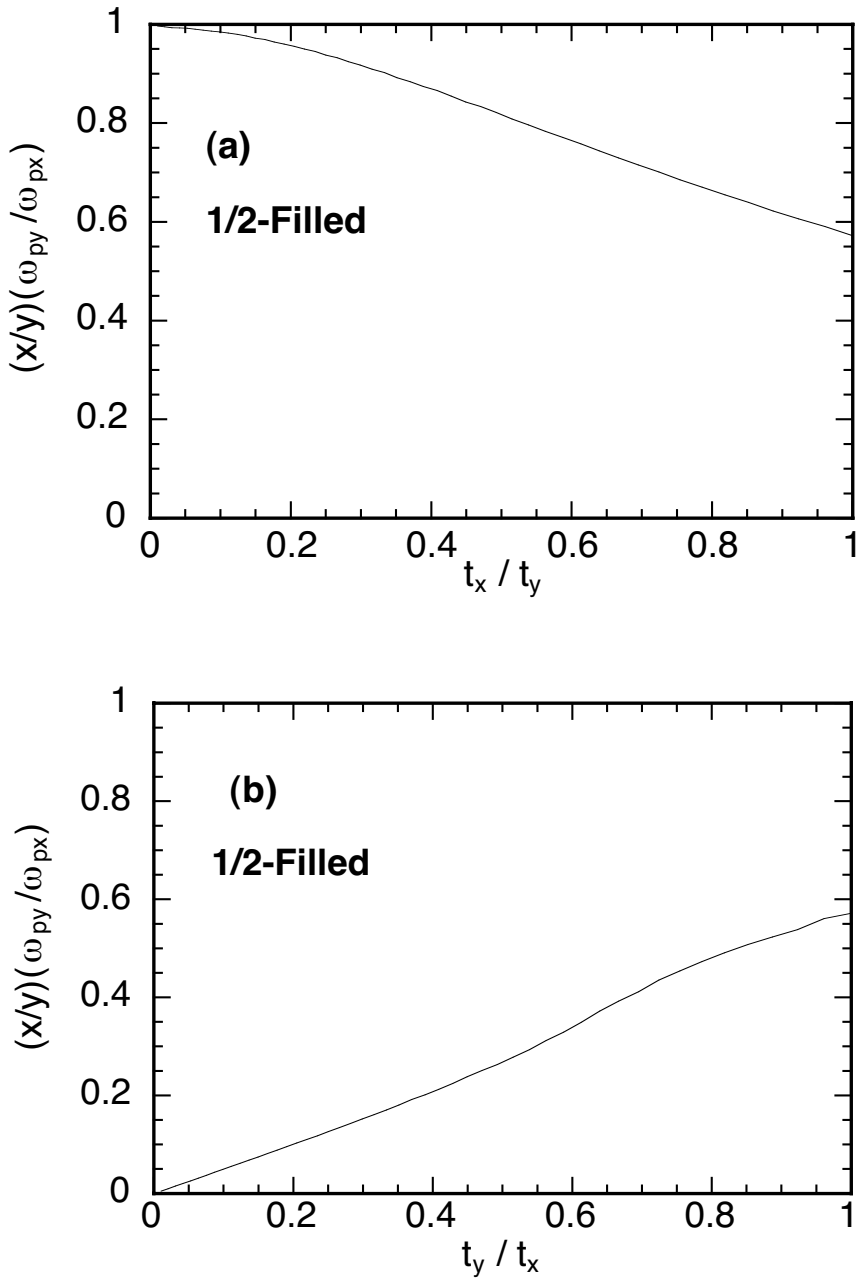

Fig. 3.2. Anisotropy of plasma frequency plotted against the transfer integral ratio, for the 1/2-filled model band with $t_y = t_y'$. (a) for $t_x < t_y$, and (b) for $t_x > t_y$.

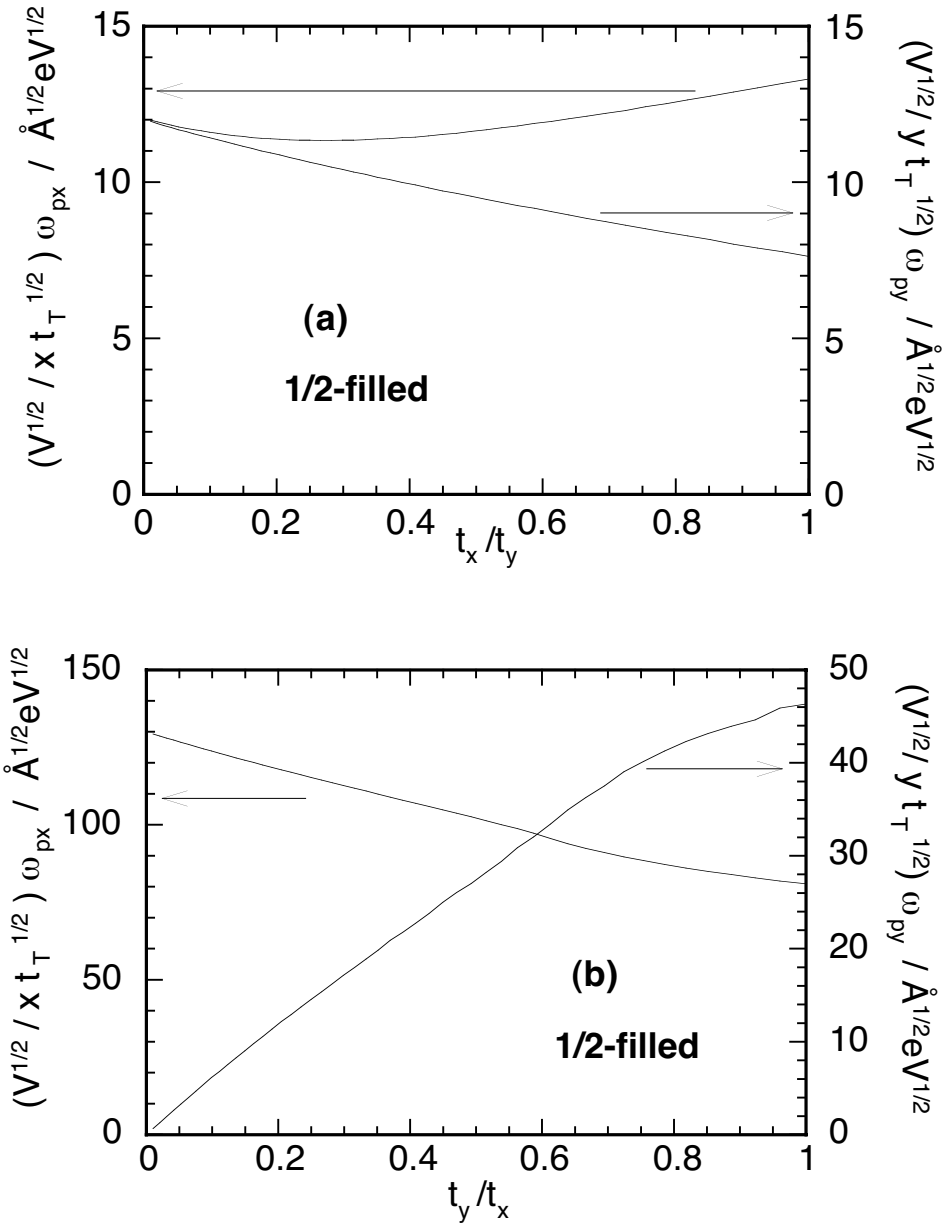

Fig. 3.3. Plasma frequencies normalized for the lattice constants and for total transfer integral, $t_T = t_x + t_y$, is plotted against the transfer integral ratio, for the 1/2-filled model band with $t_y = t_y'$. (a) for $t_x < t_y$, and (b) for $t_x > t_y$.

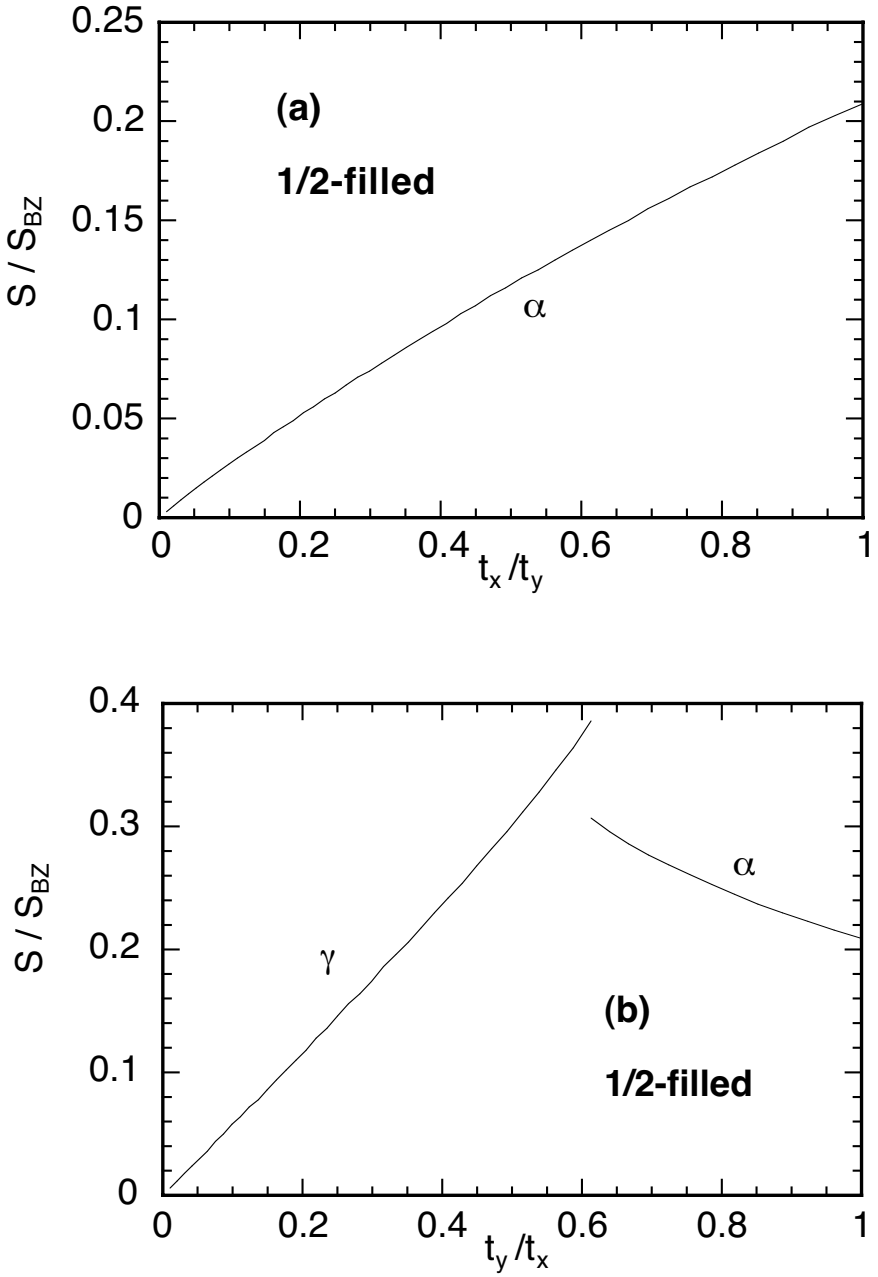

Fig. 3.4. Fractional cross-sectional area of each cyclotron orbit plotted against the transfer integral ratio, for the 1/2-filled model band with $t_y = t_y'$. (a) for $t_x < t_y$, and (b) for $t_x > t_y$. For the notation of the orbits, see Fig. 3.12.

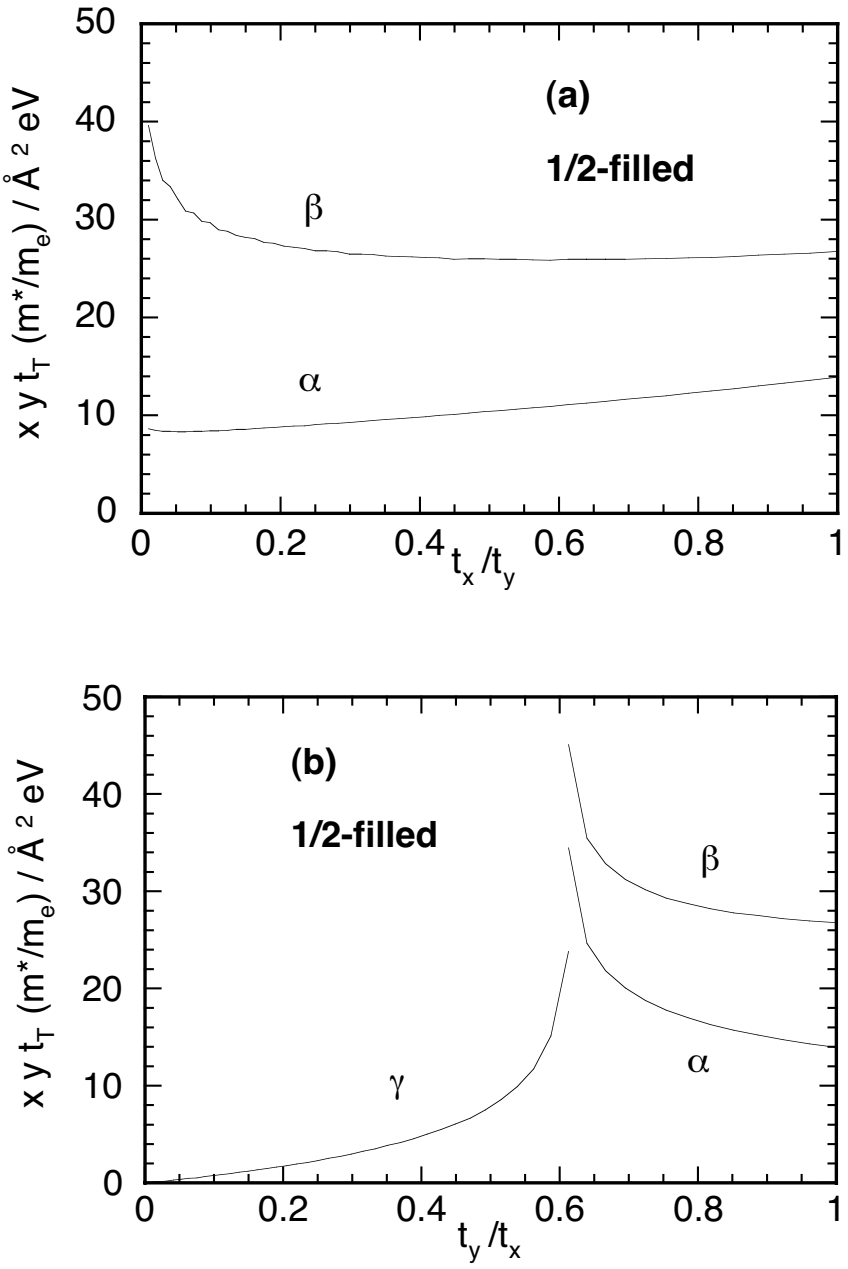

Fig. 3.5. Cyclotron mass of each orbit normalized for the lattice constants and for total transfer integral, , $t_T = t_x + t_y$, is plotted against the transfer integral ratio, for the 1/2-filled model band with $t_y = t_y'$. (a) for $t_x < t_y$, and (b) for $t_x > t_y$. For the notation of the orbits, see Fig. 3.12.

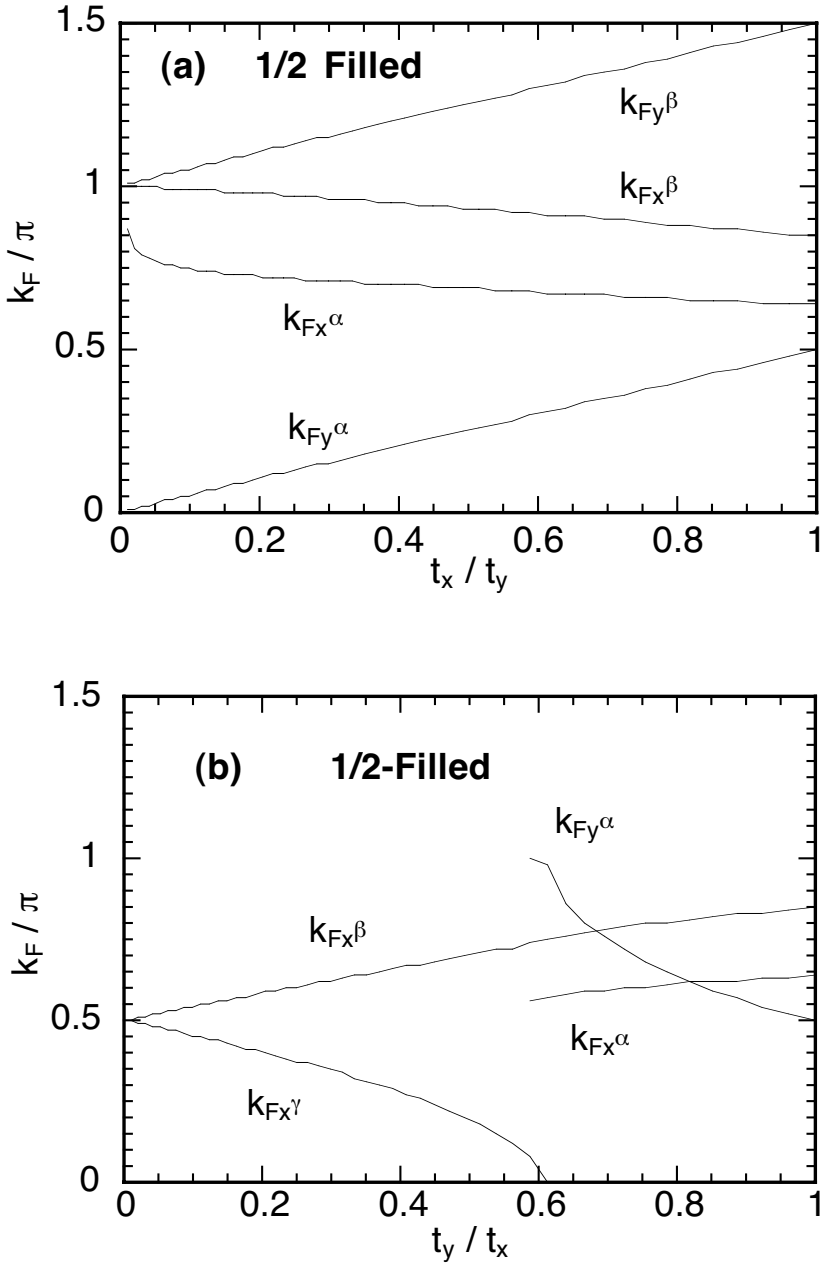

Fig. 3.6. Fractional radii of each cyclotron orbit plotted against the transfer integral ratio, for the 1/2-filled model band with $t_y = t_y'$. (a) for $t_x < t_y$, and (b) for $t_x > t_y$. For the notation of the orbits, see Fig. 3.12.

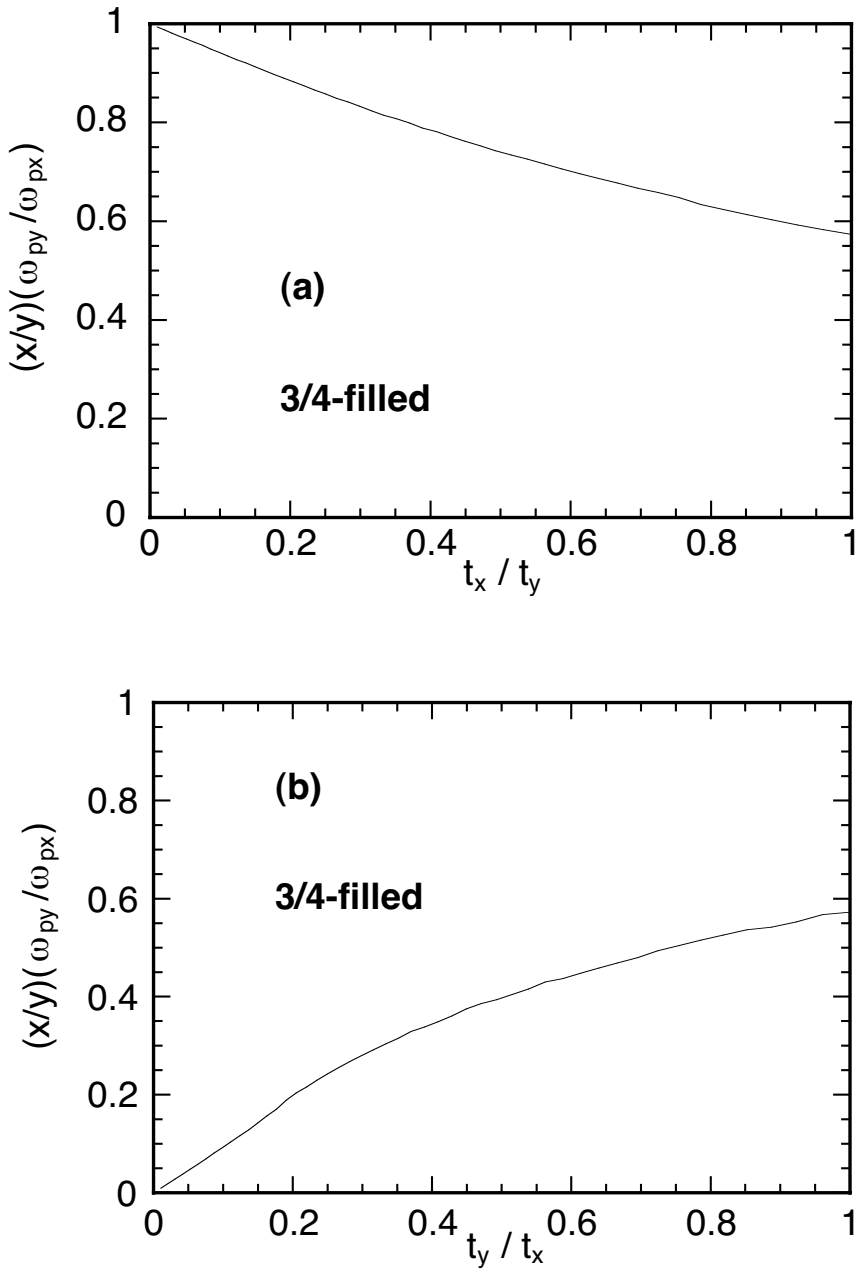

Fig. 3.7. Anisotropy of plasma frequency plotted against the transfer integral ratio, for the 3/4-filled model band with $t_y = t_y'$. (a) for $t_x < t_y$, and (b) for $t_x > t_y$.

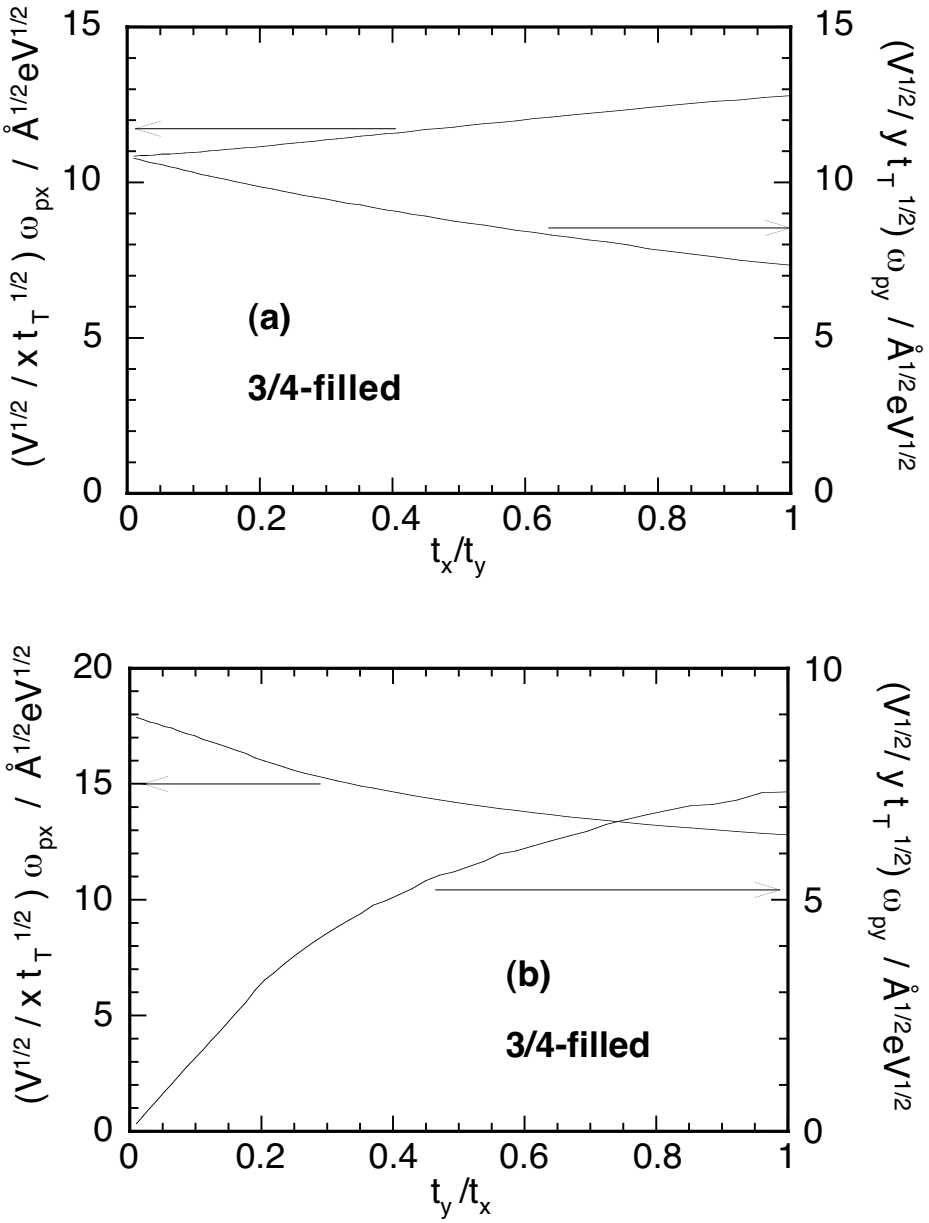

Fig. 3.8. Plasma frequencies normalized for the lattice constants and for total transfer integral, $t_T = t_x + t_y$, is plotted against the transfer integral ratio, for the 3/4-filled model band with $t_y = t_y'$. (a) for $t_x < t_y$, and (b) for $t_x > t_y$.

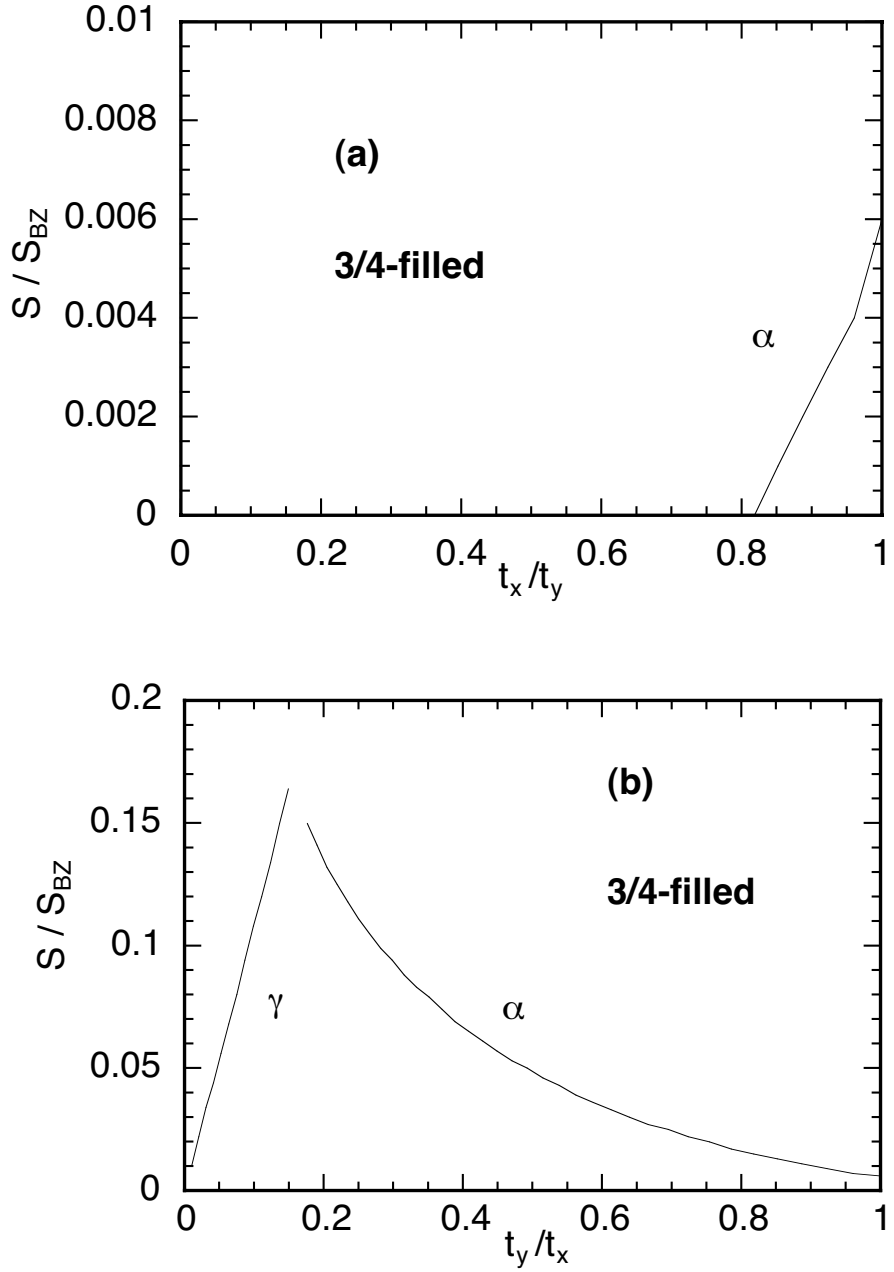

Fig. 3.9. Fractional cross-sectional area of each cyclotron orbit plotted against the transfer integral ratio, for the 3/4-filled model band with $t_y = t_y'$. (a) for $t_x < t_y$, and (b) for $t_x > t_y$. For the notation of the orbits, see Fig. 3.12.

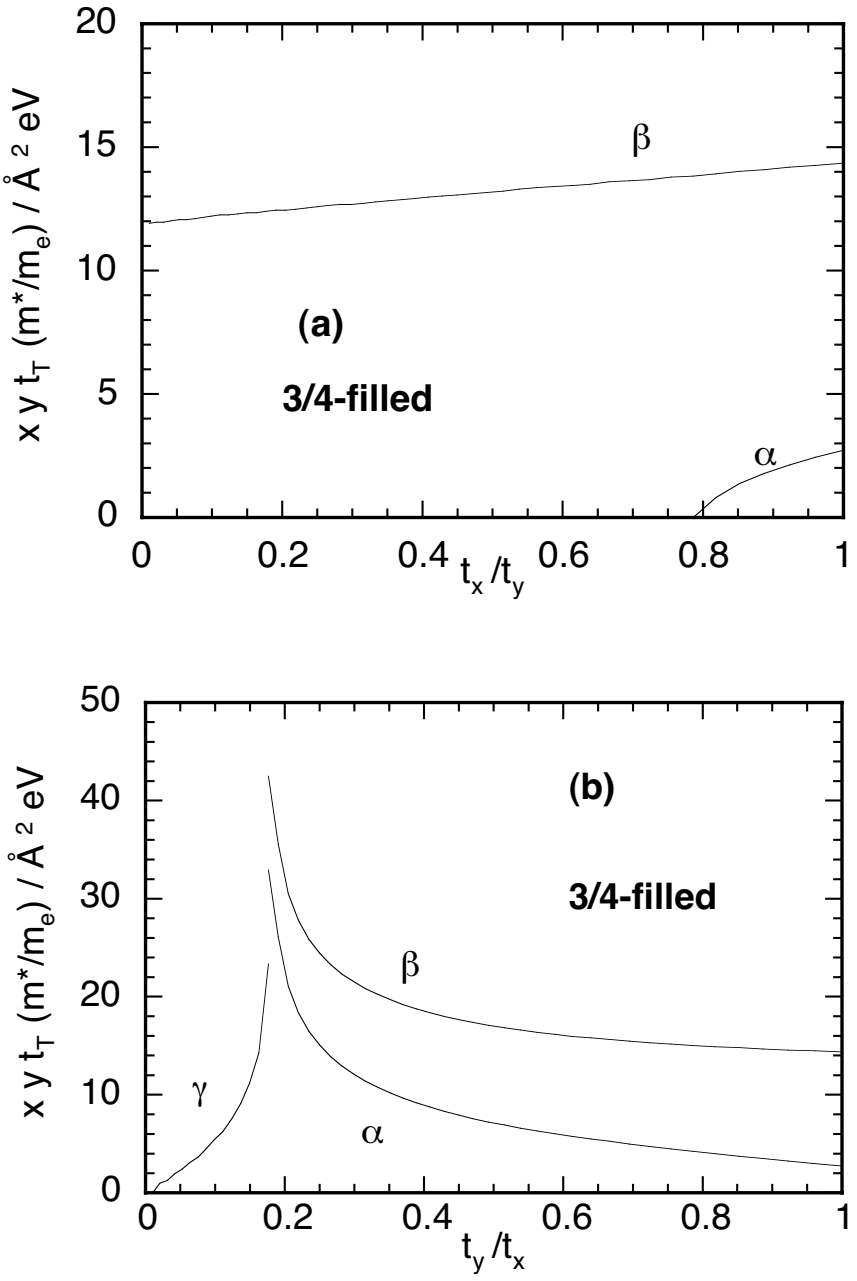

Fig. 3.10. Cyclotron mass of each orbit normalized for the lattice constants and for total transfer integral, , $t_T = t_x + t_y$, is plotted against the transfer integral ratio, for the 3/4-filled model band with $t_y = t_y'$. (a) for $t_x < t_y$, and (b) for $t_x > t_y$. For the notation of the orbits, see Fig. 3.12.

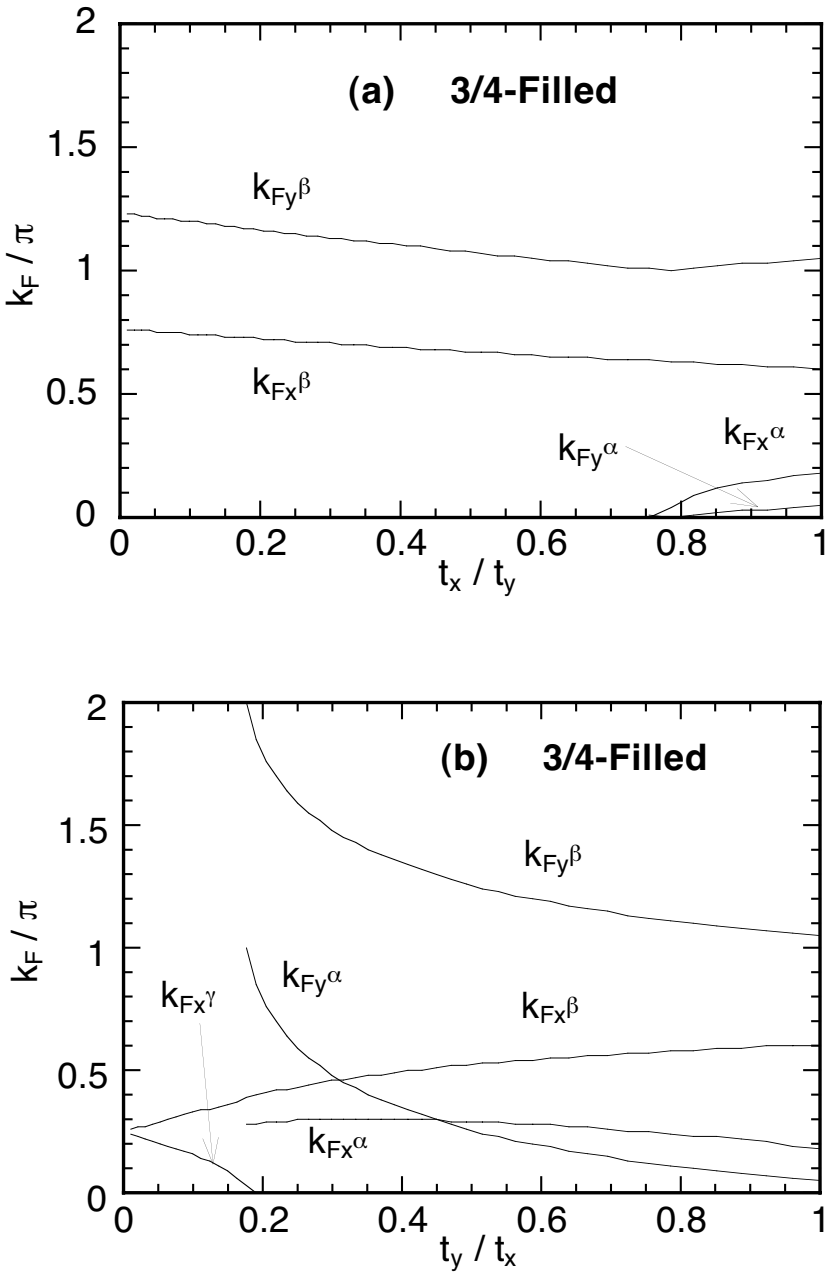

Fig. 3.11. Fractional radii of each cyclotron orbit plotted against the transfer integral ratio, for the 3/4-filled model band with $t_y = t_y'$. (a) for $t_x < t_y$, and (b) for $t_x > t_y$. For the notation of the orbits, see Fig. 3.12.

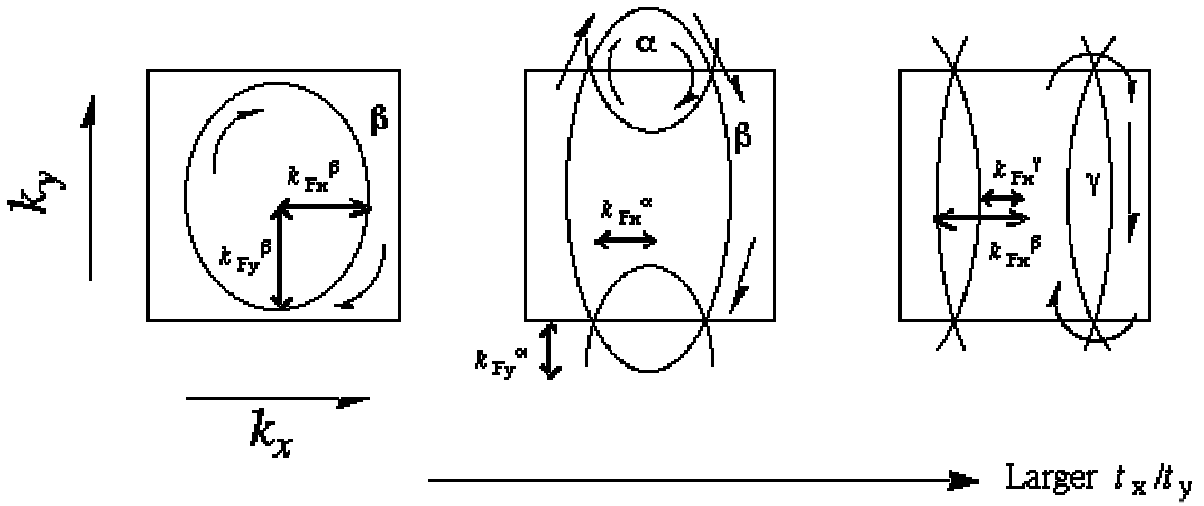

Fig. 3.12. Schematic display of the Fermi surface topology. Notation of the cyclotron orbits and their radii are also shown. The topology changes to right, with increasing t_x / t_y.

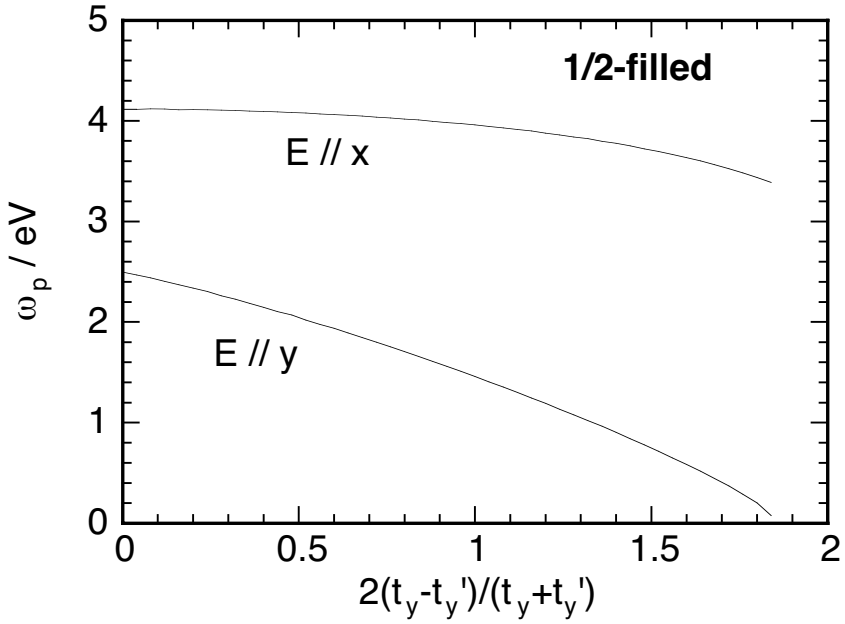

Fig. 3.13. Effect of symmetry lowering ($t_y > t_y$ ´) on the plasma frequencies in the case of $V = 1$ Å^3, $x = y = 1$ Å, $t_x = 0.048$ eV and $t_y + t_y$ ´ $= 0.104$ eV.

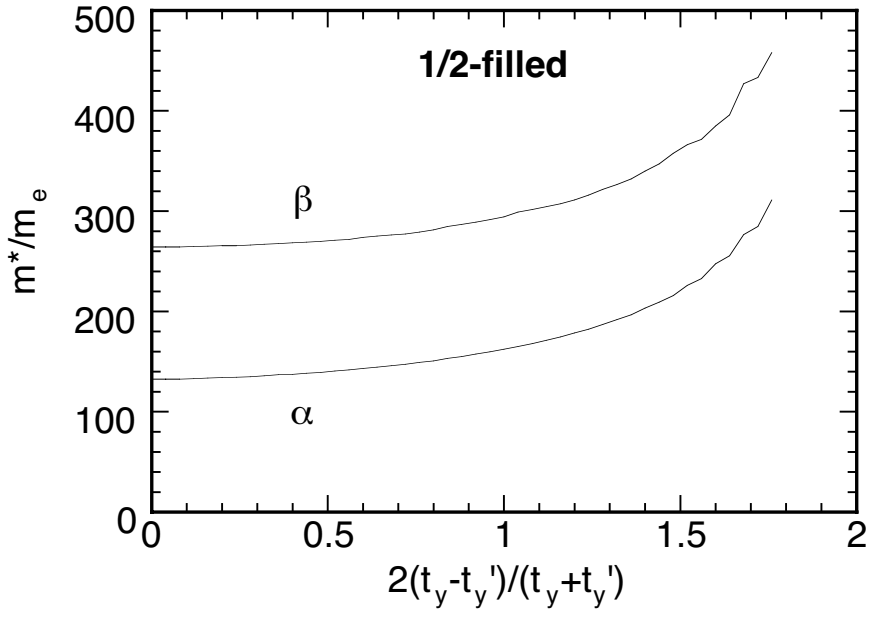

Fig. 3.14. Effect of symmetry lowering ($t_y > t_y$ ´) on the cyclotron mass in the case of $V = 1$ Å^3, $x = y = 1$ Å, $t_x = 0.048$ eV and $t_y + t_y$ ´ $= 0.104$ eV.

References

1. H. Tajima: Doctorate Thesis, The Univ. of Tokyo, 1986.
2. H. Tajima, K. Yakushi, H. Kuroda, G. Saito and H. Inokuchi: Solid State Commun. **49** (1984) 769.
3. J. M. Ziman: *Principles of the Theory of Solids* (Cambridge Univ. Press, Cambridge, 1972) 2nd Ed., Chap. 8.
4. R. K. Ahrenkiel: J. Opt. Soc. Am. **61** (1971) 1651.
5. J. M. Ziman: *Principles of the Theory of Solids* (Cambridge Univ. Press, Cambridge, 1972) 2nd Ed., Chap. 9.

Chapter 4.

Electronic Structure of θ-(BEDT-TTF)$_2$I$_3$

4.1. Introduction

A quasi-two-dimensional (2D) molecular conductor θ-(BEDT-TTF)$_2$I$_3$, where BEDT-TTF is bis(ethylenedithio)tetrathiafulvalene, exhibits its superconducting transition at 3.6 K under ambient pressure [1], which is the first discovery of an organic superconductor in Japan (1986). The arrangement of BEDT-TTF molecules in the donor sheets of this salt (Fig. 4.1.1) [2] contains no distinct dimerization, but has approximately high symmetry which affords a considerably simple band structure with a large 2D free-electron-like Fermi surface [2]. For this reason, this salt occupies a unique position among the molecular conductors; one-dimensional stacking or dimerization is the most popular structural motif in the molecular conductors.

However, the situation becomes somewhat complicated, when the doubled periodicity stemming from the anion arrangement [3] is taken account of. First, most crystals are twinned [2-4], which may yield ambiguity in the experimental study of this salt. Second, the band structure calculated on the basis of the detailed crystal structure gives complex topology of the Fermi surface [4]. Therefore, experimental examinations of the electronic structure of this salt have been desired.

The optical experiment [5] was first applied to the band structure of this salt (Sec. 4.3). Unlike other metallic BEDT-TTF salts, θ-(BEDT-TTF)$_2$I$_3$ exhibited Drude-like spectra even at room temperature. It was concluded from this that the optical properties of this salt are basically understandable on the basis of the simple band structure emerging from the highly symmetric molecular arrangement. Unlike the calculated ones

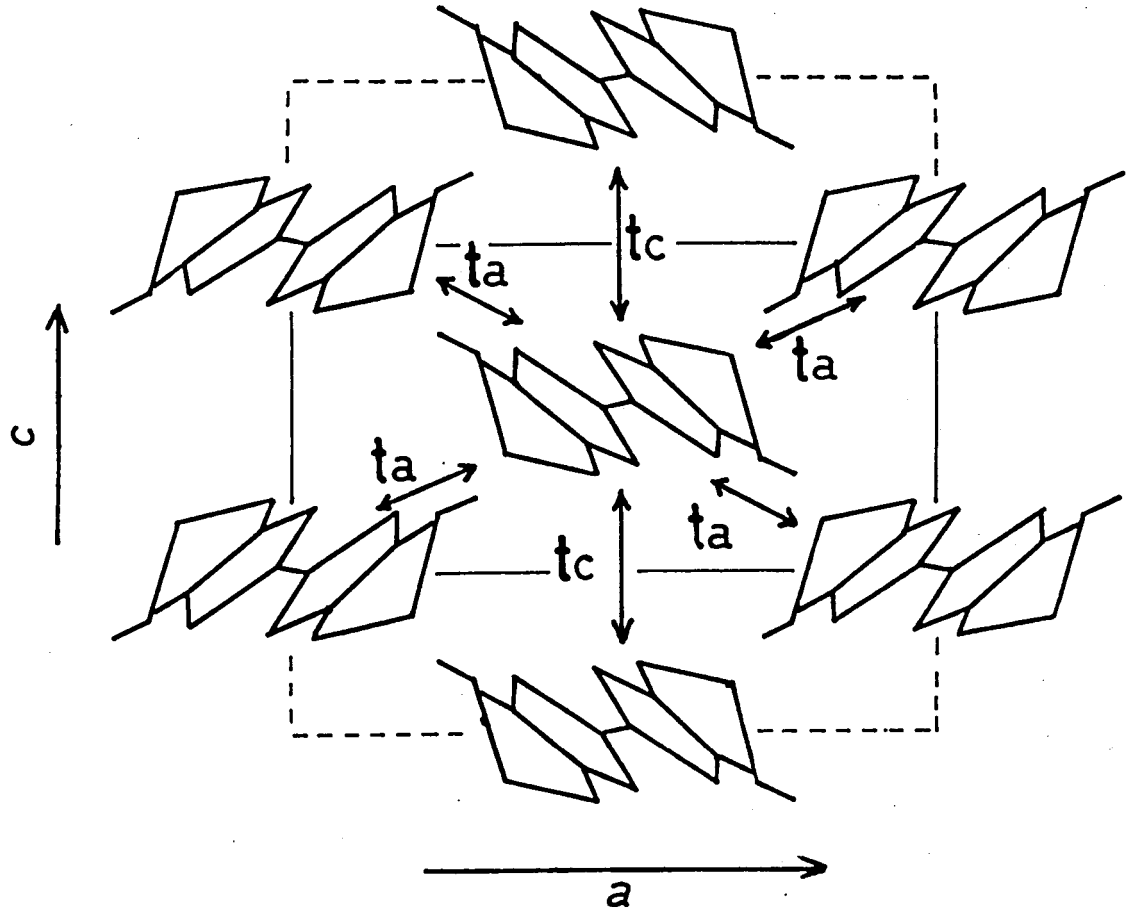

Fig. 4.1.1. The arrangement of BEDT-TTF in the conduction layer of θ-$(BEDT\text{-}TTF)_2I_3$. The solid and broken lines indicate the orthorhombic and monoclinic unit cells, respectively.

[2,4], the shape of the Fermi surface predicted from the optical results is a simple elliptic one [5]. Following this, the de Haas-van Alphen (dHvA) oscillations were observed in this salt [6]. A clear saw-tooth-like waveform, which is characteristic of a nearly ideal 2D system, was directly detected for the first time [6]. The topology of the Fermi surface deduced from the dHvA results [6] have supported the prediction by the optical study [5]. The detailed analysis of the dHvA oscillations [7], which takes account of the magnetic breakdown effect, have confirmed the geometry of the Fermi surface (Sec. 4.6).

Another significant finding in this salt is the angle dependent magnetoresistance oscillation (ADMRO); this phenomenon was found first in this salt by Kajita el at. [8], though it was found also independently in β-(BEDT-TTF)$_2$IBr$_2$ [9,10]. The origin of the ADMRO has been theoretically explained by considering a quasi-2D cylindrical Fermi surface with small warping [11,12]. However, the interpretation of the ADMRO in θ-(BEDT-TTF)$_2$I$_3$ in terms of a realistic band structure has not been reported yet, although the ADMRO is expected to provide valuable information on the Fermi surface geometry. For this reason, the ADMRO in this salt is reexamined and interpreted [13] (Sec. 4.7).

In this way, the study of θ-(BEDT-TTF)$_2$I$_3$ well illustrates how the band structure of a molecular conductor is explored. It also demonstrates how the optical study is efficient. The main purpose of this chapter is the description of these aspects. The optical study is given in Sec. 4.3. Section 4.4. deals with the magnetic properties in the superconducting state, as a characterization of the superconductivity. Section 4.5. treats the thermoelectric power measurement, which provides an aspect from a

different viewpoint. In Secs. 4.6 and 4.7, the dHvA results and the Subnikov-de Haas (SdH) results [14] are described, respectively. In the latter, the recent finding of an extraordinarily small three-dimensional Fermi surface [14] is also presented. Finally, the reexamination of the ADMRO is reported in Sec. 4.8.

4.2. Experimental

The single crystals of θ-(BEDT-TTF)$_2$I$_3$ used for the optical experiments were provided by Prof. Hayao Kobayashi (Toho Univ.), Prof. Akiko Kobayashi and Prof. Reizo Kato (Univ. of Tokyo). The crystals were grown by electrochemical oxidation of BEDT-TTF in a tetrahydrofuran solution containing 95:5 mixture of (*n*-C_4H_9)$_4$NI$_3$ and (*n*-C_4H_9)$_4$NAuI$_2$ as supporting electrolyte around 20 C° [15]. The single crystals used in the other studies (Secs. 4.4-8) were prepared by the author in a similar way. The content of Au in the crystals was usually so small that this salt is considered to be essentially the I_3 salt. In fact, it was found in the present study that the addition of (*n*-C_4H_9)$_4$NAuI$_2$ is not necessary in the crystal growth. Electrocrystallization without (*n*-C_4H_9)$_4$NAuI$_2$ using Pt plates or wires as the electrodes afforded the single crystals with satisfactorily high quality even under air. It took about a weak to obtain the crystals with a constant current of 1 μA applied. However, it was also found that the result of the crystallization strongly depends on the cell used. In most cases, the product was α-(BEDT-TTF)$_2$I$_3$.

Two nomenclatures of the crystal axes are used: the one is based on the averaged orthorhombic structure with the space group of *Pnma* [2],

and the other is based on the monoclinic structure with the space group of $P2_1/c$ [3,4], which explicitly takes account of the doubled periodicity and the twinned lattice. The relation between the two [3] is, $\boldsymbol{a}_m = 2\boldsymbol{c}_o$, $\boldsymbol{b}_m = \boldsymbol{a}_o$ and $\boldsymbol{c}_m = \boldsymbol{b}_o - \boldsymbol{c}_o$, where the subscripts, m and o, mean the monoclinic and orthorhombic lattices, respectively. The 2D plane is the a_oc_o-plane in the orthorhombic lattice. Since the present study concerns mainly the orthorhombic structure, the notation based on it is used in Secs. 4.3-4.5, though Secs. 4.7 and 4.8 are written in terms of the monoclinic notation. The crystal axes were identified by X-ray diffraction or by reflectance anisotropy in all the experiments.

Polarized reflectance spectra (Sec. 4.3) were measured on the (010) crystal face for the light polarizations parallel to the *a*- and *c*-axes. These are the principal directions within the 2D plane. The spectra were measured by the method described in Sec. 3.1, at 295, 200, 120, 75 and 16 K. The spectrum for the polarization parallel to the *b*-axis (perpendicular to the plane) was also measured at 295 K on the (001) crystal face.

Static magnetization measurements were carried out by use of an SHE SQUID magnetometer model 905. The correction for the sample holder was made only when the magnetization of the sample is about as small as that of the holder.

Thermoelectric power (Sec. 4.5) was measured by Prof. Takehiko Mori (Tokyo Institute for Technology) in The Institute for Molecular Science. The measurement was made along the *a*- and *c*-axes. The results are little affected by whether gold foil as the thermal contact is used or not.

The dHvA measurements (Sec. 4.6) were carried out by Prof. J. S.

Brooks, Dr. A. G. Swanson (Boston Univ.), Prof. C. C. Agosta (Clark Univ.), S. T. Hannahs (Massachusetts Institute of Technology) and Dr. Madoka Tokumoto (Electrotechnical Laboratory) with the assistance by the staff of the Francis Bitter National Magnet Laboratory at Massachusetts Institute of Technology [16]. For the measurements, the single crystal sample was installed in a ^{3}He cryostat designed to operate in high field magnets at the Francis Bitter National Magnet Laboratory. The magnetization of the sample was measured up to about 23 T by Brooks' method using the small-sample force magnetometer [17]. Transverse magnetoresistance was also measured by the standard four-probe method with gold contacts using a lock-in ac detection.

The SdH and ADMRO experiments were performed by Dr. Haruyoshi Aoki, Dr. Shinya Uji and Dr. Taichi Terashima (National Research Insitute for Metals). Electric contacts were made by gold paste. The sample used showed no superconductivity down to 0.05 K. The residual resistivity ratio, ρ(280 K) /ρ(4.2 K), of the sample amounted to about 1000. The SdH signals were recorded up to 13.8 T with electric current in the direction perpendicular to the 2D plane by using the field modulation technique. The ADMRO was also measured with this current direction.

4.3. Reflectance Spectra

4.3.1. Spectral Features

Figure 4.3.1 shows the polarized reflectance spectra measured at room temperature. Both the $\parallel \boldsymbol{a}$ and $\parallel \boldsymbol{c}$ spectra exhibit Drude-like dispersions in the infrared region showing the plasma edge around 4000-6000

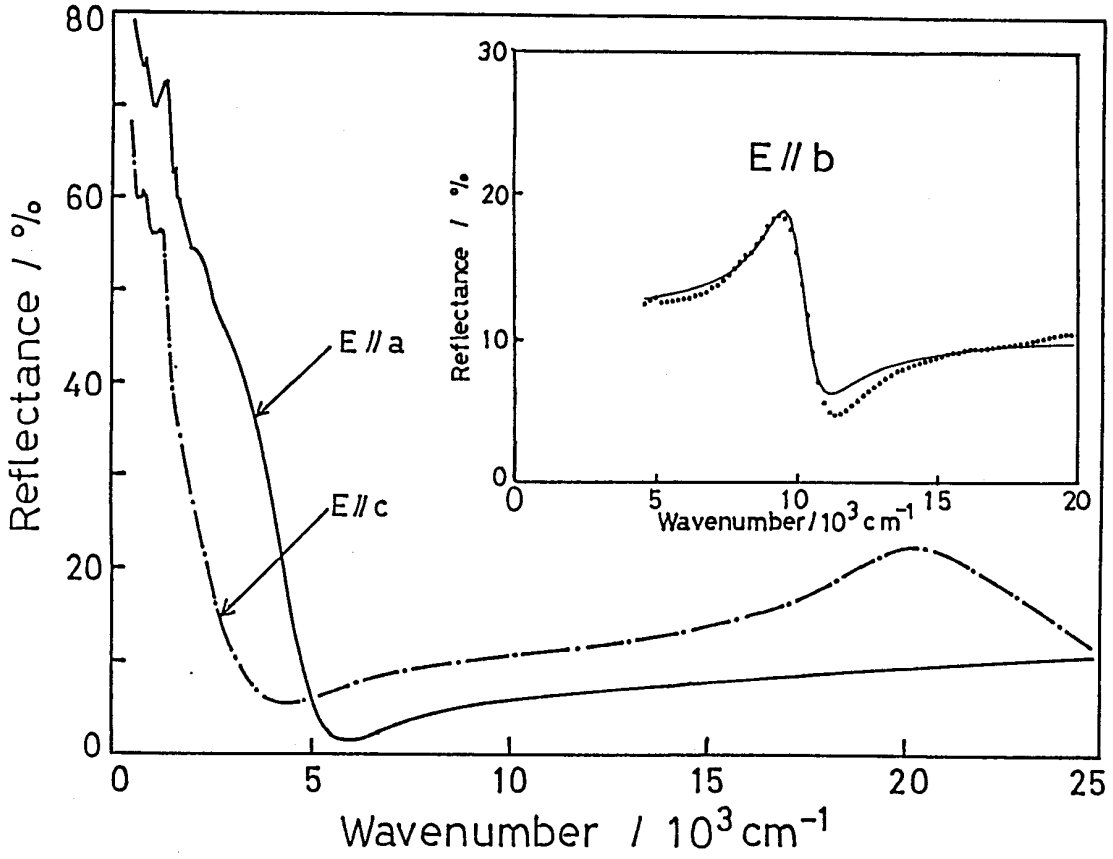

Fig. 4.3.1. Polarized reflectance spectra measured at room temperature.

cm^{-1}. In the cases of the BEDT-TTF salts investigated before [18-22], the shapes of the infrared reflectance spectra were not Drude-like, at least at room temperature. To our knowledge, θ-$(BEDT\text{-}TTF)_2I_3$ is the first example of the BEDT-TTF salt whose room temperature spectra exhibit Drude-like infrared dispersion for the two independent light polarizations within the two-dimensional molecular sheet of BEDT-TTF.

As already mentioned, the reflectance spectra of metallic BEDT-TTF salts usually show a non-Drude-like infrared dispersion. To elucidate the origin of these dispersions, a systematic investigation of reflectance spectra on a series of BEDT-TTF salts has been carried out [18-22]. In these studies, the probabilities of the optical interband transitions from the lower filled bands to the upper vacant (or partially filled) bands have been calculated in the framework of the one-electron band model. In the cases of the BEDT-TTF salts, these bands are formed from the HOMOs of BEDT-TTFs. It has been shown that the observed infrared dispersions are primarily associated with the interband transitions and have relatively small contribution of the intraband transitions [18-22].

Similar calculations based on the orthorhombic BEDT-TTF lattice of θ-$(BEDT\text{-}TTF)_2I_3$ yield no contribution of the interband transitions. This is consistent with the rule given in Appendix A.: The BEDT-TTF layer has glide symmetry along the *a*-axis and two-fold screw symmetry along the *c*-axis, and contains two BEDT-TTFs in the two-dimensional unit cell. This well explains the absence of dominant contribution of the interband transitions. The infrared dispersions of θ-$(BEDT\text{-}TTF)_2I_3$ are thus attributed basically to the intraband transitions.

The broad peak near 20×10^3 cm^{-1} in the $\parallel \boldsymbol{c}$ spectrum can be

assigned to the intramolecular excitation of I_3^-, which is expected to be completely polarized in the direction of the long axis of this linear anion. The || ***b*** reflectance spectrum measured on the (001) crystal face is shown in the inset of Fig. 4.3.1. The prominent dispersion near 10×10^3 cm^{-1} is attributable to the intramolecular excitation of the cation radical of BEDT-TTF, since the transition moment of this dispersion is almost parallel to the long axis of the BEDT-TTFs. The excitation energy was evaluated to be 1.22 eV by the curve-fitting analysis assuming a Lorentz oscillator. The spectroscopic study on BPDT-TTF (bis(propylenedithio)tetrathiafulvalene) radical salts also supports this assignment [23]. Incidentally, the fact that there is no indication of in the || ***b*** spectrum for the presence of a reflectivity minimum around 5000 cm^{-1} associated with the plasma edge, indicates that the delocalization of charge carriers along the *b*-axis is strongly interrupted by the layers of the counter anions sandwiched by the BEDT-TTF molecular sheets.

Figure 4.3.2 shows the reflectance spectra of θ-$(BEDT\text{-}TTF)_2I_3$ measured at several different temperatures. On lowering temperature, the plasma edge becomes sharper accompanying the increase in reflectivity in the low wavenumber region.

Although the spectra shown are Drude-like, it is not possible to reproduce exactly the observed reflectance curves only with the Drude model. Figure 4.3.3 shows the conductivity spectra in the infrared region obtained from the Kramers-Kronig analysis of the reflectance data. Small broad shoulders around 2500 cm^{-1}, which is indicated by the arrows in Fig. 4.3.3, appear on the Drude tails. These shoulders seem to be the ones associated with the interband transitions which used to appear in the

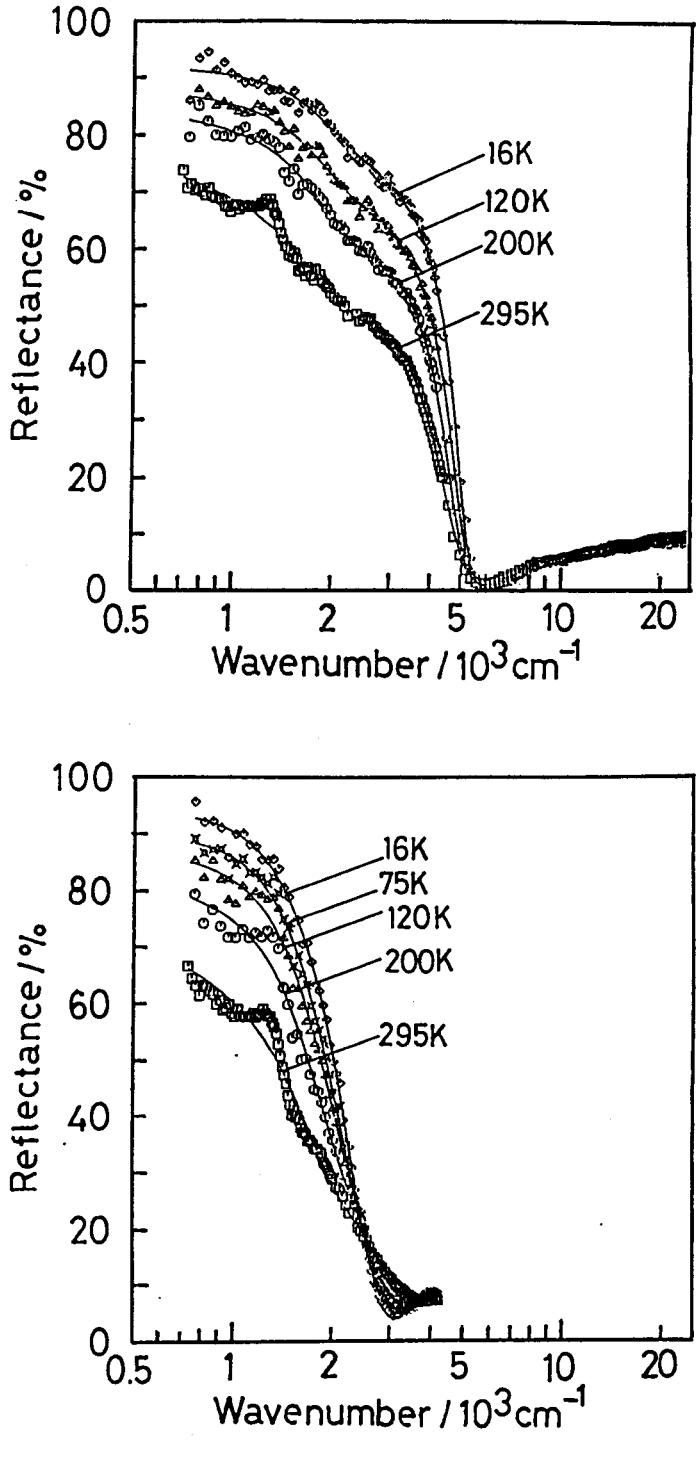

Fig. 4.3.2. Temperature dependence of the reflectrance spectra. The upper and lower panels show the ***E*** //***a*** and ***E*** // ***c*** spectra, respectively. Solid curves show the fit to the Drude-Lorentz model.

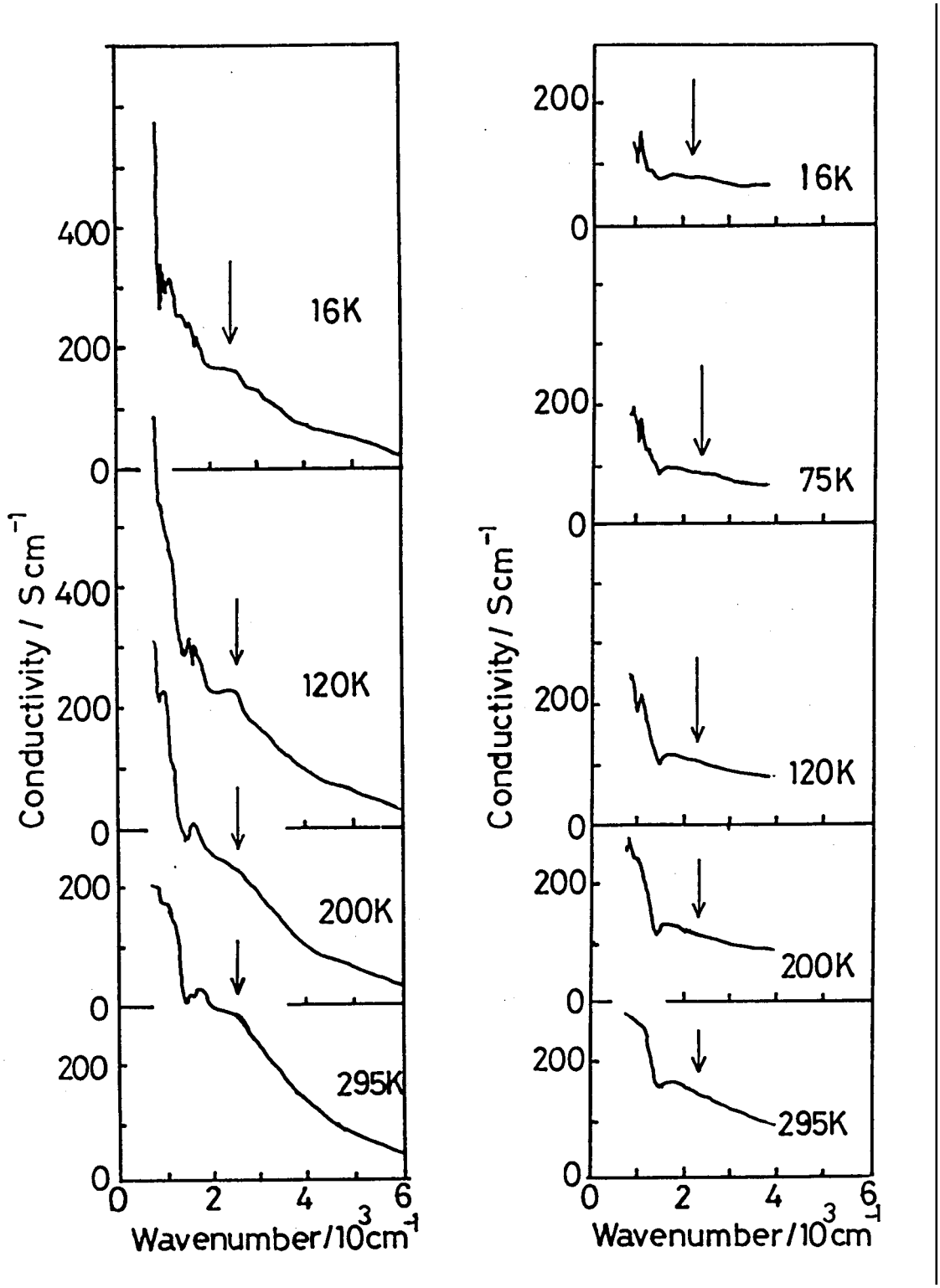

Fig. 4.3.3. Conductivity spectra at various temperatures. The arrows indicate the weak absorption due to the interband transitions.

spectra of the BEDT-TTF salts in the infrared region. If the arrangement of the BEDT-TTFs is exactly describable by the orthorhombic lattice, the interband transition should be absent, as mentioned above. The appearance of the weak interband transitions indicates the slight deviation of the arrangement from the orthorhombic structure.

According to the X-ray analysis of the crystal structure [3], the real structure is described by the monoclinic lattice. The glide mirror and the screw symmetries are no longer hold within the molecular layer of this monoclinic structure. The unit cell is doubled along the *c*-axis. Therefore, the symmetry discussion based on the orthorhombic lattice is an approximate one; weak interband transitions can be observed. Nevertheless, the fact that the interband contributions are very small supports that the consideration based on the orthorhombic lattice is a good approximation.

The small hump appearing around 1100 cm^{-1} in the $\parallel \boldsymbol{a}$ and $\parallel \boldsymbol{c}$ spectra (Figs. 4.3.1 and 4.3.2) is attributable to the totally-symmetric vibrational mode of BEDT-TTF coupled with the conduction electrons, because its position and linewidth agree with the corresponding peak observed in the spectra of other BEDT-TTF salts [24]. This electron-molecular-vibration (e-mv) coupling peak arises by borrowing the intensity of the interband transitions. The appearance of the weak e-mv peak in the spectra of θ-$(BEDT\text{-}TTF)_2I_3$ also supports the presence of the weak interband transitions in this salt.

4.3.2. Curve-fitting Analysis and Optical Effective Mass

In order to separate the contribution of the intraband transitions and those of the interband transitions and the intramolecular transitions, the

curve-fitting method based on the following Drude-Lorentz dielectric function,

$$\varepsilon(\omega) = \varepsilon_C - \omega_P^2 / (\omega^2 + i\omega/\tau) + \sum_j f_j / [(\omega_j^2 - \omega^2) - i\gamma_j\omega]. \quad (4.3.1)$$

was used. The first term stands for the dielectric constant stemming from the higher energy excitations outside the experimental spectral region, the second term is the Drude term representing the intraband transitions, and the third term describes the interband transitions (j = 1) and the local excitation of I_3^- anion (j = 2). The results of the curve-fitting were shown by the solid curves in Fig. 4.3.2, and the obtained parameters are summarized in Table 4.3.I, together with the dc conductivity values deduced from this model. The local excitation of I_3^- near 20000 cm^{-1} is explicitly included for the analysis of the $\| \boldsymbol{c}$ spectrum at room temperature, but it is not for the low temperature spectra, which is limited below 4200 cm^{-1}. However, the local excitation is implicitly included in the first term, ε_C, because the contribution of the third term for this excitation is almost constant below 4200 cm^{-1}. The reflectivity is related to dielectric function by the equation,

$$R = [1 + |\varepsilon| - \sqrt{2(|\varepsilon| + \mathrm{Re}(\varepsilon))}\,] / [1 + |\varepsilon| + \sqrt{2(|\varepsilon| + \mathrm{Re}(\varepsilon))}\,]. \quad (4.3.2)$$

In terms of a two-dimensional parabolic band model (a nearly-free-electron model), the anisotropic effective mass of the carriers can be derived from the plasma frequency for each polarization. The band model is expressed

as,

$$\varepsilon = -\hbar^2 [k_a^2/2m^*_a + k_c^2/2m^*_c] \ , \qquad (4.3.3)$$

where m^*_a and m^*_c are the *a*- and *c*-components of the effective mass tensor. The plasma frequency is given by,

$$(\omega_P^2)_x = 4\pi n e^2/m^*_x \ , \quad x = a \text{ and } c \qquad (4.3.4)$$

From the plasma frequency data at 16 K, the effective masses are calculated to be $m^*_a = 1.5\ m_e$ and $m^*_c = 3.0\ m_e$.

Table. 4.3.I. The Drude parameters obtained by the Drude-Lorentz fit of the reflectance data.

Polarization	T / K	ε_c	ω_p / eV	τ^{-1} / eV	σ_{dc}^{opt} / S cm^{-1} a)
// *a*	295	3.55	0.92	0.16	730
	200	3.49	0.97	0.087	1440
	120	3.62	1.04	0.068	2130
	16	3.42	1.05	0.042	3550
// *c*	295	2.52	0.62	0.12	440
	200	5.59 b)	0.71	0.074	900
	120	5.68 b)	0.72	0.049	1400
	75	5.76 b)	0.72	0.039	1910
	16	5.98 b)	0.73	0.022	3290

a) The values obtained by extrapolating the Drude conductivity to zero wavenumber.

b) These values are larger than the room temperature one, because they involve the contribution of the local excitation of anions. See Text.

4.3.3. Tight-binding Band Structure Derived from Optical Data

According to the tight-binding model taking account of HOMOs of BEDT-TTFs, the energy band of θ-(BEDT-TTF)$_2$I$_3$ is expressed as,

$$E(k_a, k_c) = 2t_c \cos(ck_c) \pm 4\, t_a \cos(ak_a / 2) \cos(ck_c / 2)\ , \quad (4.3.5)$$

where the transfer integrals, t_a and t_c, are defined as indicated in Fig. 4.1.1. Because of the high symmetry of the molecular arrangement in the assumed orthorhombic BEDT-TTF sublattice, the band structure is described only by three parameters, E_F, t_a and t_c, where E_F is the Fermi energy. These parameters can be related to the three experimental data, i.e. , the plasma frequencies, $(\omega_P)_a$ and $(\omega_P)_c$, and the number of holes, N_h, which is estimated from the crystal structure and the stoichiometry. The Fermi energy is determined implicitly by,

$$N_h = (2 / 4\pi^2)\,(4/a)\int_0^{k_{Fc}} \cos^{-1}\{[E_F - 2t_c\cos(ck_c)] / 4\, t_a \cos(ck_c / 2)\}\, dk_c, \quad (4.3.6)$$

where N_h is the number of holes per unit area of the (010) plane (the conduction plane), and k_{Fc} denotes the maximum value of the c-component of the Fermi wave vector. The plasma frequencies are related to the Fermi velocities by,

$$(\pi^2\hbar / e^2)(\omega_P^2)_a = [2\pi/(b/2)]\int_{-k_{Fc}}^{k_{Fc}} | v_{Fa}(k_c) |\, dk_c\ , \quad (4.3.7)$$

$$(\pi^2\hbar / e^2)(\omega_P^2)_c = [2\pi /(b / 2)]\int_{-k_{Fa}}^{k_{Fa}} | v_{Fc}(k_a) | dk_a , \qquad (4.3.8)$$

where k_{Fa} is the maximum value of the *a*-component of the Fermi wave vector, v_{Fa} and v_{Fc} denote the *a*- and *c*-components of the Fermi velocity, respectively, and *b* is the lattice constant perpendicular to the (010) plane. Note that the unit cell of θ-(BEDT-TTF)$_2$I$_3$ includes two equivalent conduction layers. The Fermi velocity is defined as,

$$\boldsymbol{v}_F = \hbar^{-1} [\mathrm{grad}_{\boldsymbol{k}} E(k_a, k_c)]; \; E = E_F. \qquad (4.3.9)$$

The parameters, k_{Fa} and k_{Fc} are related to the Fermi energy by,

$$E_F = 2t_c + 4 t_a \cos(ak_{Fa} / 2), \qquad (4.3.10)$$

$$E_F = 2t_c \cos(ck_{Fc}) + 4 t_a \cos (ck_{Fc} / 2) , \qquad (4.3.11)$$

By numerically solving the simultaneous equations, (4.3.6)-(4.3.11), a set of solution, E_F, t_a, t_c, k_{Fa} and k_{Fc} were obtained. The results are shown in Table 4.3.II. For example, at 16 K, the parameters are E_F = 0.12 eV, t_a = 0.080 eV, t_c = 0.046 eV, k_{Fa} = 0.30 Å^{-1} and k_{Fc} = 0.42 Å^{-1}. Figure 4.3.4 shows the energy band structure and the Fermi surface calculated by use of these parameters. This is the first example of BEDT-TTF salt where the transfer integrals of the tight-binding band model are directly inferred from the optical data.

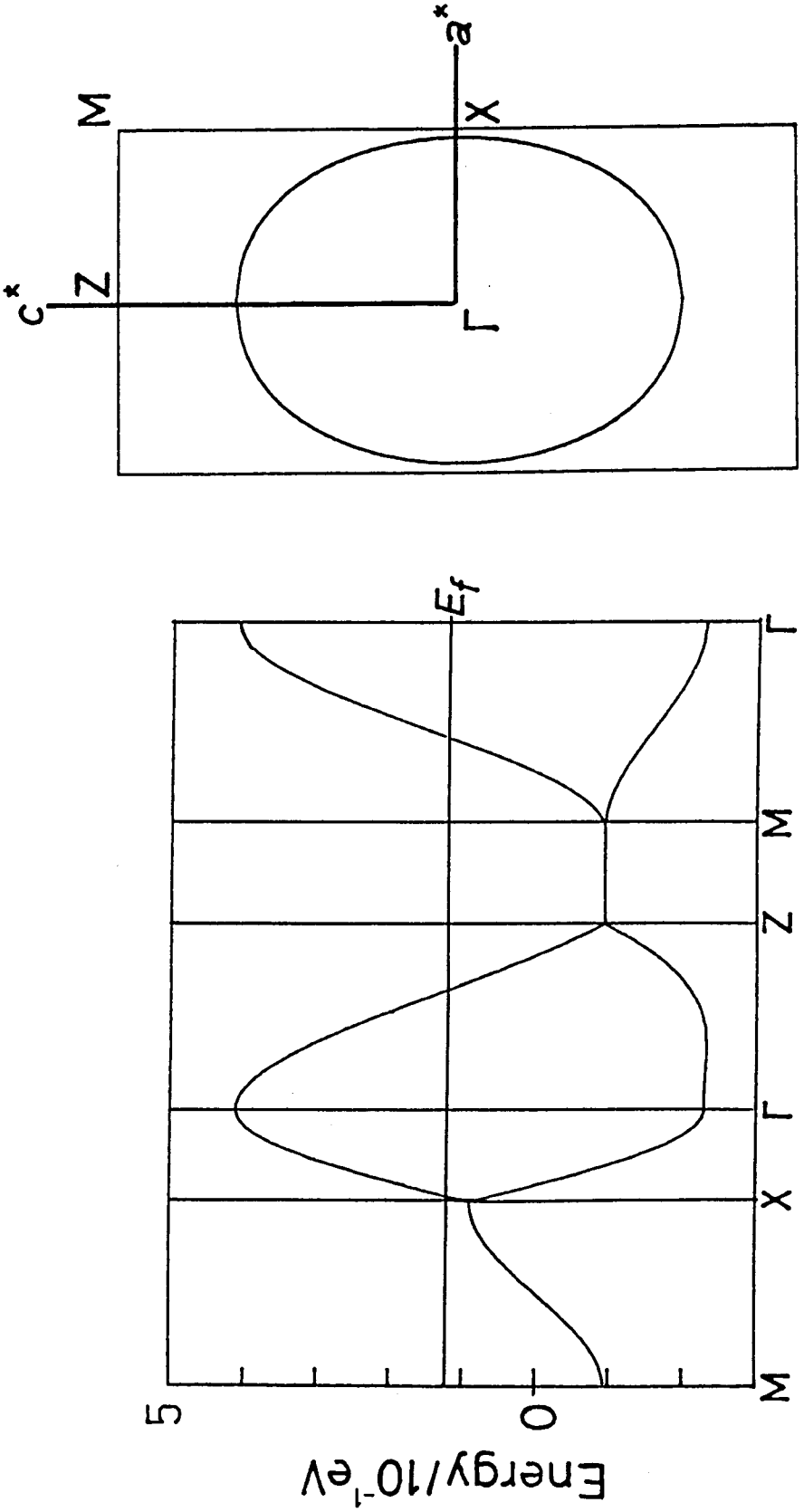

Fig. 4.3.4. The tight-binding band structure and the Fermi surface estimated from the reflectance spectra at 16 K.

Table 4.3.II. The tight-binding band parameters estimated from the optical data.

T / K	t_a / eV	t_c / eV	E_F / eV	ε_F / eV [a)]	k_{Fa} / Å^{-1}	k_{Fc} / Å^{-1}
200	0.069	0.045	0.10	0.26	0.30	0.41
120	0.078	0.043	0.11	0.28	0.29	0.42
16	0.080	0.046	0.12	0.29	0.30	0.42

a) The Fermi energy measured from the top of the conduction band, i.e., $\varepsilon_F = 2\,t_c + 4\,t_a - E_F$.

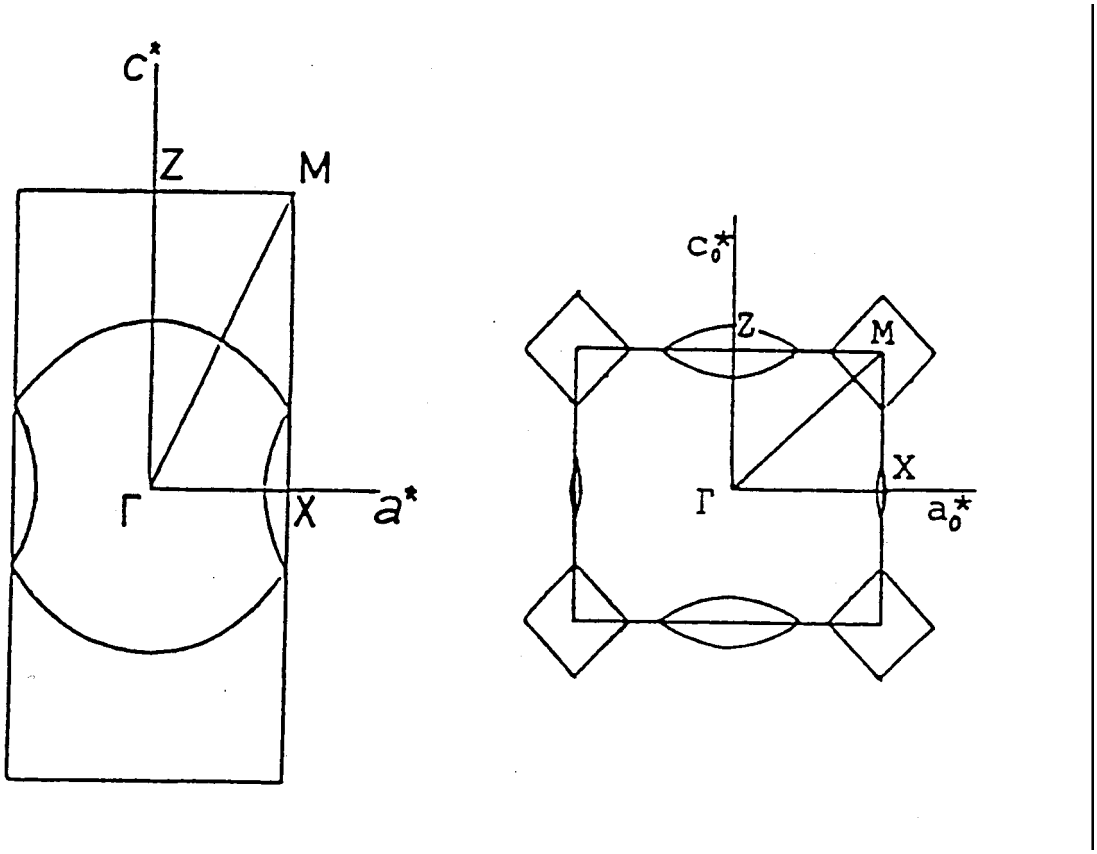

Fig. 4.3.5. The shape of the Fermi surface calculated from the crystal structure by means of the tight-binding approximation. Left: for the orthorhombic lattic [2]. Right: for the monoclinic lattice [4].

The band structure and the shape of the Fermi surface thus obtained are somewhat different from those calculated from the crystal structure [2,4] (Fig. 4.3.5). In the calculations of the band structure from the crystal structure, the transfer integrals (t's) are assumed to be proportional to the overlap integrals (S's) between the HOMOs of BEDT-TTFs. The present optical study has yielded t_a / t_c = 1.7, whereas the calculated ratio of the overlap integrals is S_a / S_c = 0.66 [2]. This difference, which is the origin of the difference between the experimental and calculated band structures, is not negligible. In order to establish the band structure of θ-(BEDT-TTF)$_2$I$_3$, it is desired to study it by further experiments.

It should be also remarked here again that the present results are based on the orthorhombic average structure. The doubled periodicity along the c-axis in the monoclinic structure yields the Brillouin zone folded at the mid point of the ΓZ line. This folding results in the closed pocket area around the new zone boundary. The area of this pocket amounts to 14 % of that of the first Brillouin zone. Furthermore, the lowered symmetry gives rise to removal of degeneracy on the new zone boundary, which is not included in the present band model. The mid-infrared optical properties are insensitive to the expected small gap structures of the Fermi surface. Therefore, an experiment sensitive to the detailed structure of the Fermi surface can afford results slightly different from the present ones. However, the origin of such difference should be understood in this way. The essential point of the present conclusion is that the Fermi surface is an elliptic one elongated along the c-direction.

4.3.4. Temperature Dependence of the Spectra

The temperature dependence of the spectra is caused mainly by the temperature dependence of the relaxation time, τ, as noticed from Table 4.3.I. From the Fermi velocity values and τ, the mean free path of the carriers is estimated as,

$$\Lambda = v_F \tau, \tag{4.3.12}$$

Within the (010) plane, the v_F values of about 2×10^7 cm s^{-1}, are derived from the band structure obtained as above. The mean free path within the (010) plane amounts to about 40 Å at 16 K, larger than the lattice constants. On the other hand, the corresponding values at room temperature are shorter than 10 Å, comparable or smaller than the lattice constants. This implies the breakdown of the simple picture of metal. Another contradictory point concerns the dc conductivities deduced from the optical data (Table 4.3.I). The agreement between them and the values obtained directly by the dc measurement is satisfactory at low temperatures. However, the agreement becomes remarkably worse as temperature increases; at room temperature the former are about 400 - 700 S cm^{-1}, whereas the latter is less than 100 S cm^{-1}. This fact suggests the possibility of anomalous non-Drude dispersion at lower wavenumbers outside the experimentally accessible region at high temperatures. The extraordinarily short mean free paths at high temperatures indicates that the carriers are strongly scattered by some thermally excited modes in the crystal. The physical picture has not been established for such a situation yet. Nevertheless, this is expected to be the origin of the anomaly. At low temperatures, the

concluded electronic structure seems to be free from such complication. However, it is desired to test it by different experiments.

4.4. Magnetic Properties in the Superconducting State

Temperature dependence of the shielding and Meissner effect and anisotropy of the magnetization curve are investigated to characterize the superconductivity in θ-(BEDT-TTF)$_2$I$_3$. In the following, the sample dependence is reported first. Next, the anisotropy of the magnetization curve is discussed.

4.4.1. Sample Dependent Superconductivity

The magnetic behavior in the superconducting state is found to vary from sample to sample. This should be related to the sample dependent behavior of the resistivity [25,26]. The sample-dependence of magnetization was examined after cooling the sample down to 1.8 K in zero field. After the cooling, a magnetic field up to 10 G was applied along the *b*-axis in order to probe the diamagnetism. The samples could be divided into two groups: Group I exhibited a diamagnetic shielding of 0.3 emu/g at 10 G and Group II exhibited a very small shielding, 1/1000 of the value of the Group I. Among the 12 crystals examined, two were found to be of the Group I.

Figures 4.4.1 and 4.4.2 show the temperature dependence of static magnetization of the Group I and II samples, respectively. In this measurement, the sample was first cooled down to 1.8 K in zero field, then

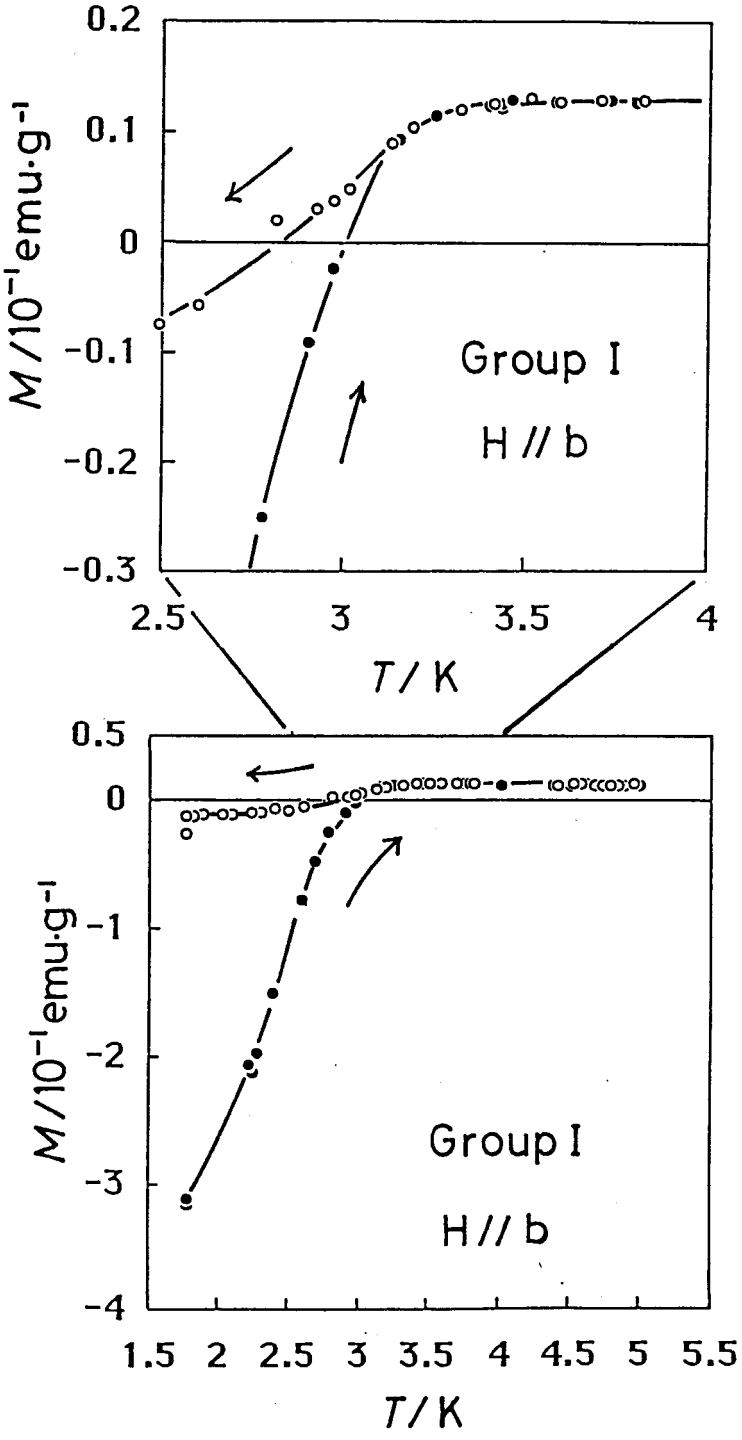

Fig. 4.4.1. Temperature dependence of the shielding and Meissner effect of the Group I sample (#13-5 in Table 4.4.I) in the magnetic field of 10 G applied along the *b*-axis. Correction for the background is not made.

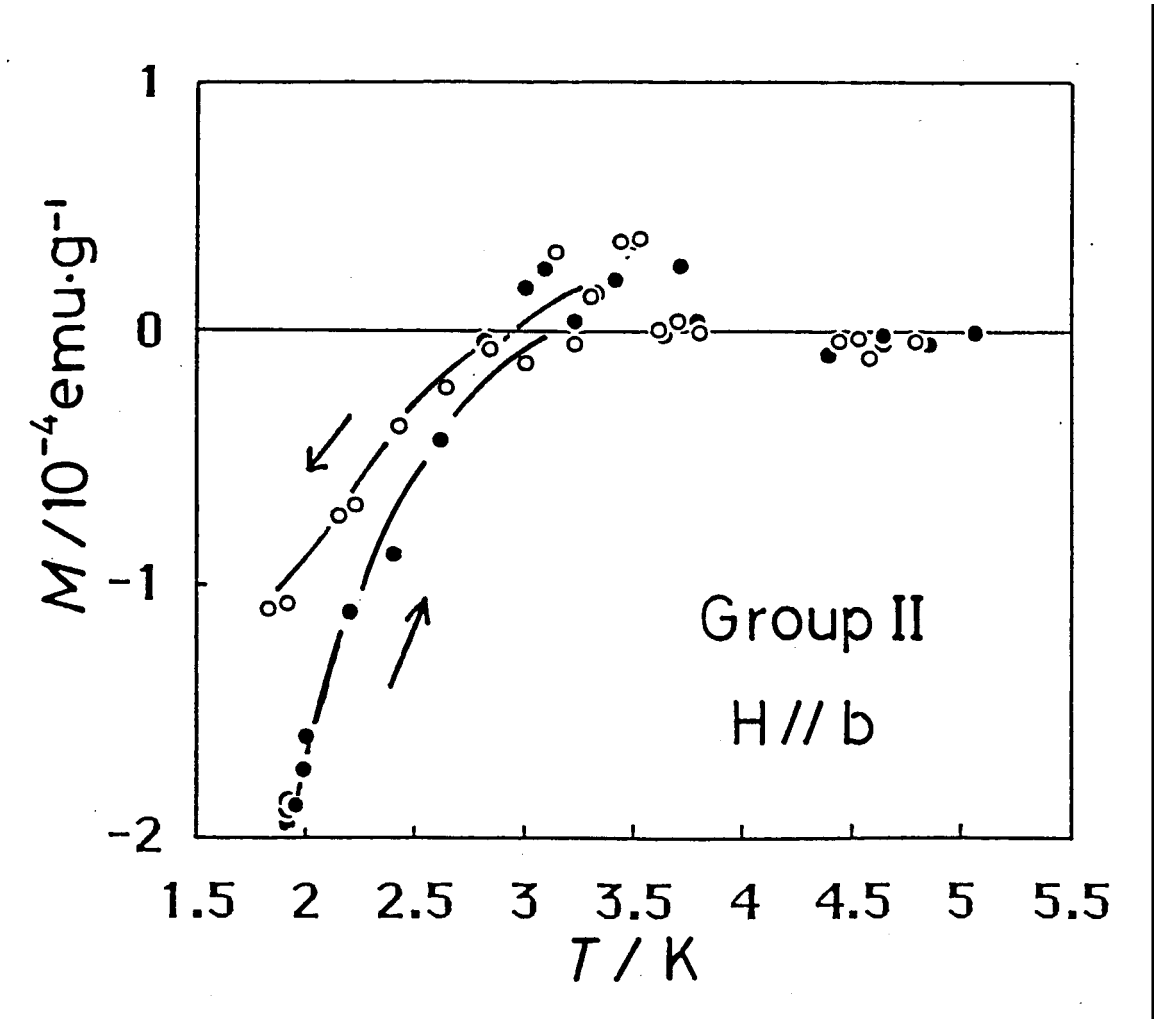

Fig. 4.4.2. Typical temperature dependence of the shielding and Meissner effect of the Group II sample in the magnetic field of 10 G applied along b-axis. Since the zero point of magnetization (ordinate) is ambiguous in this case, it was taken as the magnetization value at 5K. Compare the scale of magnetization with that in Fig. 4.4.1.

the magnetic field of 10 G was applied, and the diamagnetic shielding signal was measured on the warming process up to 5 K. Again the sample was cooled down to 1.8 K in the same field in order to measure the Meissner signal. As shown in Figs. 2 and 3, the diamagnetism of the Group I samples was much larger than that of the Group II samples in the lower temperature. The diamagnetic shielding decreased with increasing temperature up to about 3.5 K. Above this temperature, the Group I sample shows a small and constant signal due to the Pauli paramagnetism, while the magnetization signals of the Group II sample were too small to distinguish from background noises above 3 K. This behavior is not in conflict with the reported temperature dependence of the resistivity at zero field, because the applied field (10 G) slightly exceeds the lower critical field even at 1.8 K as described below.

On the cooling process in the magnetic field, the Group I sample exhibited a diamagnetism due to the Meissner effect which gradually increased on cooling down to 1.8 K. The Meissner signal, which was defined as the ratio of the Meissner expulsion to the shielding signal, was about 1 above 3 K, while it reduced with decreasing temperature. It was found to be about 0.1 at 1.8 K for the Group I sample. The Group II sample showed a similar Meissner behavior. However, the Meissner signal was estimate to be 5 times as large as that of the Group I sample at 1.8 K. Since the shielding signal of the Group II sample is remarkably small for its size, the large Meissner signal never involves large superconducting volume.

Judging only from the Meissner signal value of about 0.1, the superconductivity in θ-(BEDT-TTF)$_2$I$_3$ seems to be a bulk one. In this case,

the shielding effect is suppressed by insufficient development of supercurrent path loop on the crystal surface as observed in the Group II samples. Since the penetrating flux tends to be trapped mainly in the defect domain in the Group II crystal, the Meissner to shielding ratio could be held at rather larger value (0.5) than that of the Group I sample (0.1). Anyway in the Group II crystals, the fractional volume of the superconducting part is significantly suppressed. The reduction of the superconducting volume can result in the appearance of the residual resistivity [25,26].

4.4.2. Anisotropy of the Lower Critical Field (H_{c1})

The anisotropy of magnetization curve of the Group I sample up to 40 or 60 G was investigated at 1.8 K. Figures 4.4.3 and 4.4.4 show the initial magnetization and the magnetization curves obtained by applying magnetic field along the crystal axis, *b*, *a* and *c*. The *b*-axis is normal to the conduction layer, and the *a*- and *c*-axes are the in-plane directions. Strong irreversibility in the magnetization curves found for all the field directions is attributable to the flux trapping, which is a characteristic feature of the non-ideal type II superconductor.

The initial magnetization for $\boldsymbol{H} \parallel \boldsymbol{b}$ was from ten to twenty times as large as those for the fields along the in-plane directions, $\boldsymbol{H} \parallel \boldsymbol{a}$ and $\boldsymbol{H} \parallel \boldsymbol{c}$. The magnetization curve for $\boldsymbol{H} \parallel \boldsymbol{b}$ has a definite diamagnetic maximum, whereas the magnetization is approximately constant or gradually decreasing in the high field region for $\boldsymbol{H} \parallel \boldsymbol{a}$ and $\boldsymbol{H} \parallel \boldsymbol{c}$. This difference indicates that the upper critical field, H_{c2}, has smaller value for $\boldsymbol{H} \parallel \boldsymbol{b}$ than that for $\boldsymbol{H} \parallel \boldsymbol{a}$ or $\boldsymbol{H} \parallel \boldsymbol{c}$. This observation agrees with the result of resistivity measurements [26], in which the values of H_{c2} for $\boldsymbol{H} \parallel \boldsymbol{b}$ was found to be

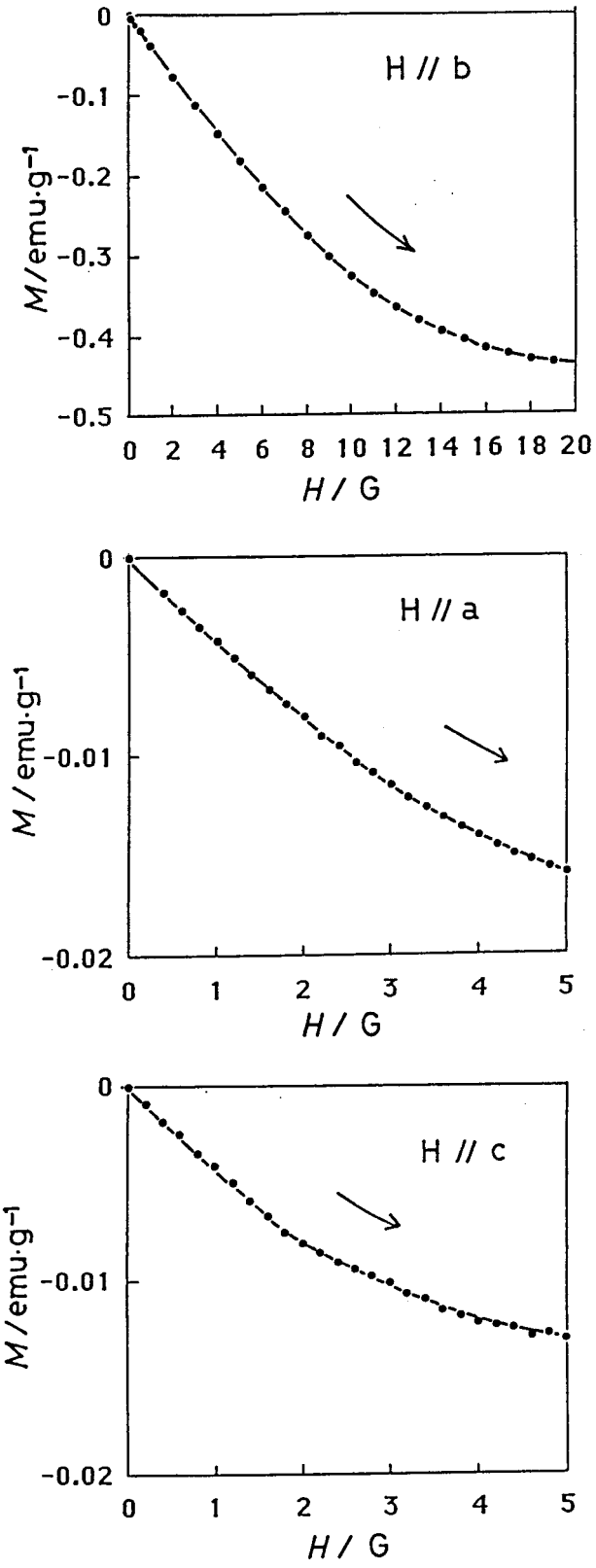

Fig. 4.4.3. Initial magnetization of the Group I sample (#13-5 in Table 4.4.I) at 1.8 K for the three field directions, *b*, *a*, and *c*. The solid lines are the least square fit of the first several data points to linearity, indicating the initial slope.

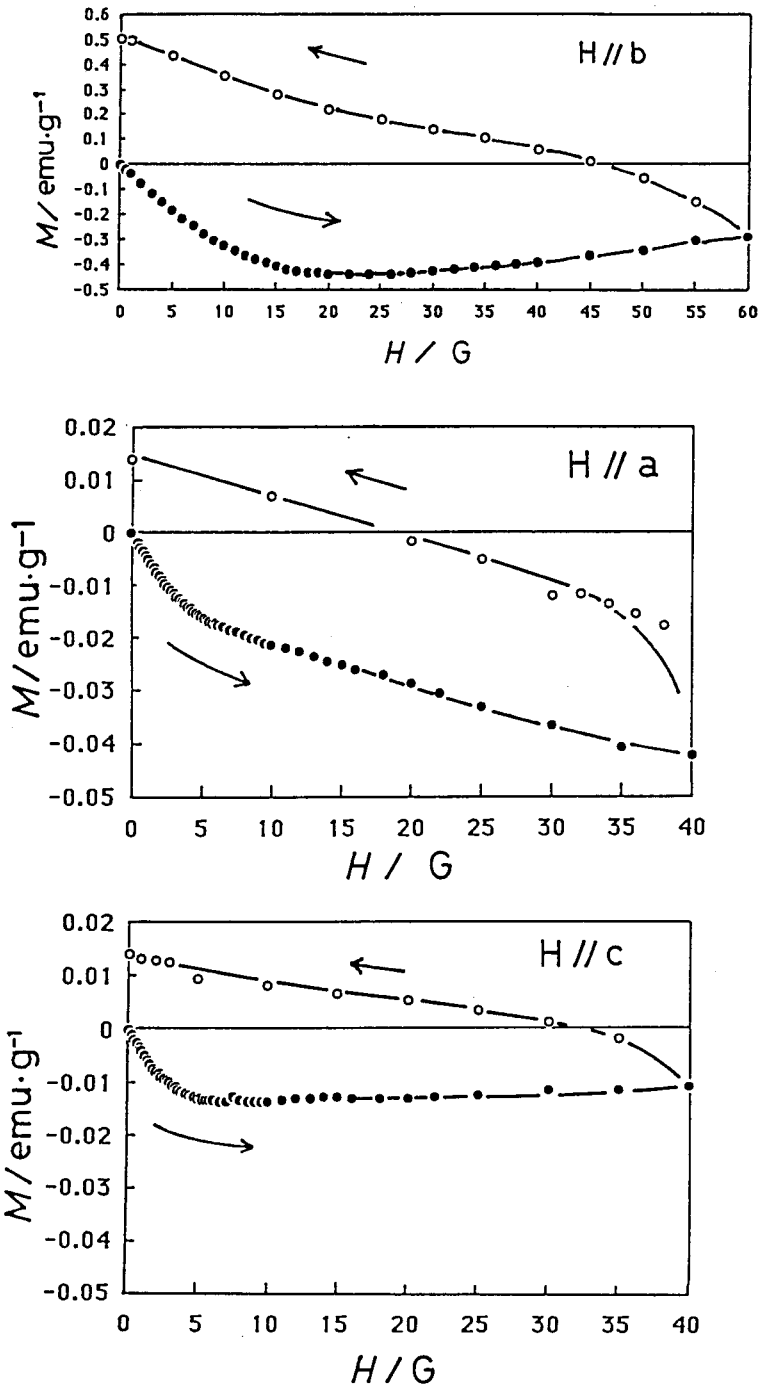

Fig. 4.4.4 Magnetization curves of the Group I sample (#13-5 in Table 4.4.I) at 1.8 K for the three field directions, *b*, *a* and *c*.

larger than that for an in-plane field by a factor of about 30. Furthermore, a strong flux trapping may also prevent the field from penetrating into the sample in the higher field along the *ac*-plane.

We define H_{c1}^{obs} as the field where the first deviation from linearity in the magnetization curve of the shielding signal occurs. In fact, we required that H_{c1}^{obs} should satisfy the following two conditions: i) at H_{c1}^{obs} the diamagnetic signal reduces to the value less than 98% of that extrapolated linearly from the least square fit of the first 4 or 5 data points, and ii) at the fields higher than H_{c1}^{obs} the signals show no recovery to the extrapolated values. The ambiguity in estimating H_{c1}^{obs} was less than ± 1 G for $\boldsymbol{H} \parallel \boldsymbol{b}$ and ± 0.2 G for $\boldsymbol{H} \parallel \boldsymbol{a}$ and $\boldsymbol{H} \parallel \boldsymbol{c}$. The H_{c1}^{obs} values thus estimated for the three field directions are compiled in Table I, together with the sizes of the samples used. At a glance, they do not seem to be very anisotropic; the deviation from linearity starts at the field of about 2 G for all the directions. However, they could be underestimated values of the lower critical field, H_{c1}, because of the demagnetization effect. The samples used in our experiments were rather thin plates, so that the effective field felt around the sample is much enhanced owing to the demagnetization, especially for the field normal to the plane. Since the shapes of our samples were far from ellipsoids, the magnetic field felt near the sample surface should be inhomogeneous. Thus it is difficult to carry out an accurate correction for the demagnetization effect. However, we have carried out a rough estimation by approximating the sample shape as an ellipsoid touching internally to crystal faces in order to obtain the demagnetization factors. The enhancement of the effective field is written as

$$H_{\mathrm{eff}} = H_{\mathrm{app}} / (1-D) = f\ H_{\mathrm{app}}\ , \qquad (4.4.1)$$

where D ($0 \le D \le 1$) is the demagnetization factor and f is the enhancement factor. The ellipsoid approximation gives an enhancement factor of about 5 for the field normal to the plane, while the factors are near 1 for the in-plane fields. This estimation is considered to reflect the lower limits of the enhancement factors. The values of H_{c1}'s, estimated roughly in this way, are also listed in Table 4.4.I, together with the enhancement factors calculated from the demagnetization coefficients for the ellipsoids [11].

Another way to evaluate the anisotropy of H_{c1} is to use the initial magnetization slope. Without the demagnetization effect, the slopes of the curves for the three field directions should be equal to each other in the linear region at low field. Even if there is the demagnetization effect, we could still obtain the same slopes using H_{eff} instead of H_{app}. We changed the scale of each field so that the three curves have the same slope in the linear region. The result is shown in Fig. 4.4.5, where the demagnetization factor for $\boldsymbol{H} \parallel \boldsymbol{c}$ is assumed to be equal to that calculated by the ellipsoid approximation. This method gives the anisotropic H_{c1} values, $H_{c1,\,b}$ = 40 G, $H_{c1,\,a}$ = 1.4 G, and $H_{c1,\,c}$ = 2.0 G. Since the field applied perpendicular to the plane exhibits strong inhomogeneity, the difference between $H_{c1,\,b}$ values estimated by the two methods is not surprising. The $H_{c1,\,b}$ value given by the ellipsoid approximation is clearly underestimated.

Thus, anisotropic H_{c1} values were estimated for this material, which is compatible with the anisotropy of H_{c2} reported previously. Similar anisotropic behavior was found in other organic superconductors,

Table 4.4.I. The lower critical filed, the demagnetization factor and the size of the sample for each field direction.

Sample	*Direction*	*Size* /mm	H_{c1}^{obs} / G	H_{c1} / G [a)]	*D*	*f*	H_{c1} / G [b)]
#13-5	*b*	0.16	4.0	17	0.77	4.35	40
	a	0.74	1.2	1.4	0.15	1.18	1.4
	c	1.10	1.8	2.0	0.08	1.09	2.0
#2-1	*b*	0.13	2.0	11.1	0.82	5.56	
	a	0.94	1.0	1.1	0.09	1.10	
	c	1.05	1.5	1.6	0.08	1.09	

a) The lower critical fields obtained by the ellipsoid approximation.

b) The lower critical fields evaluated by adjusting the initial magnetization slope.

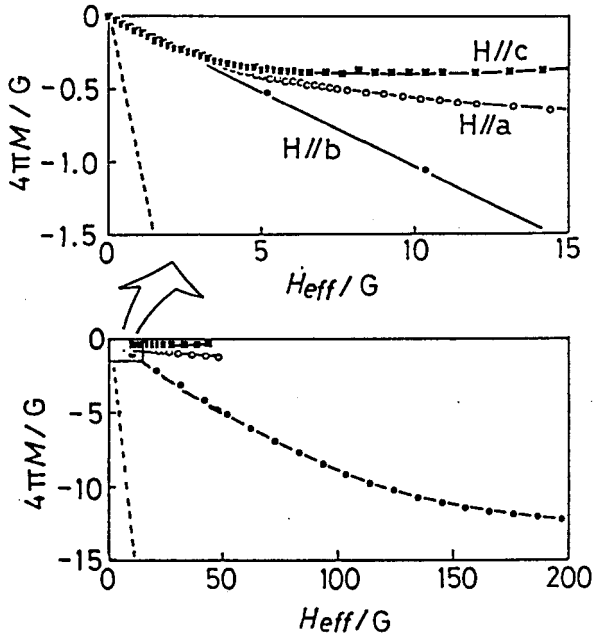

Fig. 4.4.5 Initial magnetization of the Group I sample (#13-5 in Table 4.4.I) at 1.8 K, plotted versus H_{eff}. For the H //c data (filled squares), H_{eff} is calculated by the ellipsoid approximation, while those for the H //a (open circles) and H //b (filled circles) data are adjusted so that the initial slopes match with that of the H //c curve. Note that the initial magnetization is about 10 % of that of the perfect diamagnetism (broken lines). The sample volume was calculated from the density, 2.25 g / cm^3, and the crystal weight, 0.33 mg.

$(TMTSF)_2ClO_4$ [28,29], β-$(BEDT\text{-}TTF)_2I_3$ [30], β-$(BEDT\text{-}TTF)_2IBr_2$ [31], β-$(BEDT\text{-}TTF)_2AuI_2$ [31], and κ-$(BEDT\text{-}TTF)_2$[Cu(NCS)2] [32].

In the framework of the Ginzburg-Landau (GL) theory, H_{c1} and H_{c2} are related to GL parameter, κ, and the thermodynamical critical field, H_c, by the equations,

$$\kappa = (1/2)^{1/2} (\ln \kappa + 0.497)\, H_c / H_{c1,} \tag{4.4.2}$$

$$\kappa = (1/2)^{1/2}\, H_{c2} / H_c\,. \tag{4.4.3}$$

The parameter, κ, is defined as

$$\kappa = \lambda / \xi\,, \tag{4.4.4}$$

where λ is the penetration depth and ξ is the coherence length. The observed anisotropy of H_{c1}, as well as of H_{c2}, is probably ascribable to the anisotropy of ξ, which is largest in the *ac*-plane [26]. The estimated H_{c1} values are about 40 G for $\boldsymbol{H} \parallel \boldsymbol{b}$ (by the initial slope scaling method) and from 1.1 to 2 G for the in-plane fields. The ratio, 20 to 36, is consistent with that of $1/H_{c2}$, about 30.

Although the in-plane anisotropy of H_{c2} has not been known, the anisotropic optical effective mass was estimated as [6],

$$m^*_a = 1.5\, m_e \text{ and } m^*_c = 3.0\, m_e, \tag{4.4.5}$$

where m_e denotes the electron mass. It was elucidated that the nearly-

free-electron model with parabolic dispersion can well reproduce the tight-binding band structure of this material [6]. Using the former model, we obtain the ratio,

$$\kappa_c / \kappa_a = v_{Fa} / v_{Fc} = (m^*_a / m^*_c)^{1/2} = 0.7 , \qquad (4.4.6)$$

where v_{Fa} and v_{Fc} are the *a*- and *c*-components of the Fermi velocity, respectively. On the other hand, to the limit of large κ, we can calculate the ratio, κ_c / κ_a, from Eq.(4.4.2) as,

$$\kappa_c / \kappa_a = (H_{c1})_a / (H_{c1})_c . \qquad (4.4.7)$$

By use of the H_{c1} values obtained in this work, the ratio, κ_c / κ_a, is estimated to be 0.7. This is consistent with the result of Eq.(4.4.6).

4.5. Thermoelectric Power

In Sec. 4.3, the structures of the conduction band and the Fermi surface of θ-(BEDT-TTF)$_2$I$_3$ have been derived from the optical properties by assuming the orthorhombic averaged structure. However, strictly speaking, the assumed structure, and thus the derived band structure, does not exactly hold for a real crystal of θ-(BEDT-TTF)$_2$I$_3$, because the true structure is the monoclinic one with lowered symmetry of the molecular arrangement. Since the effect of this difference is small, as noted by the weakness of the interband transitions, the global shape of the Fermi surface

derived from the optical data is reliable. In other words, the optical experiments probe only the global features and are insensitive to local small structures of the Fermi surface. For more detailed examination of the electronic structure of this salt, it is necessary to do other experiment which is sensitive to small structures.

Thermoelectric power (TEP) measurement is one of such tools [33,34]. As well as dc conductivity measurement, it reflects the lowest energy excitation ($< k_B T$) around the Fermi level. Moreover, its sign and amplitude, which may be anisotropic and temperature dependent, reflect the curvature of the energy band around the Fermi surface. In some cases, TEP information has been shown to be useful to investigate the Fermi surface of BEDT-TTF salts. Thus, it is expected that TEP measurement would reveal a new feature of the structure of the Fermi surface of θ-(BEDT-TTF)$_2$I$_3$, which was not detected in the optical study.

Figure 4.5.1 shows the TEP of θ-(BEDT-TTF)$_2$I$_3$ measured along the two directions in the conduction plane, *a* and *c*. For both directions, TEP is considerably small as compared with other BEDT-TTF salts. Along the *a*-axis, TEP is negative and very small; it is almost zero at room temperature. The TEP makes a broad shoulder and minimum around 50 K and 200 K, respectively. Along the *c*-axis, TEP is positive, with a prominent peak at about 20 K, and gradually decreases with increasing temperature up to about 220 K. These features are qualitatively similar to those of a series of BEDT-TTF salts, (BEDT-TTF)$_2$MHg(SCN)$_4$ (M=K, Rb and NH$_4$), except for the considerably suppressed values of TEP and for the minimum at 220 K along the *c*-axis. The peak along the *c*-axis should be ascribed to the phonon contribution, such as the phonon drug

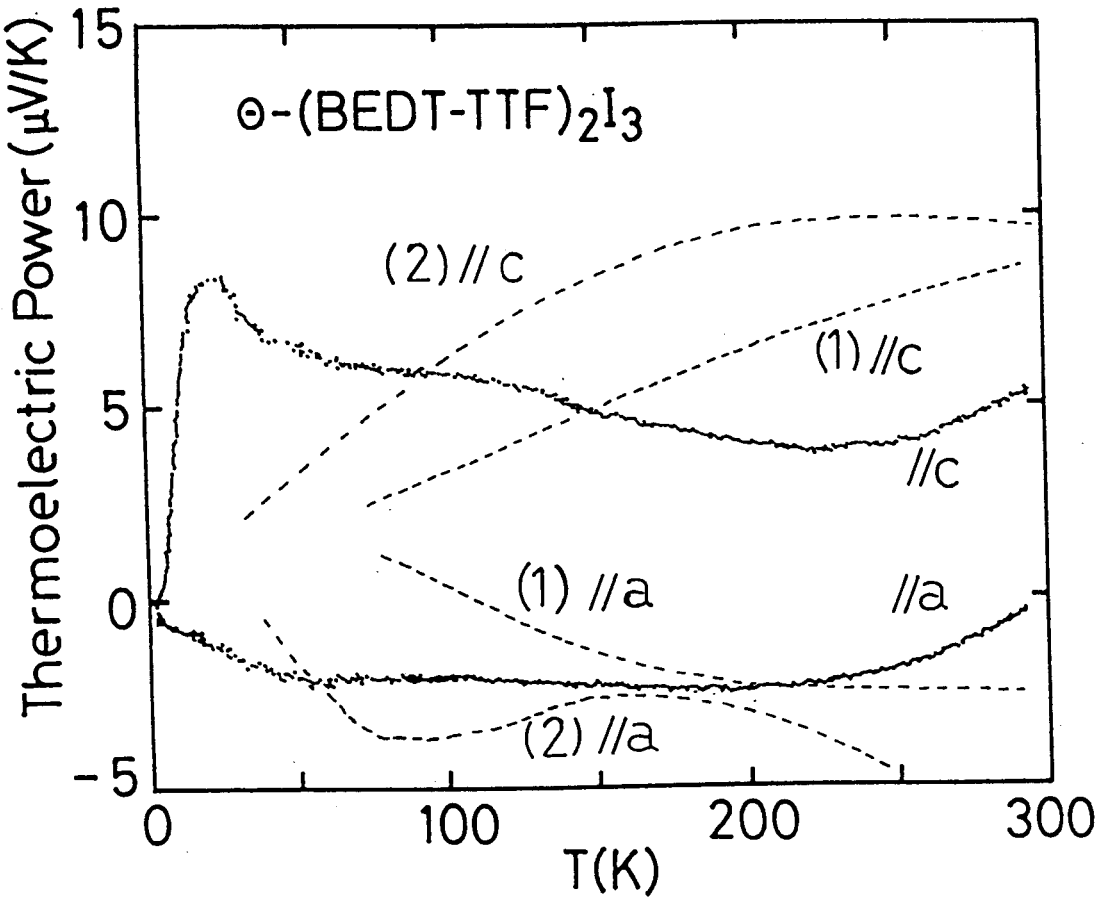

Fig. 4.5.1. Thermoelectric power of θ-(BEDT-TTF)$_2$I$_3$. The broken curves stand for the calculations with the following parameter sets:

(1): $t_a = 0.090$ eV, $t_a' = 0.120$ eV and $t_c = 0.055$ eV.

(2): $t_a = 0.045$ eV, $t_a' = 0.060$ eV and $t_c = 0.030$ eV.

For the definition of the transfer integrals, see Fig. 4.5.2.

effect, rather than to the electronic band origin. The TEP values are so small that it is difficult to distinguish exactly the contributions of phonons and electrons at low temperatures. In the following, the TEP values above about 100 K are mainly considered.

It possible to simulate the temperature dependence of TEP on the basis of the tight-binding band structure [33]. According to the Boltzmann equation [35], TEP (S) of a metal is expressed as

$$S_{ij} = (1 / eT) \sum_{k=1}^{3} (K_0 - 1)_{ij} K_{1,kj} \quad (i, j, k = x, y, z) \ , \qquad (4.5.1)$$

$$K_{0,ij} = (\tau / 4\pi^3 \hbar) \iint (v_F)_i \, (v_F)_j (-\partial f_0 / \partial \varepsilon) \, (dS / v_F) \, d\varepsilon \ , \qquad (4.5.2)$$

$$K_{1,ij} = (\tau / 4\pi^3 \hbar) \iint (v_F)_i \, (v_F)_j \, (\varepsilon - \varepsilon_F)(-\partial f_0 / \partial \varepsilon) \, (dS / v_F) \, d\varepsilon \ , \qquad (4.5.3)$$

where f_0 is the Fermi distribution function, ε_F is the Fermi energy, and v_F and $(v_F)_i$ are the Fermi velocity and its component, respectively. The quantities, S, K_0 and K_1 are tensors. In the simulations presented here, the integrals over the Fermi surface were numerically calculated by dividing the first Brillouin zone into 160 × 160 meshes.

A simulation based on the band structure derived from the optical study yields positive TEP both for a- and c-axis, which is in contradiction to the observation. This band structure is derived by assuming the ortho-rhombic lattice. In this assumed structure, the energy band is described only by two transfer integrals, t_a and t_c. The Fermi surface is determined

so as to satisfy the requirement of 3/4-filling of this band. The charge carriers are considered to be holes for this 3/4-filled band. This is the origin of the positive sign of the simulated TEP.

It is thus evident that the band structure is more complicated one than assumed previously. The effect of lowered symmetry should be taken account of. For example, a simple model given in Fig. 4.5.2 can approximate this feature. In Fig. 4.5.1, the curves calculated from two parameter sets for this model are depicted. Qualitative agreement with the observation, i.e., the sign for each direction and the small values, is obtained. This model can describe the removal of degeneracy on the XM zone boundary. This affords the positive curvature of the upper band near the XM boundary, so that this portion of the Fermi surface retains the electron character (Fig. 4.5.3). The origin of the negative TEP along the *c*-axis can be understood in this way.

The curvature of the band near the zone boundary is a subtle problem. This is because of the $\cos(ak_a / 2)$ dependence of the band dispersion for the basic orthorhombic packing, where the curvature is exactly zero at the boundary. This situation is similar to those in κ-(BEDT-TTF)$_2$[Cu(NCS)$_2$] [33] and (BEDT-TTF)$_2$MHg(SCN)$_4$ [34]. The small values of TEP can also be understood in this framework, while the considerably wide band width of this salt also responsible for the suppression of TEP. It is also noticed that the TEP values are prescribed not only by the amplitudes of transfer integrals but also by the differences between them. Therefore, further improvement of the fit between the calculation and observation is difficult. For instance, the different two parameter sets yields similar temperature dependence of TEP.

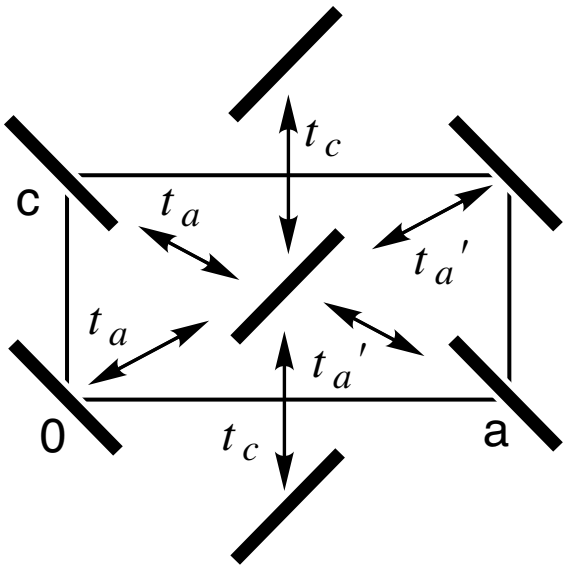

Fig. 4.5.2. The model molecular arrangementt assumed in the simulation of TEP

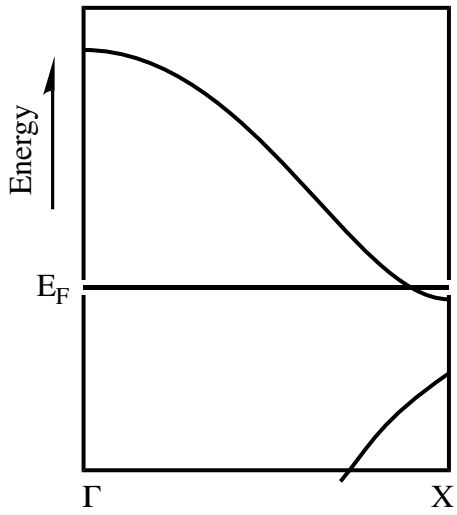

Fig. 4.5.3. Schematic display of the effect of the symmetry lowering ($t_a > t_a'$) on the band structure near the zone boundary. Thick and broken lines are with and without the symmetry lowering, respectively.

The present TEP results have revealed that the effect of lowered symmetry, i.e., the removal of degeneracy, plays a crucial role in the transport phenomena in θ-(BEDT-TTF)$_2$I$_3$. This affords a viewpoint different from that of the optical study.

4.6. The de Haas-van Alphen (dHvA) Oscillations

The first observation of the "saw-tooth" dHvA oscillation in θ-(BEDT-TTF)$_2$I$_3$ has shown that a satisfactory clear 2D electronic system is realized in this salt [6]. The topology of the Fermi surface (FS) has been deduced from the interpretation of the dHvA oscillations in terms of the magnetic breakdown (MB) effect, the effect of tunnelling across the gap at Fermi surface under high magnetic field [6]. This point is examined in more detail in this section. Moreover, the dHvA results, including the cyclotron mass, are compared with the band structure inferred from the optical study (Sec. 4.3)

4.6.1. Analysis of the dHvA Oscillations and Magnetic Breakdown Effect

Figure 4.6.1 shows the magnetization as a function of magnetic field at the selected temperatures [16]. The data was recorded for the crystal other than the one previously reported [6,36-38]. A significant difference between these two samples is the appearance of the nodes at about 12, 15 and 20 T in the data in Fig. 4.6.1. The Fourier transform of the data displayed in Fig. 4.6.2. shows that these nodes result from the beat of the

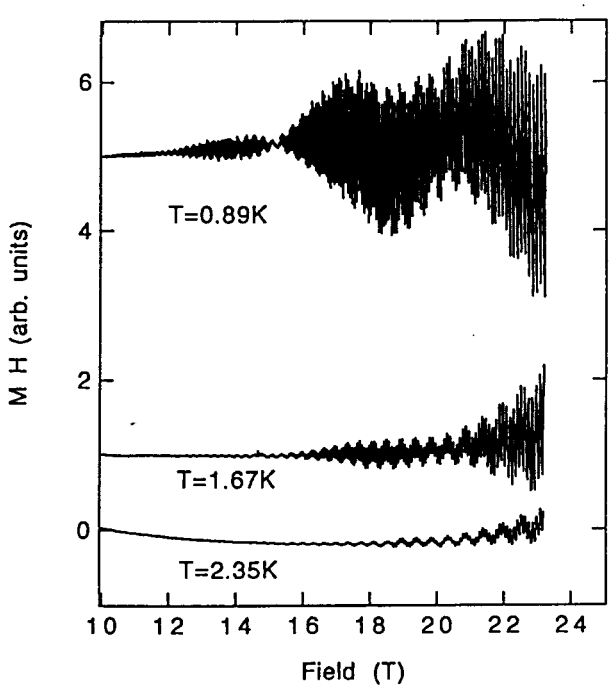

Fig. 4.6.1. dHvA oscillations of θ-(BEDT-TTF)$_2$I$_3$ as a function of field at selected temperatures. The curves for T=0.89 K and T=1.67 K are shifted up for clarity. Twinning effect is visible as the nodes at about 12, 15 and 20 T.

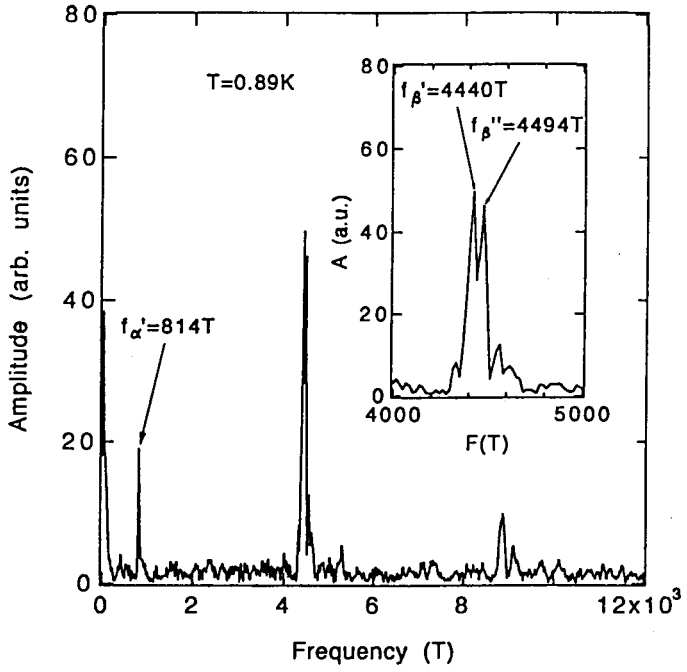

Fig. 4.6.2. Fourier transform of the 0.89 K data in Fig. 4.6.1. The inset is the close-up around the higher frequencies.

two close frequency components at f_β'=4440 T and f_β''=4494 T. The coexistence of such two fast oscillations, corresponding to approximately 100 % of the first Brillouin zone (BZ), in an exactly single crystal contradicts to the basic chemical architecture of the salt. As mentioned above, θ-(BEDT-TTF)$_2$I$_3$ often crystallizes in a twinning form. Therefore, it is very likely to think of the beat as a result of the twinning in the crystal examined. If this is the case, the nodes due to this beat should be observed at the field, H_n, satisfying,

$$\cos[\pi(f_\beta'' - f_\beta') / H_n] = 0, \quad (n = 0, 1, 2,....) \tag{4.6.1}$$

or,

$$(f_\beta'' - f_\beta') / H_n = n + 1/2. \quad (n = 0, 1, 2,....) \tag{4.6.2}$$

Corresponding to n = 3 and 4, the fields H_n= 15.4 and 12.0 T are respectively obtained, which is consistent with the observation. The oscillation without such beat was able to be observed for the other crystal [6,36-38] (Fig. 4.6.3). On the other hand, beat behavior may come from small warping of a single cylindrical FS. The beat having such origin should give nodes at the field, H'_n, satisfying,

$$\cos[\pi(f_\beta'' - f_\beta') / H'_n - \pi/4] = 0, \ (n = 0, 1, 2,....) \tag{4.6.1'}$$

or,

$$(f_\beta'' - f_\beta') / H'_n = n + 3/4, \quad (n = 0, 1, 2, ...) \qquad (4.6.2')$$

where f_β' and f_β'' correspond to the minimum and maximum of the cross-sectional area of the warped FS, respectively. For n=3 and 4, we obtain H'_n = 14.4 and 11.4 T, respectively. These values are appreciably lower than those observed for θ-(BEDT-TTF)$_2$I$_3$. Thus we conclude that the observed behavior is composed of the contributions from two domains in different orientations; each domain exhibits the fast and slow oscillations, f_α and f_β at about 800 T and 4000 T, respectively.

We derive the cyclotron mass values from the data showing twinning effect (Figs. 4.6.1 and 4.6.2) below, because only they are available for the analysis of the temperature dependence. The inset of Fig. 3 displays the Fourier transform of the magnetization data without a remarkable beat, showing the fast oscillation at f_β = 4290 T. Assuming that the field direction was parallel to the principal axis in this measurement, we can estimate the inclination of each twinning domain with respect to the field from the deviation of f_β' and f_β'' from f_β. The angles between the principal axes of the domains and the field direction are 15° and 17°, corresponding to f_β' and f_β'', respectively. This misorientation may yield at most 6 % of error in our mass analysis for a cylindrical FS.

In Fig. 4.6.4, the mass-plot, the plot of A / T versus T, is shown, where A is the amplitude of the Fourier component at each frequency. From the slope of each plot, the cyclotron masses are evaluated: m_β = 3.6 m_e for the fast oscillations, and m_α = 2.0 m_e for the slow oscillation, are obtained.

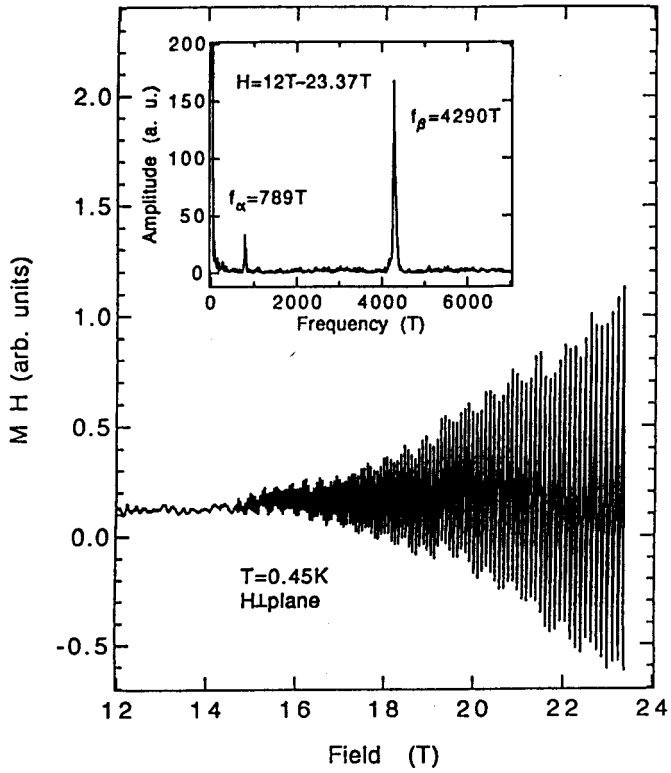

Fig. 4.6.3. dHvA oscillations and its Fourie tranform (inset) of θ-(BEDT-TTF)$_2$I$_3$ showing no distinct beat.

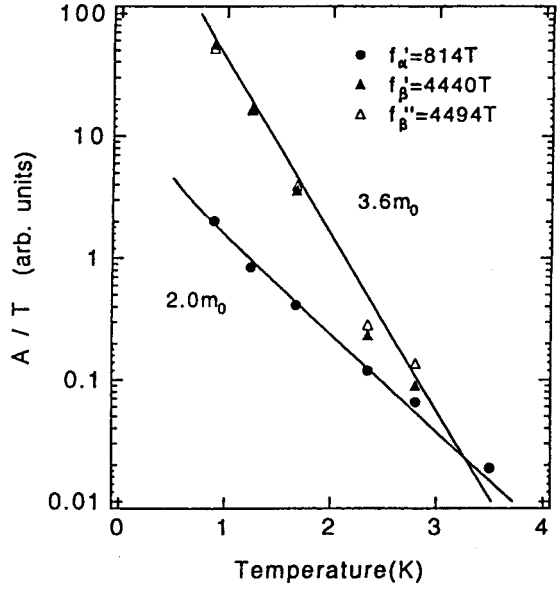

Fig. 4.6.4. The mass-plot, i.e., the plot of A / T versus T, where A is the amplitude of the Fourier component at each frequency.

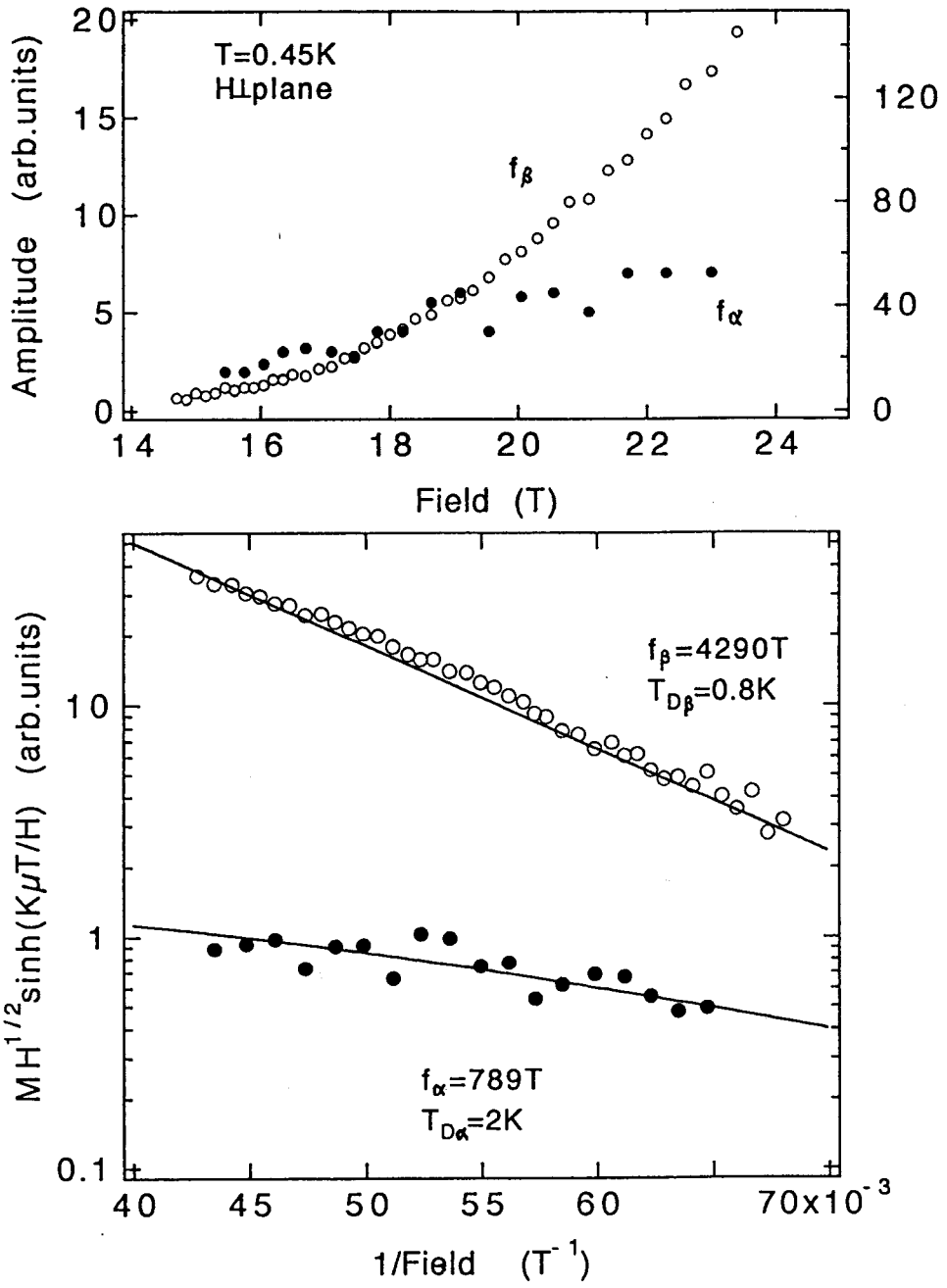

Fig. 4.6.5. Top: Field dependence of the oscillation amplitude. Bottom: The Dingle plot of the data in Fig. 4.6.3. The solid lines stand for the calculations considering the magnetic breakdown effect.

Field dependence of the oscillation amplitude is also analyzed in terms of the Lifshitz-Kosevich (LK) formula [39]. In the presence of the magnetic breakdown (MB) effect, the tunnelling probability is approximately expressed as,

$$P = \exp(-H_B/H), \tag{4.6.3}$$

where H_B denotes the breakdown field. We consider here the tunnelling junctions between the closed pocket (α) and the pair of open portion. Such a situation modifies the original LK formula for a single orbit. The results can be expressed as [40],

$$\begin{aligned} S_\beta &= M_\beta(H)\, H^{1/2} \sinh[K(m_\beta / m_e)T / H] \\ &\propto P^4 \exp[-K(m_\beta / m_e)T_{D\beta} / H], \end{aligned} \tag{4.6.4}$$

and,

$$\begin{aligned} S_\alpha &= M_\alpha(H)\, H^{1/2} \sinh[K(m_\alpha/m_e)T / H] \\ &\propto (1-P)^2 \exp[-K(m_\alpha/m_e)T_{D\alpha} / H], \end{aligned} \tag{4.6.5}$$

where $K = 2\pi^2 m_e c k_B / e\hbar = 14.7$ T / K, $M(H)$ is the amplitude of the oscillation, and T_D is the Dingle temperature; the subscripts, α and β, denote the slow and fast oscillations, respectively. By using m_α and m_β evaluated as above, $T_{D\alpha}$, $T_{D\beta}$ and H_B can be estimated from the slope of

log(S) versus 1 / H plots. Figure 4.6.5 shows such a plot of the data given in Fig. 4.6.3. Too small amplitude of the oscillations below 15 T prevents us from evaluating the parameters precisely. Nevertheless, the parameter set $T_{D\alpha}$ = 2 K, $T_{D\beta}$ = 0.8 K, and H_B = 15 T seems to reproduce the data well, as depicted by the solid curves in Fig. 4.6.5. The overall field dependence is thus explained by the MB effect.

Another evidence for the MB effect is the overall field dependence of the resistivity [16]. Figure 4.6.6 shows the transverse magnetoresistance of θ-(BEDT-TTF)$_2$I$_3$ at 0.7 K for the field perpendicular to the basal plane. SdH oscillation appears above about 15 T. Superconductivity was not observed for this sample. The low field behavior is consistent with that reported in Ref.8. Noteworthy is the maximum around 6 T.

By taking account of the MB effect, the decrease in resistance above H_{max}= 6 T can be qualitatively explained as follows. In the low field limit, H « H_B, where the MB effect is negligible, the resistivity is dominated by the electron scattering. The resistivity should increase quadratically until the MB effect becomes appreciable. In the high field limit, the dominant term in the resistivity can be calculated by means of a path integral method including the possibility of the magnetic breakdown. This contribution is written as [40-42],

$$R = (H / n\, e\, c\,)8(1 - P) / \pi P, \qquad (4.6.6)$$

where n is the number density of the carriers. As $H \rightarrow \infty$, this term takes the form 1 + H_B / 2H, so that the resistivity decreases with increasing field. Hence, a maximum of resistivity should appear at an intermediate

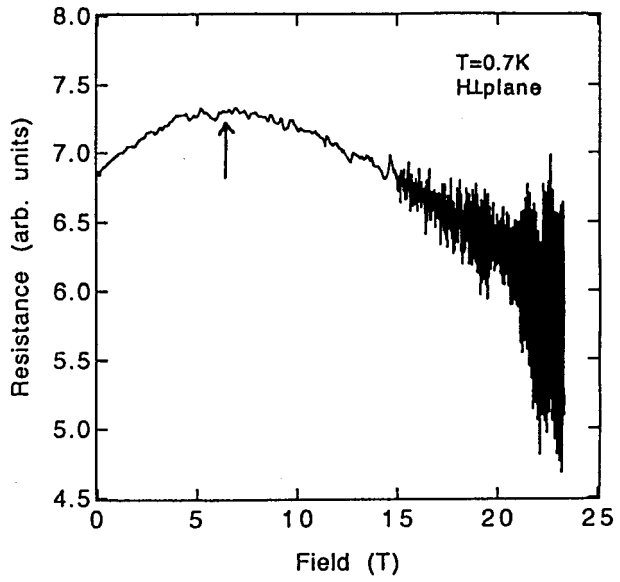

Fig. 4.6.6. Transverse magnetoresistance of θ-(BEDT-TTF)$_2$I$_3$ at 0.7 K. The field was applied perpendicular to the two-dimensional plane.

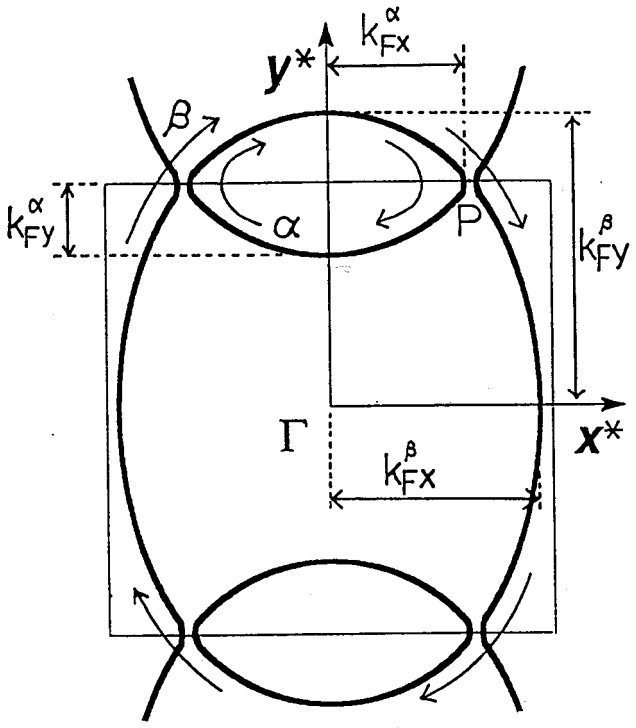

Fig. 4.6.7. The Fermi surface topology concluded in this study, together with the notation of the cyclotron orbits, α and β. The directions, x and y, corresponds to the *b* and *a* axes in the monoclinic lattice defined in Ref. 3, respectively.

field, H_{max}, which depends on H_B and the scattering time. Such behavior has been found also for (BEDT-TTF)$_2$KHg(SCN)$_4$ [43], which has FS topology similar to that of θ-(BEDT-TTF)$_2$I$_3$. According to the semiclassical model assuming a field independent scattering time, H_{max} lies between H_B/ 3 and H_B/ 10 [41]. The present results, H_B=15 T and H_{max}= 6 T, can be qualitatively explained by this scheme.

4.6.2. Fermi Surface and Band Structure

The intermolecular transfer interactions in the donor sheets of θ-(BEDT-TTF)$_2$I$_3$ can be categorized into two groups; there are three face-to-face ones and four face-to-side ones [4]. The difference within each group is related to the structural modulation on the uniform packing of BEDT-TTFs arising from I_3^- ion arrangement. Since this modulation is expected to be small, we first consider only two types of transfer integrals, $t_{f\text{-}f}$ and $t_{f\text{-}s}$, standing for the two groups in describing the band structure. (On the basis of the notation in Sec. 4.3, $t_{f\text{-}f}$ and $t_{f\text{-}s}$ correspond to t_c and t_a, respectively.) This simplification enables us to treat the Fermi surface geometry and other physical properties exactly. In this picture, the open and closed portions of FS stick together at the MB junctions. The geometry of the FS is determined only by the ratio of the transfer integrals, $t_{f\text{-}f}$/ $t_{f\text{-}s}$.

On the basis of such approximation, the infrared reflectance spectra of this salt were first analyzed and the band structure was deduced [5] (Sec. 4.3). The ratio of the transfer integrals, $t_{f\text{-}f}$/ $t_{f\text{-}s}$, found to reproduce the optical results, is 0.59 [5]. From the reported band parameters [5], the cyclotron mass corresponding to the orbit on each portion of FS can be

calculated by use of the following equations,

$$m_c = (\hbar^2 / 2\pi)\,(\partial A_c / \partial \varepsilon);\ \ \varepsilon = \varepsilon_F \qquad (4.6.7)$$

and,

$$(\partial A_c / \partial \varepsilon) = S_{BZ}\,\rho_c(\varepsilon);\quad \varepsilon = \varepsilon_F \qquad (4.6.8)$$

where m_c and A_c are the mass and cross sectional areas for the cyclotron orbit c, S_{BZ} the area of the first BZ, and $\rho_c(\varepsilon_F)$ density of states per 2D unit cell per spin for the portion of FS corresponding to the orbit c. It is also possible to estimate the cross sectional areas. The cyclotron masses calculated in this way are, m_β^{opt}=2.2 m_e and m_α^{opt}=1.0 m_e, with the cross sectional areas, A_β and A_α, 100 % (exact) and 14 % of S_{BZ}, respectively. Here, c = β and c = α denote the whole FS and the closed portion, respectively (Fig. 4.6.7).

Equations (7) and (8) indicate that the cyclotron mass for a 2D system is proportional to the (partial) density of states of the relevant portion of the Fermi surface. It follows from this that the larger cyclotron mass value for the fast oscillation arising from the MB effect is the simple sum of the partial densities of states of the portions to be coupled each other by the breakdown; it is not an average along the coupled orbit. Therefore, for a coupled large orbit composed of a closed pocket and open portions, we usually obtain cyclotron mass value larger than that for the small pocket only. The larger value of the coupled orbit mass, as in the present case, is not surprising and does not necessarily

involve the larger mass for the open portions. We have to be careful in comparing the cyclotron masses for different types of orbits. The enhanced mass for the open portions of the FS larger than that for the coupled orbit [45] cannot be concluded.

The geometry of the FS concerns the two ratios, m_β/m_α and A_α / A_β. The values, $m_\beta/m_\alpha = 2.2$ and $A_\alpha / A_\beta = 0.14$, are inferred from the optical results, while the present dHvA results give $A_\alpha / A_\beta = f_\alpha / f_\beta = 0.18$ and $m_\beta / m_\alpha = 1.8$. This comparison supports the picture shown in Fig. 7, although there remains discrepancy which probably comes from the simplification introduced in the analysis of the optical data. The MB effect clearly shows opening of a small gap at the junction of FS. This gap should give rise to interband optical transitions. However, the transition energy, i.e., the gap width, is so small that this interband contribution cannot be well separated from the intraband one in the observed spectra. In Ref. 5, therefore, the band parameters were estimated from the plasma frequencies including the low energy interband contributions. Since the FS is still connected along the x-direction in Fig. 4.6.7 even in the presence of the gap, such overestimation of the plasma frequency is expected mainly for the y-direction data. This means that k_{Fy}^{β} in Fig. 4.6.7 is relatively underestimated, which results in the underestimation of m_α and A_α in the analysis of the optical data. The discrepancy between the optical and the dHvA results can be qualitatively explained in this way.

On the other hand, the values of cyclotron mass, $m_\beta = 3.6\, m_e$ deduced from the dHvA oscillations is larger than that calculated from the optical results by the factor of about 1.6. In order to remove this discrepancy, the transfer integrals smaller than the reported ones [5] by the factor of

0.6 should be used. Such difference cannot be ascribable only to experimental error. It is also difficult to explain this by taking account of the difference in the transfer integrals within each group. Mass enhancement near the Fermi level due to many-body effect, such as electron-phonon interaction, is thereby suggested. The optical spectra probe the global structure of the conduction band rather than the detailed features near the Fermi level, so that the optical mass is insensitive to the many-body effect on the quasiparticle energy near the Fermi level.

Next, let us direct our attention to the gap affording the MB effect. The breakdown field, H_B, is approximately related to the energy gap near the junction, ε_g, by the equation [40,45],

$$H_B = (\pi / 4)\, (c / e\hbar)\, (\varepsilon_g^{\,2} / v_x v_y), \tag{4.6.9}$$

where v_x and v_y are the components of the Fermi velocity at the junction parallel and perpendicular to the zone boundary, respectively. The simplified tight-binding model with the parameters inferred from the optical results [5] yields $v_x = 1.5 \times 10^7$ cm/s and $v_y = 1.1 \times 10^7$ cm/s. From this, together with H_B = 15 T, it follows that $\varepsilon_g = 1.5 \times 10^{-2}$ eV. If the mass enhancement near the Fermi level is taken into account, the gap should be about the half of this value. A more popular formula [40],

$$H_B \approx (m_\alpha\, c / e\hbar)\, (\varepsilon_g^{\,2} / \varepsilon_F), \tag{4.6.10}$$

with the cyclotron mass, $m_\alpha = 3.6\, m_e$, results in the same order of magnitude, i.e., $\varepsilon_g \approx 1 \times 10^{-2}$ eV. The corresponding spacing between the open and

the closed portions of the FS at the junction is as small as about 2 % of π / b, where b is the lattice constant along the x-direction. This justifies the application of the simplified band model to approximate estimation of the masses and ε_F.

In the framework of the tight-binding band model, the origin of the gap at the zone boundary is the difference of transfer integrals within the groups, which reflects the small deviations from the uniform packing of BEDT-TTFs. In the present case, it seems difficult to predict such a small energy structure accurately enough. Nevertheless, the empirical tight-binding band calculations can provide a reasonable estimation of the order of magnitude of the gap [4]. Another problem which exists in the present case is the failure in prediction of the topology of FS by the calculations [4]. Even in the presence of the deviations from the uniform packing, the geometry of FS is basically determined by the ratio of the group averages of the transfer integrals, $\langle t_{f\text{-}f} \rangle / \langle t_{f\text{-}s} \rangle$. Since the modes and characters of the intermolecular contacts are entirely different between the groups, attention should be paid in comparing $t_{f\text{-}f}$ with $t_{f\text{-}s}$. The calculations [4] yielded $\langle t_{f\text{-}f} \rangle / \langle t_{f\text{-}s} \rangle = 1.7$, while the optical and the dHvA experiments support $\langle t_{f\text{-}f} \rangle / \langle t_{f\text{-}s} \rangle = 0.59$. The former one is sensitive to the details in the parameterization in the extended Hückel molecular orbital calculations, and can be suppressed down to about 0.2 by taking account of the contributions of sulfur 3d orbitals [46]. Therefore, the contradiction between the experiments and the calculations is expected to be removed, when moderate weight of the sulfur 3d contributions is adopted. In spite of such arbitrariness in the empirical parameterization, it is evident that in studying the electronic structures of the molecular conductors the frame-

work of the tight-binding band model works well with the help of experiments, as demonstrated in this study.

4.6.3. Summary

From the analysis of the dHvA oscillations in θ-(BEDT-TTF)$_2$I$_3$, the cyclotron masses have been evaluated to be 2.0 m_e and 3.6 m_e, for the slow and fast oscillations, about 800 T and 4000 T. The latter has been shown to be as a consequence of the magnetic breakdown effect which connects the closed and open portions of the Fermi surface. These two portions are separated by the gap of 1.5×10^{-2} eV at the junction. These results are consistent with the topology of the Fermi surface deduced from the tight-binding band model with the parameters inferred from the optical measurement. It is also proposed that the contribution of the sulfur 3d orbitals should be taken account of in the extended Hückel calculations of the HOMO of BEDT-TTF.

4.7. The Subnikov-de Haas (SdH) Oscillations and Small Fermi Surface

In this section, the notation of the crystal axes follows that of the monoclinic system.

A typical SdH signal observed in a high magnetic field range is shown in Fig. 4.7.2 (a). The Fourier spectrum shows the two fundamental frequencies marked by the symbols, α and β, and their combination frequencies. The α and β oscillations are attributed to the closed orbit

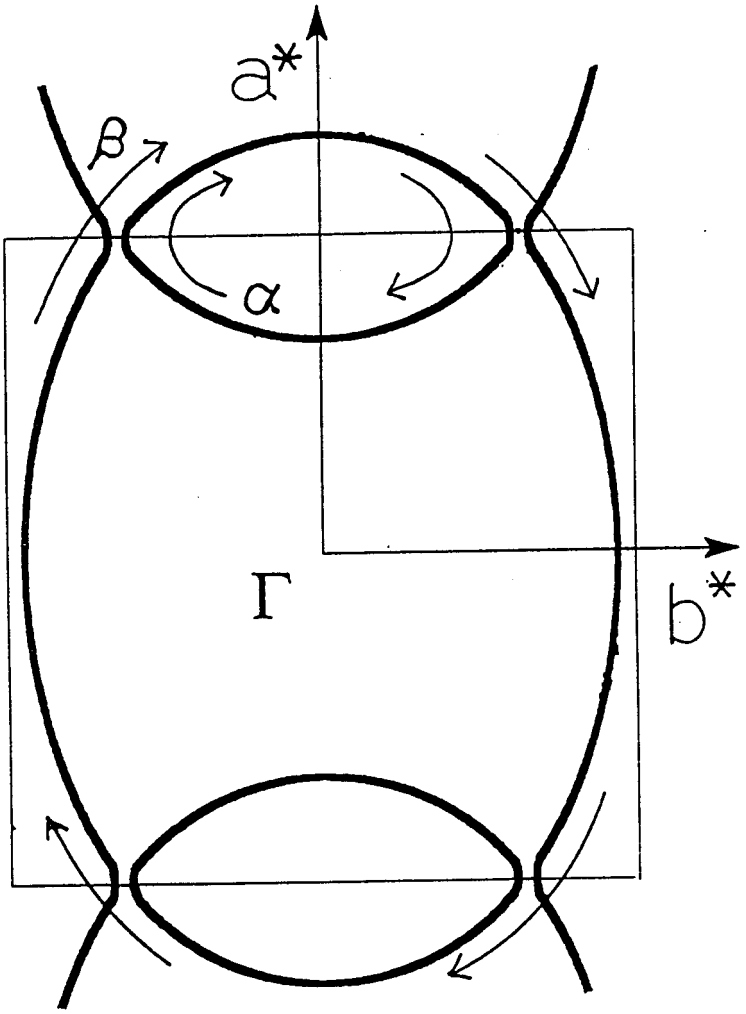

Fig. 4.7.1. The Fermi surface of θ-(BEDT-TTF)$_2$I$_3$ concluded from the optical and the dHvA results in the framework of the tight-binding model.

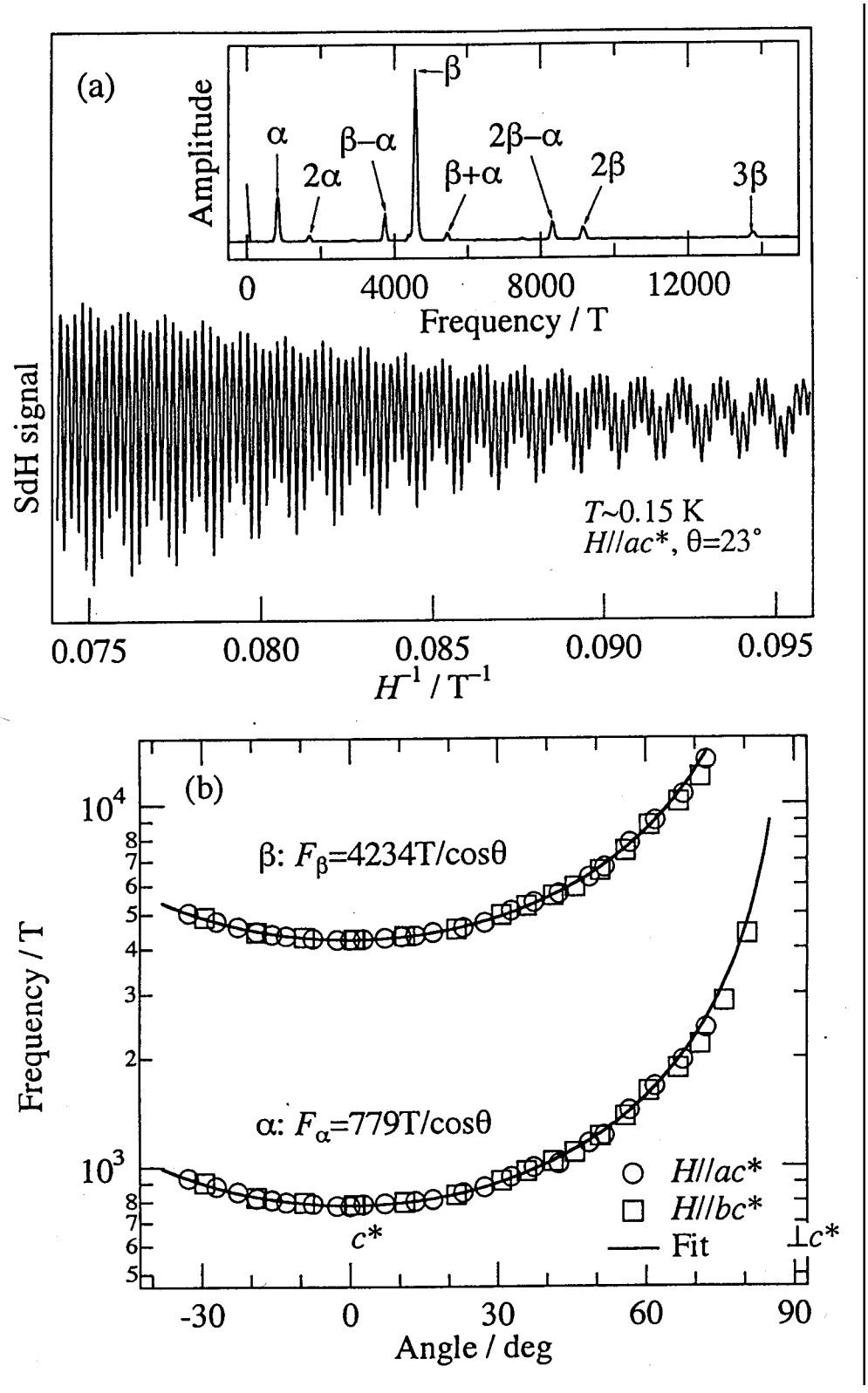

Fig. 4.7.2. (a) Typical SdH oscillations in a high magnetic field range. The inset shows the corresponding Fourier spectrum. (b) Frequencies of α and β as a function of the field angle measured from the c^*-axis. The lines show the $1 / \cos\theta$ fits.

around the zone boundary and the magnetic breakdown orbit, respectively (Fig. 4.7.1). The angle dependence of their frequencies is summarized in Fig. 4.7.2 (b). The angle dependence fits well with the formula, $f = f_0 / \cos\theta$, both for $\boldsymbol{H} \parallel ac^*$ and for $\boldsymbol{H} \parallel bc^*$, where θ is the angle between the magnetic field and the c^*-axis. The $1/\cos\theta$ dependence indicates that the Fermi surfaces responsible for the α and β oscillations are almost perfect cylinders, as expected for the two-dimensionality of the electronic structure of θ-(BEDT-TTF)$_2$I$_3$. The frequency, f_0, is 779 T for α and 4234 T for β. The corresponding cross-sectional areas are 19 % and 102 % of the area of the first Brillouin zone viewed along the c^*-axis for α and β, respectively. From the temperature dependence of the amplitudes between 0.05 and 0.6 K, the cyclotron masses of the α and β orbits are estimated to be (1.8 ± 0.1) m_e and (3.5 ± 0.1) m_e, respectively. The frequencies and the cyclotron masses are in good agreement with the dHvA results [6,7] given in the preceding section. The cross-sectional area of the orbit α, 19 %, is also closed to that predicted from the optical study, 14 % [5]. The angle dependence, the frequencies, and the cyclotron mass have definitely established the topology and the shape of the two-dimensional Fermi surface of θ-(BEDT-TTF)$_2$I$_3$.

New SdH oscillations are found in a low magnetic field range below about 3 T. Figure 4.7.3 shows the SdH oscillations together with their Fourier spectra for several field directions. The angle dependence of the frequencies is summarized in Fig. 4.7.4, where the frequencies are tentatively classified into branches, γ (γ′,γ″), δ and ε. We have examined the angle dependence from about – 40 ° to 90 ° for each of θ_a, θ_b, and ϕ, and confirmed the symmetry with respect to c^* and b axes.

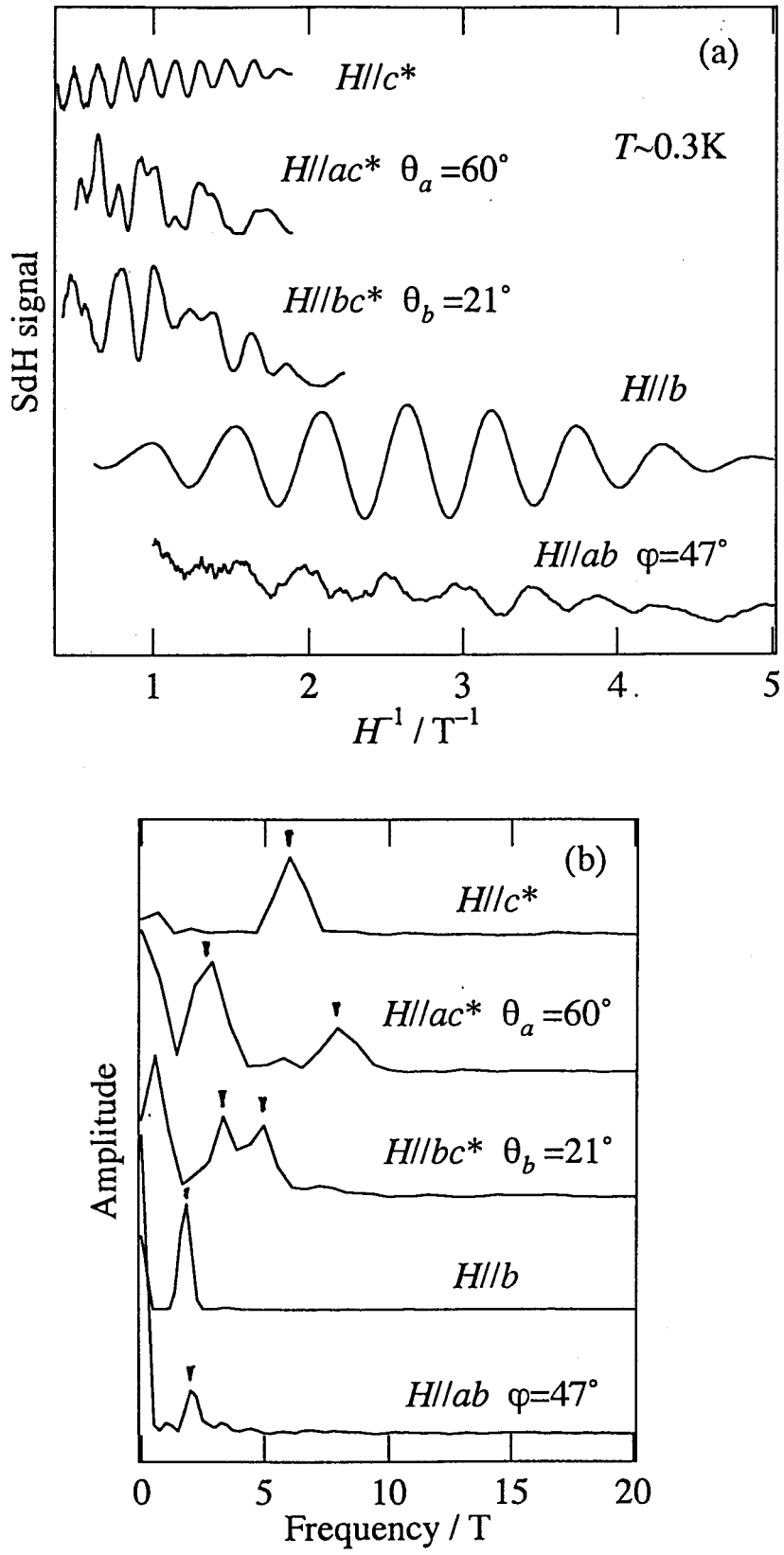

Fig. 4.7.3. (a) SdH oscillations in a low field range. (b) Corresponding Fourier spectra.

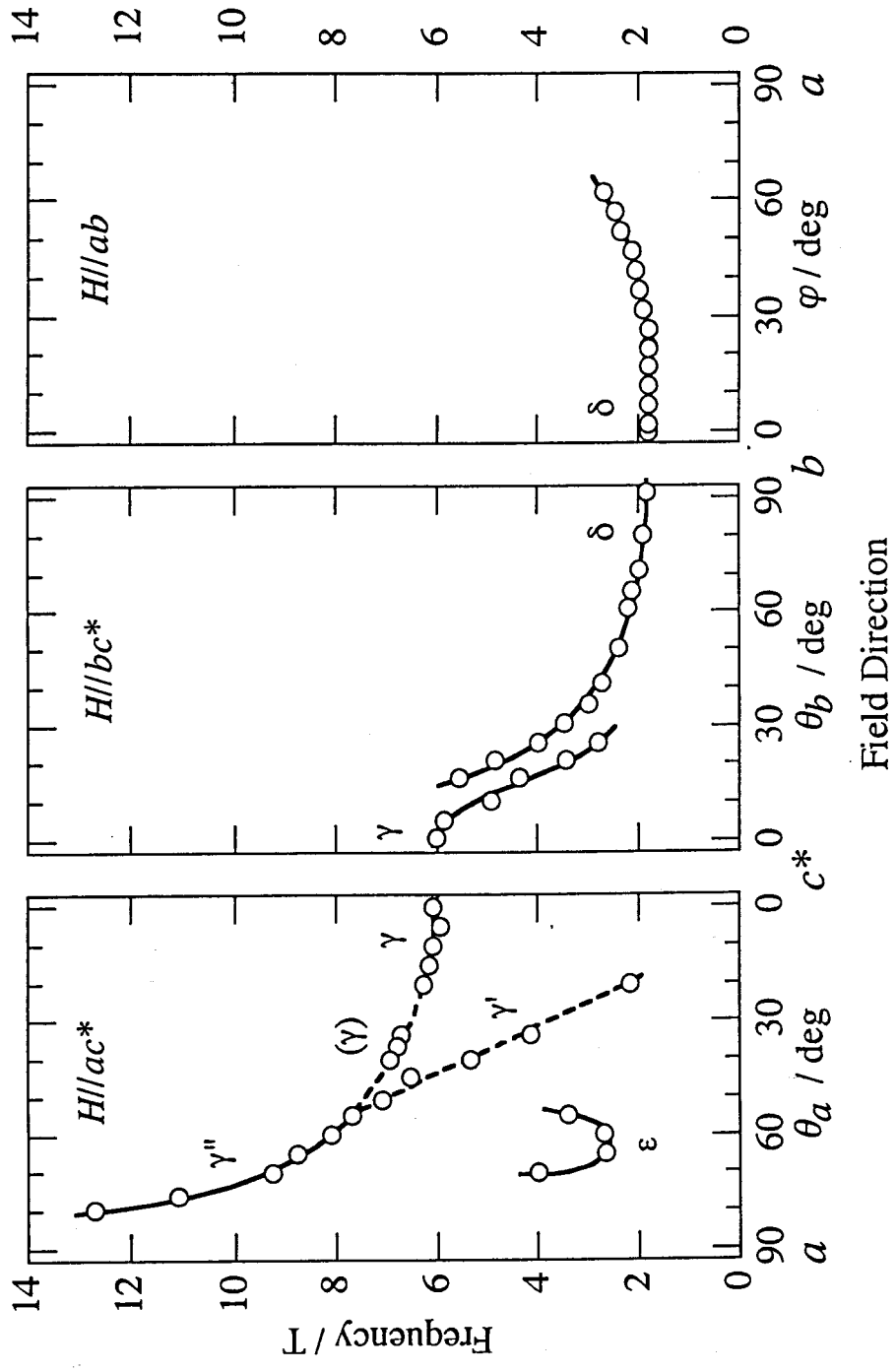

Fig. 4.7.4. Angle dependence of the new series of SdH frequencies.

The γ oscillation is observed for field directions around $\boldsymbol{H} \parallel \boldsymbol{c}^*$. For $\boldsymbol{H} \parallel \boldsymbol{c}^*$, the frequency is about 6 T and the corresponding cross-sectional area is only 0.15 % of the first Brillouin zone viewed along the *c**-axis. As the field is tilted towards the *b*-axis, the frequency of γ decreases and the γ oscillation disappears above $\theta_b \geq 31^\circ$. When the field is tilted from the *c**-axis towards the *a*-axis up to $\theta_a = 20^\circ$, the frequency slightly increases. The three data points for $\theta_a \geq 33^\circ$, which are denoted by the symbol, (γ), in Fig. 4.7.4, seem to be related to the γ branch, though SdH oscillation was not detected for $\theta_a = 26^\circ$ nor $\theta_a = 30^\circ$. On the other hand, another branch marked by γ′ appears for $\theta_a \geq 20^\circ$. Its frequency increases rapidly with θ_a, approaching that of γ. The peaks appearing in the Fourier spectra for $\theta_a = 45^\circ$ and 50° are relatively broad. Accordingly, the two branches, γ and γ′, may join and be connected with γ″.

The δ oscillation is remarkable; it is visible for the magnetic fields parallel to the two-dimensional conducting plane (the *ab* plane) in a wide angle range. A Clear SdH oscillation observed for observed for $\boldsymbol{H} \parallel \boldsymbol{b}$ is shown in Fig. 4.7.3. With the field rotating within the ab-plane, we could observe the δ oscillation up to $\phi = 60^\circ$. Its amplitude decreases as the field direction approaches the *a*-axis. The frequency of δ gradually increases as ϕ increases. When the field is rotated from the *b*-axis towards the *c**-axis, the frequency increases as well.

The cyclotron effective masses were determined from the amplitudes in the Fourier spectra between 0.05 and 1.2 K for γ ($\boldsymbol{H} \parallel \boldsymbol{c}^*$) and δ ($\boldsymbol{H} \parallel \boldsymbol{b}$). Figure 4.7.5(a) shows a mass-plot for the γ oscillation ($\boldsymbol{H} \parallel \boldsymbol{c}^*$). The cyclotron mass can be estimated to be $(0.05 \pm 0.02)\, m_e$ for γ, though the data points are scattered because of the small amplitudes. A very

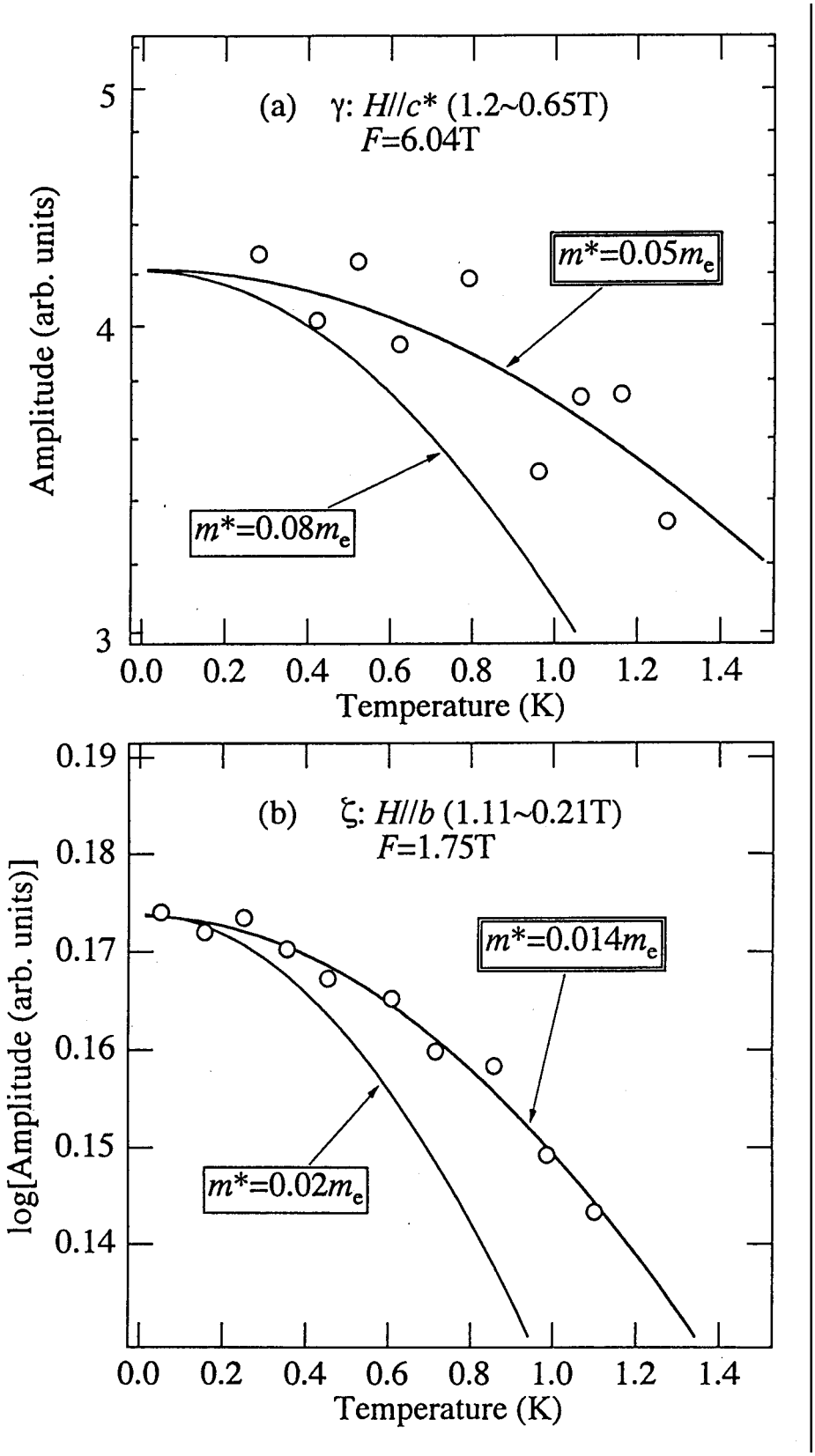

Fig. 4.7.5. The SdH amplitudes are plotted against temperature for (a) γ (***H*** //***c*** *) and (b) δ (***H*** // ***b***). The lines are those calculated with the Lifshitz-Kosevich formula using the cyclotron mass values designated in the figure.

small mass value of (0.014 ± 0.002) m_e is found for the δ oscillation, as shown in Fig. 4.7.5(b).

The band structures of BEDT-TTF-based conductors have been considered to be highly two-dimensional, as expected from their typical layered structures. The two-dimensional band structures are calculated on the basis of the tight-binding approximation in terms of the HOMOs of BEDT-TTF molecules. Usually, only the transfer integrals within one BEDT-TTF layer are taken into consideration. For several BEDT-TTF salts, the dHvA or SdH experiments have indeed revealed the 1/cos θ dependence of the frequencies, indicating the presence of almost cylindrical Fermi surfaces as evidence for the two-dimensionality [47]. The α and β branches are clearly explained within this framework. They come from the large cylindrical Fermi surface, as is demonstrated by the 1/cos θ dependence (Fig. 4.7.2(b)). They can be regarded as originating from the HOMOs of BEDT-TTFs.

On the other hand, the interlayer interactions have been believed to play only a minor role in determining the band structures; they have been treated as much smaller (10^{-3}) transfer interactions between the BEDT-TTF layers only leading to slight corrugation of the cylindrical Fermi surfaces. The angle-dependent magnetoresistance oscillation observed for several BEDT-TTF salts has been thought to arise from such slight warping of the Fermi surface [9-12].

The above framework does not necessarily exclude the possibility of a very small closed Fermi surface; it can be formed around the zone boundary, if a slightly corrugated Fermi surface touches the boundary. However, this cannot explain the new SdH oscillations, γ, δ and ε. First,

the frequency of γ decreases as the field is tilted from the *c**-axis towards the *b*-axis. This implies that there exists a considerable energy dispersion along the *c**-axis at least around the γ cyclotron orbit. That is, if we think of an ellipsoidal shape of Fermi surface for the γ oscillation, it must be elongated along the *b*-axis. Such a shape of the Fermi surface cannot be expected from the presumed small interlayer interactions. Second, the cyclotron mass of the δ orbit for $\boldsymbol{H} \parallel \boldsymbol{b}$ is very small (0.014 m_e). Within an effective mass band model (parabolic band), the observed mass is expressed as $(m_c^* m_a)^{1/2}$, where m_c^* and m_a are the *c**- and *a*-components of the effective mass tensor, respectively. Thus, not only m_c^* but also m_a should be small. It is difficult to explain this only by the small interlayer interactions.

Accordingly, the conclusions can be summarized as follows. Two different types of the Fermi surface coexist in θ-(BEDT-TTF)$_2$I$_3$. The first group consists of the large quasi-two-dimensional Fermi surfaces originating from the HOMOs of BEDT-TTFs, corresponding to the α and β oscillations. The second group, related to the γ, γ′, γ″, δ and ε oscillations, comprises the very small Fermi surfaces exhibiting a pronounced dispersion even for the direction perpendicular to the BEDT-TTF layer. They cannot be understood within the conventional tight-binding framework based only on the HOMOs of BEDT-TTFs. In order to interpret the present results, further improvement of the band structure calculations, which takes account of the other molecular orbitals of BEDT-TTFs or anions, seems necessary. Thus, this SdH study has established the HOMO-based band structure on one hand, and revealed the new features outside the simple picture on the other hand.

4.8. The Angle Dependent Magnetoresistance Oscillation (ADMRO)

As shown first by Yamaji [11], the period of the ADMRO peaks can be related to the Fermi wavenumber k_F, by

$$k_F = \pi / d \, \Delta \tan \theta \,, \tag{4.8.1}$$

where d is the periodicity in the direction perpendicular to the two-dimensional plane, and θ is the angle between the magnetic field direction and the normal direction. Therefore, the ADMRO is expected to provide detailed information on the geometry of the Fermi surface. Although θ-(BEDT-TTF)$_2$I$_3$ is one of the first material in which the ADMRO is observed [8], the interpretation of the oscillation period based on a realistic band structure has not been done yet. Nowadays, the Fermi surface of this salt has been well understood by the optical (Sec. 4.3) [5], dHvA (Sec. 4.4) [6,7] and SdH (Sec. 4.5) [14] studies. In order to establish the relation between the ADMRO and the Fermi surface geometry in this salt, the ADMRO is reexamined here. The notation of the crystal axes based on the monoclinic lattice is referred to again in this section.

Figure 4.8.1 shows the resistance measured along the c*-axis with the magnetic field rotated in the ac*-plane, where θ is the angle between the c*-axis and the field direction. Two oscillations with short and long period can be distinguished. The short-period oscillation with sharp peaks is prominent for small values of tan θ (| tan θ | < *ca*. 5). The values of tanθ at the peaks are plotted against the peak number in Fig. 4.8.2 (a),

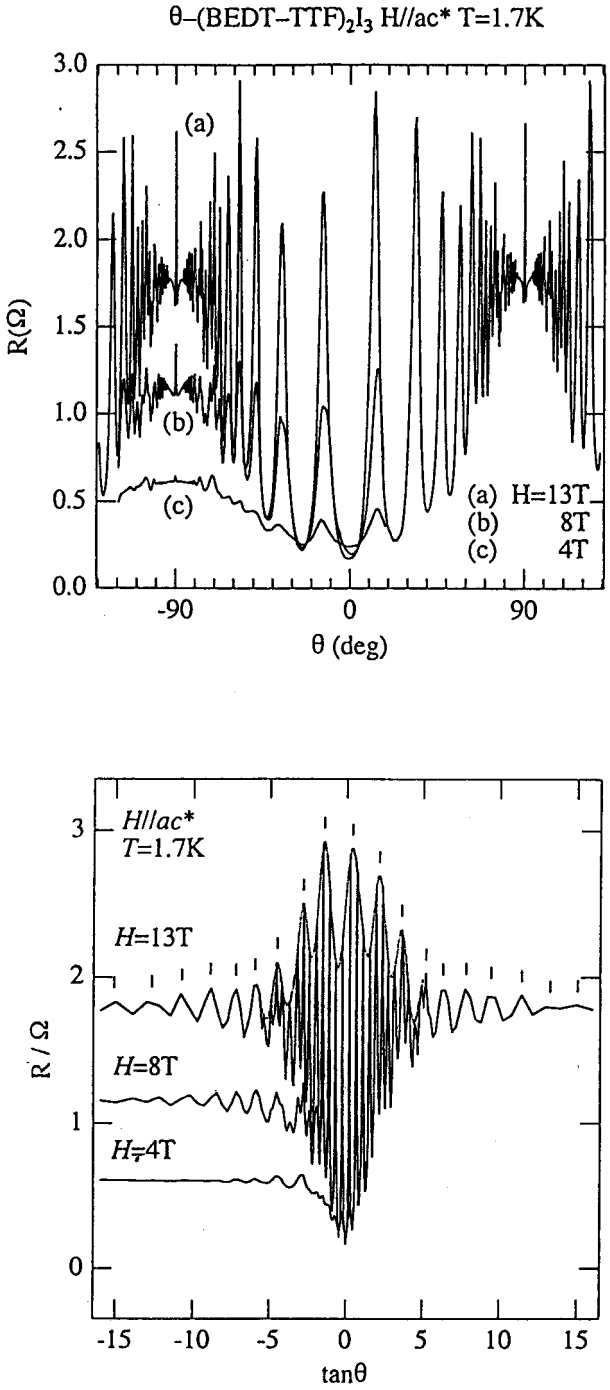

Fig. 4.8.1. The ADMRO for ***H*** // ***ac*** *. Top: Plot against the angle θ. Bottom: Plot against tan θ. The short-period oscillation at small values of $|\tan\theta|$ and the long-period oscillation at large values of $|\tan\theta|$ are evident. The broken line shows the envelope function which smoothly connects the peaks due to the short-period oscillation. The ticks indicate the peak positions due to the long-period oscillation.

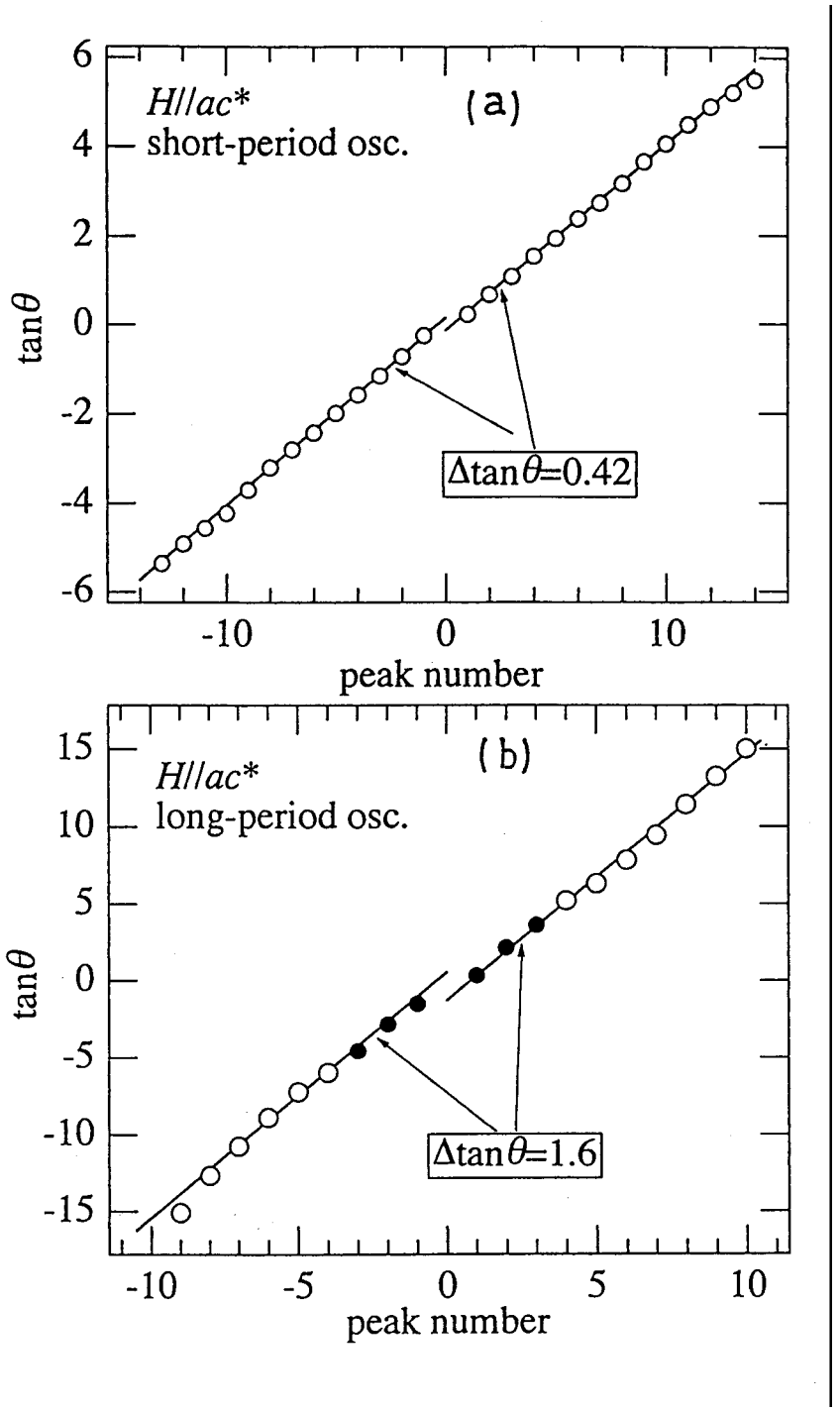

Fig. 4.8.2. The plot of tan θ versus peak number for $\boldsymbol{H}$ // $\boldsymbol{ac}$ *. (a) The short period oscillation. (b) The long-period oscillation.

where the peaks for tan $\theta > 0$ (tan $\theta < 0$) are numbered with positive (negative) integers from the one closest to tan $\theta = 0$. The period, Δ tan θ, is determined to be 0.42, which is in good agreement with the value reported by Kajita et al. [8]. On the other hand, a long-period oscillation, which was not reported so far, becomes evident for large values of tan θ. This finding may be ascribed to the quite high quality of the crystal (*RRR* = 1200, where *RRR* is the residual resistivity ratio, ρ(280 K) / ρ(4.2 K)) and to the fine angle-step (0.3 $^\circ$) around θ = 90 $^\circ$ used in recording the resistance. The long-period oscillation is visible as an oscillation of the envelop function for small values of tan θ; the height of the peaks due to the short-period oscillation periodically oscillates as is shown by the dotted curve in Fig. 4.8.1. The peak positions are independent of the magnetic field for the long-period oscillations, as is the case for the short-period one. The values of tan θ at the peaks, including those of the envelop function, are plotted against the peak number in Fig. 4.8.2 (b). The data points lie on the straight line, from which the period, Δ tan θ = 1.6, is obtained.

The resistance for the magnetic field rotating in the *bc**-plane is plotted against tan θ in Fig. 4.8.3. In this case, the oscillatory features are considerably weak, and therefore the second derivative, $d^2R / d\theta^2$, is also shown to identify the peaks. The values of tan θ at the peaks are plotted against the peak number in Fig. 4.8.4. The peak positions lie on the straight line with Δ tan θ = 0.68 and 0.97. The discrepancy between the periods for tan $\theta > 0$ and tan $\theta < 0$ does not seem intrinsic. The long-period oscillation seems to overcome the short-period one at large values of $|\tan\theta|$.

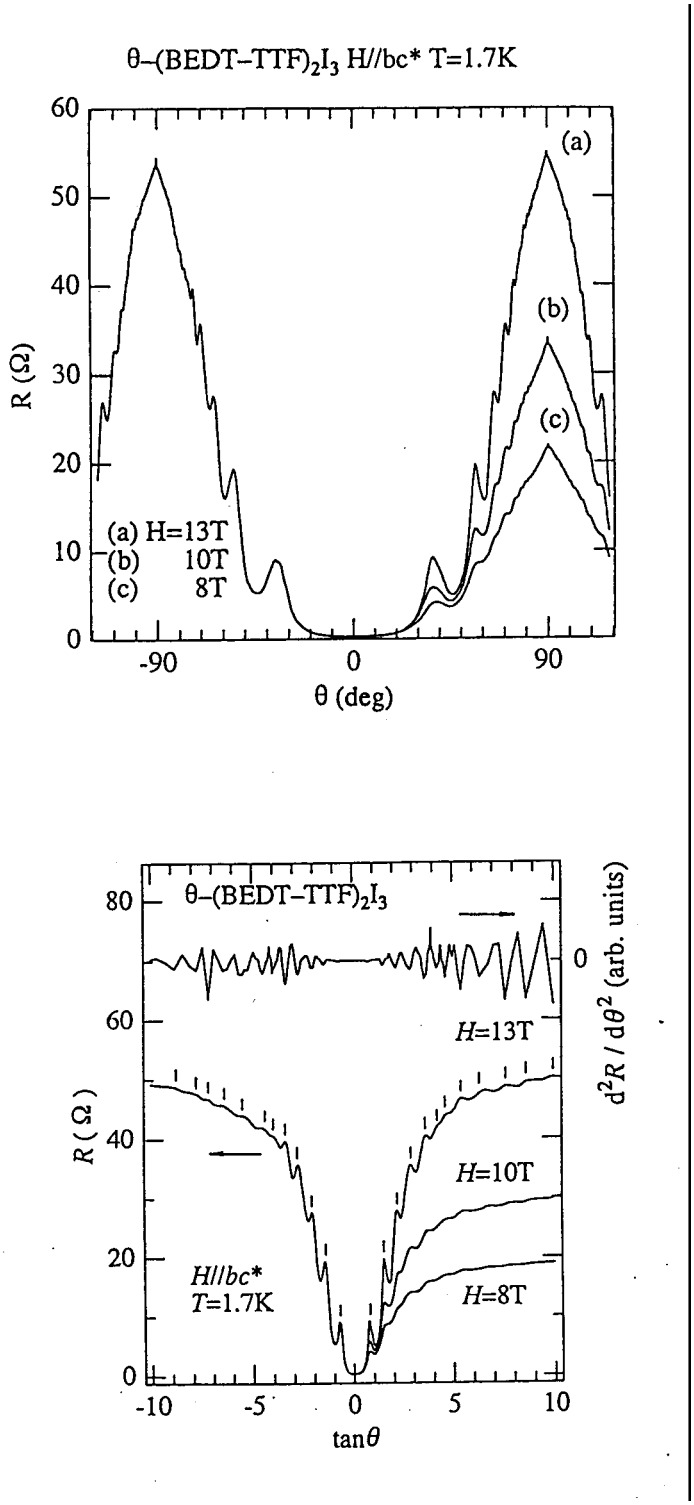

Fig. 4.8.3. The ADMRO for ***H*** // ***bc*** *. Top: Plot against the angle, θ. Bottom: Plot against tan θ, where the most upper curve shows the second derivative at H = 13 T. The ticks indicate the peak positions due to the long-period oscillation.

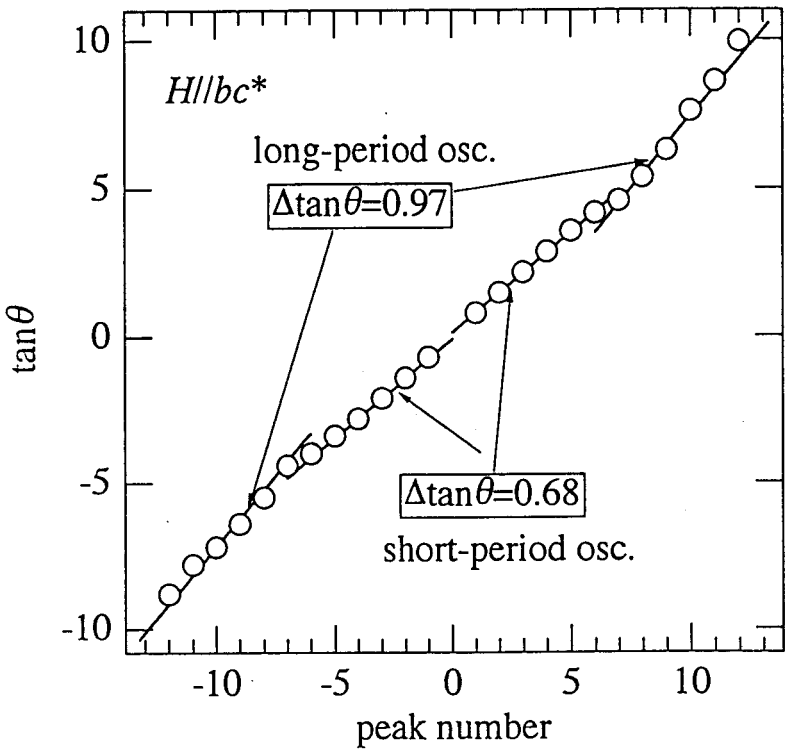

Fig. 4.8.4. The plot of tan θ versus peak number for $\boldsymbol{H}$ // $\boldsymbol{bc}$ *.

In order to examine the present results by using Eq. (4.8.1), we have to know the fundamental period of the energy band structure along the c^*-direction in the k-space, $2\pi / d$. By applying the Bloch theorem with respect to this direction, the wavefunction can be expanded in a Fourier series,

$$\Psi_k(\boldsymbol{r}) = \sum_G \phi_{k,\mathrm{G}}(x, y) \exp[-\mathrm{i}(k_\mathrm{c} + G) z], \tag{4.8.2}$$

where x, y and z are the components of $\boldsymbol{r}$ in the real space, and G is the c^*-component of the reciprocal lattice vector. The matrix element of the Hamiltonian of the tight-binding band model is written as,

$$\begin{aligned} <K_z \mid H \mid K'_z> &= \sum_{m,m'} <K_z \mid \chi_m><\chi_m \mid \mathrm{H} \mid \chi_{m'}><\chi_{m'} \mid K'_z> \\ &= \sum_{m,m'} <K_z \mid \chi_m><\chi_{m'} \mid K'_z> t_{m,m'} \ , \end{aligned} \tag{4.8.3}$$

in terms of the representation based on plane waves propagating along the z-direction, where $\mid \chi_m>$ is the molecular orbital, $t_{m,m'}$ is the transfer integral between the molecular orbitals $\mid \chi_m>$ and $\mid \chi_{m'}>$ and

$$\mid K_z> = (2L)^{-1/2} \exp(-\mathrm{i}K_z z) \ , \tag{4.8.4}$$

L being the length of the crystal along the z-direction.

Let us consider the symmetry operation of the crystal, α, defined by

$$\alpha: \boldsymbol{r} \rightarrow \rho_\alpha \boldsymbol{r} + \boldsymbol{\tau}_\alpha , \tag{4.8.5}$$

where ρ_α and $\boldsymbol{\tau}_\alpha$ are the rotation and translation part of the operation, α. Operating αon χ_m and $\chi_{m'}$, we have,

$$t_{\alpha m, \alpha m'} = t_{m, m'} , \tag{4.8.6}$$

because the Hamiltonian is not affected by the symmetry operation. Therefore, Eq. (4.8.3) can be written as,

$$< K_z \mid H \mid K'_z > = \sum_{(m\,,\,m')} t_{m, m'} \sum_n < K_z \mid \alpha^n \chi_m > < \alpha^n \chi_{m'} \mid K'_z > , \tag{4.8.7}$$

where $(m\,,\,m')$ runs over the pairs in which m cannot be related to m' by α^n, with n running up to a very large integer.

There is a glide mirror symmetry along the c-axis in the monoclinic structure of θ-$(BEDT\text{-}TTF)_2I_3$. Regarding this as the operation, α, i.e., $\boldsymbol{\tau}_\alpha = \boldsymbol{c} / 2$, we obtain,

$$\begin{aligned} < K_z \mid \chi\ [\alpha^n m\,] > &= \int \exp(\mathrm{i} K_z \cdot z)\, \chi_m (\rho\, \alpha^{-1} \boldsymbol{r} - n\, \boldsymbol{c} / 2)\, \mathrm{d}^3 \boldsymbol{r} \\ &= \int \exp[\mathrm{i} K_z \cdot (z + n\, c \sin \beta / 2)]\, \chi_m (\mathrm{r})\, \mathrm{d}^3 \boldsymbol{r} \\ &= \exp(\mathrm{i} n\, K_z \cdot c \sin \beta / 2) < K_z \mid \chi_m >, \end{aligned} \tag{4.8.8}$$

taking account of the fact that ρ_α (π-rotation around the z-axis) does not affect the z-component. Accordingly, the matrix element (4.8.7) is converted into,

$$<K_z \mid \mathrm{H} \mid K'_z> = \sum_n \exp[\mathrm{i}\, n\, (K_z - K'_z)\, c \sin\beta / 2] \times \sum_{(m\,,\,m')} t_{m,m'} <K_z \mid \chi_m><\chi_{m'} \mid K'_z>. \quad (4.8.9)$$

The factor,

$$\sum_n \exp[\mathrm{i}\, n\, (K_z - K'_z)\, c \sin\beta / 2] \ , \quad (4.8.10)$$

is the Laue function appearing in the X-ray diffraction theory. From the nature of the Laue function, it follows that $<K_z \mid \mathrm{H} \mid K'_z>$ becomes negligible unless there exists an integer, I, satisfying,

$$K'_z = K_z + 4\pi I \ / c \sin\beta \ . \quad (4.8.11)$$

Therefore, only the terms with

$$G = 4\pi I \ / c \sin\beta \, , \quad (4.8.12)$$

is required in the expansion (4.8.2). This indicates that the fundamental period along the c^*-direction in the $\boldsymbol{k}$-space is $4\pi / c \sin\beta$.

With this knowledge, the observed periods of ADMRO can be related

to the Fermi wavenumbers by Eq. (4.8.1); the interlayer distance, d , should be c sin β / 2 = 16.93 Å. From the periods, Δ tan θ, of the short-period oscillation, the Fermi wavenumbers are estimated to be 0.44 Å^{-1} and 0.27 Å^{-1} along the a- and b-axes, respectively. First of all, the short-period oscillation is ascribable to the large magnetic breakdown orbit, β, because the Fermi wavenumber along the a-axis points outside the first Brillouin zone (a^* / 2 = 0.32 Å^{-1}). The both Fermi wavenumbers, i.e., the long and short radii of the elliptic Fermi surface, are in excellent agreement with those predicted from the optical study.

Accordingly, it is natural to attribute the long-period oscillation to the closed orbit, α, around the zone boundary. Using the observed periods, Δ tan θ = 1.6 and 0.97, the Fermi wavenumbers are evaluated to be 0.12 Å^{-1} and 0.19 Å^{-1} along the a- and b-axes, respectively. Again, these values are in good agreement with the size of the orbit α deduced from the Fermi surface determined by the optical study.

Recently, another study of the angle dependent magnetoresistance oscillation has been carried out [48]. In this study, the short-period oscillation is examined for tilting of the field from the c^*-axis towards various directions in the ab-plane. From the obtained period as a function of the tilting direction, the shape of the magnetic breakdown orbit, β, has been inferred as shown in Fig. 4.8.6 [48]. This shape is in satisfactory agreement with the results above.

Thus, the angle dependent magnetoresistance oscillation in θ-(BEDT-TTF)$_2$I$_3$ has been clearly explained on the basis of the Fermi surface concluded from the optical study.

Table 4.8.I. The Fermi wavenumbers, k_F.

Orbit		ADMRO $\Delta \tan\theta$	ADMRO k_F /Å^{-1}	Optical Study [5] k_F /Å^{-1}
α	// *a*	1.6	0.12	0.10
	// *b*	0.97	0.19	0.20
β	// *a*	0.42	0.44	0.42
	// *b*	0.68	0.27	0.30

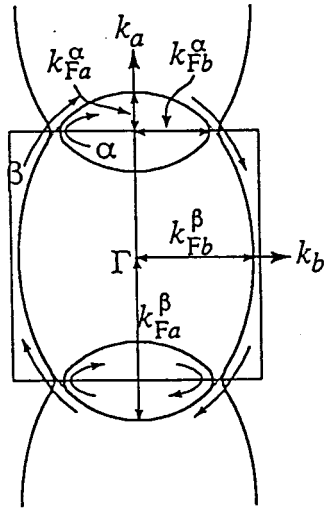

Fig. 4.8.5. The Fermi surface of θ-(BEDT-TTF)$_2$I$_3$.

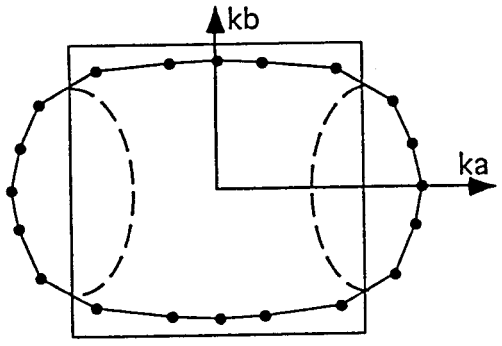

Fig. 4.8.6. The geometry of the Fermi surface derived from the ADMRO with various tilting way of field [48].

4.9. Concluding Remarks

The geometry of the 2D Fermi surface of θ-(BEDT-TTF)$_2$I$_3$ has been almost entirely established. As regards the Fermi surface geometry, the simple tight-binding band model inferred from the optical data is found to be satisfactorily accurate. The discrepancy between the calculated and experimental band structures has been attributed to the neglect of the sulfur 3d contribution in the calculations of the HOMO of BEDT-TTF. This conclusion has been provided by the dHvA, SdH and ADMRO experiments, which also clarify that this salt affords an almost ideal 2D electron system showing magnetic breakdown effect.

However, the cyclotron mass values predicted from the optical data do not well agree with those obtained from the dHvA and SdH results. This may be an indication of enhancement of the density of states just near the Fermi level due to the many-body effect [49-51]. In this connection, attention should be directed to the discrepancy between the observed dc conductivity and that estimated from the optical data at high temperatures. On the other hand, the TEP results indicate that the simplified band model fails to give the local curvatures near the Fermi surface. From the viewpoint of the optical properties, this corresponds to the appearance of weak interband transitions, which are not allowed in the simplified band model. In order to explain these features, it is desired to improve theoretical tools.

The finding of the extraordinarily small three-dimensional Fermi surface by the SdH experiments is striking: it seems impossible to explain this within the HOMO based tight-binding model. Contribution of another

degree of freedom is suggested.

References

1. H. Kobayashi, R. Kato, A. Kobayashi, Y. Nishio, K. Kajita and W. Sasaki: Chem. Lett. 789 (1986).
2. H. Kobayashi, R. Kato, A. Kobayashi, Y. Nishio, K. Kajita and W. Sasaki: Chem. Lett. 833 (1986).
3. A. Kobayashi, R. Kato, H. Kobayashi, S. Moriyama, Y. Nishio, K. Kajita and W. Sasaki: Chem. Lett. 2017 (1986).
4. H. Kobayashi, R. Kato, A. Kobayashi, T. Mori, H. Inokuchi, Y. Nishio, K. Kajita and W. Sasaki: Synth. Metals **27** (1988) A289.
5. M. Tamura, K. Yakushi, H. Kuroda, A. Kobayashi, R. Kato and H. Kobayashi: J. Phys. Soc. Jpn. **57** (1988) 3239.
6. M. Tokumoto, A. G. Swanson, J. S. Brooks, M. Tamura, H. Tajima and H. Kuroda: Solid State Commun. **75** (1990) 439.
7. M. Tamura, H. Kuroda, S. Uji, H. Aoki, M. Tokumoto, A. G. Swanson, J. S. Brooks, C. C. Agosta and S. T. Hannahs: J. Phys. Soc. Jpn. **63** (1994) 615.
8. K. Kajita, Y. Nishio, T. Takahashi, W. Sasaki, R. Kato, H. Kobayashi, A. Kobayashi and Y. Iye: Solid State Commun. **70** (1989) 1189.
9. M. V. Kartsovnik, P. A. Kononovich, V. N. Laukhin and I F. Shchegolev: JETP Lett. **48** (1988) 541.
10. M. V. Kartsovnik, V. N. Laukhin, S. I. Pesotskii, I. F. Shchegolev and V. M. Yakovenko: J. Phys. I. Paris **2** (1991) 89.
11. K. Yamaji: J. Phys. Soc. Jpn. **58** (1989) 1520.

12. R. Yagi, Y. Iye, T. Osada and S. Kagoshima: J. Phys. Soc. Jpn. **59** (1990) 3069.

13. T. Terashima, S. Uji, H. Aoki, M. Tamura, M. Kinoshita and M. Tokumoto: Synth. Metals, in press.

14. T. Terashima, S. Uji, H. Aoki, M. Tamura, M. Kinoshita and M. Tokumoto: Solid State Commun. **91** (1994) 595.

15. R. Kato, H. Kobayashi, A. Kobayashi, Y. Nishio, K. Kajita and W. Sasaki: Chem. Lett. 957 (1986).

16. A. G. Swanson: Ph. D. Thesis, Boston University, 1991.

17. J. S. Brooks, M. J. Naughton, Y. P. Ma, P. M. Chaikin and R. V. Chamberlin: Rev. Sci. Instrum. **58** (1987) 117.

18. H. Kuroda, K. Yakushi, H. Tajima and G. Saito: Mol. Cryst. liq. Cryst. **125** (1985) 135.

19. H. Tajima, K. Yakushi, H. Kuroda and G. Saito: Solid State Commun. **56** (1985) 159.

20. H. Tajima, K. Yakushi, H. Kuroda, and G. Saito: Solid State Commun. **56** (1985) 251.

21. H. Tajima, H. Kanbara, K. Yakushi, H. Kuroda and G. Saito: Solid State Commun. **57** (1986) 911.

22. K. Yakushi, H. Kanbara, H. Tajima, H. Kuroda, G. Saito and T. Mori: Bull. Chem. Soc. Jpn. **60** (1987) 4251.

23. K. Yakushi, H. Tajima, T. Ida, M. Tamura, H. Hayashi, H. Kuroda, A. Kobayashi, H. Kobayashi and R. Kato: Synth. Metals **24** (1988) 301.

24. M. Meneghetti, R. Bozio and C. Pecile: J. Phys. Paris **47** (1986) 1377.

25. R. Kato, H. Kobayashi, A. Kobayashi, Y. Nishio, K. Kajita and W. Sasaki: Chem. Lett. 957 (1986).

26. K. Kajita, Y. Nishio, S. Moriyama, R. Kato, A. Kobayashi, H. Kobayashi and W. Sasaki: Jpn. J. Appl. Phys. **26** Suppl. **26-3** (1987) 1363; Solid State Commun. **64**

(1987) 1279.

27. J. A. Osborn: Phys. Rev. **67** (1945) 351.

28. D. Mailly, M. Ribault and K. Bechgaard: J. Physique C**3** (1983) 1037.

29. H. Scwenk, K. Andres and F. Wudl: Soilid State Commun. **49** (1984) 723.

30. H. Schwenk, C. P. Heidmann, F. Gross, E. Hess, K. Andres, D. Schweizer and H. J. Keller: Phys. Rev. B **31** (1985) 3138.

31. H. Scwenk, S. S. P. Parkin, V. Y. Lee and R. L. Greene: Phys. Rev. B **34** (1986) 3156.

32. M. Tokumoto, H. Anzai, K. Takahashi, K. Murata, N. Kinoshita and T. Ishiguro: Synth. Metals **27** (1988) A305.

33. T. Mori and H. Inokuchi: J. Phys. Soc. Jpn. **57** (1988) 3674.

34. T. Mori, H. Inokuchi, H. Mori, S. Tanaka, M. Oshima and G. Saito: J. Phys. Soc. Jpn. **59** (1990) 2624.

35. J. M. Ziman: *Principle of the Theory of Solids* (Cambridge Univ. Press, Cambridge, 1972) 2nd. ed., Secs. 7.7 and 7.9.

36. M. Tokumoto, N. Kinoshita, H. Anzai, A. G. Swanson, J. S. Brooks, S. T. Hannahs, C. C. Agosta, M. Tamura, H. Tajima, H. Kuroda, A. Ugawa and K. Yakushi: Synth. Metals **42** (1991) 2459.

37. M. Tokumoto, A. G. Swanson, J. S. Brooks, C. C. Agosta, S. T. Hannahs, N. Kinoshita, H. Anzai, M. Tamura, H. Tajima, H. Kuroda and J. R. Anderson: in *Organic Superconductivity*, ed. V. Z. Kresin and W. A. Little (Plenum Press, New York, 1990) p.167.

38. M. Tokumoto, A. G. Swanson, J. S. Brooks, C. C. Agosta, S. T. Hannahs, N. Kinoshita, H. Anzai, M. Tamura, H. Tajima, H. Kuroda, A. Ugawa and K. Yakushi: Physica B **184** (1993) 508.

39. I. M. Lifshitz and A. M. Kosevich: Sov. Phys. JETP **2** (1956) 40. D. Shoenberg: *Magnetic Oscillations in Metals* (Cambridge Univ. Press, Cambridge, 1984) Chap.

7.

41. L. M. Falicov and P. R. Sievert: Phys. Rev. Lett. **12** (1964) 558.

42. L. M. Falicov, A. B. Pippard and P. R. Sievert: Phys. Rev. **151** (1966) 498.

43. S. Uji, H. Aoki, J. S. Brooks, A. S. Perel, G. J. Athas, S. J. Klepper, C. C. Agosta, D. A. Howe, M. Tokumoto, N. Kinoshita, Y. Tanaka and H. Anzai: Solid State Commun. **88** (1993) 683.

44. T. Sasaki, H. Sato and N. Toyota: Solid State Commun. 76 (1990) 507.

45. E. I. Blount: Phys. Rev. **126** (1962) 1636.

46. A. Kobayashi and H. Kobayashi: private communications.

47. To our knowledge, only one exception is the case of β-(BEDT-TTF)$_2$IBr$_2$ given in Ref. 10, where decrease in the small SdH frequency with the tilting of field from the normal direction has been reported.

48. S. J. Klepper, G. J. Athas, J. S. Brooks, M. Tokumoto, M. Tamura and M. Kinoshita: Synth. metals, in press.

49. J. Caulfield, W. Lubczynski, F. L. Pratt, J. Singleton, D. Y. K. Ko, W. Hayes, M. Kurmoo and P. Day: J. Phys. Condens. Metter **6** (1994) 2911.

50. S. Hill, J. Singleton, F. L. Pratt, M. Doporto, W. Hayes, T. J. B. M. Janssen, J. A. A. J. Perenboom, M. Kurmoo and P. Day: Synth. Metals **56** (1993) 2566.

51. S. Hill, A. Wittlin, J. van Bentum, J. Singleton, W. Hayes, J. A. A. J. Perenboom, M. Kurmoo and P. Day: Synth. Metals, in press.

Chapter 5.

Reflectance Spectra of κ-(BEDT-TTF)$_2$I$_3$

5.1. Introduction

The κ-form of di[bis(ethylenedithio)tetrathiafulvalene] triiodide, κ-(BEDT-TTF)$_2$I$_3$, exhibits superconducting transition at 3.6 K under ambient pressure [1]. So far, other κ-type BEDT-TTF salts, such as [Cu(NCS)$_2$] salt [2], [CuN(CN)$_2$Br] salt [3], were found to be ambient pressure superconductors. The transition temperatures (T_c) of the [Cu(NCS)$_2$] and [CuN(CN)$_2$Br] salts exceed 10 K, which being the highest ones among the organic superconductors. In this connection, the κ-type molecular arrangement is believed to have a key to the higher T_c; extensive studies have been made on these κ-type salts. The κ-type structure is characterized by a two-dimensional arrangement of the dimeric units of donor molecules [4], as shown in Fig. 5.1.

The reflectance spectra of metallic BEDT-TTF salts have been investigated, in order to elucidate their electronic structures [5-15]. The dispersion of the reflectance spectra of the BEDT-TTF salts often deviates from the Drude-type one in the infrared region. With the aid of the calculations of the optical transition probabilities based on the one-electron theory [7], the origin of the non-Drude dispersion has been pointed out to be the interband transitions between the split band arising from non-uniform arrangements of BEDT-TTF molecules. In this connection, κ-(BEDT-TTF)$_2$I$_3$ looks to be a suitable example to examine whether the optical properties of metallic BEDT-TTF salts are understandable within the framework of the conventional band model, since the κ-salt has a typical dimeric structure.

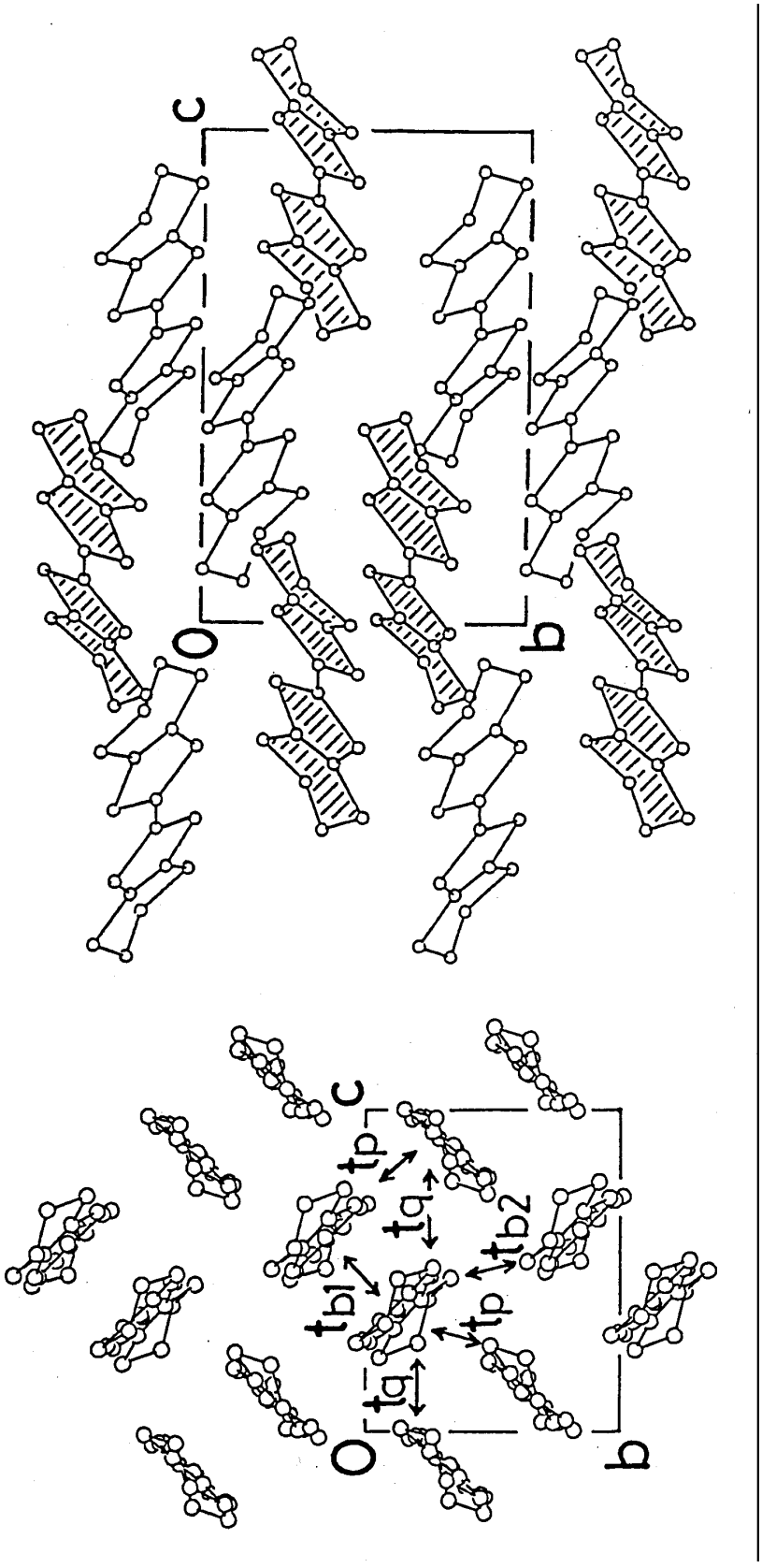

Fig. 5.1. Left: Arrangement of BEDT-TTF molecules in κ-(BEDT-TTF)$_2$I$_3$ viewed along the long-axis of BEDT-TTF, and the definition of the transfer integrals. Right: Orientaion of BEDT-TTFs within the *bc*-plane.

In this study, reflectance spectra of κ-(BEDT-TTF)$_2$I$_3$, in the infrared and visible region (500-25000 cm^{-1}) at 295 K and 15 K, are presented. In 5.3.1, a distinct correlation between the appearance of the non-Drude anomaly and the dimeric arrangement of BEDT-TTF molecules is described in detail. The curve-fitting analysis of the observed spectra is explained in 5.3.2. Strong two-dimensionality of the optical effective mass is elucidated. In 5.3.4, the inter-dimer transfer integrals describing the HOMO bands of κ-(BEDT-TTF)$_2$I$_3$ are evaluated by use of the band scheme based on the dimer model. The four inter-molecular transfer integrals are also estimated, and the optical conductivity spectra are calculated using these integrals.

5.2. Experimental

The single crystals of κ-(BEDT-TTF)$_2$I$_3$ were provided by Prof. H. Kobayashi (Toho Univ.), Prof. A. Kobayashi and Prof. R. Kato (Univ. of Tokyo). The single crystals were obtained by electrochemical oxidation of BEDT-TTF in a tetrahydrofuran solution containing mixed electrolyte, (*n*-C$_4$H$_9$)$_4$NX (X=I$_3$ and AuI$_2$, or IBr$_2$ and AuI$_2$) [16]. The content of Au and Br of the samples used were less than the detectable limit of electron-probe micro-analyzer (EPMA) [17]. The crystal axes of the samples were identified by X-ray diffraction. Reflectance Spectra were measured on the (100) crystal face, which is the most developed one, following the method described in Sec. 3.1. Details of the apparatus used in this work were described elsewhere [5]. A composite bolometer (Infrared Lab-

oratories Inc.) was used in the measurement below 2000 cm^{-1}. The principal axes of reflectance in the *bc*-plane were confirmed to be the *b*- and *c*-axes by measuring the change in reflectance at 2500 cm^{-1} on rotating the light polarizer.

Since there were many scratches on the crystal surface, we had to select out a small area free from scratches by use of a microspectrophotometer with a highly magnifying objective lens in the visible and near-infrared region. However, we can not use such a procedure in the infrared region. Thus it was not possible to determine directly an absolute reflectivity in this region. Consequently, a calibration was carried out by comparing the reflected lights from the sample surface with that from the gold-coated sample surface.

5.3. Results

5.3.1 Reflectance Spectra

Figure 5.2 shows the reflectance spectra of κ-$(BEDT\text{-}TTF)_2I_3$ at 295 K and 15 K. The intra-molecular transition of I_3^- anion appeared around 23000 cm^{-1} for the polarization direction parallel to the *c*-axis, along which the linear I_3^- anions are oriented. The peak position shifts to higher wavenumber on lowering the temperature. This transition was observed also for other $(BEDT\text{-}TTF)_2I_3$ salts [7-10,12,13]. A hump was found near 10000 cm^{-1} in the $\parallel \boldsymbol{c}$ spectrum, but no such dispersion appears in the $\parallel \boldsymbol{b}$ spectrum. Since the long axes of BEDT-TTF molecules are almost perpendicular to *b*-axis in κ-$(BEDT\text{-}TTF)_2I_3$, this dispersion is

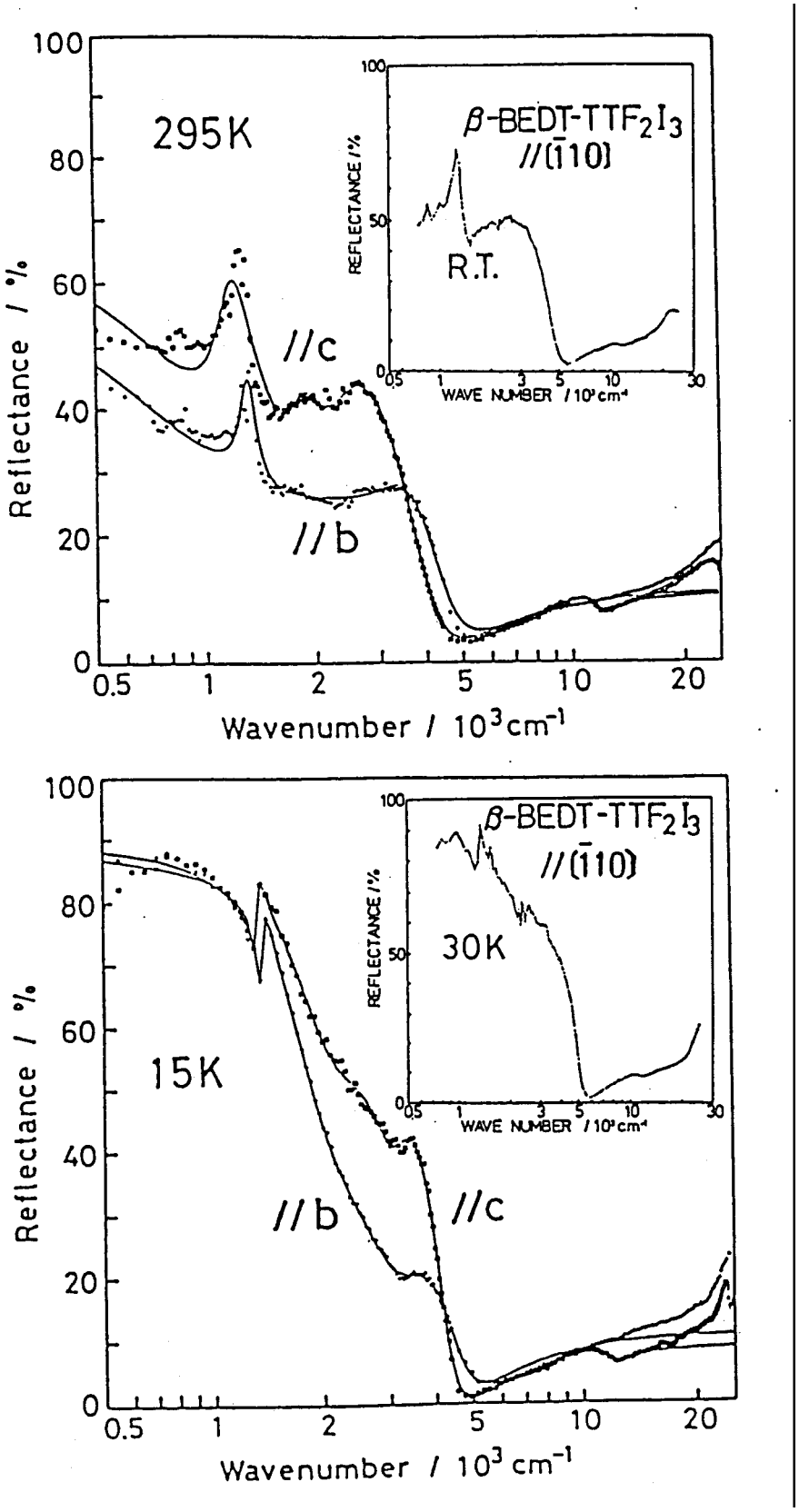

Fig. 5.2. Reflectance spectra of κ-(BEDT-TTF)$_2$I$_3$. The solid lines are the fit to the Drude-Lorentz model. The inset shows the reflectance spectra of β-(BEDT-TTF)$_2$I$_3$.

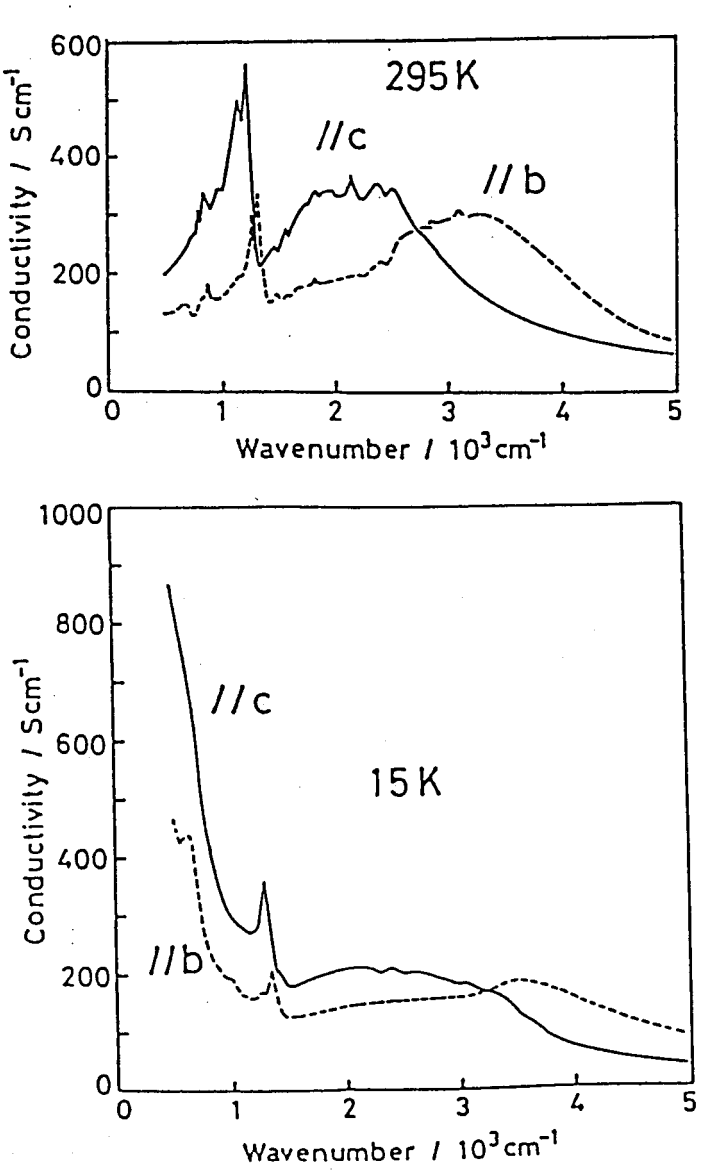

Fig. 5.3. Conductivity spectra of κ-(BEDT-TTF)$_2$I$_3$.

assigned to the intra-molecular transition of BEDT-TTF^{+} radical. This assignment is supported by our studies on θ-(BEDT-TTF)$_2$I$_3$ [13] and BPDT-TTF salts [17] (BPDT-TTF denotes bis(propylenedithio)tetrathia-fulvalene). The curve-fitting procedure described below gives the peak position for this transition as 11200 cm^{-1} at 295 K and 11300 cm^{-1} at 15 K.

Let us concentrate our attention on the electronic transition observed in the infrared region. As Fig. 5.2 shows, the dispersion curves for the two different polarization directions are similar to each other, suggesting the strongly two-dimensional character of this salt. Although both ∥ ***b*** and ∥ ***c*** spectra indicate the plasma-edge-like minima around 5000 cm^{-1}, the line shapes do not follow the Drude behavior below 4000 cm^{-1}. The reflectance curves exhibit broad shoulders around 3000 cm^{-1} and prominent vibronic structures at about 1100 cm^{-1}. The latter can be assigned to the molecular vibration coupled with the intermolecular transition. Another vibronic transition was found around 800 cm^{-1}. A similar spectral feature has been reported for the ∥ [$\bar{1}$10] spectrum of β-(BEDT-TTF)$_2$I$_3$ at room temperature [7], which is depicted in the inset of Fig. 5.2.

In many BEDT-TTF salts, BEDT-TTF molecules form two-dimensional networks as regards the electron transfer interactions. Generally this network is not uniform but sometimes has a dimeric unit. For example, in the donor sheets of β-(BEDT-TTF)$_2$I$_3$, BEDT-TTF molecules form dimers along the [$\bar{1}$10] axis [19]. The network structure of κ-salt is the most typical case of dimerization. A strong intra-dimer interaction splits the conduction band formed from HOMO's of BEDT-TTF into two branches, between which the dimerization gap open [20]. The lower

branch has a bonding character of the dimer, while the upper branch has an anti-bonding character. Thus, the optical transition between these branches is infrared active and polarized along the dimerization direction, i.e., the direction connecting the centers of molecules in the dimer.

As a consequence of this interband transition, the infrared dispersion is expected to be a superposition of the two contributions, i.e., the Drude-like dispersion due to the intraband transitions and the contribution of the interband transitions. If this is the case, the temperature dependence of the spectra should give insight into the presence of these two contributions. At room temperature, the Drude-like dispersion is broad and obscured by the electron scattering near the Fermi energy. On lowering the temperature, the scattering rate becomes saliently suppressed, and decreases more and more. This yields large negative values of the real part of dielectric function at lower wavenumbers and a distinct plasma-edge in the reflectance curve. On the other hand, the line shape of the interband transitions is basically ruled by the band dispersion, thus being rather insensitive to the temperature than that of the intraband transitions. Consequently, the spectra are expected to approach a Drude-like dispersion on lowering the temperature. Such a temperature dependence is in fact observed for κ-(BEDT-TTF)$_2$I$_3$, as shown in Fig. 5.2. A similar result was also reported for β-(BEDT-TTF)$_2$I$_3$ (Fig. 5.2 inset) [8]. The conductivity spectra obtained by means of the Kramers-Kronig analysis of the reflectance data at 295 K and 15 K are shown in Fig. 5.3. For both the $\| \boldsymbol{b}$ and $\| \boldsymbol{c}$ polarizations, the contribution of the intraband transitions centered at zero wavenumber becomes fairly sharp at 15 K. On the other hand, the absorption band around 2500 cm^{-1} corresponding to the interband transitions shows an

intensity decrease and a slight red-shift at 15 K. These facts support the view that the intra- and interband transitions coexist in the infrared region.

Now, let us compare the reflectance spectra of different forms of $(BEDT\text{-}TTF)_2I_3$ to see the relationship between the structure and optical property. In β-$(BEDT\text{-}TTF)_2I_3$, BEDT-TTF molecules form a dimerized stack and all the dimers are oriented in parallel [19,20]. The prominent conductivity peak appears only in the ∥ [$\bar{1}$10] spectra. It has been proposed that the inter-band transition across the dimerization gap is responsible for this prominent peak by comparing with the calculation of conductivity spectra [7]. On the other hand, there are two different dimerization axes in the κ-salt, which are almost perpendicular to each other. As was pointed out before, the infrared peak appears along two polarization directions in the *bc*-plane. In the average structure of θ-$(BEDT\text{-}TTF)_2I_3$, all the BEDT-TTF molecules are crystallographically equivalent, forming a uniform two-dimensional network [21,22]. The molecular arrangement in the κ-salt [4] is connected with the average structure of θ-salt [22], by replacing each BEDT-TTF with a BEDT-TTF dimer. The infrared property of the θ-salt is Drude-like as expected for a two-dimensional metal [9,13]. The calculation of conductivity spectra also showed that there would be no contribution from the interband transitions. This is because the interband transition is forbidden by the high crystal symmetry. (See also Appendix A.)

As mentioned above, the prominent peak in the infrared region is ascribed to the inter-band transition across the dimerization gap. The low temperature spectra also supported this interpretation. This infrared peak always appears only along the dimerization direction: It appears in two

directions in the κ-salt, in one direction in the β-salt, and disappears in any directions in the θ-salt. One of the simplest way to explain this strong correlation between the structures and the spectra is to ascribe this infrared peak to the one associated with the interband transitions across the dimerization gap based on the tight-binding band scheme [7,12,15].

Let us make here a brief comment on the relation between the electron-molecular vibration (e-mv) coupling and the interband transition. The e-mv coupling have been investigated mainly for one-dimensional organic conductors [23,24]. Strong e-mv peaks appear in the spectra of the β-salt [7,8] and κ-salt, whereas only weak e-mv peaks were observed for the θ-salt [13]. This suggests a correlation between the e-mv coupling and the interband transition; the intensity and the dichroism of the e-mv mode seem to reflect those of the interband transition. These modes, usually observed around 1200 cm^{-1} for BEDT-TTF salts, correspond to the totally symmetric (breathing) intramolecular vibrational modes with the character of C=C stretching [25,26]. In a free molecule these modes are infrared-inactive. However, they appear in the infrared spectra by borrowing the intensity of the interband transitions. On the analogy of the theory for a dimer chain [23,24], the inter-band transition across the dimerization gap, referring to the electronic charge oscillation between the two molecules within the dimer, can couple to the asymmetric combination of the totally symmetric vibrations of the two molecules. Consequently, it appears as peaks observed at frequencies slightly lower than those of the original C=C stretching modes.

From an experimental viewpoint, it can be pointed out that the observation of the e-mv modes affords a probe to the properties of the interband

transitions; the high intensity of the e-mv peak should indicate the presence of strong interband transitions in the same light polarization. This consideration is consistent with the experimental results for several BEDT-TTF salts [5-15]. It works as a convenient index, because the e-mv coupling modes are easier to distinguish than the interband transition itself; The interband transitions have a broad-band dispersion, which is often indistinguishable from that of the intraband transitions. (See also Appendix B., about the discussion presented here.)

Let us apply the above consideration to the cases of the β-, θ-, and κ-(BEDT-TTF)$_2$I$_3$. The appearance of strong e-mv peaks in the β- [7,9] and the κ-salts reflects large intensities of the interband transitions in these salts. In spite of the Drude-like behavior, weak e-mv modes were observed in the θ-salt [13], suggesting the existence of weak interband transitions. In fact there are small shoulders in the conductivity spectra around 2500 cm^{-1} [13]. This can be interpreted as a result of the lowering of symmetry in the real structure of the θ-salt [27]. The present investigation is limited to qualitative one because of low resolution of our spectra. Detailed experimental features of the vibronic structures have been reported for some BEDT-TTF salts [25,26,28-31].

5.3.2 Curve-Fitting Procedure

The intraband transitions contain the information concerning the dispersion of the conduction band, while the interband transitions reflect the band splitting due to the dimeric intermolecular interaction. We estimated the band parameters by analyzing the intraband transitions separated from the interband transitions. The separation was carried out by a

curve-fitting by use of the Drude-Lorentz model,

$$\varepsilon(\omega) = \varepsilon_C - \omega_P^2 / (\omega^2 + i\omega / \tau) + \sum_j^{3 \text{ or } 4} f_j / [(\omega_j^2 - \omega^2) - i\gamma_j \omega] . \quad (5.1)$$

The reflectivity is related to the dielectric function by the equation,

$$R = [1 + |\varepsilon| - \sqrt{2(|\varepsilon| + \mathrm{Re}(\varepsilon))}] / [1 + |\varepsilon| + \sqrt{2(|\varepsilon| + \mathrm{Re}(\varepsilon))}] . \quad (5.2)$$

The first term in the right-hand side of Eq.(5.1) stands for the constant contribution from the higher energy transitions outside the experimental spectral region. The second term, the Drude term, gives the contribution of the intraband transitions. The third term describes the contribution of other transitions: the interband transitions, the e-mv coupling modes and the intramolecular electronic transitions. The line shape of the interband transitions is empirically expressed as a superposition of two Lorentzian oscillators, since the shape of the interband transitions shown in Figs. 5.2 and 5.3 could not be reproduced well by a single Lorentzian. Instead of including the contribution of the transitions beyond 20000 cm^{-1} explicitly, we limited the fitting region below 15000 cm^{-1}, so that they were implicitly included in the first term, ε_c. The curve-fitting results were shown as the solid curves in Fig. 5.2, and the obtained parameters were compiled in Table 5.I.

Table 5.I. Curve-fitting results.

Polarization	T / K	ε_c	ω_p / eV	τ / eV^{-1}	Ω_p / eV [a)]	m^*/m_e	σ_{dc}^{opt} / Scm^{-1} [b)]
// *b*	295	4.0	0.63	2.7	0.93	4.1	150
	15	4.0	0.74	22	0.98	3.0	1600
// *c*	295	3.9	0.76	3.2	0.95	2.9	250
	15	3.6	0.82	16	0.96	2.4	1500

a) $\Omega_p^2 = \omega_p^2 + \sum_j f_j$, where the summation is taken over the e-mv mode and the interband transitions.

b) The values obtained by extrapolating the Drude conductivity to zero wavenumber.

5.3.3 Optical Effective Mass

To obtain the information on the conduction band structure from the optical data, the effective mass model is widely used as a simple description of the band dispersion. In this model the structure of the two-dimensional conduction band is expressed as a parabola around the Γ point, that is,

$$\varepsilon = -\hbar^2 [k_b^2 / 2m^*_b + k_c^2 / 2m^*_c] \quad , \tag{5.3}$$

where m^*_b and m^*_c are the principal values of the two-dimensional effective mass tensor defined in the *bc* plane. The effective mass values are estimated from the intraband plasma frequencies, ω_P's, by using Eq.(5.4),

$$m^*_x = 4\pi n e^2 / m^*_x (\omega_P^2)_x \quad , \quad x = b \text{ and } c \tag{5.4}$$

where n and e denote the number density of the holes per unit volume and the electron charge, respectively. The effective mass values are calculated to be $m^*_b = 3.0\ m_e$ and $m^*_c = 2.4\ m_e$, when the plasma frequency values obtained from the 15 K spectra, $(\omega_P)_b = 0.74$ eV and $(\omega_P)_c = 0.82$ eV, together with $n = 1.185 \times 10^{21}$ cm^{-1}, are used. Small temperature dependence of the lattice constant and the hole density are neglected here. The obtained ratio, $m^*_b / m^*_c = 1.3$, is very small among the known organic conductors, a similar value being known for κ-(BEDT-TTF)$_2$[Cu(NCS)$_2$] [11]. For β- and θ-(BEDT-TTF)$_2$I$_3$, the corresponding effective mass ratios are estimated to be 3.5 and 2.0, respectively [8,13]. This elucidates the strong two-dimensionality of the electronic structure of κ-(BEDT-TTF)$_2$I$_3$. The obtained results are shown in Table 5.I.

5.3.4 Analysis by Tight-Binding Band Model

The effective mass model is simple and applicable to any metallic material. However, this model gives little information on the intermolecular interaction. Moreover, when the Fermi level is far from the edge of the conduction band, this model is no longer a good approximation. In this respect, it is worthwhile to examine the analysis based on the tight-binding approximation. This approximation is formulated in terms of transfer integrals between the frontier molecular orbitals of the nearest-neighbor molecules calculated by the extended Hückel method [32-34]. This approach has been successfully applied on several BEDT-TTF salts [6-8,13,32-38]. The recent self-consistent-field band calculations suggest that the molecular orbital identities of BEDT-TTF are maintained in the crystal electronic structure of β-(BEDT-TTF)$_2$X [39].

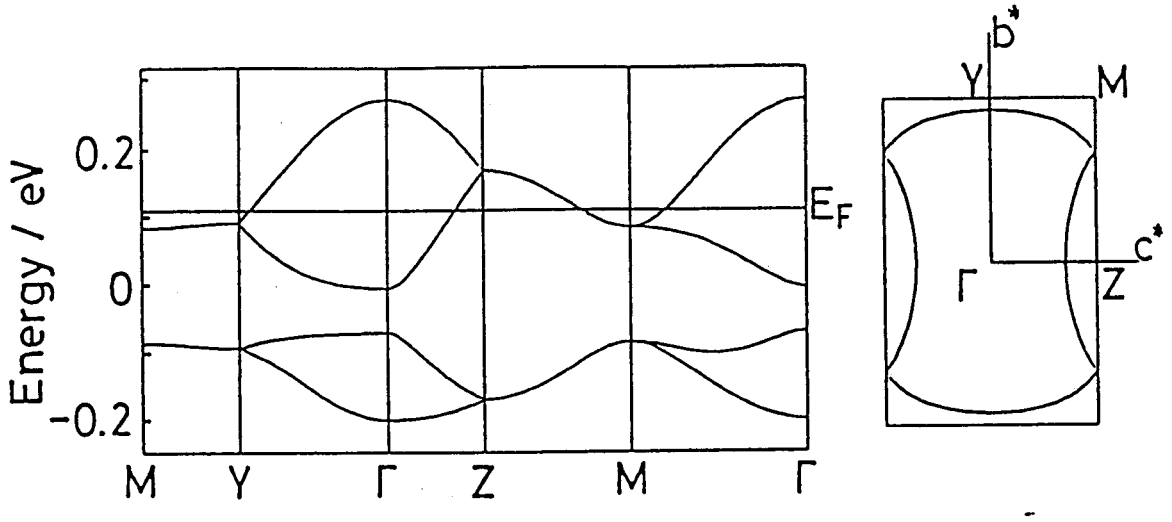

Fig. 5.4. Calculated tight-banding band structure and the Fermi surface of κ-(BEDT-TTF)$_2$I$_3$ [4]. It is assumed that t / eV = – 10 S.

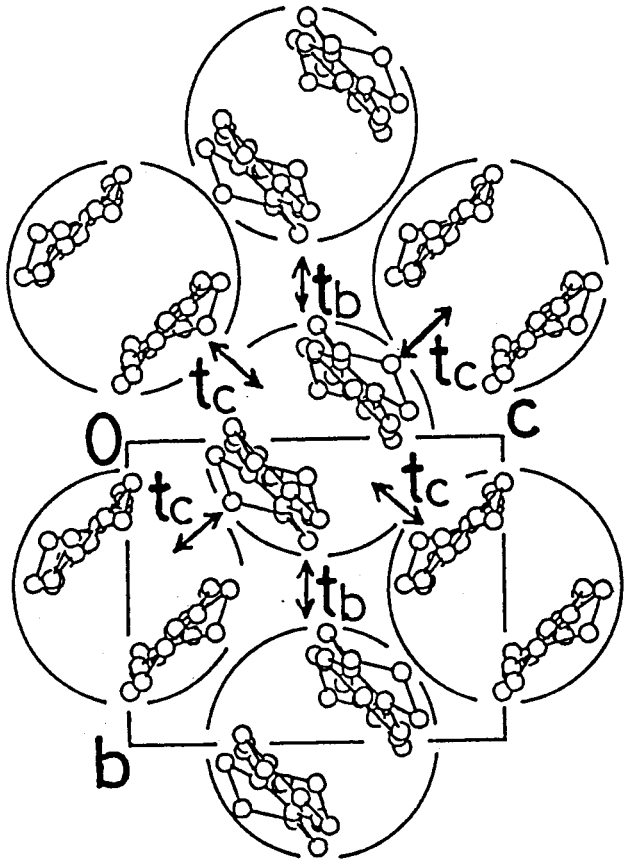

Fig. 5.5. Effective interdimer interactions in κ-(BEDT-TTF)$_2$I$_3$.

For the sake of estimating the tight-binding band parameters from the optical data, we have developed a dimer-based treatment using a perturbation theory. The overlap integrals between the HOMO's of the neighboring molecules are given as $S_{b1} = 10.92 \times 10^{-2}$, $S_{b2} = 2.46 \times 10^{-3}$, $S_p = 5.05 \times 10^{-3}$, and $S_q = -1.85 \times 10^{-3}$ for κ-(BEDT-TTF)$_2$I$_3$ [4]. The intradimer overlap, t_{b1}, is considerably larger than the others, indicating the dimeric structure of this salt. According to the calculation by the tight-binding approximation, the higher two branches and the lower two are separated by the dimerization gap, as shown in Fig. 5.4. If the dimerization is sufficiently strong, i.e., the intradimer transfer integral sufficiently excels the interdimer ones, we can start from the unperturbed dimer state with two energy levels, the bonding (lower) and the anti-bonding (higher) levels of the dimer. Due to the perturbation of interdimer interaction, the two levels form two bands, keeping the dimerization gap between them. Indeed, the energy band structure shown in Fig. 5.4 has this character.

The one-electron Hamiltonian, which is diagonalized to give tight-binding band energies, is divided into two terms as follows:

$$H(t_{b1}, t_{b2}, t_p, t_q; \boldsymbol{k}) = H_0(t_{b1}; \boldsymbol{k}) + H_1(t_{b2}, t_p, t_q; \boldsymbol{k}). \qquad (5.5)$$

Since there are four molecules in the unit cell, the Hamiltonian is 4 × 4 matrix. We first solve the diagonalization problem for the unperturbed Hamiltonian, H_0, and find the eigenvalues,

$$E_1^{\,0} = E_2^{\,0} = t_{b1} \text{ and } E_3^{\,0} = E_4^{\,0} = -t_{b1}. \qquad (5.6)$$

E_1^0 and E_2^0 correspond to the bonding levels and E_3^0 and E_4^0 to two anti-bonding levels of the dimer. These levels are independent of wavevector, $\boldsymbol{k}$, since H_0 contains no interdimer interaction. The degeneracy comes from the presence of the two crystallographically equivalent dimers in the unit cell. The next step is to calculate the matrix elements of H_1, $(H_1)_{i,j} = \langle \Psi_i^0 | H_1 | \Psi_j^0 \rangle$, where Ψ_i^0 stands for the Bloch sum of the HOMO's of the molecules, i. Following this, we obtain the first-order correction energy, δE, by solving the secular equation,

$$\det [(H_1)_{i,j} - \delta E \ \delta_{i,j}] = 0 \ , \tag{5.7}$$

for each pair of the doubly degenerating states, (1, 2) and (3, 4). The resultant energies to the first-order, $E^1 = E^0 + \delta E$, are written in the explicit forms,

$$\begin{aligned}
E_1^1(\boldsymbol{k}) &= E_1^0 + t_{b2}\cos(\boldsymbol{b}\cdot\boldsymbol{k}) - 2\,|\,t_p + t_q\,|\cos(\boldsymbol{b}\cdot\boldsymbol{k}/2)\cos(\boldsymbol{c}\cdot\boldsymbol{k}/2), \\
E_2^1(\boldsymbol{k}) &= E_2^0 + t_{b2}\cos(\boldsymbol{b}\cdot\boldsymbol{k}) + 2\,|\,t_p + t_q\,| \\
&\qquad\qquad \cos(\boldsymbol{b}\cdot\boldsymbol{k}/2)\cos(\boldsymbol{c}\cdot\boldsymbol{k}/2), \\
E_3^1(\boldsymbol{k}) &= E_3^0 - t_{b2}\cos(\boldsymbol{b}\cdot\boldsymbol{k}) - 2\,|\,t_p - t_q\,|\cos(\boldsymbol{b}\cdot\boldsymbol{k}/2)\cos(\boldsymbol{c}\cdot\boldsymbol{k}/2), \\
E_4^1(\boldsymbol{k}) &= E_4^0 - t_{b2}\cos(\boldsymbol{b}\cdot\boldsymbol{k}) + 2\,|\,t_p - t_q\,|\cos(\boldsymbol{b}\cdot\boldsymbol{k}/2)\cos(\boldsymbol{c}\cdot\boldsymbol{k}/2) \ .
\end{aligned} \tag{5.8}$$

The obtained energy dispersion is similar to that of θ-(BEDT-TTF)$_2$I$_3$ (the average structure), which is given by,

$$E(\boldsymbol{k}) = 2\, t_c \cos(\boldsymbol{c} \cdot \boldsymbol{k}) \pm 4\, |t_b| \cos(\boldsymbol{c} \cdot \boldsymbol{k}/\, 2) \cos(\boldsymbol{a} \cdot \boldsymbol{k} / 2)\ . \qquad (5.9)$$

Since the arrangement of BEDT-TTF dimers in the κ-structure has the same symmetry as that of the molecules in the θ-structure, the similarity between Eqs.(5.8) and (5.9) is natural. In this approximation, as a result of the interdimer interactions, t_{b2}, t_p and t_q, the doubly degenerate bonding levels of the two dimers in the unit cell form the pair of branches, $E_1^{\,1}(\boldsymbol{k})$ and $E_2^{\,1}(\boldsymbol{k})$, and the anti-bonding levels form the other pair, $E_3^{\,1}(\boldsymbol{k})$ and $E_4^{\,1}(\boldsymbol{k})$. In other words, we regard the dimers as supermolecules (Fig.5.5). This approximation is good, when the energy separation $E_3^{\,1}(\boldsymbol{k}) - E_2^{\,1}(\boldsymbol{k})$ sufficiently exceeds $E_3^{\,1}(\boldsymbol{k}) - E_4^{\,1}(\boldsymbol{k})$ and $E_1^{\,1}(\boldsymbol{k}) - E_2^{\,1}(\boldsymbol{k})$. As Fig.5.4 shows, this condition is actually satisfied around the Fermi surface.

Taking account of this perturbation theory, we can estimate the values of effective interdimer transfer integrals from the Drude plasma frequencies. The plasma frequencies, $(\omega_P)_b$ and $(\omega_P)_c$ are the function of the Fermi velocities. Since the Fermi level crosses the upper two branches, $E_3^{\,1}$ and $E_4^{\,1}$, we can explicitly relate the two plasma frequencies and the number of states beyond the Fermi level per unit area, N_h, to the three parameters, $t_b = -t_{b2} / 2$, $t_c = |\, t_p - t_q \,| / 2$ and the Fermi energy, E_F, by the following equations,

$$(\pi^2\hbar / e^2)\, (\omega_P^{\,2})_b = (2\pi / a \sin\beta) \int |\, (v_F)_b \,|\, \mathrm{d}k_c\ , \qquad (5.10)$$

$$(\pi^2\hbar / e^2)\, (\omega_P^{\,2})_c = (2\pi / a \sin\beta) \int |\, (v_F)_c \,|\, \mathrm{d}k_b\ , \qquad (5.11)$$

$$N_h = (2/4\pi^2) \int |\, k_{Fc}(k_b) \,|\ \mathrm{d}k_b\ , \qquad (5.12)$$

where $(v_F)_b$ and $(v_F)_c$ denote the *b*- and *c*-components of the Fermi velocity, respectively. The components of the Fermi wavenumber, k_{Fb} and k_{Fc}, satisfy $E(k_{Fb}, k_{Fc}) = E_F$. These three integrals are taken over the two-dimensional Fermi surface in the *bc*-plane. As have been done in the case of θ-(BEDT-TTF)$_2$I$_3$ [13], it is possible to solve these three equations simultaneously to determine t_b, t_c and E_F for given values of $(\omega_P)_b$, $(\omega_P)_c$ and N_h. By using $(\omega_P)_b = 0.74$ eV, $(\omega_P)_c = 0.82$ eV, a = 16.387 Å, sin(β)= 0.948, and $N_h = 1.841 \times 10^{14}\,\mathrm{cm}^{-2}$, we obtained the result: $t_b = 0.034$, $t_c =$ 0.054 and $E_F = -0.037$ eV. Thus, the effective band parameters have been determined for the upper half of the HOMO band of κ-(BEDT-TTF)$_2$I$_3$. In this "θ-model", the band structure of κ-salt is modeled on that of θ-salt.

Next the procedure to estimate the full parameter set (t_{b1}, t_{b2}, t_p, t_q) of the exact κ-band is described. The intradimer transfer integral, t_{b1}, is closely related to the excitation energy of the inter-band transition. Since the line shape of the conductivity spectra (Fig.5.3) is broad, it is difficult to specify the accurate excitation energy values of the inter-band transitions. Nevertheless, we assumed that,

$$t_{b1} \approx -0.15 \text{ eV} , \tag{5.13}$$

because this value gives preferable peak positions in the calculation of the inter-band transitions described below (Fig.9). There is no experimental information on the values of t_p and t_q, so that we assumed the ratio, t_p / t_q, based on the calculations of the overlap integrals as Eq.(5.14):

$$t_p / t_q = -5.05 / 1.85 \approx -2.7 \ . \qquad (5.14)$$

Then, to be searched is the set of parameters (t_{b1}, t_{b2}, t_p, t_q) which satisfies the following conditions: i) $t_{b1} = -0.15$ eV, ii) $t_p / t_q \approx -2.7$ eV, and iii) the plasma frequencies fits with the observed ones. The most reliable parameters are $t_{b1} = -0.15$ (by assumption), $t_{b2} = -0.037$, $t_p = -0.074$, and $t_q = 0.027$ eV. Figure 5.6 shows the band structure and the Fermi surface drawn by the use of these parameters and those of the θ-model described by t_b and t_c. In the θ-model the top of the band is 0.32 eV from the Fermi level, while in the exact band the corresponding value is 0.24 eV. The obtained shape of the Fermi surface is substantially the same with each other. These results are in agreement with the calculation [4] displayed in Fig. 5.4.

There are the relations to the first-order linking t_b and t_c with t_{b2}, t_p and t_q, i.e.,

$$t_b = -t_{b2} / 2 \text{ and } t_c = |t_p - t_q| / 2 \ . \qquad (5.15)$$

Due to the contribution of t_{b1}, which is neglected here, the effective parameters, t_b and t_c, should be somewhat larger than those expected from these relations. In fact, we have,

$$t_b = 0.034 > -t_{b2} / 2 = 0.019 \text{ eV}, \qquad (5.16)$$

$$t_c = 0.054 > |t_p - t_q| / 2 = 0.051 \text{ eV}. \qquad (5.17)$$

The density of states (DOS) for the tight-binding bands of κ- and

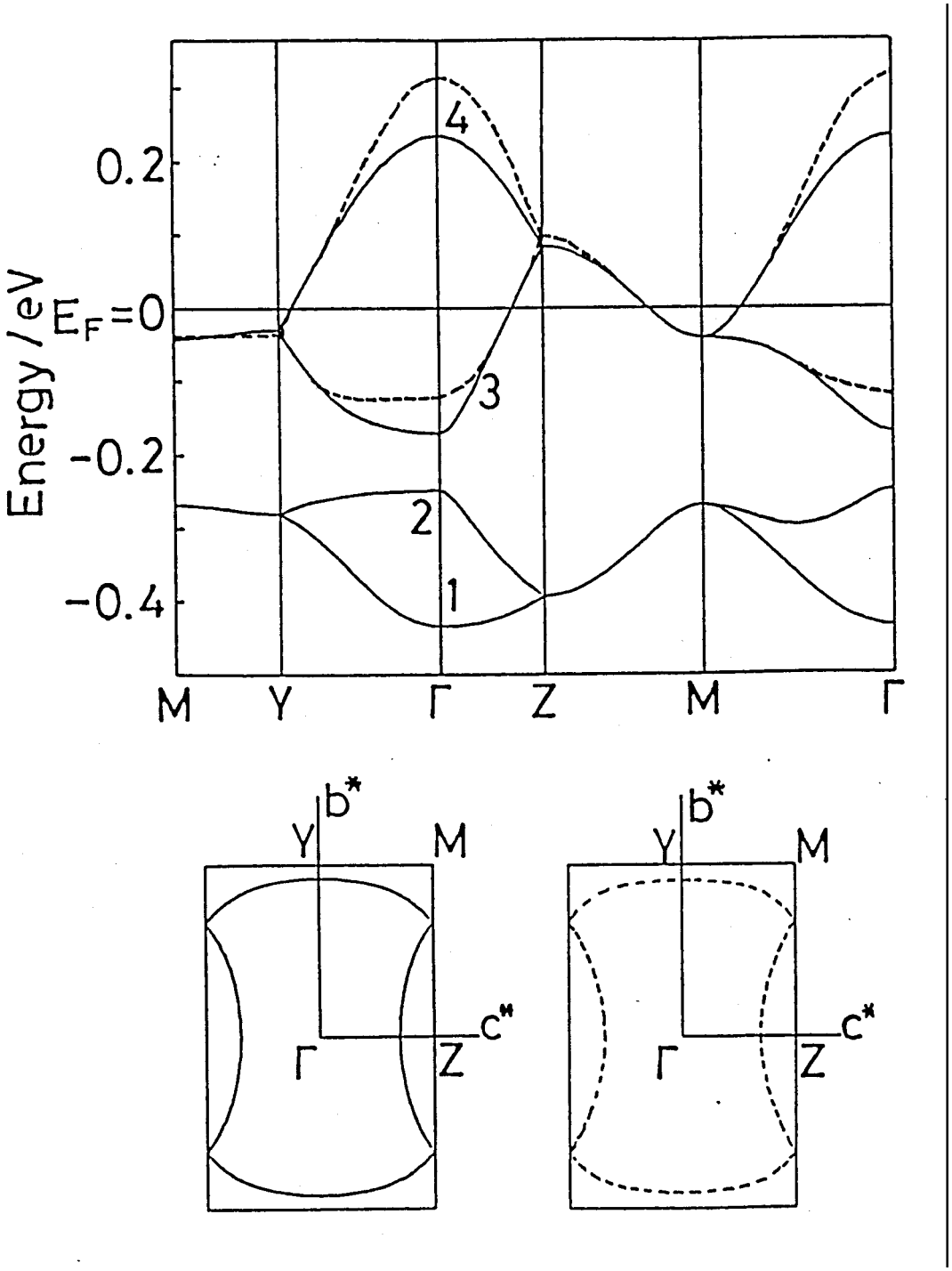

Fig. 5.6. Tight-binding band structure and the Fermi surface estimated from the reflectance spectra at 15 K. Solid curves are by the "exact κ-band" and broken curves are by the "θ-model".

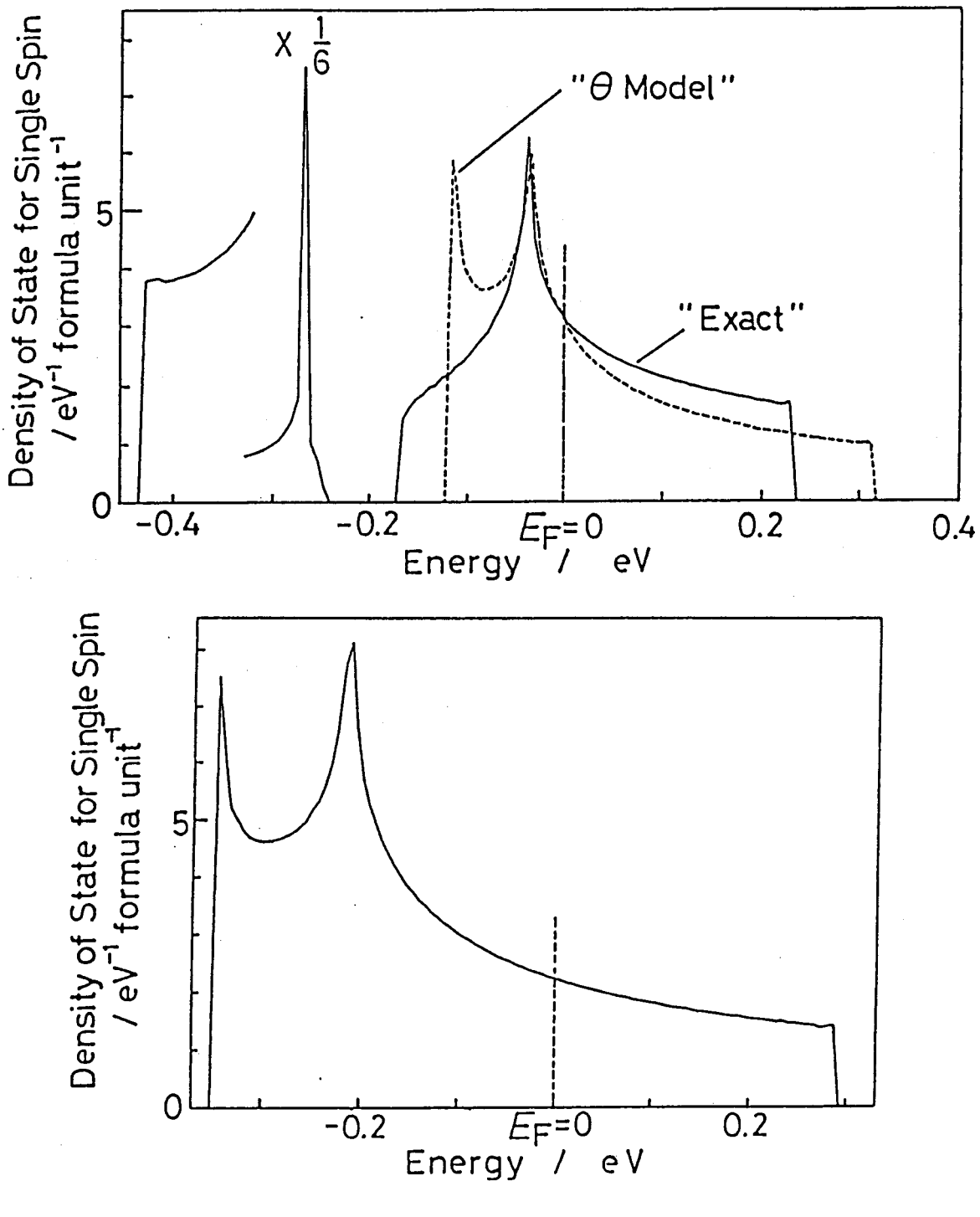

Fig. 5.7. Density of states of κ-(BEDT-TTF)$_2$I$_3$ (upper panel) and θ-(BEDT-TTF)$_2$I$_3$ (lower panel) calculated from the tight-binding bands estimated from the reflectance spectra.

θ-(BEDT-TTF)$_2$I$_3$ is calculated. The transfer integrals for θ-(BEDT-TTF)$_2$I$_3$ are taken from Ref. 13. The obtained DOS curves are shown in Fig. 5.7. The DOS values around the Fermi level of the two models for κ-(BEDT-TTF)$_2$I$_3$ are in agreement with each other. Just below the Fermi level, a singular point appears, which comes from the degenerate states along the Y-M line. Another singularity at the bottom of the θ-model band arises from pseudo-one-dimensional character near the bottom of the θ-type band structure. This singularity is artificial, because the perturbation theory cannot be applied around this energy region. The DOS at the Fermi level per formula unit for a single spin was calculated; $\rho(E_F)$= 3.1 eV^{-1} for κ-(BEDT-TTF)$_2$I$_3$ (from both models) and $\rho(E_F)$= 2.2 eV^{-1} for θ-(BEDT-TTF)$_2$I$_3$. The latter value match with that calculated from the effective mass band model.

Two de Haas-van Alphen (dHvA) results have been reported for the Fermi surface of κ-(BEDT-TTF)$_2$I$_3$ [40,41]. As explained in Chap. 3, the cross-sectional area and cyclotron mass for the cyclotron orbit relevant to the dHvA effect can be calculated from the band structure. From the present band structure, the area of the closed pocket around the Z-point is estimated to be 14 % of that of the first Brillouin zone. The corresponding value from the dHvA results by Oshima et al. is 20 % [40] and that by Wosnitza et al. is 15 % [41]. These are close to each other. The cyclotron masses for the pocket and for the whole Fermi surface are also calculated to be 1.2 m_e and 2.7 m_e, respectively, from the band structure determined in this study. The latter is in accord with that reported by Oshima et al. (2.7 m_e) [40], while Wosnitza et al. have stated that it is 3.9 m_e [41].

Furthermore, we calculated the conductivity spectra in the framework

of the point-charge approximation using the parameter set (t_{b1}, t_{b2}, t_p, t_q). As the DOS calculation shows, there is a peak just below the Fermi level in the DOS curve. The electrons here are thermally excited even at room temperature, thus introducing vacant levels below E_F. Therefore, the intensity of the interband transition from the lower band to the upper band is expected to increase. Consequently, the low energy portion of the interband transition should grow on increasing temperature. To examine this effect, we take account of the temperature dependence of the Fermi-Dirac distribution function in the calculation. Small temperature dependence of chemical potential is neglected. The calculated spectra were shown in Fig. 5.8 and the intensities were listed in Table 5.II. The position of the main peak, about 2500 cm^{-1} in the $\| \boldsymbol{c}$ spectra, and the growth of the low energy portion of the transition at room temperature are reproduced by this calculation. However, the overall intensities of the interband transition are less than the observed ones. The hump around 3500 cm^{-1} in the $\| \boldsymbol{b}$ spectra cannot be given by the calculation.

Table 5.II. Intensities of the interband transitions.

Polarization	T / K	*Intensity* / eV^2	
		calc.	obs.[a)]
// *b*	300	0.14	0.47 (295 K)
	0	0.086	0.42 (15 K)
// *c*	300	0.058	0.34 (295 K)
	0	0.032	0.24 (15 K)

a) $\sum_j f_j$, where the summation is taken over the e-mv mode and the interband transitions.

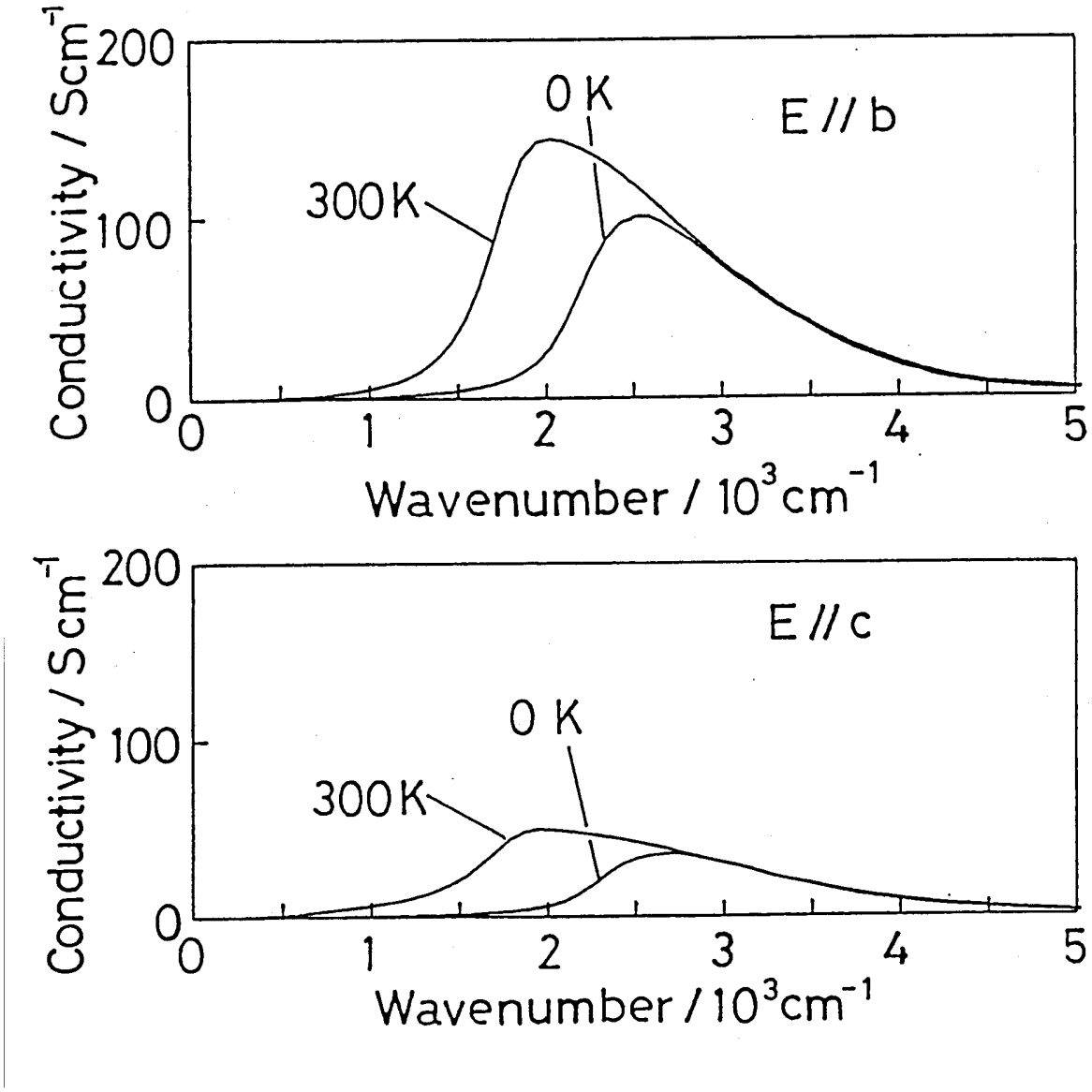

Fig. 5.8. Conductivity spectra calculated by use of the parameters: $t_{b1} = -0.15$, $t_{b2} = -0.037$, $t_p = -0.074$ and $t_q = 0.027$ eV.

5.4. Discussion

The comparison of the reflectance spectra of κ-, β-, and θ-(BEDT-TTF)$_2$I$_3$ shows that there is a definite correlation between the dimeric arrangement of BEDT-TTF and the appearance of the non-Drude mid-infrared absorption. In the light of the tight-binding band model, we interpreted these mid-infrared features as the interband transitions across the dimerization gap. This is consistent with the results for other BEDT-TTF salts [5-15]. The calculations of the interband transitions of κ-(BEDT-TTF)$_2$I$_3$ give preferable peak position. On the other hand, an interdimer charge-transfer [26] assisted by the electron-electron Coulomb repulsion cannot explain the correlation between the spectra and the crystal structure.

The intensities of the interband transitions are calculated, taking account of the temperature dependence of the Fermi-Dirac distribution function. Although the qualitative tendency of the observed spectra was reproduced by this calculation, the absolute values of the observed intensity could not be explained. This discrepancy is conspicuous particularly at room temperature. Similar result was found for β-(BEDT-TTF)$_2$I$_3$ [7]. The larger intensity of the interband transition requires a larger intradimer transfer integral or smaller interdimer ones. However, the larger intradimer integral gives too high transition energies and the smaller interdimer integrals yield too small intraband plasma frequencies. This is a dilemma. Thus, in order to explain the large intensity of the interband transition, we have to take other factors into consideration.

One of the possible reasons for the discrepancy is the inaccuracy of our simple point-charge approximation. The point-charge approximation,

in which a molecule is treated as a point located at the center of each molecule, is useful to predict the characteristics of the interband transition dominated by the crystal symmetry. However, the inter-molecular dipole moments calculated from the point-to-point vectors in this approximation are not very precise in the real crystal.

Many-body effect may influence the infrared property. To the limit of large intradimer Coulomb repulsion, we have one hole localized on each dimer. Interdimer charge-transfer transition across the (extended) Hubbard gap occurs in this localized picture. However, the observations of the Shubnikov-de Haas effect in κ-(BEDT-TTF)$_2$[Cu(NCS)$_2$] [35], the temperature dependence of thermoelectric power in β-(BEDT-TTF)$_2$I$_3$ and κ-(BEDT-TTF)$_2$[Cu(NCS)$_2$] [37] and the de Haas-van Alphen effect in θ-(BEDT-TTF)$_2$I$_3$ [38] suggest that in the metallic BEDT-TTF salts the one-electron picture is preferable than the localized picture, at least at low temperatures. Thereby, we surmise that the qualitative structure of the conduction band agrees with that predicted by the band calculation, even if the renormalization effect [42] reduces the band width.

In this picture, the intensity and the energy of the interband transition are probably affected by the electron-electron scattering or the Coulomb attraction within the electron-hole pair created by the excitation. Since the metallic BEDT-TTF salts exhibit rather low dc conductivity, particularly at room temperature, the screening effect is expected to be so insufficient that the Coulomb interaction survives and coexists with the metallic conduction. Since the strong dimerization causes the system to approach the half-filled limit, the DOS around the Fermi level is sensitive to many-body effect. As the present calculations show, the interband transition is sensitive

to DOS enhancement. The hump around 3500 cm^{-1} on the || ***b*** spectra may indicate additional transitions assisted by these effects. Even if the many-body effect influences the infrared transition, it should be noticed that the transition energy does not necessarily indicate the Coulomb potential energy as long as the one-electron picture holds. However, the effect of the Coulomb interaction on the intensity of the inter-band transition still remains unsettled. To make it clear, we need further investigations on the conduction mechanism of these materials at high temperatures. Very short mean free path in many organic conductors [13,43] at room temperature is also possibly in connection with the infrared properties.

The superconducting transition temperature of κ-(BEDT-TTF)$_2$[Cu(NCS)$_2$], T_c = 10.4 K [2], is about three times as large as that of κ-(BEDT-TTF)$_2$I$_3$, 3.6 K [1], though their donor sheet structures are quite similar to each other. Moreover, the dc conductivity of the I_3 salt is metallic between room temperature and T_c [1,44], while the [Cu(NCS)$_2$] salt exhibits a resistivity maximum [2] or shoulder [11] near 100 K. Several studies have been made on the infrared properties of the [Cu(NCS)$_2$] salt [11,26,29,30,45-47]. The observed line shapes of the two salts resemble each other; no evidence for a substantial difference in the band structure is found in the shape of the observed spectra. However, the plasma frequencies of the I_3 salt are somewhat higher than those of the [Cu(NCS)$_2$] salt. The increase in the plasma frequency indicates increase in the band width and decrease in the density of states. In fact, the DOS at the Fermi level per formula unit for a single spin is estimated to be 3.1 eV^{-1} for the I_3 salt, while for the [Cu(NCS)$_2$] salt the corresponding value is deduced as 7.1eV^{-1} [2] (from the static paramagnetic susceptibility at room tem-

perature) or 7.5 eV^{-1} [11] (from reflectance spectra). Therefore, the higher plasma frequencies of the I_3 salt can be related to the lower T_c. The fact that the values of the cyclotron mass of the I_3 salt [40,41] are much smaller than those of the [$Cu(NCS)_2$] salt [42] also supports this interpretation. A possible origin of the difference in the electronic structure is the interlayer electron transfer with the help of the donor-anion interaction [36].

5.5. Concluding Remarks

The band parameters describing the structure of the HOMO band of κ-(BEDT-TTF)$_2$I$_3$ have been estimated from the Drude plasma frequencies by the method based on the dimer approximation developed in this work. The advantage of this method is that the procedure requires only the intraband plasma frequencies and that the energy dispersion can be expressed by a simple and explicit formula. This approximation, which is formulated by use of simple perturbation theory, can be easily generalized and should be applicable to other dimeric organic metals: other κ-type BEDT-TTF salts, β-(BEDT-TTF)$_2$X, κ-(DMET)$_2$AuBr$_2$ [48,49], κ-(MDT-TTF)$_2$AuI$_2$ [50], and so on. It has been shown that the interband transitions across the dimerization gap [12,15] are essential to the mid-infrared absorption observed for κ-(BEDT-TTF)$_2$I$_3$. We pointed out the possibility of many-body effect on the intensity of the optical transition. Further investigations will be necessary to elucidate the origin of the large intensity of the mid-infrared transitions.

References

1. R. Kato, H. Kobayashi, A. Kobayashi, S. Moriyama, Y. Nishio, K. Kajita, and W. Sasaki: Chem. Lett. 507 (1987).
2. H. Urayama, H. Yamochi, G. Saito, K. Nozawa, T. Sugano, M. Kinoshita, S. Sato, K. Oshima, A. Kawamoto, and J. Tanaka: Chem. Lett. 1988, 55; H. Mori: Int. J. Mod. Phys. B **8** (1994) 1.
3. A. M. Kini, U. Geiser, H. H. Wang, K. D. Carlson, J. M. Williams, W. K. Kwok, K. G. Vandervoort, J. E. Thompson, D. L. Stupka, D. Jung, and M.-H. Whangbo: Inorg. Chem. **29** (1990) 2555.
4. A. Kobayashi, R. Kato, H. Kobayashi, S. Moriyama, K. Kajita, and W. Sasaki: Chem. Lett. 463 (1988).
5. H. Tajima, K. Yakushi, H. Kuroda, G. Saito, and H. Inokuchi: Solid State Commun. **49** (1984) 769.
6. H. Kuroda, K. Yakushi, H. Tajima, and G. Saito: Mol. Cryst. Liq. Cryst. **125** (1985) 135.
7. H. Tajima, K. Yakushi, H. Kuroda, and G. Saito: Solid State Commun. **56** (1985) 159.
8. H. Tajima, K. Yakushi, H. Kuroda, and G. Saito: Solid State Commun. **57** (1986) 911.
9. K. Yakushi, H. Tajima, H. Kanbara, M. Tamura, H. Kuroda, G. Saito, H. Kobayashi, R. Kato, and A. Kobayashi: Physica **143B** (1986) 463.
10. K. Yakushi, H. Kanbara, H. Tajima, H. Kuroda, G. Saito, and

T. Mori: Bull. Chem. Soc. Jpn. **60** (1987) 4251.

11. A. Ugawa, G. Ojima, K. Yakushi, and H. Kuroda: Phys. Rev. B **38** (1988) 5122.
12. H. Kuroda, K. Yakushi, H. Tajima, A. Ugawa, M. Tamura, Y. Okawa, A. Kobayashi,

R. Kato, H. Kobayashi, and G. Saito: Synth. Metals **27** (1988) A491.

13. M. Tamura, K. Yakushi, H. Kuroda, A. Kobayashi, R. Kato, and H. Kobayashi: J. Phys. Soc. Jpn. **57** (1988) 3239.

14. H. Tajima, M. Tamura, H. Kuroda, T. Mori, and H. Inokuchi: Bull. Chem. Soc. Jpn. **63** (1990) 538.

15. A. Ugawa, K. Yakushi, H. Kuroda: Mol. Cryst. Liq. Cryst. **181** (1990) 269.

16. R. Kato, H. Kobayashi, A. Kobayashi, S. Moriyama, Y. Nishio, K. Kajita, and W. Sasaki: Chem. Lett. 507 (1987).

17. K. Yakushi, H. Tajima, T. Ida, M. Tamura, H. Hayashi, H. Kuroda, A. Kobayashi, H. Kobayashi, and R. Kato: Synth. Metals **24** (1988) 301.

18. The author are grateful to Professor A. Masuda, Professor H. Shimizu and Dr. K. Takahashi for the EPMA measurement.

19. V. F. Kaminskii, T. G. Prokhorova, R. P. Shibaeva, and E. B. Yagubskii: JETP Lett. **39** (1984) 17.

20. T. Mori, A. Kobayashi, Y. Sasaki, H. Kobayashi, G. Saito, and H. Inokuchi: Chem. Lett. 957 (1984).

21. H. Kobayashi, R. Kato, A. Kobayashi, Y. Nishio, K. Kajita, and W. Sasaki: Chem. Lett. 789 (1986).

22. H. Kobayashi, R. Kato, A. Kobayashi, Y. Nishio, K. Kajita, and W. Sasaki: Chem. Lett. 833 (1986).

23. M. J. Rice, V. M. Yartsef and C. S. Jacobsen: Phys. Rev. B **21** (1980) 3437.

24. M. J. Rice: Phys. Rev. Lett. **37** (1976) 36.

25. M. Meneghetti, R. Botio, and C. Pecile: J. Physique **47** (1986) 1377.

26. K. Kornelsen, J. E. Eldridge, C. C. Homes, H. H. Wang, and J. M. Williams: Solid State Commun. **72** (1989) 475.

27. A. Kobayashi, R. Kato, H. Kobayashi, S. Moriyama, Y. Nishio, K. Kajita, and W. Sasaki: Chem. Lett. 2017 (1986)

28. M. E. Kozlov, K. I. Pokhodnia and A. A. Yurchenko: Spectrochim. Acta, Sect. A **43** (1987) 323; ibid. **43** (1987) 323.

29. K. Kornelsen, J. E. Eldridge, H. H. Wang, and J. M. Williams: Solid State Commun. **74** (1990) 501; Phys. Rev. B **44** (1991) 5235.

30. J. E. Eldridge, K. Kornelsen, H. H. Wang, J. M. Williams, A. V. S. Crouch, and D. M. Watkins: Solid State Commun. **79** (1991) 583.

31. O. O. Drozdova, V. N. Semkin, R. M. Vlasova, N. D. Kushch, and E. B. Yagubskii: Synth. Metals **64** (1994) 17.

32. T. Mori, A. Kobayashi, Y. Sasaki, H. Kobayashi, and G. Saito: Bull. Chem. Soc. Jpn. **57** (1984) 627.

33. M. H. Whangbo, J. M. Williams, P. C. W. Leung, M. A. Beno, T. J. Emge, H. H. Wang, K. D. Carlson, G. W. Crabtree: J. Am. Chem. Soc. **107** (1984) 957.

34. T. Mori, A. Kobayashi, Y. Sasaki, and H. Kobayashi: Chem. Lett. 1923 (1982).

35. K. Oshima, T. Mori, H. Inokuchi, H. Urayama, H. Yamochi, and G. Saito: Phys. Rev. B **38** (1988) 938.

36. D. Jung, M. Evain, J. J. Novoa, M. H. Whangbo, M. A. Beno, A. M. Kini, A. J. Schultz, J. M. Williams, and P. J. Nigrey: Inorg. Chem. **28** (1989) 4516; **29** (1990) 1594.

37. T. Mori and H. Inokuchi: J. Phys. Soc. Jpn. **57** (1988) 3674.

38. M. Tokumoto, A. G. Swanson, J. S. Brooks, M. Tamura, H. Tajima, and H. Kuroda: Solid State Commun. **75** (1990) 439.

39. R. V. Kasowskii, M. H. Whangbo: Inorg. Chem. **29** (1990) 360.

40. K. Oshima, H. Yamazaki, K. Kato, Y. Maruyama, R. Kato, A. Kobayashi, and H. Kobayashi: Synth. Metals **56** (1993) 2334.

41. J. Wosnitza, N. Herrmann, X. Liu, and D. Schweizer: Synth. Metals, in press.

42. N. Toyota, E. W. Fenton, T. Sasaki, and M. Tachiki: Solid State Commun. **72** (1989) 859.

43. M. Weger: Phil. Mag. B**56** (1987) 889.

44. K. Kajita, Y. Nishio, S. Moriyama, W. Sasaki, R. Kato, H. Kobayashi, A. Kobayashi: Solid State Commun. **64** (1987) 1279.

45. M. G. Kaplunov, N. D. Kushch, and E. B. Yagubskii: Phys. Status Solidi(a)**110** (1988) K111.

46. T. Sugano, H. Hayashi, H. Takenouchi, K. Nishikida, H. Urayama, H. Yamochi, G. Saito, and M. Kinoshita: Phys. Rev. B **37** (1988) 9100.

47. M. Tokumoto, H. Anzai, K. Takahashi, N. Kinoshita, K. Murata, T. Ishiguro, Y. Tanaka, Y. Hayakawa, H. Nagamori, and K. Nagasaka: Synth. Metals **27** (1988) A171.

48. K. Kikuchi, K. Murata, Y. Honda, T. Namiki, K. Saito, K. Kobayashi, T. Ishiguro, and I. Ikemoto: J. Phys. Soc. Jpn. **56** (1987) 2627.

49. K. Kikuchi, Y. Honda, Y. Ishikawa, K. Saito, I. Ikemoto, K. Murata, H. Anzai, T. Ishiguro, and K. Kobayashi: Solid State Commun. **66** (1988) 405.

50. G. C. Papavassiliou, G. A. Mousdis, J. S. Zambounis, A. Terzis, S. Hountas, B. Hilti, C. W. Mayer, J. Pfeiffer: Synth. Metals **27** (1988) B379.

Chapter 6.

Reflectance Spectra of $Me_4N[Ni(dmit)_2]_2$

6.1. Introduction

The anion radical salt of [Ni(dmit)$_2$], $Me_4N[Ni(dmit)_2]_2$, is the first example of a metallic molecular conductor based on π-radical anion and closed-shell cation [1,2]. The reported temperature dependence of dc resistivity of this salt is somewhat complicated [1]; it depends on the cooling-heating cycles and is accompanied by a resistivity jump around 100 K with hysteresis or by non-metallic behavior at low temperatures. These anomalies have been suggested to be a metal-semimetal transition associated with the freezing of the rotational degrees of freedom of the methyl groups [1]. The anomalies have been found to be suppressed by application of pressure, and superconducting transition have been discovered above 3 kbar, for the first time in the closed-shell cation salt of [Ni(dmit)$_2$] [1]. The superconducting transition temperature rises with increasing pressure, up to 5 K at 7 kbar, which is in contrast to the case of the salts of TTF derivatives [1].

In the crystal of $Me_4N[Ni(dmit)_2]_2$, the conduction layers of [Ni(dmit)$_2$] and cation sheets are arranged alternately along the *c*-axis (Fig. 6.1) [1]. Two types of conduction layers are distinguished; the one has [Ni(dmit)$_2$] stacks elongated in the [110] direction, and the other has the equivalent stacks in the $[\bar{1}10]$ direction. These two layers appear alternately along the *c*-axis (Fig. 6.2). Two pairs of quasi-one-dimensional Fermi surfaces are expected, each pair arising from each type of layer. Thus, the whole system has a two-dimensional electronic structure. In fact, tight-binding

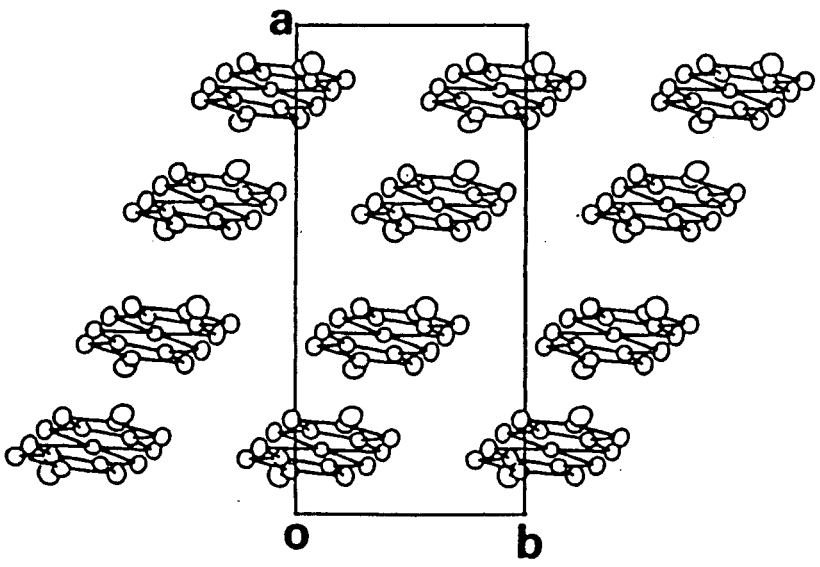

Fig. 6.1. Arrangement of $[Ni(dmit)_2]$ in the conduction layer [2].

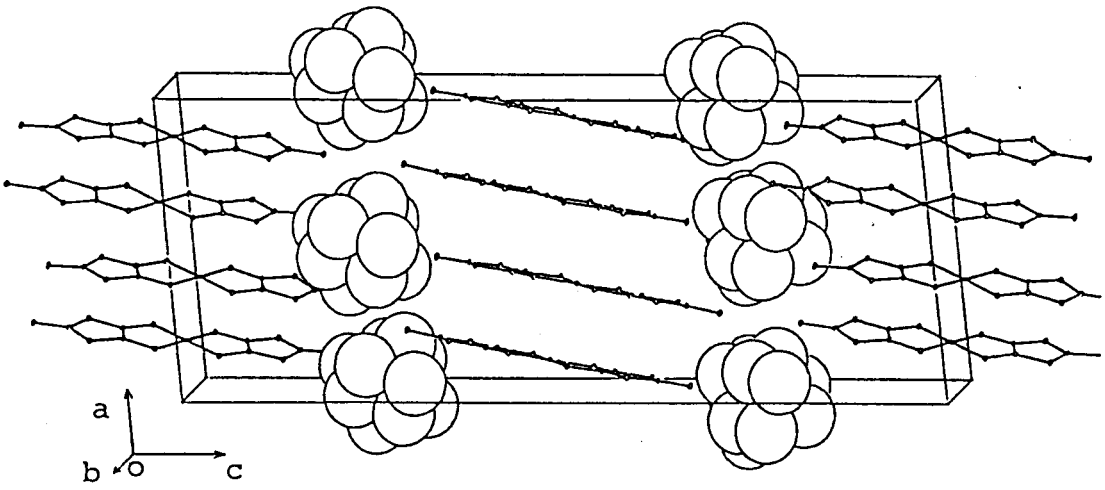

Fig. 6.2. Crystal structure of $Me_4N[Ni(dmit)_2]_2$ [1].

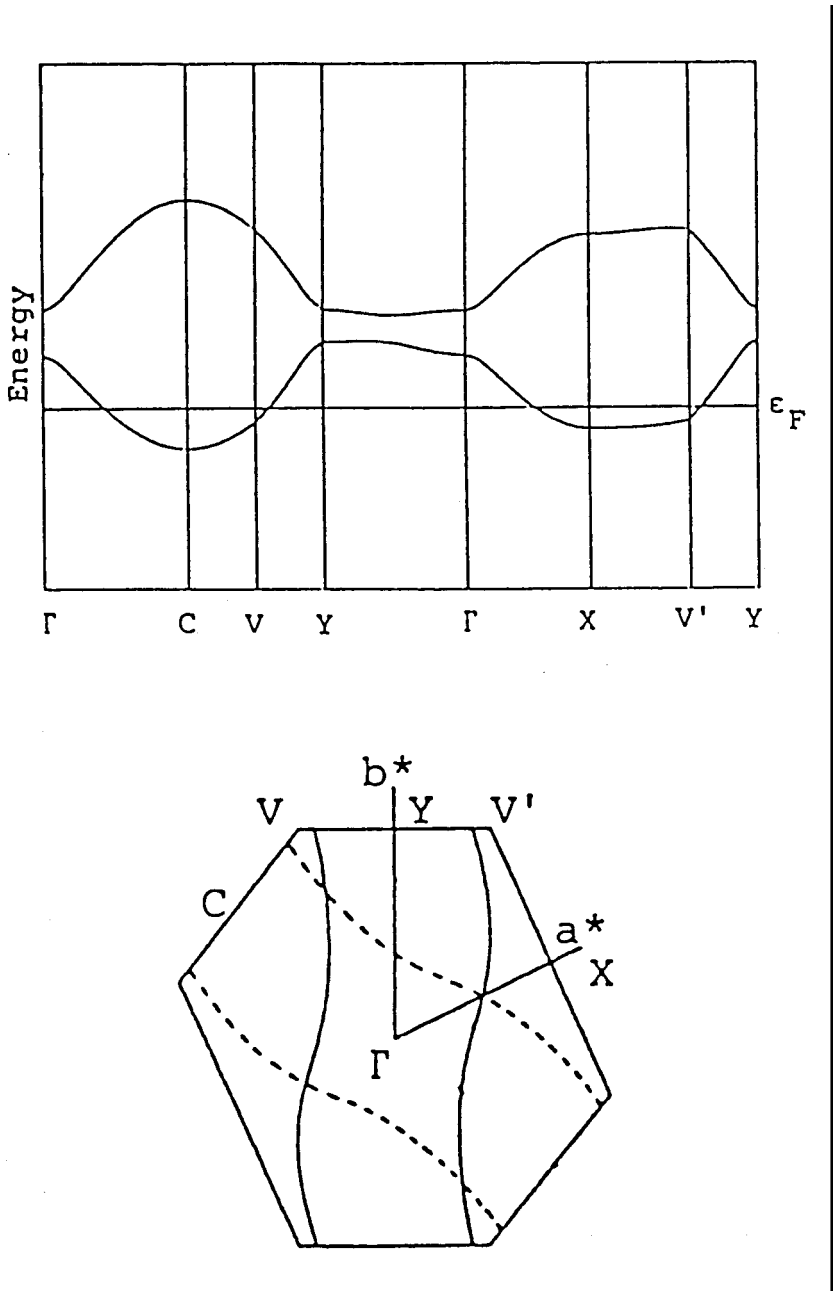

Fig. 6.3. The tight-binding band structure and Fermi surface of $Me_4N[Ni(dmit)_2]_2$ inferred from the intermolecular LUMO overlap calculations [1, 2]. The primitive lattice, ($\boldsymbol{a}'$, $\boldsymbol{b}'$, $\boldsymbol{c}'$), was adopted, where $\boldsymbol{a}' = (\boldsymbol{a} + \boldsymbol{b}) / 2$, $\boldsymbol{b}' = -\boldsymbol{b}$ and $\boldsymbol{c}' = -\boldsymbol{c}$. Dotted lines indicate the Fermi surface of the adjacent conduction layer.

band calculations based on the LUMOs of $[Ni(dmit)_2]$ results in such features (Fig. 6.3) [1]. Similar structures have been found also for α- and β-$Me_4N[Pd(dmit)_2]_2$ [3,4], $Me_4N[Pt(dmit)_2]_2$ [5], $Cs[Pd(dmit)_2]_2$ [6] and $Me_4As[Pd(dmit)_2]_2$ [3].

The main purpose of this study is an experimental examination of this two-dimensional electronic band structure. The observed spectrum should correspond to a superposition of that of the two types of layers. However, it is possible to derive each part of the contribution, by taking account of the fact that the two types of layers are equivalent. Furthermore, introduction of a simplification of the molecular arrangement in the layers affords an estimation of an approximate shape of the Fermi surface.

6.2. Experimental

The single crystal samples of $Me_4N[Ni(dmit)_2]_2$ were provided by Prof. H. Kobayashi (Toho Univ.), Prof. A. Kobayashi (Univ. of Tokyo) and Prof. R. Kato (Univ. of Tokyo). The black plate single crystals were obtained by galvanostatic electrolysis of an acetonitrile solution of $Me_4N[Ni(dmit)_2]$ and Me_4NClO_4. Polarized reflectance spectra were measured on the (001) crystal face, by the methods described in Sec. 3.1, with the light polarization, $\boldsymbol{E} \parallel \boldsymbol{a}$ and $\boldsymbol{E} \parallel \boldsymbol{b}$, which are the principal axes within the (001) plane. The crystal axes were identified by X-ray oscillation photographs.

6.3. Results and Discussion

Figure 6.4 shows the reflectance spectra measured at room temperature, 150 K and 25 K. The two-dimensionality is obvious, as is expected from the crystal structure. The reflectivities at low wavenumbers are somewhat low, particularly for $\boldsymbol{E} \parallel \boldsymbol{b}$. However, they are remarkably enhanced with lowering temperature, in accord with the metallic behavior as expected for this material. At low temperatures, the spectral shape is basically metallic accompanied by the plasma edges around 4000 cm^{-1} in the $\boldsymbol{E} \parallel \boldsymbol{a}$ spectra and 2000 cm^{-1} in the $\boldsymbol{E} \parallel \boldsymbol{b}$ spectra, though there are small deviations from the Drude type dispersion, that is, the humps around 1100 and 1500 cm^{-1} in the $\boldsymbol{E} \parallel \boldsymbol{a}$ spectra and that around 3000 cm^{-1} in the $\boldsymbol{E} \parallel \boldsymbol{b}$ spectra. The Drude-like dispersion suggests that this salt is essentially metallic even at ambient pressure in spite of the anomalies in behavior of the dc resistivity, at least from the viewpoint of the optical properties. This is consistent with the suggestion that the anomalous behavior of the dc resistivity may be caused localization due to weak randomness such as the rotation of the methyl groups.

The small humps indicate the presence of the contribution of the interband transitions across band gaps. In fact, weak broad maxima corresponding to the humps can be recognized in the conductivity spectra (Fig. 6.5) obtained by the Kramers-Kronig analysis of the reflectance spectra. Tails of the Drude contributions are evident at low temperatures. On the other hand, peaks of conductivity appear below 1000 cm^{-1} in both

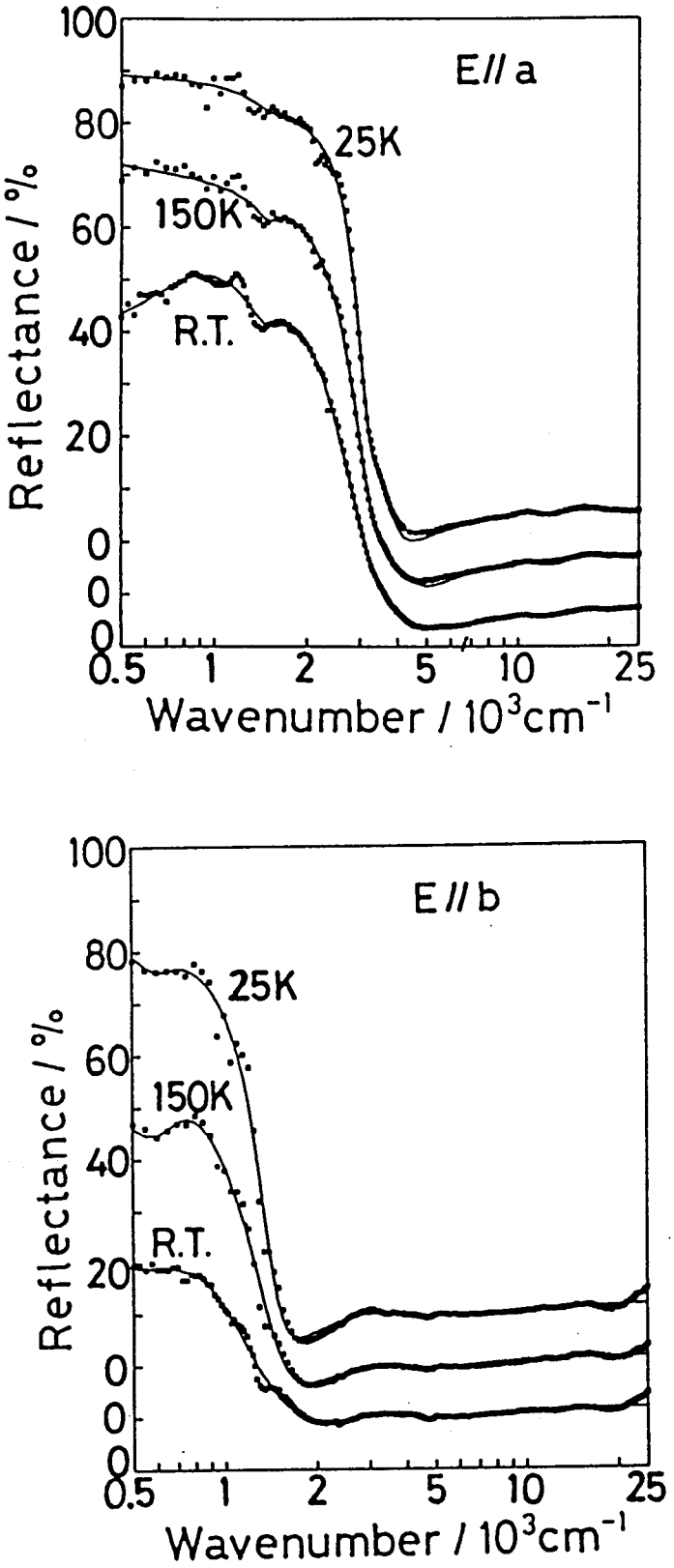

Fig. 6.4. Reflectance spectra of $Me_4N[Ni(dmit)_2]_2$. Solid curves shows the fit to the Drude-Lorentz model.

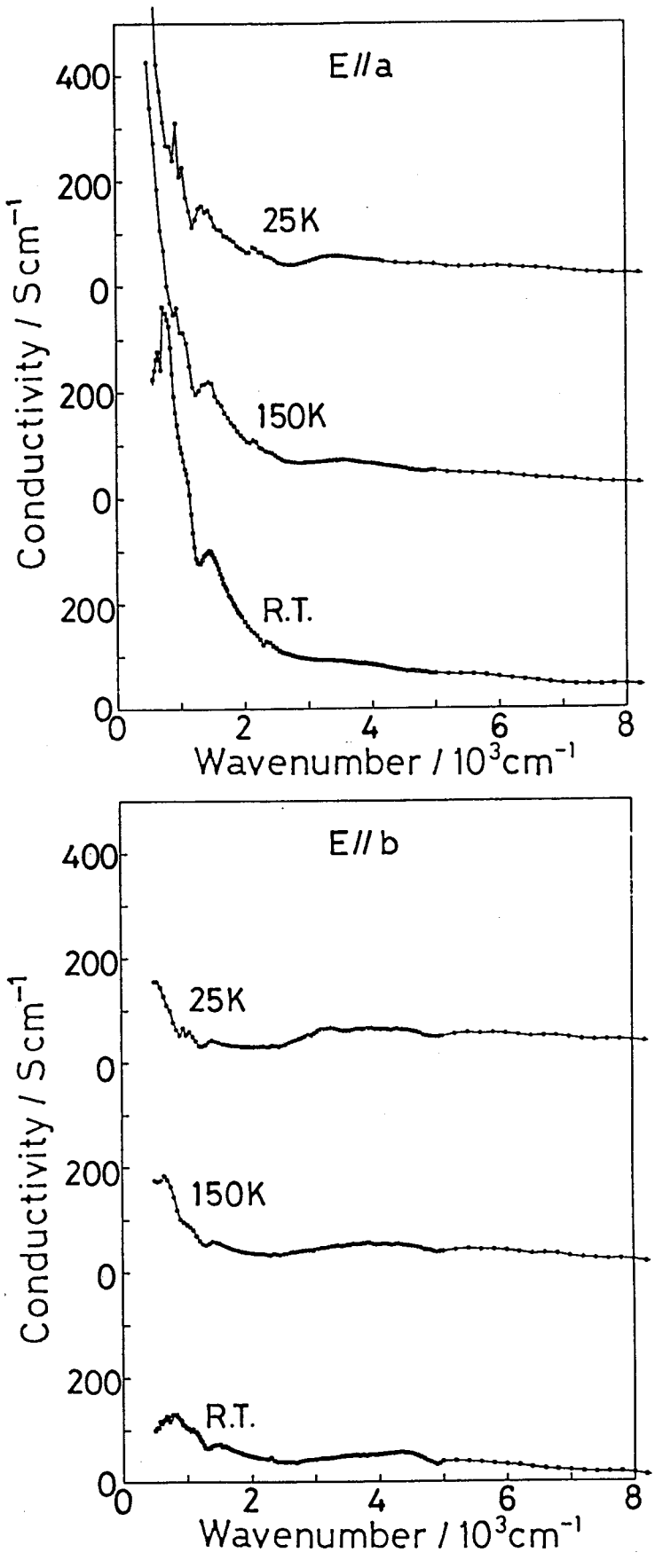

Fig. 6.5. Conductivity spectra of $Me_4N[Ni(dmit)_2]_2$.

$\boldsymbol{E} \parallel \boldsymbol{a}$ and $\boldsymbol{E} \parallel \boldsymbol{b}$ spectra at room temperature. However, they are due to the inaccuracy of the extrapolation of the considerably low reflectivity data towards zero wavenumber. The extrapolation is required for the Kramers-Kronig analysis. But it is difficult for metals with low reflectivity, because reflectivity should increase very rapidly towards zero wavenumber outside the experimental region. So that, the peaks should be regarded as artificial ones, and do not necessarily imply the gap formation at room temperature.

In order to extract the contribution of the intraband transitions (the Drude terms), a curve-fitting analysis of the reflectance spectra was carried out, on the basis of the Drude-Lorentz dielectric function,

$$\varepsilon(\omega) = \varepsilon_C - \omega_P^2 / (\omega^2 + i\omega / \tau) + \sum_{j=1}^{1 \text{ or } 2} f_j / [(\omega_j^2 - \omega^2) - i\gamma_j \omega] . \qquad (6.1)$$

The first term in the right-hand side of Eq.(6.1), the Drude term, describes the intraband transitions. The second term stands for the interband transitions corresponding to the conductivity maxima around 1600 cm^{-1} and 4000 cm^{-1} in the $\boldsymbol{E} \parallel \boldsymbol{a}$ spectra and that around 4000 cm^{-1} in the $\boldsymbol{E} \parallel \boldsymbol{b}$ spectra. The reflectivity is related to dielectric function by the equation,

$$R = [1 + |\varepsilon| - \sqrt{2(|\varepsilon| + \mathrm{Re}(\varepsilon))}\,] / [1 + |\varepsilon| + \sqrt{2(|\varepsilon| + \mathrm{Re}(\varepsilon))}\,] . \qquad (6.2)$$

The obtained parameters are summarized in Table 6.I. At room temperature,

the fitting results are not reliable because of the too damped Drude contributions.

Table 6.I. Drude parameters obtained by the Drude-Lorentz fit of the reflectance spectra

Polarization	T / K	ε_c	ω_p / eV	τ^{-1} / eV
// *a*	150	3.1	0.75	0.083
	25	2.8	0.69	0.040
// *b*	150	4.1	0.41	0.094
	25	4.1	0.41	0.038

The squares of the obtained plasma frequencies, ω_p^2, are the sums of the contributions of the two types of [Ni(dmit)$_2$] layers with different orientations. Since the *a*- and *b*-axes are the principal axes of the crystal and the two types of layers are equivalent, the sum is simply the twice of ω_p^2 of the one type of the layer. In this way, the observed values of ω_p^2 can be compared with those calculated from the band structure.

The calculations of inter-molecular overlap integrals of $Me_4N[Ni(dmit)_2]_2$ suggest the following features. The amplitudes of the two intrastack transfer integrals are almost equal to each other, and they have opposite signs. Only one type of transfer integrals is predominant among the interstack ones, referring to that marked by the symbol p in Ref. 1. Thereby, the band structure of this salt is approximately described

by the two transfer integrals, the intra- and interstack ones, t_1 and t_2, respectively, as schematically illustrated in Fig. 6.6. This approximation, i.e., the assumption of no dimerization in a [Ni(dmit)$_2$] stack, is also supported by the weakness of the observed interband transitions.

The plasma frequencies can be calculated from the band structure by the equations,

$$(\omega_p^{\,2})_a = 2\,(e^2/\pi^2\hbar)\,(\pi/c\sin\beta)\int |\,(v_F)_a\,|\,dk_{Fb}\,, \tag{6.3}$$

$$(\omega_p^{\,2})_b = 2\,(e^2/\pi^2\hbar)\,(\pi/c\sin\beta)\int |\,(v_F)_b\,|\,dk_{Fa}\,, \tag{6.4}$$

where the factor 2 stands for the sum over the two different [Ni(dmit)$_2$] layers, and $(v_F)_a$ and $(v_F)_b$ are the *a*- and *b*-components of the Fermi velocity, $\boldsymbol{v}_F$, given by,

$$\boldsymbol{v}_F = \hbar^{-1}\,\mathrm{grad}_{\boldsymbol{k}}\,E(t_1, t_2; k_a, k_b)\;;\quad E = E_F \tag{6.5}$$

The band filling, which determines the Fermi energy E_F, is set to be 1/4, as inferred from the stoichiometry. By use of these equations, the optimal set of t_1 and t_2 which reproduces the observed plasma frequencies was searched. When the values of plasma frequencies at 25 K, $(\omega_p)_a$ = 0.69 eV and $(\omega_p)_b$ = 0.41 eV, together with the lattice parameters at 95 K, a = 13.675, b = 6.476, c = 36.048 Å and β = 94.74 ° , are used, the results t_1 = 0.10 eV and t_2 = 0.052 eV are obtained.

Figure 6.7 shows the band structure and Fermi surface estimated in this way. The overall shapes of the band dispersion and the Fermi surface

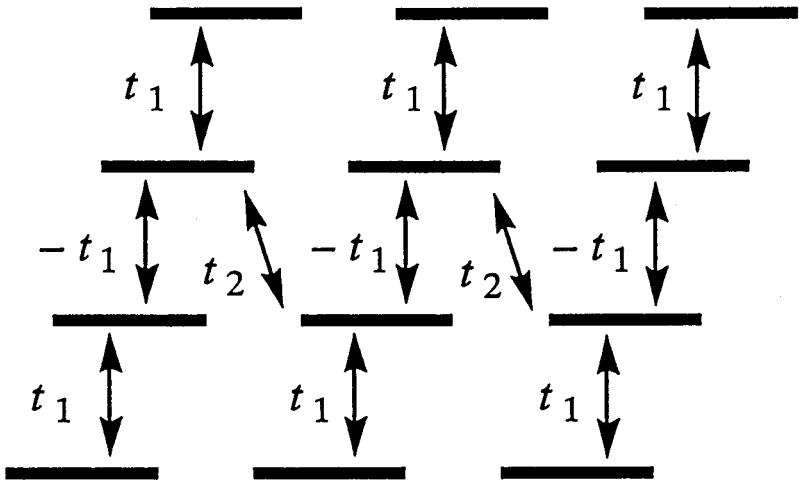

Fig. 6.6. Schematic display of the two dominant intermolecular interactions, t_1 and t_2, in the conduction layer of $Me_4N[Ni(dmit)_2]_2$.

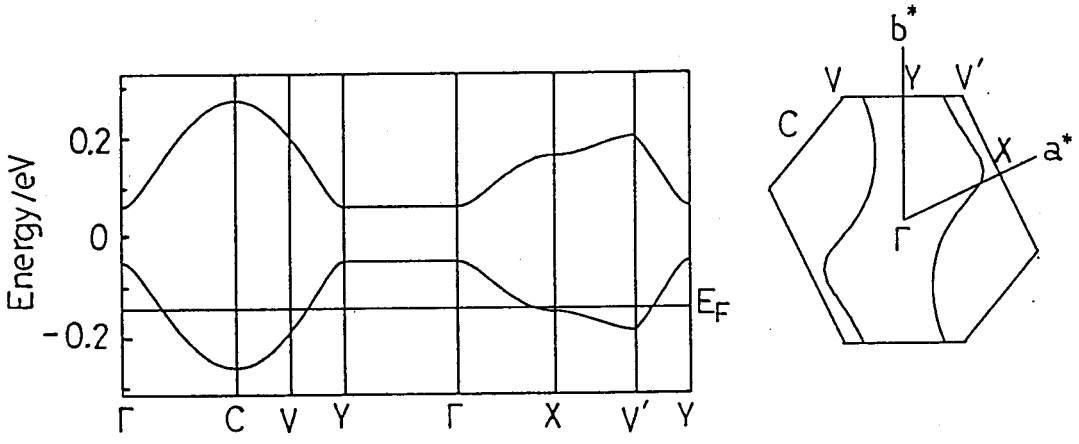

Fig. 6.7. The band structure and the Fermi surface inferred from the optical results at 25 K. The primitive lattice, ($\boldsymbol{a}'$, $\boldsymbol{b}'$, $\boldsymbol{c}'$), was adopted, where $\boldsymbol{a}' = (\boldsymbol{a} + \boldsymbol{b}) / 2$, $\boldsymbol{b}' = -\boldsymbol{b}$ and $\boldsymbol{c}' = -\boldsymbol{c}$.

are in agreement of those of the calculated ones (Fig. 6.3). The optical results give slightly larger corrugation of the quasi-one-dimensional Fermi surface. This comes from the larger ratio $t_2/t_1 = 0.52$; the corresponding ratio is about 0.3 according to the band calculations. This deviation may stem partly from the simplification of the molecular arrangement introduced in the analysis of the optical data.

In the light of this band structure, the interband transitions appear around 4000 cm^{-1} are ascribable to the transitions from around the bottom of the lower band to around the top of the upper band. Such transitions for zigzag stacks, as in this material, should have larger intensities for the light polarization perpendicular to the stacks, which is consistent with the observation. The transition energy of them corresponds to the overall width of the LUMO bands, which is slightly larger than $4t_1$.

6.4. Conclusion

The reflectance spectra of $Me_4N[Ni(dmit)_2]_2$ suggest that this salt is essentially metallic even at low temperature, in spite of the non-metallic behavior of the dc resistivity. The band structure and the Fermi surface deduced from the Drude plasma frequencies are consistent with the tight-binding calculations.

References

1. A. Kobayashi, H. Kim, Y. Sasaki, R. Kato, H. Kobayashi, S. Moriyama, Y. Nishio, K. Kajita and W. Sasaki: Chem. Lett. 1819 (1987).
2. H. Kim, A. Kobayashi, Y. Sasaki, R. Kato, and H. Kobayashi: Chem. lett. 1799 (1987).
3. A. Kobayashi, H. Kim, Y. Sasaki, K. Murata, R. Kato, H. Kobayashi: J. Chem. Soc. Faraday Trans. **86** (1990) 361.
4. A. Kobayashi, R. Kato, R. A. Clark, A. E. Underhill, A. Miyamoto, K. Bun, T. Naito and H. Kobayashi: Synth. Metals **55-57** (1993) 2927.
5. A. Kobayashi, A. Miyamoto, H. Kobayashi, R. A. Clark, A. E. Underhill: J. Mater. Chem. **1** (1991) 827.
6. R. A. Clark and A. E. Underhill: Synth. Metals **27** (1988) B515.

Chapter 7.

Reflectance Spectra of α-$Et_2Me_2N[Ni(dmit)_2]_2$

7.1. Introduction

The anion radical salt of $[Ni(dmit)_2]$, α-$Et_2Me_2N[Ni(dmit)_2]_2$, retains metallic conductivity down to liquid helium temperature [1]. Three modifications, α-, β- and γ-types, have been hitherto identified in this compound [2]. The β-type is semiconducting. The α-type exhibits resistivity jump at 240 K due to cracks of the crystals caused by the abrupt structural phase transition, which has been revealed very recently [2]. The γ-type crystal shows smooth decrease in resistivity down to low temperature [2].

The crystal of α-$Et_2Me_2N[Ni(dmit)_2]_2$ is composed of the conduction layers of $[Ni(dmit)_2]$ and cation sheets, which are arranged alternately along the *a*-axis [1]. In the $[Ni(dmit)_2]$ layers, all the molecular planes are almost perpendicular to the *c*-axis and the molecules are packed in a face-to-face fashion. However, there is a special characteristic overlapping mode in this crystal, which is called as the "spanning overlap" mode [1]. That is, a molecule overlaps with two molecules equivalently, in this mode (Fig. 7.1). As a result, molecular bridging array is formed. Another significant overlapping mode is a conventional face-to-face one to form a dimeric packing of $[Ni(dmit)_2]$. The calculations of the intermolecular overlap integrals [1] have shown that these two overlaps are dominant. These interactions afford a honey-comb-like two-dimensional network. According to the tight-binding band calculations [1], this molecular arrangement in fact yields two-dimensional Fermi surface (Fig. 7.2). The shape of the Fermi surface is similar to those of the typical two-dimensional BEDT-TTF salts with the κ-type structure. Therefore, this structure is an important example providing a way to construct a two-dimensional structure

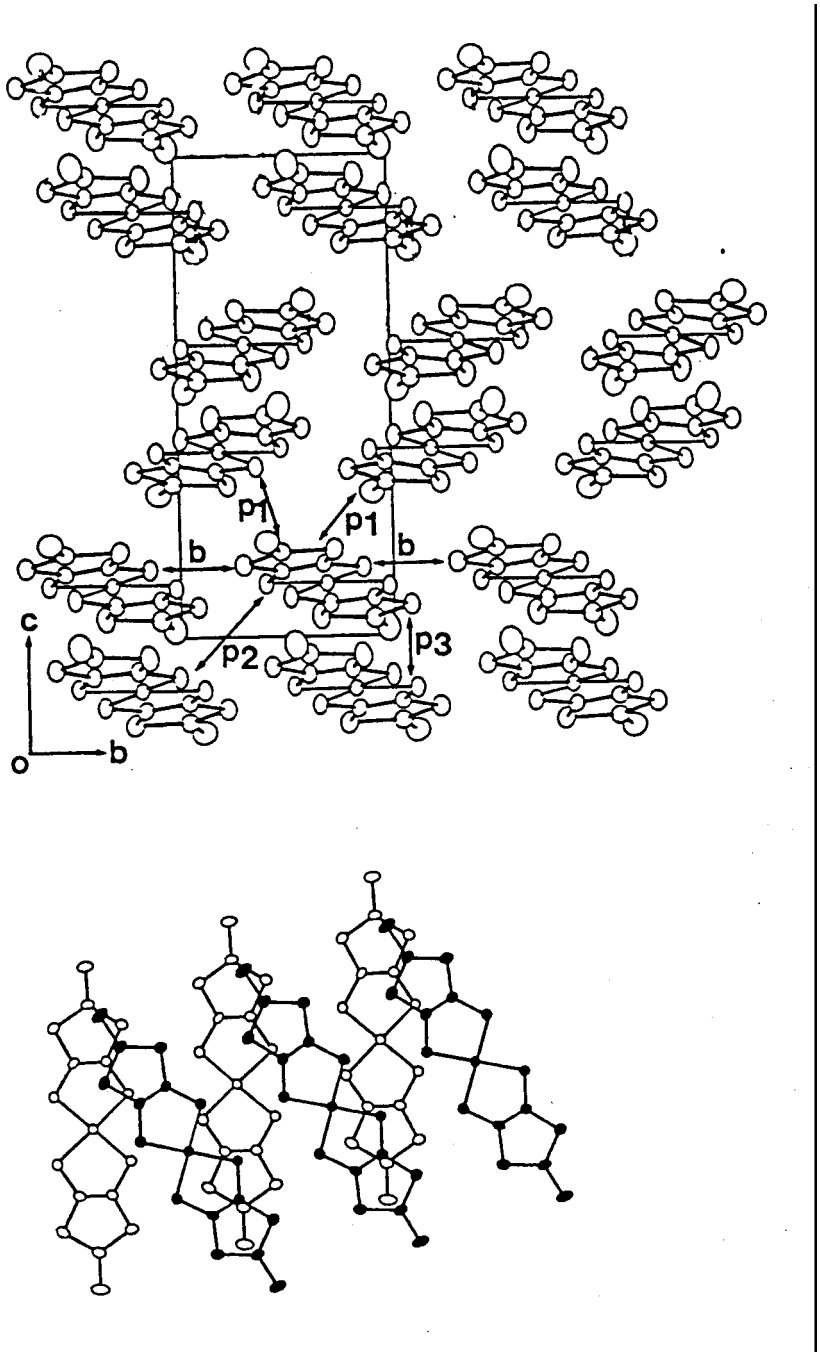

Fig. 7.1. Top: Arrangement of $[Ni(dmit)_2]$ in the conduction layer of α-$Et_2Me_2N[Ni(dmit)_2]_2$ [1]. Bottom: Spanning overlap mode, designated as **p1** in the top.

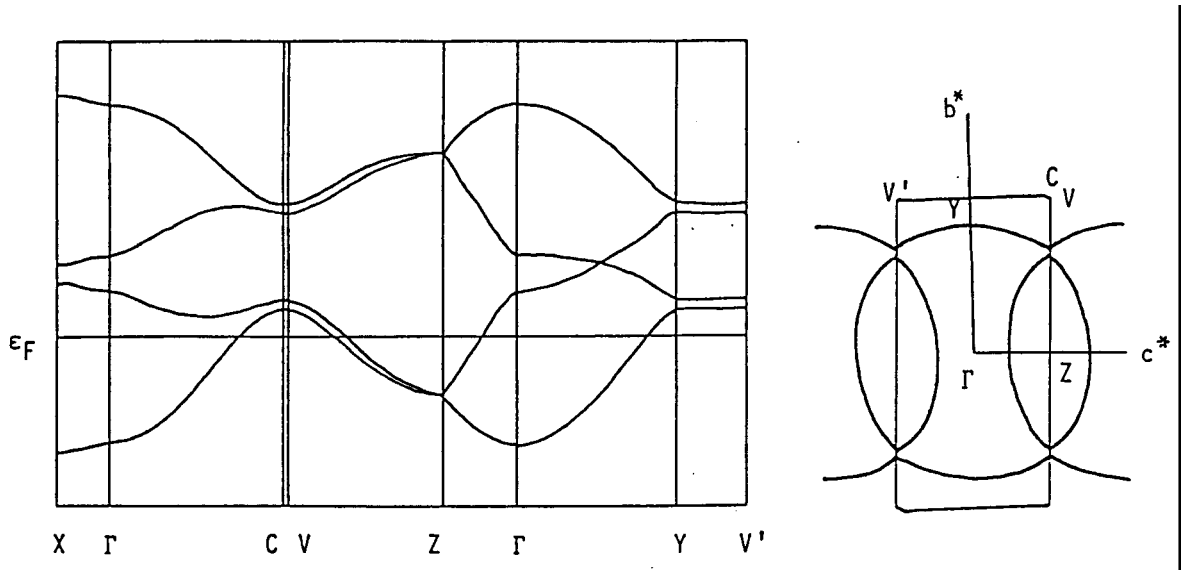

Fig. 7.2. The tight-binding band structure and Fermi surface of α-$Et_2Me_2N[Ni(dmit)_2]_2$ inferred from the intermolecular LUMO overlap calculations using the room temperature structure [1].

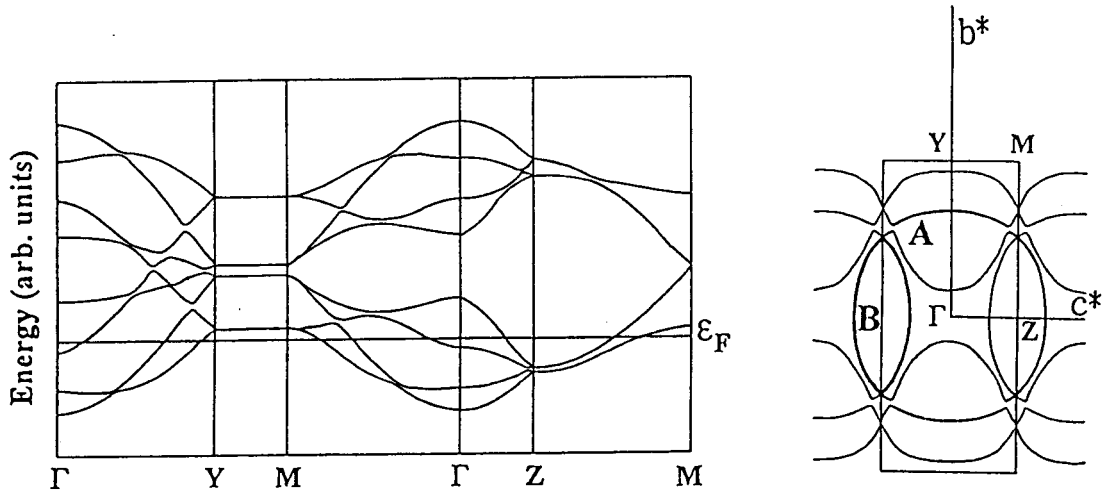

Fig. 7.3. The tight-binding band structure and Fermi surface of α-$Et_2Me_2N[Ni(dmit)_2]_2$ inferred from the intermolecular LUMO overlap calculations using the crystal structure at 11 K [2]. The doubled periodicity along the *b*-axis is omitted for simplicity.

only by the face-to-face overlapping most favored by planar π-molecules. Similar molecular packing is also found for α-$(C_7H_{16}N)[Ni(dmit)_2]_2$, where $C_7H_{16}N^+$ is piperidinium cation [3].

However, the recent low temperature X-ray study has revealed that the crystal structure below the phase transition at 240 K is more complicated than that at room temperature [2]. The phase transition is associated with an ordering of $Et_2Me_2N^+$ cations and changes in the locations of $[Ni(dmit)_2]$. The low temperature structure includes two independent $[Ni(dmit)_2]$ layers arranged alternately along the *a*-axis. Though the molecular arrangement in each layer still includes the spanning overlap modes and is similar to that of the room temperature structure, the band structure and the Fermi surface are modified into those shown in Fig. 7.3 [2]. This low-temperature band structure can explain several features of the recent measurements of the magnetoresistance and the Shubnikov-de Haas effect [4,5].

The main purpose of this study is the experimental examination of the two-dimensional electronic structure of this material and the estimation of the transfer integral corresponding to the spanning overlap. For this purpose, the anisotropy of the intensities of intraband transitions can be used. The analysis of the optical properties may be involved due to the complicated low temperature structure. Nevertheless, it is interesting to examine what information is provided by the optical measurements applied to such a complicated situation.

7.2. Experimental

The single crystals of α-$Et_2Me_2N[Ni(dmit)_2]_2$ are provided by Prof. H. Kobayashi (Toho Univ.), Prof. A. Kobayashi (Univ. of Tokyo) and Prof. R. Kato (Univ. of Tokyo). Galvanostatic electrochemical oxidation of $Et_2Me_2N[Ni(dmit)_2]$, in an acetonitrile-acetone (1:1) solution containing $Et_2Me_2NClO_4$ as supporting electrolyte, yielded black plate single crystals. Polarized reflectance spectra were measured on the (100) crystal face, by the methods described in Sec. 3.1, with the light polarization, $\boldsymbol{E} \parallel \boldsymbol{b}$ and $\boldsymbol{E} \parallel \boldsymbol{c}$, which are the principal axes within the (100) plane. The crystal axes were identified by X-ray oscillation photographs.

7.3. Results and Discussion

Figure 7.4 shows the reflectance spectra measured at room temperature, 200 K, 100 K and 25 K. The spectra clearly show the two-dimensionality of this salt, with the plasma edges appearing around 2000 cm^{-1} for $\boldsymbol{E} \parallel \boldsymbol{b}$ and 4000 cm^{-1} for $\boldsymbol{E} \parallel \boldsymbol{c}$. As is expected for metals, the plasma edges become sharper with decreasing temperature accompanied by the increase in reflectivity at low wavenumbers. No significant change was observed on the Drude-like spectral shape at low wavenumbers in the cooling through the phase transition. However, non-Drude features grew around 4000 cm^{-1} with lowering temperature, which can be seen as small humps in the reflectance spectra.

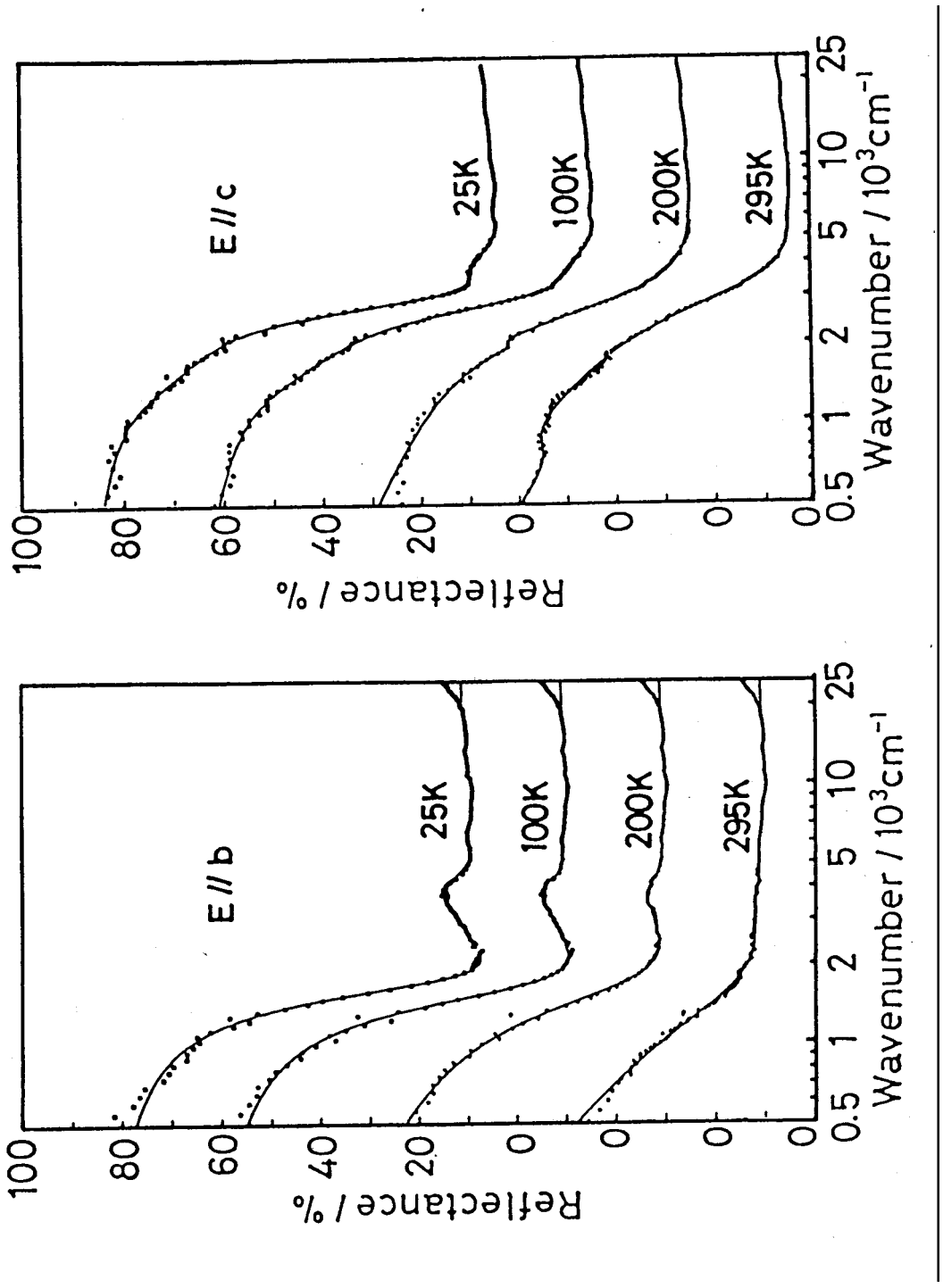

Fig. 7.4. Reflectance spectra of α-$Et_2Me_2N[Ni(dmit)_2]_2$. Solid curves shows the fit to the Drude-Lorentz model.

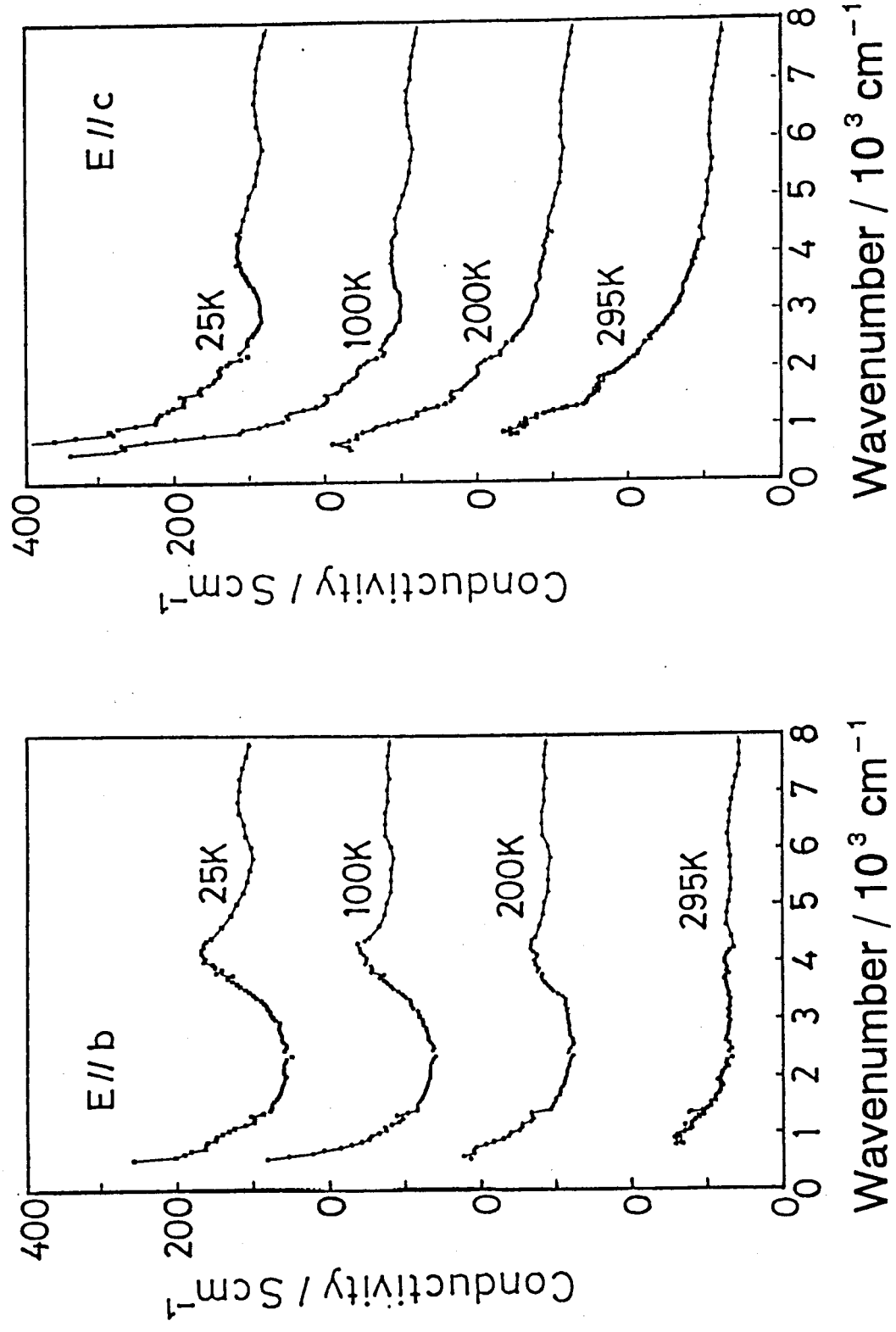

Fig. 7.5. Conductivity spectra of α-$Et_2Me_2N[Ni(dmit)_2]_2$.

The deviation from the Drude behavior indicates the presence of the contribution of the interband transitions across band gaps. In fact, broad maxima corresponding to the humps can be recognized around 4000 cm^{-1} and around 7000 cm^{-1} for both polarizations in the conductivity spectra, which were obtained by the Kramers-Kronig analysis of the reflectance spectra (Fig. 7.5). The contribution of the interband transitions is relatively small, particularly at room temperature. This is in contrast to the spectral features of the dimeric κ-type BEDT-TTF salts (see Chap. 5) [6], in spite of the resemblance of the shape of the Fermi surface (Fig. 7.2). From this it follows that the dimeric character in α-$Et_2Me_2N[Ni(dmit)_2]_2$ is not remarkable from the viewpoint of the electronic structure. In other words, at least one of the interdimer transfer integrals, such as the spanning overlap one, is comparable to the intradimer one. The increase in the intensities of the interband transitions with decreasing temperature, on the other hand, suggests a gradual structural change such that modifies the character of the electronic structure, and may be related to the relative displacement of the $[Ni(dmit)_2]$ molecules shown by the low temperature X-ray study [2].

In order to extract the contribution of the intraband transitions (the Drude terms), a curve-fitting analysis of the reflectance spectra was carried out, on the basis of the Drude-Lorentz dielectric function,

$$\varepsilon(\omega) = \varepsilon_C - \omega_P^2 / (\omega^2 + i\omega / \tau) + \sum_{j=1}^{1 \text{ or } 2} f_j / [(\omega_j^2 - \omega^2) - i\gamma_j\omega] . \qquad (7.1)$$

The first term in the right-hand side of Eq.(7.1), the Drude term, describes

the intraband transitions. The second term stands for the interband transitions corresponding to the conductivity maxima. The reflectivity is related to dielectric function by the equation,

$$R = [1 + |\varepsilon| - \sqrt{2(|\varepsilon| + \mathrm{Re}(\varepsilon))}\,] / [1 + |\varepsilon| + \sqrt{2(|\varepsilon| + \mathrm{Re}(\varepsilon))}\,] . \tag{7.2}$$

The obtained parameters are summarized in Table 7.I. The solid curves in Fig. 7.4 stand for the calculated spectra based on these parameters. The fitting results are much less reliable for the room temperature data because of the overdamped (small τ) shape of the plasma edges.

If we consider only the two dominant transfer integrals, t_1 and t_2, within the [Ni(dmit)$_2$] layer, the band structure can be explicitly expressed as the form,

$$E(k_b, k_c) = \pm [t_1^{\,2} + 4t_2^{\,2}\cos^2(b \cdot k_b / 2) \pm 4t_1 t_2 \cos(c \cdot k_c / 2)\cos(b \cdot k_b / 2)]^{1/2}, \tag{7.3}$$

where t_1 is the intradimer transfer integral and t_2 is that corresponds to the spanning overlap. For the lower branches, which concern the Fermi surface, only the case of $E(k_b, k_c) < 0$ should be considered. The situation described by this model is schematically illustrated in Fig. 7.6. This band model brings about the degeneracy at the boundaries of the first Brillouin zone, in accord with the assumed high symmetry.

The squares of the obtained plasma frequencies, $\omega_p^{\,2}$, can be calculated from this band structure described by t_1 and t_2. That is to say,

Table 7.I. Drude parameters obtained by the Drude-Lorentz fit of the reflectance spectra

Polarization	*T* / K	ε_c	ω_p / eV	τ^{-1} / eV
// *b*	295	4.0	0.51	0.27
	100	4.2	0.52	0.077
	25	4.1	0.52	0.061
// *c*	295	1.2 [a)]	0.67	0.26
	100	3.1	0.73	0.082
	25	3.1	0.73	0.065

a) In the fitting of this spectrum, the near-infrared line-shape used is different from those of the other cases. This results in the small value of ε_c.

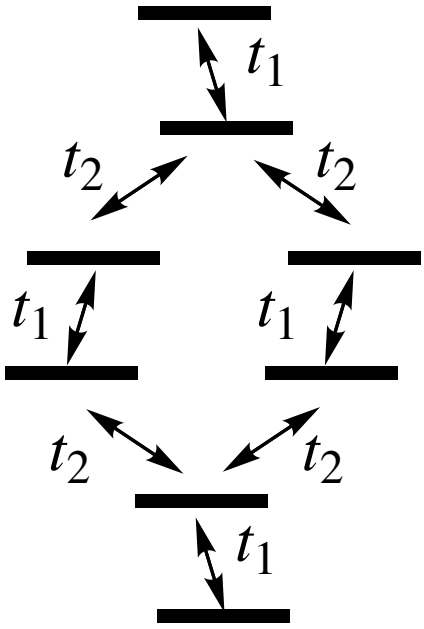

Fig. 7.6. Schematic display of the two dominant intermolecular interactions in the conduction layer of α-$Et_2Me_2N[Ni(dmit)_2]_2$. The spanning overlap corresponds to t_2.

$$(\omega_p^2)_b = 2\,(e^2/\pi^2\hbar)\,(2\pi/a\sin\beta)\int |(v_F)_b|\,dk_{Fc}\,, \qquad (7.4)$$

$$(\omega_p^2)_c = 2\,(e^2/\pi^2\hbar)\,(2\pi/a\sin\beta)\int |(v_F)_c|\,dk_{Fb}\,, \qquad (7.5)$$

where $(v_F)_b$ and $(v_F)_c$ are the *b*- and *c*-components of the Fermi velocity, $\boldsymbol{v}_F$, given as

$$\boldsymbol{v}_F = \hbar^{-1}\,\mathrm{grad}_{\boldsymbol{k}}\,E(t_1, t_2; k_b, k_c)\;;\quad E = E_F\,. \qquad (7.6)$$

Half-filling over the lower two branches, i.e., 1/4-filling for the overall LUMO band, is assumed so as to satisfy the requirement of stoichiometry. This determines the Fermi energy E_F. By use of these equations, the optimal set of t_1 and t_2 which reproduce the observed plasma frequencies were searched. For example, when the values, $(\omega_p)_b$ = 0.67 eV and $(\omega_p)_c$ = 0.52 eV, at room temperature are used together with the lattice constants at room temperature, a = 38.95 Å, b = 6.494 Å, c = 13.835 Å and β = 99.63 ˚ , the transfer integrals are estimated to be t_1 = 0.09 eV and t_2 = 0.11 eV. As was expected from the spectral features, the intra- and interdimer interactions are comparable to each other.

Before applying this method to the low temperature spectra, the effect of the structural phase transition [2] should be considered. A possible interpretation of the low temperature Fermi surface is as follows. There are two independent [Ni(dmit)$_2$] layers, between which only very weak interlayer interactions are found. Each layer, having a similar structural character, forms each two-dimensional band. However, the

difference in the position and width between these bands split the degenerate Fermi surface into the larger and smaller ones. Moreover, the larger Fermi surface changes its topology into the one open along the *c*-axis due to the reconstruction around the Γ point, while the small one almost retains its original topology. This situation is depicted in Fig. 7.7, where the solid and dotted lines show the smaller closed Fermi surface and the larger open one, respectively, and the doubled periodicity along the *b*-axis is omitted for simplicity. The magnetoresistance and SdH results have been interpreted in terms of the small Fermi surface [5].

It seems quite natural to regard the observed optical properties at low temperatures as the average of the large and small Fermi surface. If this is the case, the analysis of the optical data should yield an intermediate shape of the Fermi surface between the two. By use of the values at 25 K, $(\omega_p)_b$ = 0.73 eV and $(\omega_p)_c$ = 0.52 eV, and the lattice constants at 11 K, a = 37.499 Å, b = 6.444 Å, c = 13.718 Å and β = 92.69 ˚ , the transfer integrals were estimated to be $\langle t_1 \rangle$ = 0.12 eV and $\langle t_2 \rangle$ = 0.10 eV from the same method as above, where the brackets denote the average over the two different [Ni(dmit)$_2$] layers. Figure 7.8 shows the band structure and the Fermi surface based on these average values.

The validity of this estimation can be checked by the comparison with the results of the SdH and magnetoresistance oscillations. The cyclotron mass for the small Fermi surface connected by the magnetic breakdown effect has been reported to be m^*_c = 4.3 ± 0.2 m_e, with the corresponding cross-sectional area of 85.9 % of the first Brillouin zone [4,5]. The cyclotron mass can be calculated also for the average Fermi surface based on the optical results, by use of the relation,

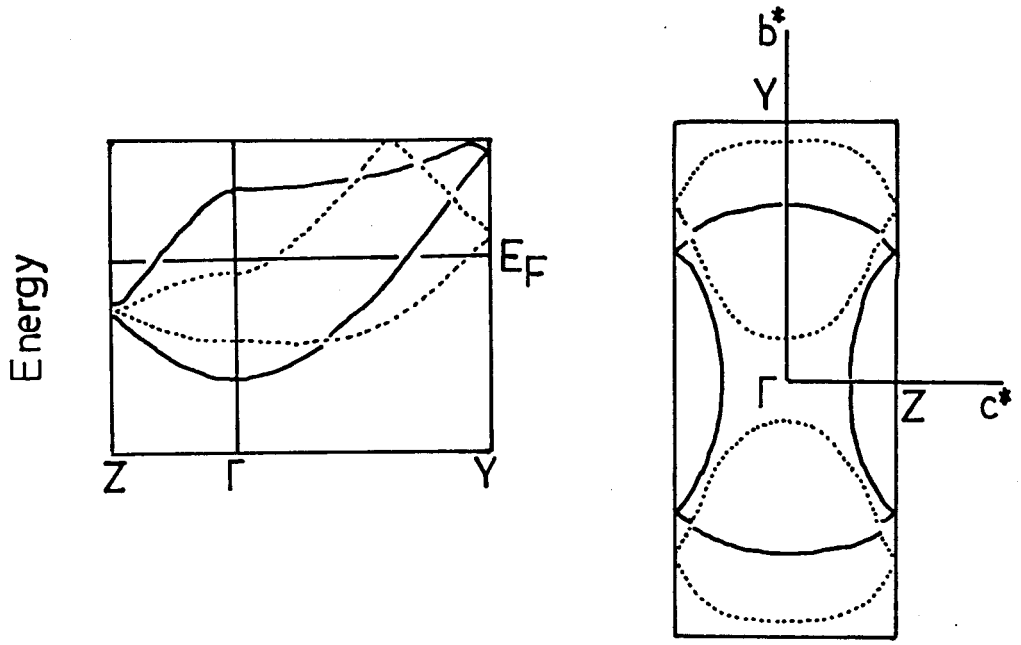

Fig. 7.7. The band structure and Fermi surface split due to the structural transition. A possible assignment of the character is indicated by the solid and dotted lines. Only the lower half of the LUMO band is shown.

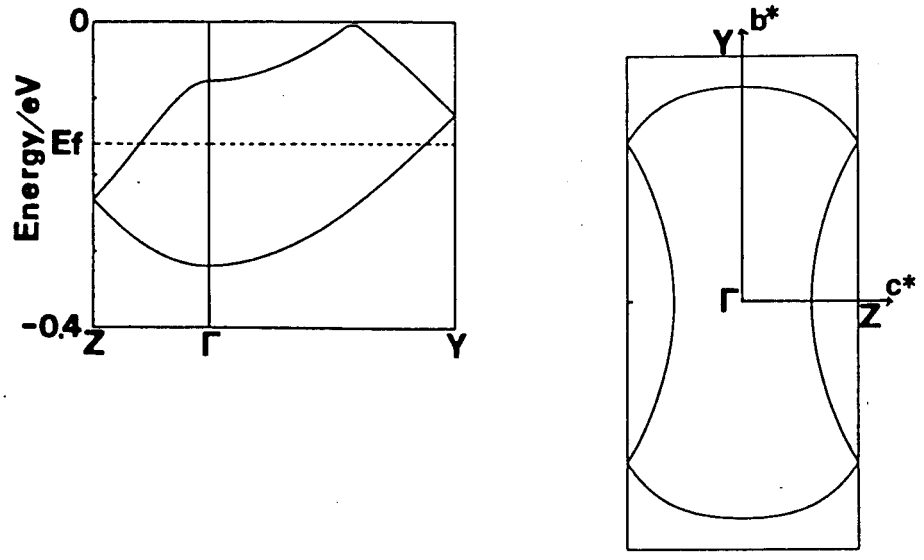

Fig. 7.8. The average band structure and Fermi surface inferred from the optical data at 25 K.

$$\langle m^*_c \rangle = (\hbar^2 / 2\pi)\,(dS / dE)\ ; \qquad E = E_F\ , \tag{7.7}$$

where S is the cross-sectional area. This yields $\langle m^*_c \rangle = 4.3\ m_e$, which coincides with the observed cyclotron mass for the smaller Fermi surface. Note that the cross-sectional area is assumed to be 100 % in the analysis of the optical data. The optical results would give the cyclotron mass for the smaller Fermi surface slightly less than $\langle m^*_c \rangle = 4.3\ m_e$, because the smaller Fermi surface corresponds to the wider band according to Fig. 7.7. Considering the simplicity of the approximation made for such a complicated low temperature Fermi surface, this result does not seem to be inconsistent with the observed cyclotron mass. The origin of the difference may be attributed to the modified topology of the large Fermi surface around the Γ point (Fig. 7.7).

Next, the value of the Fermi wavenumber inferred from the angle dependent magnetoresistance oscillation is considered. For the diameter of the closed portion of the small Fermi surface around the Z point, 0.29 b^* along the c-axis, is suggested by the magnetoresistance results [5]. The corresponding value for the average Fermi surface should be slightly larger, and calculated to be 0.32 b^* from the optical results. This result is satisfactory.

7.4. Conclusion

The present results can be regarded as the estimation of the averaged geometry of the multiple Fermi surfaces emerging from the two independent

[$Ni(dmit)_2$] layers. The transfer integrals estimated from the low temperature data should be the average of the corresponding ones over the independent layers. The present study well illustrates the nature of the optical investigation of the Fermi surface using the intraband transitions. The intraband transitions are less sensitive to the detailed features of the Fermi surface as in the low temperature one in this case. Nevertheless, they efficiently reflect the global and overall geometry of the Fermi surface and always afford the satisfactory estimation of the basic dimensionality of a metal, whatever the detailed structure of the Fermi surface is.

References

1. R. Kato, H. Kobayashi, H. Kim, A. Kobayashi, Y. Sasaki, T. Mori, H. Inokuchi: Chem. Lett. 865 (1988).
2. A. Kobayashi, T. Naito and H. Kobayashi: Phys. Rev. **B**, in press.
3. H. Kobayashi, R. Kato, A. Kobayashi: Synth. Metals **41-43** (1991) 2495.
4. H. Tajima, S. Ikeda, M. Inokuchi, A. Kobayashi, T. Ohta, T. Sasaki, N. Toyota, R. Kato, H. Kobayashi and H. Kuroda: Solid State Commun. **88** (1993) 605.
5. H. Tajima, S. Ikeda, M. Inokuchi, A. Kobayashi, T. Ohta, T. Sasaki, N. Toyota, R. Kato, H. Kobayashi and H. Kuroda: Synth. Metals, in press.
6. For example, see: M. Tamura, H. Tajima, K. Yakushi, H. Kuroda, A. Kobayashi, R. Kato and H. Kobayashi: J. Phys. Soc. Jpn. **60** (1991) 3861.

Chapter 8.

Reflectance Spectra of κ-$(DMET)_2AuBr_2$

8.1. Introduction

An organic π-donor, DMET (dimethyl(ethylenedithio)diselenadithiafulvalene) is the hybrid molecule between TMTSF and BEDT-TTF as shown in Fig. 8.1. The TMTSF salts are the first family of organic superconductors [1,2]. They favor a quasi-one-dimensional structure and have spin-density-wave phase at low temperature [2,3]. In contrast to them, a variety of two-dimensional molecular pickings are found in the BEDT-TTF family [4]. The DMET family salts were synthesized with the expectation that they can fill the gap between the TMTSF and BEDT-TTF families [5]. In fact, the DMET family includes both a quasi-one-dimensional conductor similar to the TMTSF salts and a two-dimensional conductor similar to the BEDT-TTF salts [6-12]. The DMET family has afforded 7 superconductors, for the first time as radical salt based on a non-symmetric molecule.

The salts, $(DMET)_2AuBr_2$, crystallizes at least in two different modifications [13,14]. The crystals of κ-$(DMET)_2AuBr_2$ can be categorized into two groups, r_1 and r_2, by the difference in the electric properties (Fig. 8.2) [14]. Both show a resistivity maximum around 150 K (= T_{max}). Around this maximum, only the r_1 crystals exhibit an "anti-hysteresis" [14]. The r_2 crystal is an ambient pressure superconductor with the transition temperature T_c = 1.9 K, while the r_1 ones are metallic down to 0.5 K without superconductivity [14]. In spite of these differences, the crystal structures of the r_1 and r_2 samples are substantially the same. A crystal of the r_2 type is picked up in this study. The crystal structure is the so-called κ-type one, with the space group $P2_1/a$, in which dimers of

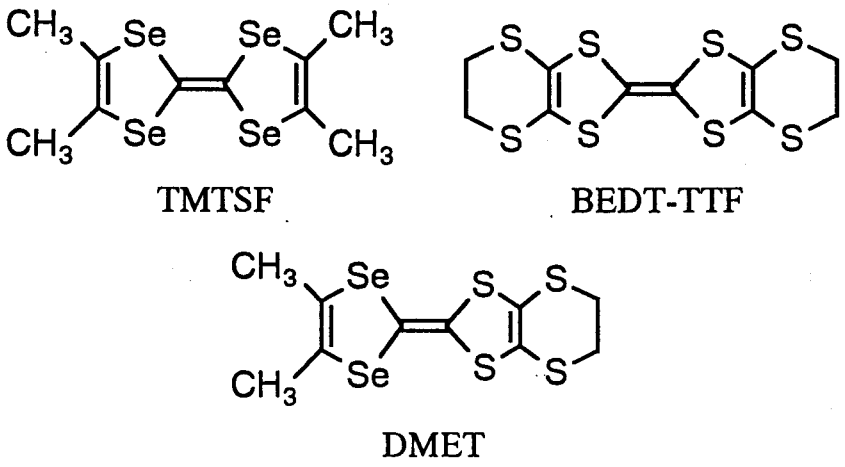

Fig. 8.1. Chemical Structures of TMTSF (tetramethyltetraselenafulvalene), BEDT-TTF (bis(ethylendithio)tetrathiafulvalene), DMET (dimethyl(ethylenedithio)diselenadithiafulvalene).

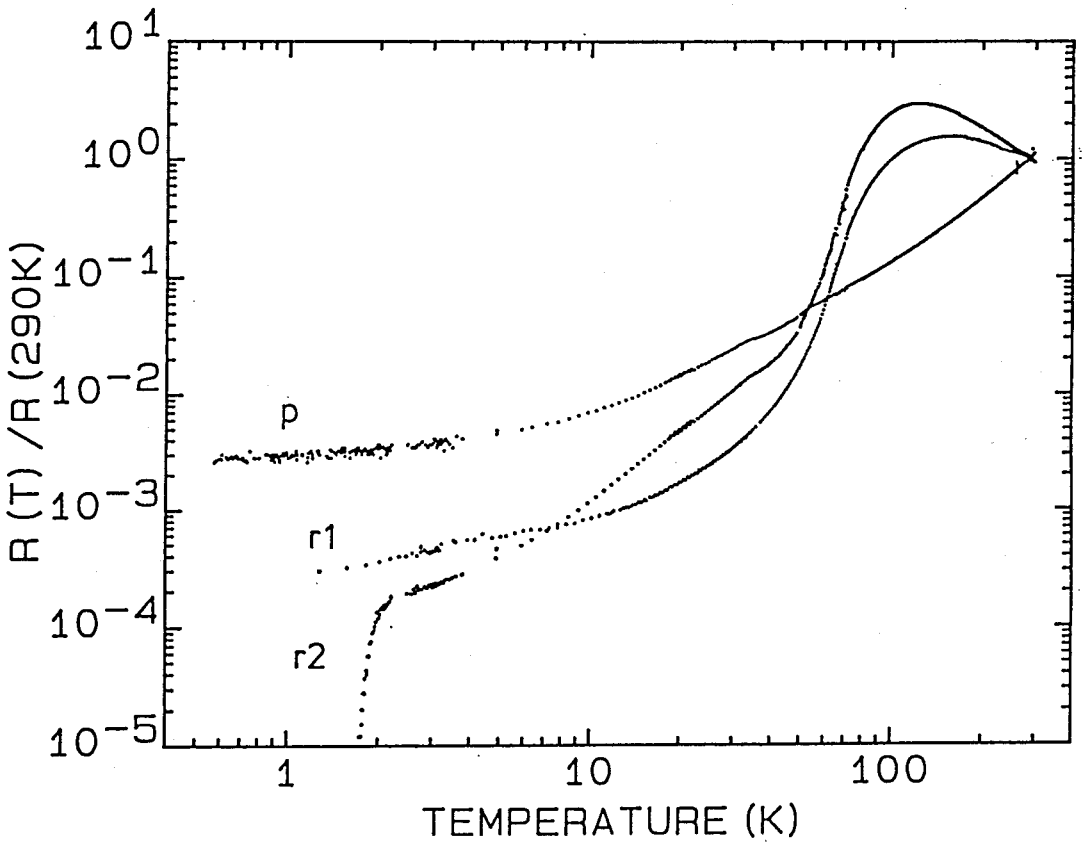

Fig. 8.2. Temperature dependence of electric resistivity of the three types of $(DMET)_2AuBr_2$. The types, p1 and p2, belong to κ-$(DMET)_2AuBr_2$.

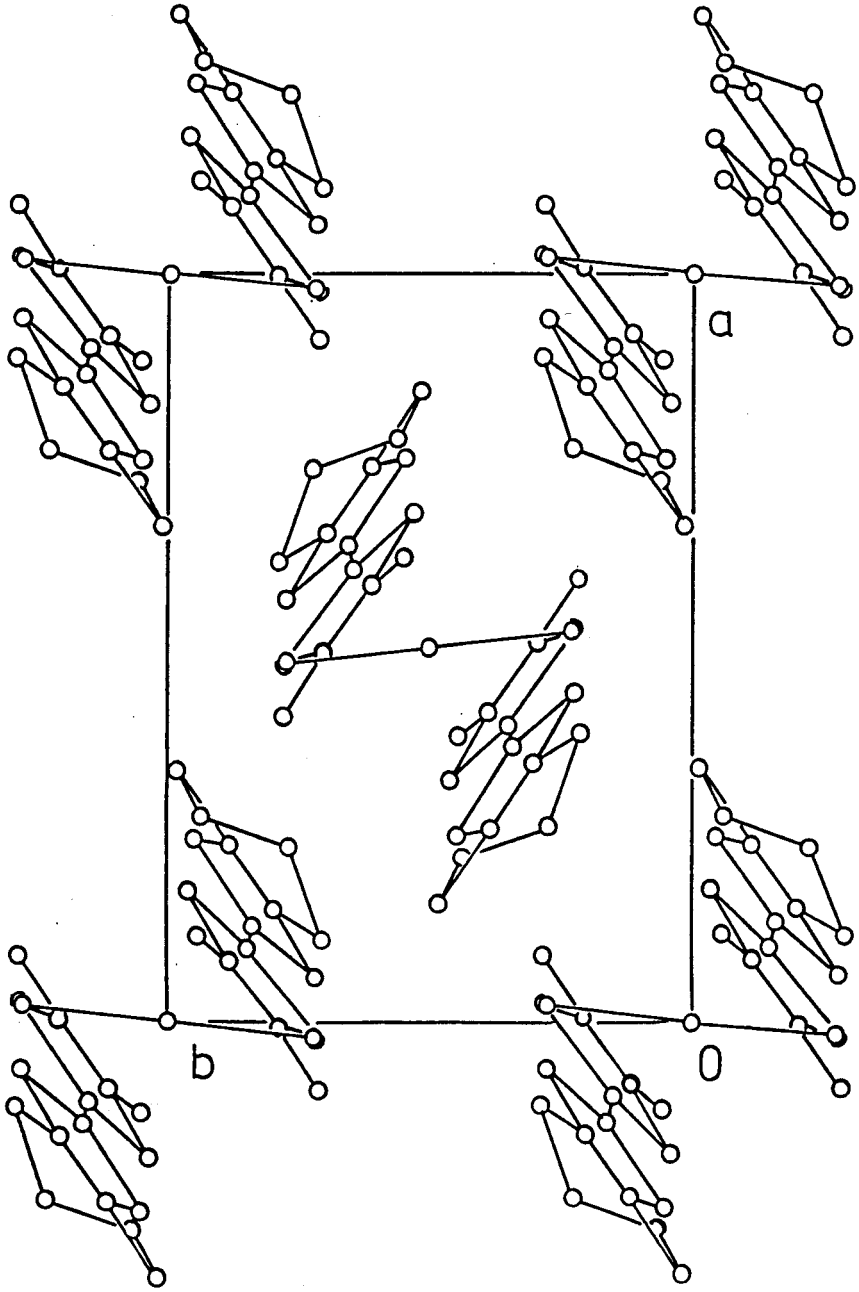

Fig. 8.3. Crystal structure of κ-(DMET) $_2$AuBr$_2$ projected on to the *ab*-plane.

DMET molecules are arranged to form a two-dimensional packing within the *ab*-plane (Fig. 8.3) [14]. In the dimer, molecules are related to each other by the inversion symmetry.

In this study, the difference between the optical properties above T_{max} and those below T_{max} is first focused on. Second, the intensities of the intraband transitions at low temperature are analyzed in order to estimate the electronic structure. The results are compared with the dHvA experiments. A comparison with the BEDT-TTF salts is also given.

8.2. Experimental

Single crystals of κ-$(DMET)_2AuBr_2$ were provided by Prof. Kikuchi (Tokyo Metropolitan Univ.). The crystals were grown by electrochemical oxidation of DMET in chlorobenzene with $(n\text{-}C_4H_9)_4NAuBr_2$ as a supporting electrolyte [13]. The most developed crystal face is the (001) one, with a rhombus-like shape. The reflectance spectra were measured on this face, with the light polarization $\boldsymbol{E} \parallel \boldsymbol{a}$ and $\boldsymbol{E} \parallel \boldsymbol{b}$, i.e., parallel to the two principal axes within the *ab*-plane. The crystal axes were identified by X-ray oscillation photographs. The measurements of the spectra were carried out by following the method described in Sec. 3.1.

8.3. Results

8.3.1. Spectral Aspects

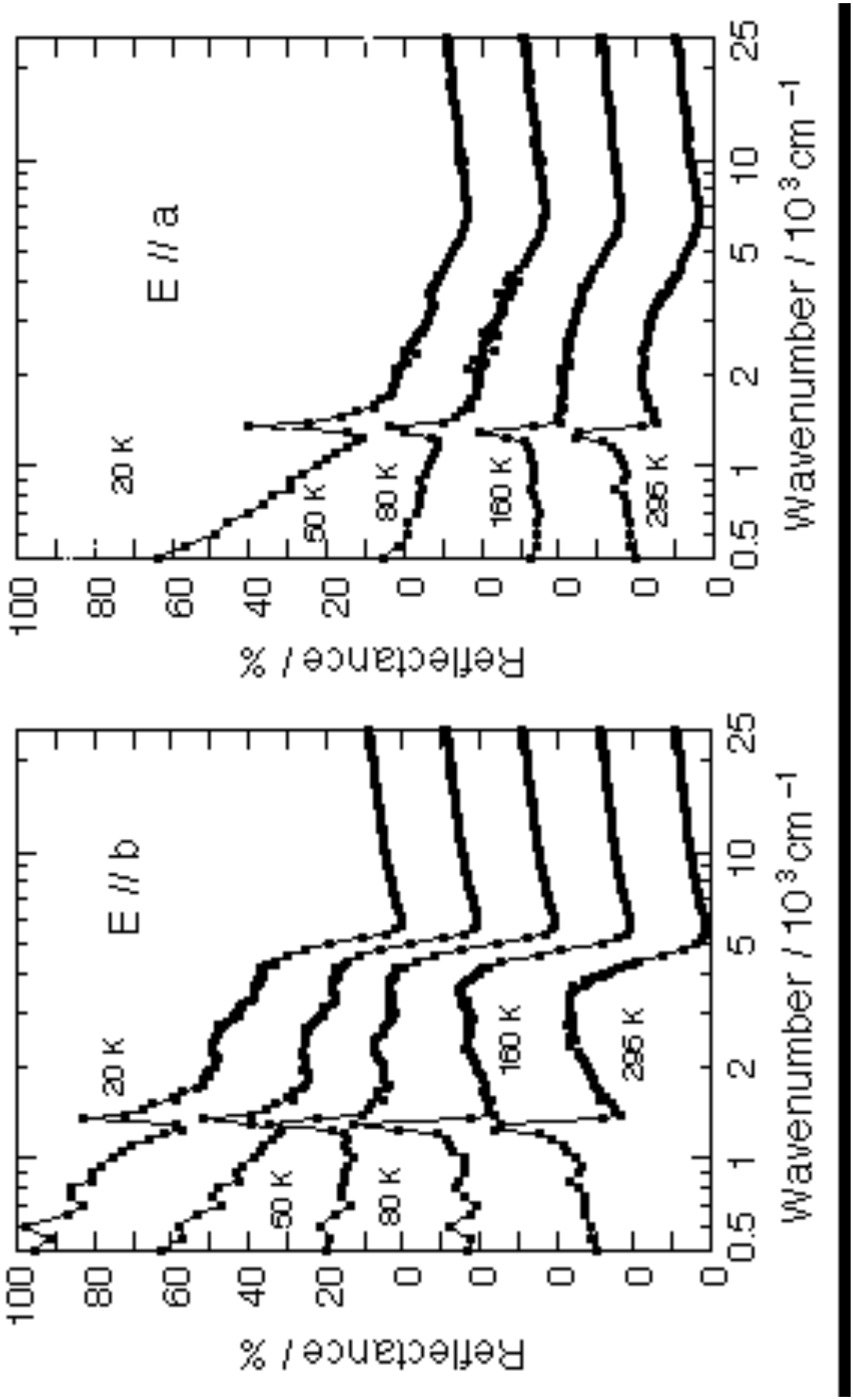

Fig. 8.4. Reflectance spectra of κ-$(DMET)_2AuBr_2$.

Figure 8.4 shows the reflectance spectra measured at room temperature, 160 K, 80 K, 50 K and 20 K. The overall spectral shapes are similar to those of the κ-type BEDT-TTF salts [15]; there are remarkable deviations from the Drude behavior, i.e., the humps around 3000 cm^{-1} and the prominent peaks at about 1300 cm^{-1}. As we have pointed out in the cases of dimeric BEDT-TTF salts [15], this non-Drude behavior is ascribable to the strong interband transitions stemming from the dimeric structure of the donor molecule. The structures around 3000 cm^{-1} is attributable to the interband transitions, whose character is close to that of the intradimer transitions. The peaks at about 1300 cm^{-1} are considered to be due to the electron-molecular-vibration coupling corresponding to C=C stretching modes. This can be induced by the interband transitions.

At room temperature and 160 K, that is, above T_{max}, the reflectivity is constant or slightly decreasing below 1000 cm^{-1} towards low wavenumber. This suggests that the intraband transitions are considerably suppressed. On the other hand, at 80 K, 50 K and 20 K, the reflectivity increases below 1000 cm^{-1} towards low wavenumber, indicating the contribution of the intraband transitions. Figure 8.5 shows the conductivity spectra obtained by the Kramers-Kronig analysis of the reflectance spectra. Above T_{max}, the conductivity seems to decrease rapidly towards zero when zero wavenumber is approached, indicating the absence of the intraband transitions. Below T_{max}, the conductivity value extrapolated to zero wavenumber does not seem to drop to zero. Thus, the optical properties above and below T_{max} are in remarkable contrast. These features are consistent with the dc resistivity behavior. This indicates that the change in the electronic properties through the resistivity maximum concerns not only

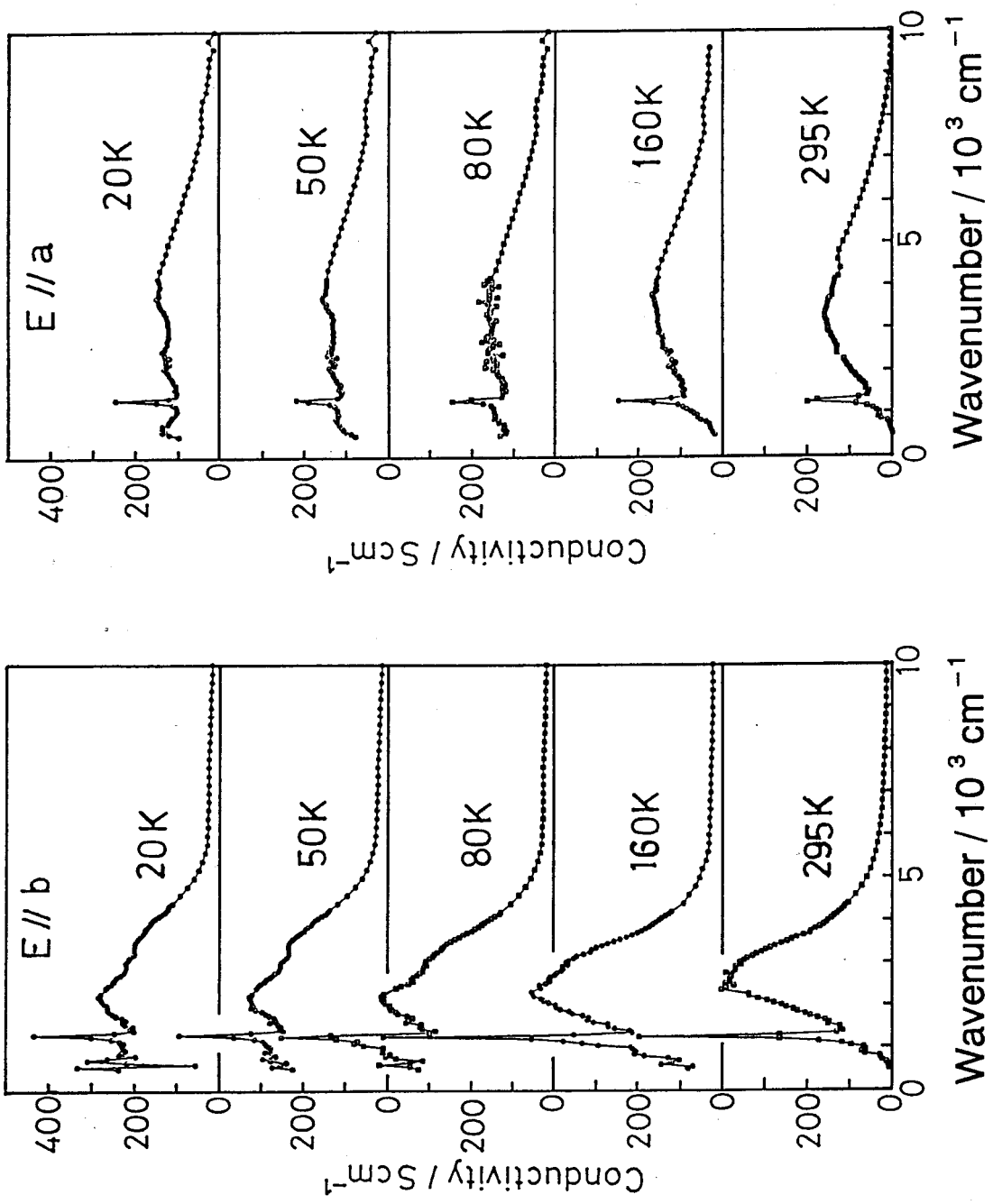

Fig. 8.5. Conductivity spectra of κ-$(DMET)_2AuBr_2$.

the states just near the Fermi level but also those lying over the energy width of, at least, 0.1 eV.

Another noticeable point is the splitting of the broad peaks of the interband transitions below T_{max} (Fig. 8.5). This is observed both for the $\boldsymbol{E} \parallel \boldsymbol{a}$ and $\boldsymbol{E} \parallel \boldsymbol{b}$ spectra, and is evident also in the reflectance spectra (Fig. 8.4). The splitting width seems to increase with decreasing temperature. A similar splitting was reported also for α-(BEDT-TTF)$_2$I$_3$ [16]. However, the origin should be different, because the splitting in α-(BEDT-TTF)$_2$I$_3$ accompanies the transition to the low temperature insulating phase; the splitting in κ-(DMET)$_2$AuBr$_2$ appears when the material becomes metallic. Moreover, as is noticed by the first order character of the metal-insulator transition of α-(BEDT-TTF)$_2$I$_3$, the appearance of the splitting can be related to the structural change, whereas no structural phase transition has been found in κ-(DMET)$_2$AuBr$_2$. Further discussion about this splitting will be given below in connection with the non-metallic resistivity behavior above T_{max}.

8.3.2. Estimation of Band Structure

In order to extract the intensities of the interband transitions at low temperature, a curve-fitting analysis based on the Drude-Lorentz model,

$$\varepsilon(\omega) = \varepsilon_C - \omega_P^2 / (\omega^2 + i\omega / \tau) + \sum_{j=1}^{3 \text{ or } 4} f_j / [(\omega_j^2 - \omega^2) - i\gamma_j \omega] . \qquad (8.1)$$

was carried out. The reflectivity is related to dielectric function by the equation,

Table 8.I. Drude parameters at 20 K obtained by the Drude-Lorentz fit of the reflectance spectra.

Polarization	ε_c	ω_p / eV	τ^{-1} / eV
// *b*	3.3	0.72	0.035
// *a*	3.2	0.48	0.061

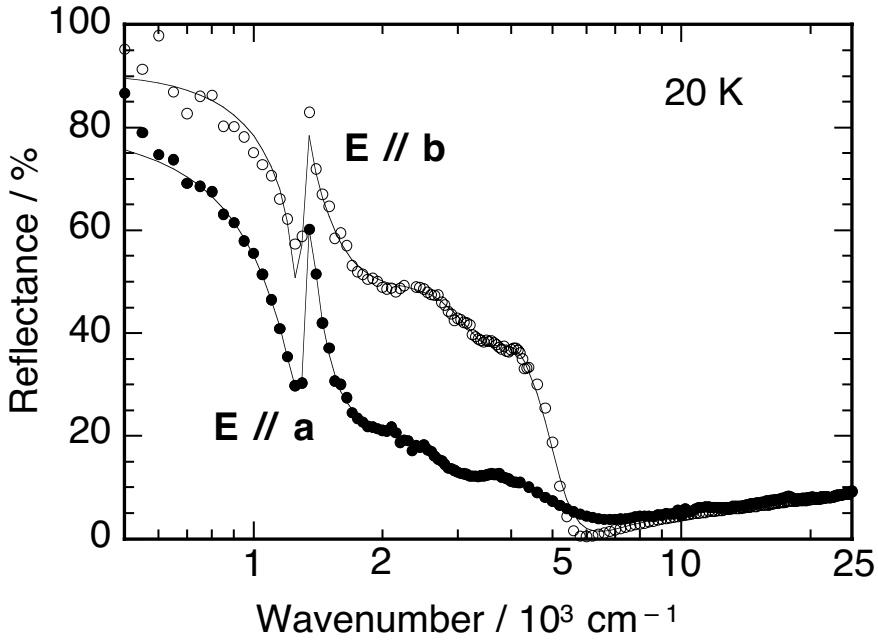

Fig. 8.6. Reflectance spectra at 20 K. Solid curves shows the fit to the Drude-Lorentz model.

$$R = [1 + |\varepsilon| - \sqrt{2(|\varepsilon| + \mathrm{Re}(\varepsilon))}\,] / [1 + |\varepsilon| + \sqrt{2(|\varepsilon| + \mathrm{Re}(\varepsilon))}\,] \,. \quad (8.2)$$

The first term in the right-hand side of Eq.(8.1) stands for the constant contribution from the higher energy transitions outside the experimental spectral region. The second term, the Drude term, gives the contribution of the intraband transition. The third term describes the contribution of other transitions: the interband transitions, the e-mv coupling modes. We empirically expressed the interband transition as a superposition of two Lorentzian oscillators to describe the split shape of the interband transition. The relatively small contributions of the intraband transitions, as compared with those of the interband ones, result in less satisfactory convergence of the fitting, particularly for the 80 K and 50 K data. For the 20 K spectra, the curve-fitting results were shown as the solid curves in Fig. 8.6, together with the observed data points. The obtained parameters related to the intraband transitions were compiled in Table 8.I.

The same method which was applied to the case of κ-(BEDT-TTF)$_2$I$_3$ (see Chap. 5) [15], is applicable again to the estimation of the band structure of this material, because of the symmetry of the packing of dimers. This method is based on the two effective interdimer transfer integrals, t_a and t_b , which describe the band structure near the Fermi surface. The definition of them is given in Fig. 8.7. In this method, the conduction bands are regarded as those formed from the anti-bonding state of the dimer; the effective Hamiltonian, which is derived by treating the interdimer transfer integrals as perturbation to the energy splitting due to the strong intradimer interactions, is used to describe the band structure.

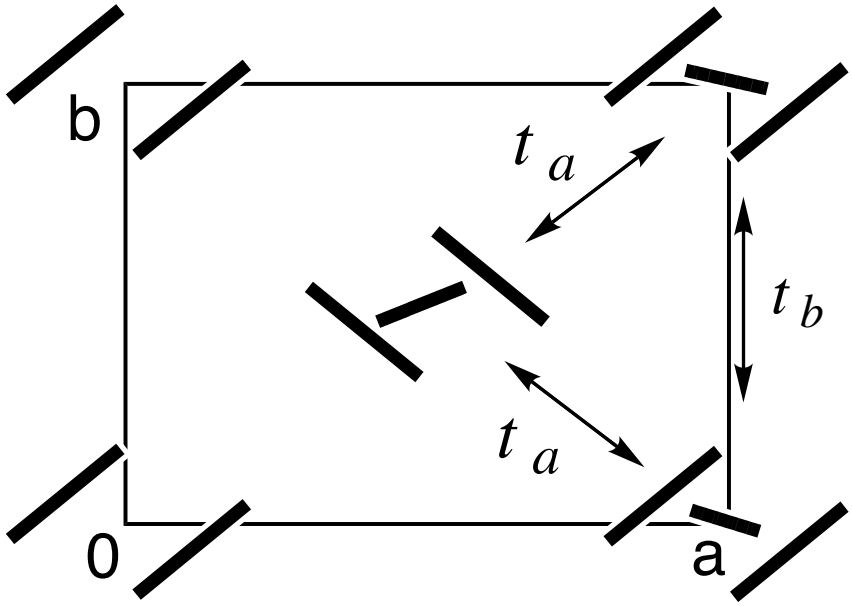

Fig. 8.7. Schematic display of the effective interdimer interactions.

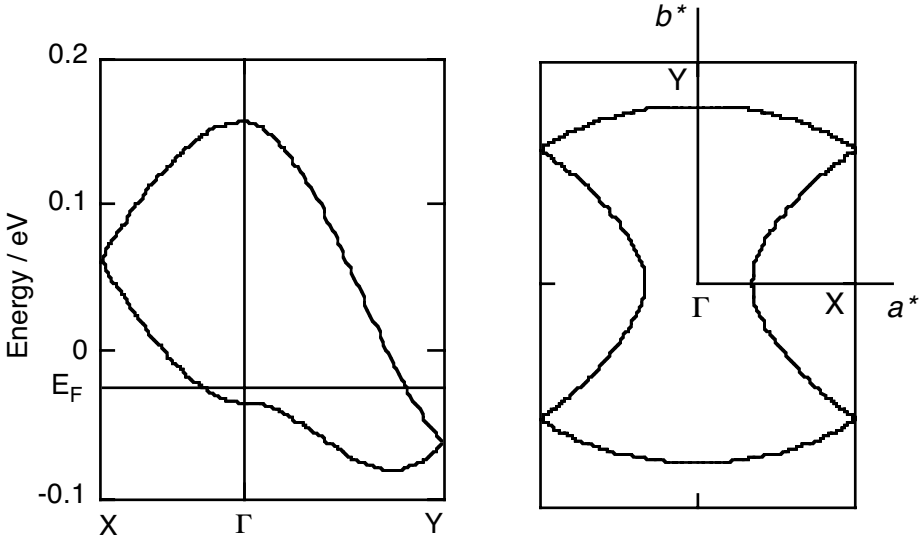

Fig. 8.8. The band strcuture and the Fermi surface estimated from the optical data at 20 K.

The band structure is expressed as,

$$E(k_a, k_b) = 2\, t_b \cos(b \cdot k_b) \pm 4\, t_a \cos(a \cdot k_a / 2) \cos(b \cdot k_b / 2)\ . \quad (8.3)$$

When the intraband plasma frequency values at 20 K given in Table 8.I are used together with the lattice parameters at room temperature, a = 11.542, b = 8.238, c = 16.168 Å and β = 90.99 ˚, the two transfer integrals are estimated to be t_a = 0.024 eV and t_b = 0.031 eV. The band structure and the shape of the Fermi surface calculated by use of these parameters are displayed in Fig. 8.8.

The results are compared with the those of the dHvA experiments [17], in order to check the validity. From the above band structure inferred from the optical data, the values of the cyclotron mass and the cross-sectional area can be calculated both for the large and small cyclotron orbits (marked by the α and β, in Fig. 8.8) detected in the dHvA experiments. The cyclotron masses for the α and β orbits are calculated to be $m^*_{\alpha}{}^{opt}$ = 3.4 m_e and $m^*_{\beta}{}^{opt}$ = 5.6 m_e, respectively, from the optical results. The corresponding values deduced from the dHvA results are, $m^*_{\alpha}{}^{dHvA}$ = 3.8 m_e and $m^*_{\beta}{}^{dHvA}$ = 6.0 m_e [17]. The agreement is satisfactory. The cross-sectional area for the β orbit should be 100 % of the first Brillouin zone, in both results. The α orbit has the cross-sectional area of 26 % of the first Brillouin zone according to the dHvA optical results [17], while the corresponding value from the optical results is 21 %, which is slightly underestimated probably due to the simplification of the band structure using the dimer-based model. However, it can be concluded that the band structure derived from the optical data is consistent with the dHvA

results upon the whole.

It should be noted that the values of the cyclotron mass in κ-$(DMET)_2AuBr_2$ are larger than those of κ-$(BEDT\text{-}TTF)_2I_3$. There are several reports which point out the correlation between the mass-enhancement and high T_c in a series of BEDT-TTF superconductors [18]. The mass-enhancement involves the enhancement of the density of states at the Fermi level. As the origin of the mass-enhancement, the role of the electron correlation has been suggested [18]. The cyclotron mass of κ-$(DMET)_2AuBr_2$ is as heavy as those of a class of BEDT-TTF salts with T_c = ca. 10 K. However, T_c of κ-$(DMET)_2AuBr_2$, 1.9 K, is lower than those of the 10 K class BEDT-TTF superconductors. The mass of κ-$(DMET)_2AuBr_2$ is about twice as heavy as that of κ-$(BEDT\text{-}TTF)_2I_3$, though T_c of the former is about half as low as that of the latter, 3.6 K. From these facts, it follows that not only the mass (and density of states) but also the nature of the molecule is responsible for T_c. This means that the argument on the correlation between the mass and T_c cannot be applied over systems based on different molecules.

8.4. Discussion

Let us return to the temperature dependence of the spectral shape. Usually the absence of the intraband transitions is evidence for the gap opening around the Fermi level. On the other hand, from an ESR study, it is concluded that the spin susceptibility is Pauli-like and insensitive to temperature above 50 K and that the temperature dependence of the ESR

line width well corresponds to that of the dc resistivity [19]. It is suggested from the ESR results that the anomalous non-metallic behavior has a dynamical origin such as some unusual molecular vibrations [19]. In fact, a simple band picture of a metal cannot explain both the absence of the intraband transitions and the Pauli-like susceptibility. It is, therefore, likely to think that the intraband transitions disappear due to some dynamical disorder above T_{max}. In this picture, the coherence of the Bloch wavefunctions is considered to be destroyed by strong inelastic scattering due to the dynamical disorder. Consequently, the mobility and the mean free path of the charge carriers would be suppressed, without drastic change in long-time average of the band structure. The conduction in such a situation should resemble to the hopping one. The seeming optical gap width, below which the optical intraband transitions are suppressed, has been found to amount to about 0.1 eV. Roughly speaking, this is a measure of the characteristic energy of the disorder or of the inelastic scattering. The order of magnitude seems to support the suggestion that the origin of the dynamical effect may be some molecular vibration [19]. In this connection, the broadening of X-ray diffraction peak aroundT_{max} is also suggestive [20].

The splitting of the interband transitions is next focused on. The interband transitions occur mainly across the gaps between the lower doubly split band and the highest branch. Therefore, the splitting in the spectra observed below T_{max} may reflect the splitting of the lower band. If this is the case, the disappearance of the spectral splitting above T_{max} can be explained as follows. According to the uncertainty principle, the dynamical effect above T_{max} removes the physical meaning of the detailed

band structure; only coarse-grained features with the scale of about 0.1 eV can remain. The splitting of the lower band is thus obscured, as well as the spectral splitting.

It should be noted that even the other molecular conductors with no resistivity maximum are close to such a dynamically disordered situation. This is based on the fact the mean free path of the charge carriers is very short. However, an exact and explicit treatment of such a dynamically disordered state of metals has not been established yet. Thus, detailed quantitative analysis of the anomalous behavior is not available.

8.5. Conclusion

The optical properties of κ-$(DMET)_2AuBr_2$ correlate with the anomalous resistivity behavior. The correlation appears not only in low wavenumber region but also the in the spectral shape in the mid-infrared region. This suggests the dynamical origin of the non-metallic behavior of dc resistivity at high temperature. The analysis of the intraband transitions at low temperature yields the band structure and Fermi surface consistent with the dHvA results.

References

1. D. Jérome, A. Mazaud, M. Ribault and K. Bechgaard: J. Physique Lett. **41** (1980) L95-98.

2. K. Bechgaard: Mol. Cryst. Liq. Cryst. **79** (1982) 1.

3. D. Jérome and H. J. Schulz: Adv. Phys. **31** (1982) 299.

4. See for example, *The Physics and Chemistry of Organic Superconductors*, Ed. by G. Saito and S. Kagoshima (Springer, Heidelberg, 1990); *Organic Superconductors: Synthesis, Structure, Properties and Theory*, Ed. by J. M. Williams, J. R. Ferraro, R. J. Thorn, K. D. Carlson, U. Geiser, H. H. Wang, A. M. Kini and M.-H. Whangbo (Prentice Hall, Englewood Cliffs, 1992).

5. K. Kikuchi, I. Ikemoto and K. Kobayashi: Synth. Metals **19** (1986) 551.

6. I. Ikemoto, K. Kikuchi, K. Saito, K. Kanoda, T. Takahashi, K. Murata and K. Kobayashi: Mol. Cryst. Liq. Cryst. **181** (1990) 185.

7. K. Kikuchi, M. Kikuchi, T. Namiki, K. Saito, I. Ikemoto, K. Murata, T. Ishiguro and K. Kobayashi: Chem. Lett. 931 (1987).

8. Y. Nogami, M. Tanaka, S. Kagoshima, K. Kikuchi, K. Saito, I. Ikemoto and K. Kobayashi: J. Phys. Soc. Jpn. **56** (1987) 3783.

9. K. Kanoda, T. Takahashi, T. Tokiwa, K. Kikuchi, K. Saito, I. Ikemoto and K. Kobayashi: Phys. Rev. B **38** (1988) 39.

10. K. Kikuchi, K. Murata, Y. Honda, T. Namiki, K. Saito, T. Ishiguro, K. Kobayashi and I. Ikemoto: J. Phys. Soc. Jpn. **56** (1987) 3436.

11. K. Murata, K. kikuchi, T. Takahashi, K. Kobayashi, Y. Honda, K. Saito, K. Kanoda, T. Tokiwa, H. Anzai, T. Ishiguro and I. Ikemoto: J. Mol. Elect. **4** (1988) 173.

12. K. Kikuchi, K. Murata, Y. Honda, T. Namiki, K. Saito, H. Anzai, K. Kobayashi, T. Ishiguro and I. Ikemoto: J. Phys. Soc. Jpn. **56** (1987) 4241.

13. K. Kikuchi, K. Murata, Y. Honda, T. Namiki, K. Saito, K. Kobayashi, T. Ishiguro and I. Ikemoto: J. Phys. Soc. Jpn. **56** (1987) 2627.

14. K. Kikuchi, Y. Honda, Y. Ishikawa, K. Saito, I. Ikemoto, K. Murata, H. Anzai, T. Ishiguro and K. Kobayashi: Solid State Commun. **66** (1988) 405.

15. For example, see: M. Tamura, H. Tajima, K. Yakushi, H. Kuroda, A. Kobayashi,

R. Kato and H. Kobayashi: J. Phys. Soc. Jpn. **60** (1991) 3861, and references cited therein.

16. K. Yakushi, H. Kanbara, H. Tajima, H. Kuroda, G. Saito and T. Mori: Bull. Chem. Soc. Jpn. **60** (1987) 4251.
17. K. Kanoda, K. Kato, A. Kawamoto, K. Oshima, T. Takahashi, K. Kikuchi, K. Saito and I. Ikemoto: Synth. Metals **56** (1993) 2309.
18. For example, see: N. Toyota, E. W. Fenton, T. Sasaki and M. Tachiki: Solid State Commun. **72** (1989) 859.
19. K. Kanoda, T. Takahashi, K. Kikuchi, K. Saito, Y. Honda, I. Ikemoto, K. Kobayashi, K. Murata and H. Anzai: Solid State Commun. **69** (1989) 415.
20. S. Kagoshima and Y. Nogami: Synth. Metals **27** (1988) A299.

Chapter 9.

Concluding Remarks for the Present Thesis

In this study, the intermolecular transfer integrals have been derived from the optical data in the five organic π-molecular conductors. Thus, it has been shown that the band structures and Fermi surfaces are essentially understandable in the framework of the simple tight-binding model, although there remain some subtle discrepancies between the optical results and the transport results. This is the first demonstration of the determination of the Fermi surface by the optical experiments, which can be compared with the transport results. The findings of the materials having rather high symmetries of the molecular arrangements have enabled this study.

It may be surprising that the conduction bands of these materials are composed only of one frontier molecular orbital on each molecule. This has made the analysis of intraband transitions very easy, in spite of the complicated structure of the materials. The strong correlation between the interband transitions and the dimeric structure also supports this view (see Chap. 5 and Appendix A.). Except for a few examples such as $[Pd(dmit)_2]$ salts [1-3], the intramolecular electronic degrees of freedom play only a minor role in the conduction. Only other kinds of flexibility, such as molecular vibrations, can contribute to subtle features of the electronic properties in most cases.

From this point of view, a molecule having degenerate frontier levels or another molecular level very close to the frontier level is of great interest. The carbon cluster, C_{60}, belongs to this class of molecules. The high symmetry of the molecule is essential for such a situation. Such kind of molecules have attracted attentions mainly from the magnetic point of view, because the degeneracy of molecular levels should induce the local magnetic interactions. However, the donor or acceptor molecule

with high symmetry would afford also some novel features in molecular conductors, because the electronic flexibility of the molecule can directly affect the conduction in such a case. This strategy would be also useful in controlling the dimensionality and the electron correlation by the molecular degrees of freedom. In this connection, the finding of the very small three-dimensional Fermi surface in θ-(BEDT-TTF)$_2$I$_3$ [3] (Sec. 4.7) is a suggestive result.

References

1. H. Tajima, T. Naito, M. Tamura, A. Kobayashi, H. Kuroda, R. Kato, H. Kobayashi, R. A. Clark and A. E. Underhill: Solid State Commun. **79** (1991) 337.
2. A. E. Underhill, R. A. Clark, I. Marsden, M. Allan, R. H. Friend, H. Tajima, T. Naito, M. Tamura, H. Kuroda, A. Kobayashi, H. Kobayashi, E. Canadell, S. Ravy and J. P. Pouget: J. Phys. Condens. Matter **3** (1991) 933.
3. E. Canadell, S. Ravy, J. P. Pouget and L. Brossard: Solid State Commun. **75** (1990) 633.
4. T. Terashima, S. Uji, H. Aoki, M. Tamura, M. Kinoshita and M. Tokumoto: Solid State Commun. **91** (1994) 595.

Appendices

A. Disappearance of Interband Transition due to Symmetry of Molecular Arrangement

In the following, a rule for disappearance of the optical interband transition due to crystal symmetry is shown. The conventional selection rule for interband transtitions concerns the transition probability at a special $\boldsymbol{k}$-point. On the other hand, this rule states that the optical interband transition disappears over the whole region in the first Brillouin zone, if the light polarization and the crystal structure satisfy the following conditions:

i) The crystal has an n-fold non-symmorphic symmetry operation along the x-direction (principal axis).

ii) The light polarization is parallel to the x-direction.

iii) All the molecular orbitals (MOs) relevant to the conduction bands are equivalent to each other.

iv) The number of the MOs relevant to the conduction bands in the unit cell is not more than n.

The non-symmorphic symmetry operation is defined as the symmetry operation accompanied by the translation by $1 / n$ of the unit lattice vector, where $n = 2$, 3, 4, or 6. This category comprises the screw and glide mirror operations. The condition iii) is satisfied, at least approximately, for wide range of the molecular conductors based on radical salts. The tight-binding approximation is applied here; the MOs are the Wannier functions for the conduction bands. The rule is analogous to the extinction rules in the diffraction crystallography, and illustrates the role of the interband transition as a probe to the symmetry of molecular packing.

The interband optical spectra for the light polarized in the x-direction with the frequency, ω, is described by the optical conductivity (see Sec. 2.4.),

$$\sigma_{x}(\omega) = (2 / iV\hbar^{3}) \sum_{j,j'} < j \mid [H, P_{x}] \mid j' >< j' \mid [H, P_{x}] \mid j > \times f(E_{j}) [1 - f(E_{j'})] (\omega / \omega_{jj'}) / (\omega^{2} - \omega_{jj'}^{2} + i\gamma\omega) \quad , \qquad (A.1)$$

where V is the crystal volume, j and j′ are the electronic states of the crystal, and

$$\hbar\omega_{jj'} = (E_{j} - E_{j'}) \quad , \qquad (A.2)$$

is the energy of the transition from the state j to j'. The function $f(E)$ stands for the Fermi distribution, and,

$$H = \sum_{m,m'} t_{mm'} a^{\dagger}_{m} a_{m'} \quad , \qquad (A.3)$$

and,

$$P_{x} = e \sum_{m,m'} (R_{m})_{x} a^{\dagger}_{m} a_{m} \, , \qquad (A.4)$$

are the Hamiltonian and the x-component of the electronic dipole, respectively, where $t_{m\,m'}$ is the transfer integral between the molecules m and m', $(R_{m})_{x}$ the x-component of the position vector pointing the molecular site m. And $a^{\dagger}$ and a are the creation and annihilation operators of electron,

respectively. These are corresponding to the MOs on the sites m and m'. Here it is assumed that each molecule has only one MO (Cf. the condition iii)). It follow that

$$[H, P_x] = e \sum_{\mathrm{m,m'}} t_{\mathrm{m\,m'}} (R_{\mathrm{m,m'}})_{\mathrm{x}} a^{\dagger}_{\mathrm{m}} a_{\mathrm{m'}} , \tag{A.5}$$

where,

$$(R_{\mathrm{m,m'}})_{\mathrm{x}} = (R_{\mathrm{m}} - R_{\mathrm{m'}})_{\mathrm{x}} . \tag{A.6}$$

Since $[H, P_x]$ is an anti-Hermitian, $[H, P_x]_{\mathrm{j'j}} = 0$ when $[H, P_x]_{\mathrm{jj'}}$.

Suppose that the unit cell contains μ_{M} molecules. In the reduced zone scheme, this results in μ_{M} bands. The vertical optical transition form the M 'th band to M' 'th band at wavevector $\boldsymbol{k}$ is prescribed by the matrix element,

$$\langle \Psi_{M,\boldsymbol{k}} | X | \Psi_{M',\boldsymbol{k}} \rangle \equiv \langle \Psi_{M,\boldsymbol{k}} | [H, P_x] | \Psi_{M',\boldsymbol{k}} \rangle . \tag{A.7}$$

The wavefunction is given by

$$\Psi_{M,\boldsymbol{k}}(\boldsymbol{r}) = \sum_{\mu=1}^{\mu_{\mathrm{M}}} C_{M,\mu,\boldsymbol{k}} \, \psi_{\mu,\boldsymbol{k}}(\boldsymbol{r}) , \tag{A.8}$$

$$\psi_{\mu,\boldsymbol{k}}(\boldsymbol{r}) = N^{-1/2} \sum_{l} \exp(-\mathrm{i}\boldsymbol{k} \cdot \boldsymbol{R}_l) \, \chi_{\mu}(\boldsymbol{r} - \boldsymbol{R}_l), \tag{A.9}$$

where N denotes the number of unit cells in the crystal, and $\boldsymbol{R}_l$ the position of the unit cell, l. The summations in Eqs. (A.8) and (A.9) are taken over the unit cell and the crystal, respectively. The coefficient in Eq. (A.8), C, is determined by the band calculations. It is assumed here that all the MOs, χ_μ, are equivalent to each other (Cf. the condition iii)).

Since

$$\exp(-\mathrm{i}\,\boldsymbol{G}\cdot\boldsymbol{R}_l) = 1\ , \tag{A.10}$$

holds for any reciprocal lattice vector, $\boldsymbol{G}$,

$$\psi_{\mu,\boldsymbol{k}+G} = \psi_{\mu,\boldsymbol{k}}\ , \tag{A.11}$$

follows from Eq. (A.9). At the same time, we obtain,

$$\psi_{\mu,\boldsymbol{k}+G} = \sum_{\mu} C_{M,\mu,\boldsymbol{k}+\boldsymbol{G}}\,\psi_{\mu,\boldsymbol{k}}\ , \tag{A.12}$$

by substituting $\boldsymbol{k}$ with $\boldsymbol{k}+\boldsymbol{G}$. This means that $C_{M,\mu,\boldsymbol{k}+\boldsymbol{G}}$, as well as $C_{M,\mu,\boldsymbol{k}}$, is the eigenvector of the Hamiltonian in the (M, $\boldsymbol{k}$) space. Therefore, we can label each state by ($\boldsymbol{G}$, $\boldsymbol{k}$) as well as by (M, $\boldsymbol{k}$). This is, namely, the extended zone scheme. The M'th band in the reduced zone scheme corresponds to the M'th Brillouin zone in the extended zone scheme. We have only to consider up to the μ_{M}'th zone, because $M \le \mu_{\mathrm{M}}$. By use of $C_{M,\mu,\boldsymbol{k}+\boldsymbol{G}}$ instead of $C_{M,\mu,\boldsymbol{k}}$, Eq.(A.8) is expressed as,

$$\Psi_{k+G}(\boldsymbol{r}) = \sum_{\mu} C_{M,\mu,k+G}\, \psi_{\mu,k}(\boldsymbol{r}). \qquad \text{(A.13)}$$

From now on, we are referring to the representation on the basis of the plane waves propagating along the x-direction,

$$| k > \; = \; \exp(-\mathrm{i}\, k \cdot x), \qquad \text{(A.14)}$$

namely, k_x-representation.

Application of Bloch's theorem to $\Psi_{k+G}(\boldsymbol{r})$ for the x-direction, that is, the Fourier expansion of $\Psi_{k+G}(\boldsymbol{r})$ with respect to x, yields,

$$\Psi_{k+G}(\boldsymbol{r}) = \sum_{G'_x} \phi\,(\boldsymbol{k}+\boldsymbol{G}, G'_x; y, z)\;\; \exp[-\mathrm{i}(k_x+G_x+G'_x)\cdot x]. \qquad \text{(A.15)}$$

The matrix element of the Hamiltonian in the k_x-representation is given by,

$$\begin{aligned} < K_x \mid H \mid K'_x > &= \sum_{\mathrm{m,\,m'}} < K_x \mid m > < m \mid H \mid m' > < m' \mid K'_x > \\ &= \sum_{\mathrm{m,\,m'}} < K_x \mid m > \; < m' \mid K'_x > t_{\mathrm{m\,m'}}\,, \end{aligned} \qquad \text{(A.16)}$$

where $| m >$ stands for the molecular orbital at site m, $\chi(\boldsymbol{r} - \boldsymbol{R}_m)$, and the summation is taken over all the molecular pairs in the crystal. It should be noted that $< K_x \mid m >$ is the Fourier transform of the molecular orbital, $| m >$.

Next let us examine the effect of a crystal symmetry operation, α. Since all the MOs are equivalent to each other, $| m' >$ may be obtained by

operating a certain α on $|\, m >$:

$$|\, m' > = |\, \alpha^n\, m >. \tag{A.17}$$

So that, Eq. (A.16) can be rewritten in the form,

$$< K_x \,|\, H \,|\, K'_x > = \sum_{(m,\, m')} t_{\mathrm{m\,m'}} \sum_n < K_x \,|\, \alpha^n\, m > < \alpha^n\ m' \,|\, K'_x >, \tag{A.18}$$

where (m, m') runs over all the molecular pairs in which the molecules are not related by α. The Fourier transform of an MO, $|\, \alpha^n\, m >$, is,

$$< K_x \,|\, \alpha^n\, m > = \int \exp(\mathrm{i} K_x\, x)\, \chi_{\,m}\, [\rho_\alpha^{\,-n}\, (\boldsymbol{r} - n\, \boldsymbol{\tau}_\alpha)]\, \mathrm{d}x\,, \tag{A.19}$$

where $\rho_{\,\alpha}$ and $\boldsymbol{\tau}_\alpha$ represent the rotation operator and translation vector of α, respectively. The integration is taken over the crystal. For a non-symmorphic operation with translation along the x-direction (Cf. the condition i)), $\rho_{\,\alpha}$ does not affect the x-component, and $\boldsymbol{\tau}_\alpha$ is parallel to the x-direction. Taking account of these facts, we obtain,

$$\begin{aligned} < K_x \,|\, \alpha^n\, m > &= \int \exp[\mathrm{i} K_x\, (x + n\, \tau_\alpha)]\, \chi_{\mathrm{m}}\, (\boldsymbol{r})\, \mathrm{d}\boldsymbol{x} \\ &= \exp\, (\mathrm{i} K_x\ n\, \tau_\alpha) < K_x \,|\, m >\,, \end{aligned} \tag{A.20}$$

for a non-symmorphic operation, α.

Equation (A.18) thus becomes,

$$\begin{aligned} &< K_x \,|\, H \,|\, K'_x > \\ &\quad = \sum_{(m,\, m')} t_{\mathrm{m\,m'}}\ < K_x \,|\, m > < m' \,|\, K'_x > \sum_n \exp[\mathrm{i}(K_x - K'_x)\, n\, \tau_\alpha]\,, \end{aligned} \tag{A.21}$$

The summation over n is equivalent to the Laue function appears in the theory of X-ray diffraction, because n runs up to a very large integer number. It is known that this function vanishes if $K_x - K'_x \neq (2\pi/\tau_\alpha)I$, for any integer I .

Therefore, in the expansion (A.15), only the terms with

$$G'_x = 2\pi I / \tau_\alpha \equiv I g_x \quad , \tag{A.22}$$

is required for the evaluation of the matrix elements. The expansion (A.15) is rewritten in the form,

$$\Psi_{k+G}(\boldsymbol{r}) = \sum_I \phi(\boldsymbol{k}+\boldsymbol{G},\ Ig_x; y, z)\ \exp[-\mathrm{i}(k_x+G_x+Ig_x)\cdot x]. \tag{A.23}$$

The matrix element (A.7) is, then, given by

$$\begin{aligned} &\langle \Psi_{M,k} | X | \Psi_{M',k} \rangle = \langle \Psi_{k+G} | X | \Psi_{k+G'} \rangle \\ &= \sum_{I,I'} \iiint \phi^*(\boldsymbol{k}+\boldsymbol{G},\ Ig_x; y, z)\ \phi(\boldsymbol{k}+\boldsymbol{G}', I'g_x; y, z)\ \mathrm{d}y\ \mathrm{d}z \\ &\quad \times \int \exp[\mathrm{i}(k_x+G_x+Ig_x)\cdot x]\ X\ \exp[-\mathrm{i}(k_x+G_x'+I'g_x)\cdot x]\ \mathrm{d}x \quad , \end{aligned} \tag{A.24}$$

where it is used that X concerns only the x-coordinate. The x-integration is modified into,

$$< k_x+G_x+Ig_x \mid X \mid k_x+G_x'+I'g_x > = \sum_{m,m'} < m \mid X \mid m' >$$

$$\times < k_x+G_x+Ig_x \mid m > < m' \mid k_x+G_x'+I'g_x >$$

$$\times \sum_n \exp[\mathrm{i}\{G_x - G_x' + (I - I')\, g_x\} n\, \tau_\alpha] \quad , \qquad \text{(A.25)}$$

by an analogous treatment from Eq. (A.16) to (A.21). Again the Laue-like factor becomes negligible unless there is an integer J satisfying

$$G_x - G_x' + (I - I')g_x = J\, g_x \,,$$

$$G_x - G_x' = J\, g_x \,, \qquad \text{(A.26)}$$

Here it should be reminded that both G_x and G_x' are limited within the μ_{M}'th Brillouin zone, that is,

$$| G_x - G_x' \ | < 2\,\pi\, \mu_{\mathrm{M}} / \xi \,, \qquad \text{(A.27)}$$

where ξ is the lattice constant in the x-direction. There is no such integer J that satisfies (A.26), unless $G_x = G_x'$. Hence, (A.25) and thus (A.24) are negligible, if,

$$\mu_{\mathrm{M}} \leq \xi \ / \ \tau_\alpha \,, \qquad \text{(A.28)}$$

and

$$G_x \neq G_x' \quad . \qquad \text{(A.29)}$$

This is equivalent to the condition iv). So that, the interband optical transition ($M \neq M'$, i.e., $G_x \neq G_x'$.) for the x-polarized light disappears at any $\boldsymbol{k}$.

In what follows, several comments are given in connection with this rule.

Let us consider the matrix element of the Hamiltonian (A.21) at the zone boundary, where both K_x and K'_x are the x-components of reciprocal lattice vectors. It is readily noticed that the matrix element may become zero in the presence of non-symmorphic symmetry operation. This corresponds to the degeneracy of the bands at the zone boundary.

The rule obtained here implies an analogy to the extinction rules for X-ray diffraction, i.e., the character of the Laue function. Both are the generalization of the law of conservation of the crystal momentum. For a system with no non-symmorphic symmetry, the present rule reduces to the simple law of conservation of crystal momentum, i.e., only the vertical transitions are allowed. It is possible and useful to regard the interband optical transition as the scattering of the electron Bloch wave by the radiation field. The analogy to the diffraction phenomena turns out to be obvious in this way. For instance, the extinction of the (1 0 0) diffraction corresponds to the disappearance of the interband transitions with $G_x - G_x' = 2\pi / \xi$.

As anticipated from this analogy, it is possible to show a similar rule for multiple primitive cell systems, such as body-centered and face-centered lattices, because these systems have the symmetry operations with translations shorter than the lattice constants. However, if the band structure is calculated for the corresponding primitive cell, such a rule is trivial.

It is interesting to rewrite the matrix element of the transition moment (A.7) in terms of the structure factor and the phase factor (the Laue function). The calculation is straightforward and we obtain,

$$<\Psi_{M,k}|X|\Psi_{M',k}> = \sum_{G''} \sum_{G'''} <k+G+G''|X|k+G'+G'''> \times \phi^*_{k+G,G''} \phi_{k+G',G'''}$$

$$= \sum_{m,m'} \sum_{G'',G'''} <m|X|m'><k+G+G''|m><m'|k+G'+G'''> \times \phi^*_{k+G,G''} \phi_{k+G',G'''}$$

$$= \sum'_{m \neq m'} \sum_{m'} t_{mm'}(R_m - R_{m'})_x \times \sum_{G'',G'''} <k+G+G''|m><m'|k+G'+G'''> \phi^*_{k+G,G''} \phi_{k+G',G'''} \times \sum_l \exp[i(G+G''-G'-G''')\cdot R_l]. \quad (A.30)$$

where the Fourier coefficient $\phi_{k+G,G''}$ is defined by,

$$\Psi_{k+G}(r) = \sum_{G''} \phi_{k+G,G''} \exp[-i(k+G+G'')\cdot r]. \quad (A.31)$$

Thus the matrix element can be expressed in terms of the factors related to the intermolecular interactions (t), structure factors (Fourier transforms) and the Laue function.

The present discussion is based on the assumption that the conduction

bands are formed from equivalent MOs. It is easily found that the interband transition never disappears if two or more MOs are relevant to the conduction bands, as in [Pd(dmit)$_2$] salts. Furthermore, the rule can be broken by strong short-range electron correlation. In the presence of very large on-site Coulomb repulsion, the state of a molecule distinctly depends on the number of electrons on the molecule. Therefore, the equivalent MO picture no longer holds, even if the MOs themselves are equivalent. In other words, the present rule is useful to probe not only the symmetry but also the composition of the conduction bands and the effect of strong correlation.

B. Interplay of Interband Transitions and Electron-molecular-vibration (e-mv) Coupling

In Sec. 5.3.1, the role of the e-mv coupling peaks as a probe to the interband transitions has been mentioned from an experimental point of view. Here, some general features of the e-mv coupling are briefly discussed.

The origin of the e-mv coupling is the dependence of the relevant molecular level on the molecular conformation. In other words, it is the interaction between the occupation of the MO and the normal modes of the molecular vibration. A Hamiltonian describing this interaction is,

$$H_{\text{e-mv}} = \sum_{\text{l, m}} \sum_{\text{v}} g_{\text{v}} a^{\dagger}_{\text{l, m}} a_{\text{l, m}} (b^{\dagger}_{\text{l, m, v}} + b_{\text{l, m, v}}) , \qquad \text{(B.1)}$$

where g_{ν} is the linear coupling constant for the normal mode, ν, $a^{\dagger}_{l,m}\ a_{l,m}$ denotes the number of electrons on the m 'th molecule in the l 'th unit cell, and the operator, $b^{\dagger}_{l,m,\nu} + b_{l,m,\nu}$ is the second-quantization expression for the normal mode coordinate. It is well known that the major contributions arise from the (nearly) totally symmetric modes, which are infrared inactive. With the unperturbed Hamiltonian, $H_e + H_{mv}$, the Hamiltonian of the system is given as, $H = H_e + H_{mv} + H_{e\text{-}mv}$, where H_e and H_{mv} stand for the unperturbed electronic and vibrational states, respectively.

Let us look at the role of the intraband transitions here, before turning to that of the interband transitions. As mentioned in Sec. 2.3., the intraband transitions are the collective transverse motions of the electrons. Such motions are accompanied by no change in distribution of electrons over the molecules, because it corresponds to a longitudinal mode. In other words, a continuous flow of electronic current does not involve any change in charge density distribution, as far as the principal axis components concern. Therefore, the intraband transitions do not contribute to the e-mv coupling, in principle. One the other hand, the distinction between the transverse and longitudinal motions loses its physical meaning for the interband transitions.

The e-mv coupling with regard to the intermolecular charge-transfer excitations have been treated mainly on the basis of the dimer model [1], or similar local models [2]. Since dimeric packing is often found in molecular crystals, it is convenient to refer to such a framework. However, from the viewpoint of the conduction band electrons, it is not necessarily efficient to stick to the treatment based on an isolated dimer or to the localized picture.

Generally speaking, the e-mv coupling should be regarded as the interference between the continuum spectrum of the interband transitions and the discrete one of the vibrational excitation. A general theory by Fano [3] is available for such kind of problem, and this phenomenon is known as the Fano resonance. For simplicity, we refer only to the case of the interference between one discrete level and one continuum.

The discrete level is given in terms of the diagonal elements of H_{mv}, as,

$$< \phi \mid H_{\mathrm{mv}} \mid \phi > = E_{\phi} \quad . \tag{B.2}$$

The continuum spectrum of purely electronic excitations is described by H_{e}, that is,

$$<\psi_{\mathrm{E}''} \mid H_{\mathrm{e}} \mid \psi_{\mathrm{E}'}> = E' \ \delta(E'' - E') \quad . \tag{B.2}$$

where the continuum states, $\mid \psi_{\mathrm{E}'}>$, are normalized with respect to energy as noted by the δ-function. The cross terms arise from $H_{\mathrm{e\text{-}mv}}$:

$$<\psi_{E'} \mid H_{\mathrm{e\text{-}mv}} \mid \phi > = H_{\mathrm{e\text{-}mv}} (E') \ . \tag{B.3}$$

The eigenstates of the total Hamiltonian, H, should have the form,

$$\Psi_E = a_{\phi}(E) \ + \int b_{E'}(E) \ \psi_{E'} \mathrm{d}\, E' \quad . \tag{B.4}$$

where E is the corresponding eigenvalues and a_{ϕ} and $b_{E'}$ are the coefficients.

The solution of this eigenvalue problem is given by Fano [3]. The results are,

$$a_{\phi}(E) = \sin \Delta(E) / \pi H_{\text{e-mv}}(E) \ , \tag{B.5}$$

$$b_{\text{E}}(E) = H_{\text{e-mv}}(E') \sin \Delta(E) \ \ \text{P} / \pi (E - E') H_{\text{e-mv}}(E)$$

$$- \delta(E - E') \cos \Delta(E), \tag{B.6}$$

where P means that Cauchy's principal value should be taken when integrated, and,

$$\tan \Delta(E) = - \pi | H_{\text{e-mv}}(E) |^2 / [E - E_{\phi} + F(E)] \ , \tag{B.7}$$

$$F(E) = \text{P} \int | H_{\text{e-mv}}(E') |^2 \, \text{d}E' \ / (E - E') \ . \tag{B.8}$$

Let H' be the interaction between the system and the radiation field. The transition moment matrix corresponding the transition from the initial state, $|i>$, to $|\Psi_E>$ is,

$$<\Psi_E | H' \ | i> = a_{\phi}^*(E) \ <\phi | H' \ | i>$$

$$+ \int b_{E'}^*(E) \ <\psi_{E'} | H' \ | i> \text{d}E' . \tag{B.9}$$

The first term vanishes, because the direct transition to $|\phi>$ is not allowed. From the second term and Eq. (B.6), we obtain,

$$<\Psi_E \mid H' \mid i> = [\sin \Delta(E) / \pi H_{\text{e-mv}}^*(E)]$$

$$\times \mathrm{P} \int <\phi \mid H_{\text{e-mv}} \mid \psi_{E'}><\psi_{E'} \mid H' \mid i > \mathrm{d}E'/(E - E')$$

$$- \cos \Delta(E) <\psi_E \mid H' \mid i > . \qquad \text{(B.10)}$$

The second term corresponds to the interband transitions to the purely electronic excited states $\mid \psi_E >$. On the other hand, the first term describes the transitions to the vibrational state, $\mid \phi >$, which are forbidden in the case of no perturbation. Clearly, this stems form the presence of $H_{\text{e-mv}}$, and corresponds to the appearance of the e-mv peaks in the optical spectrum.

The formulation of the transition moment taking account of the band structure is a too involved subject to be treated here explicitly in detail. Rather, two significant characteristics emerging from the above discussion are pointed out in the following. First, the divergence of tan $\Delta(E)$ occurs at the energy which satisfies, $E = E_\phi - F(E)$. Since $F(E)$ can be regarded as independent of E over a sufficiently narrow range, the shift of resonance energy is approximately $F(E)$. According to the expression of $F(E)$, Eq. (B.8), this indicates that the shift of an e-mv peak is nearly proportional to the square of the coupling constant, g^2, which is consistent with the dimer case [4]. Second, the first term in (B.10) is linear to $<\psi_{E'} \mid H' \mid i>$. This means the linear dependence of the intensity of the e-mv peaks on that of the interband transitions. This character enables us to judge the intensity of the interband transitions by that of the e-mv peaks, as pointed out in Sec. 5.3.1.

References

1. M. J. Rice: Solid State Commun. **31** (1979) 93.

2. A. Painelli and A. Girlando: J. Chem. Phys. **84** (1986) 5655.

3. U. Fano: Phys. Rev. **124** (1961) 1866.

4. M. Meneghetti and C. Pecile: J. Chem. Phys. **84** (1986) 4149.

List of Publications

1. Temperature Dependence of the Reflectance Spectra of BEDT-TTF Polyhalides.
   K. Yakushi, H. Tajima, H. Kanbara, M. Tamura, H. Kuroda, G. Saito, H. Kobayashi, R. Kato and A. Kobayashi
   Physica **143 B**(1-3), 463-467 (1986).
2. Optical Study on Bis(propylenedithio)tetrathiafulvalenium (BPDT-TTF) Salts.
   K. Yakushi, H. Tajima, T. Ida, M. Tamura, H. Hayashi, H. Kuroda, A. Kobayashi, R. Kato and H. Kobayashi
   Synth. Metals, **24**(4), 301-309 (1988).
3. Temperature Dependence of the Polarized Reflectance Spectra of the θ-type of Bis(ethylenedithio)tetrathiafulvalenium Triiodide θ-(BEDT-TTF)$_2$I$_3$: Estimation of Band Parameters.
   M. Tamura, K. Yakushi, H. Kuroda, A. Kobayashi, R. Kato and H. Kobayashi
   J. Phys. Soc. Jpn., **57**(9), 3239-3247 (1988).
4. Reflectance Spectra of β-, θ-, κ-(BEDT-TTF)$_2$I$_3$, and β´´- and β´-(BEDT-TTF)$_2$ICl$_2$: Relation between the Inter-band Transition and the Dimeric Structure.
   H. Kuroda, K. Yakushi, H. Tajima, A. Ugawa, M. Tamura, Y. Okawa and A. Kobayashi
   Synth. Metals, **27**(1-2), A491-A498 (1988).
5. New Molecular Conductors, α- and β-(EDT-TTF)[Ni(dmit)$_2$]. Metal with Anomalous Resistivity Maximum vs. Semiconductor with Mixed Stack.
   R. Kato, H. Kobayashi, A. Kobayashi, T. Naito, M. Tamura, H. Tajima and H. Kuroda
   Chem. Lett., **1989**(10), 1839-1842.
6. The Reflectance Spectra of (BEDT-TTF)$_5$Hg$_3$Br$_{11}$ and (BEDT-TTF)HgBr$_3$. The Estimation of Effective On-Site Coulomb Interaction.
   H. Tajima, M. Tamura, H. Kuroda, T. Mori, H. Inokuchi
   Bull. Chem. Soc. Jpn., **63**(2), 538-543 (1990).
7. Magnetization and Meissner Effect of Organic Superconductor θ-(BEDT-TTF)$_2$I$_3$.
   M. Tamura, H. Tajima, H. Kuroda and M. Tokumoto
   J. Phys. Soc. Jpn., **59**(5), 1753-1759 (1990).
8. Reflectance Spectra of [M(dmit)$_2$] Salts.
   H. Tajima, M. Tamura, T. Naito, A. Kobayashi, H. Kuroda, R. Kato, H. Kobayashi, R. A. Clark and A. E. Underhill
   Mol. Cryst. Liq. Cryst., **181**, 233-242 (1990).
9. Structural and Electronic Properties of Cs[Pd(dmit)$_2$]$_2$.
   A. E. Underhill, R. A. Clark, I. Marsden, M. Allan, R. H. Friend, H. Tajima, T. Naito, M. Tamura, H. Kuroda, A. Kobayashi, H. Kobayashi, E. Canadell, S. Ravy and J. P. Pouget
   J. Phys. Condens. Matter, **3**(8), 933-954 (1991).
10. Fermi Level Inversion in Strongly Dimerized [Pd(dmit)$_2$] Salts.
    H. Tajima, T. Naito, M. Tamura, A. Kobayashi, H. Kuroda, R. Kato, H. Kobayashi,

R. A. Clark and A. E. Underhill
Solid State Commun., **79**(4), 337-341 (1991).

11. Fermi Surface Study of Two-dimensional Organic Metals (BEDT-TTF)$_2$X.
M. Tokumoto, A. G. Swanson, J. S. Brooks, C. C. Agosta, S. T. Hannahs, N. Kinoshita, H. Anzai, M. Tamura, H. Tajima, H. Kuroda, A. Ugawa and K. Yakushi
Synth. Metals, **42**(3), 2459-2466 (1991).
12. Optical Study on [M(dmit)$_2$] Salts.
H. Tajima, T. Naito, M. Tamura, A. Takahashi, S. Toyoda, A. Kobayashi, H. Kuroda, R. Kato, H. Kobayashi, R. A. Clark and A. E. Underhill
Synth. Metals, **42**(3), 2417-2421 (1991).
13. Reflectance Spectra of Some Two-dimensional Organic Metals based on BEDT-TTF and [Ni(dmit)$_2$].
M. Tamura, R. Masuda, T. Naito, H. Tajima, H. Kuroda, A. Kobayashi, K. Yakushi, R. Kato, H. Kobayashi, M. Tokumoto, N. Kinoshita and H. Anzai
Synth. Metals, **42**(3), 2499-2502 (1991).
14. An Organic Radical Ferromagnet.
M. Kinoshita, P. Turek, M. Tamura, K. Nozawa, D. Shiomi, Y. Nakazawa, M. Ishikawa, M. Takahashi, K. Awaga, T. Inabe and Y. Maruyama
Chem. Lett., **1991**(7), 1225-1228.
15. Discovery of a Quasi-1D Organic Ferromagnet, *p*-NPNN.
M. Takahashi, P. Turek, Y. Nakazawa, M. Tamura, K. Nozawa, D. Shiomi, M. Ishikawa and M. Kinoshita
Phys. Rev. Lett., **67**(6), 746-748 (1991); Erratum **69**, 1290
16. Bulk Ferromagnetism in the β-Phase Crystal of the *p*-Nitrophenyl Nitronyl Nitroxied Radical.
M. Tamura, Y. Nakazawa, D. Shiomi, K. Nozawa, Y. Hosokoshi, M. Ishikawa, M. Takahashi and M. Kinoshita
Chem. Phys. Lett., **186**(4,5), 401-404 (1991).
17. Reflectance Spectra of κ-(BEDT-TTF)$_2$I$_3$: Electronic Structure of Dimeric BEDT-TTF Salts.
M. Tamura, H. Tajima, K. Yakushi, H. Kuroda, A. Kobayashi, R. Kato and H. Kobayashi
J. Phys. Soc. Jpn., **60**(11), 3861-3873 (1991).
18. Low-temperature Magnetic Properties of the Ferromagnetic Organic Radical, *p*-Nitrophenyl Nitronyl Nitroxide.
Y. Nakazawa, M. Tamura, N. Shirakawa, D. Shiomi, M. Takahashi, M. Kinoshita and M. Ishikawa
Phys. Rev. B, **46**(14), 8906-8914 (1992).
19. Ferromagnetic Intermolecular Interaction in an Organic Radical 3-Quinolyl Nitronyl Nitroxide (3-QNNN).

T. Sugano, M. Tamura, M. Kinoshita, Y. Sakai and Y. Ohashi
Chem. Phys. Lett., **200**(3), 235-240 (1992).

20. Magnetic Properties of an Organic Biradical, *m*-BNN: *m*-Phenylene Bis(α-Nitronyl Nitroxide).
D. Shiomi, M. Tamura, H. Sawa, R. Kato and M. Kinoshita
J. Phys. Soc. Jpn., **62**(1), 289-300 (1993).
21. Growth of Large Isomeric $YBa_2Cu_3O_x$ Single Crystals from Coexisting Region of Solid with Melt in Y_2Cu_3 Crucibles.
H. Asaoka, H. Takei, Y. Iye, M. Tamura, M. Kinoshita and H. Takeya
Jpn. J. Appl. Phys. Part 1, **32**(3A), 1091-1096 (1993).
22. Magnetic Properties and Crystal Structures of Some Nitronyl Nitroxide Derivatives.
K. Nozawa, Y. Hosokoshi, D. Shiomi, M. Tamura, N. Iwasawa, H. Sawa, R. Kato and M. Kinoshita
Synth. Metals, **56**(2,3), 3323-3326 (1993).
23. Ferro- and Antiferromagnetic Intermolecular Interactions in the Aromatic Heterocyclic Derivatives of α-Nitronyl Nitroxide.
T. Sugano, M. Tamura and M. Kinoshita
Synth. Metals, **56**(2,3), 3305-3310 (1993).
24. Novel Magnetic Interactions in Organic Polyradical Crystals Based on Nitronyl Nitroxide.
D. Shiomi, M. Tamura, H. Sawa, R. Kato and M. Kinoshita
Synth. Metals, **56**(2,3), 3279-3284 (1993).
25. Searching for Spontaneous Magnetic Order in an Organic Ferromagnet. μSR Studies of β-Phase *p*-NPNN.
L. P. Le, A. Keren, G. M. Luke, W. D. Wu, Y. J. Uemura, M. Tamura, M. Ishikawa and M. Kinoshita
Chem. Phys. Lett., **206**(1-4), 405-408 (1993).
26. Preparation and Physical Properties of an Alloyed $(DMe\text{-}DCNQI)_2Cu$ with Fully Deuterated DMe-DCNQI (DMe-DCNQI=2,5-Dimethyl-*N*,*N*'-dicyanoquinonediimine).
R. Kato, H. Sawa, S. Aonuma, M. Tamura, M. Kinoshita and H. Kobayashi
Solid State Commun., **85**(10), 831-835 (1993).
27. Weak Ferromagnetism and Magnetic Anisotropy in Cu Salt of Fully Deuterated DMe-DCNQI, $(DMe\text{-}DCNQI\text{-}d_8)_2Cu$.
M. Tamura, H. Sawa, S. Aonuma, R. Kato, M. Kinoshita and H. Kobayashi
J. Phys. Soc. Jpn., **62**(5), 1470-1473 (1993).
28. Novel Electronic States of Partially Deuterated $(DMe\text{-}DCNQI)_2Cu$.
H. Sawa, M. Tamura, S. Aonuma, R. Kato, M. Kinoshita and H. Kobayashi
J. Phys. Soc. Jpn., **62**(7), 2224-2228 (1993).
29. Metallic and Superconducting Salts Based on an Unsymmetrical π-Donor Dimethyl(ethylenedithio)tetraselenafulvalene (DMET-TSeF).

R. Kato, S. Aonuma, Y. Okano, H. Sawa, M. Tamura, M. Kinoshita, K. Oshima, A. Kobayashi, K. Bun and H. Kobayashi
Synth. Metals, **61**(3), 199-206 (1993).

30. Magnetic Quantum Oscillations in Low-dimensional Organic Conductors (BEDT-TTF)$_2$X.
M. Tokumoto, A. G. Swanson, J. S. Brooks, C. C. Agosta, S. T. Hannahs, N. Kinoshita, H. Anzai, M. Tamura, H. Tajima, H. Kuroda, A. Ugawa and K. Yakushi
Physica B **184** (1-4), 508-512 (1993).
31. Magnetic Energy Gap in the Crystal of an Organic Biradical, *m*-BNN: *m*-Phenylene Bis(α-Nitrophenyl Nitroxide).
D. Shiomi, H. A. Katori, T. Goto, H. Sawa, R. Kato, M. Tamura and M. Kinoshita
Mol. Cryst. Liq. Cryst., **232**(1), 109-116 (1993).
32. Ferro- and Antiferro-magnetic Interactions and Crystal Structures of Some Radicals Based on Nitronyl Nitroxide.
T. Sugano, M. Tamura, T. Goto, R. Kato, M. Kinoshita, Y. Sakai, Y. Ohashi, M. Kurmoo and P. Day
Mol. Cryst. Liq. Cryst., **232**(1), 61-68 (1993).
33. Magnetic Properties of Phenyl Nitronyl Nitroxides.
M. Tamura, D. Shiomi, Y. Hosokoshi, N. Iwasawa, K. Nozawa, M. Kinoshita, H. Sawa and R. Kato
Mol. Cryst. Liq. Cryst., **232**(1), 45-52 (1993).
34. Growth, Structure and Properties of $Y_2Cu_2O_5$ Single Crystal.
W.-J. Jang, M. Hasegawa, T.R. Zhao, H. Takei, M. Tamura and M. Kinoshita
J. Crystal Growth, **141**(1,2), 153-158 (1994).
35. Analysis of de Haas-van Alphen Oscillations and Band Structure of an Organic Superconductor, θ-(BEDT-TTF)$_2$I$_3$.
M. Tamura, H. Kuroda, S. Uji, H. Aoki, M. Tokumoto, A. G. Swanson, J. S. Brooks, C. C. Agosta and S. T. Hannahs
J. Phys. Soc. Jpn., **63**(2), 615-622 (1994).
36. Weak Ferromagnetism in (DBr-DCNQI)$_2$Cu (DBr-DCNQI=2,5-Dibromo-*N*,*N*'-dicyanoquinonediimine).
M. Tamura, H. Sawa, Y. Kashimura, S. Aonuma and M. Kinoshita
J. Phys. Soc. Jpn., **63**(2), 425-428 (1994).
37. Magnetic Study of Metal-Insulator-Metal Transitions in (DMe-DCNQI-α,α´-d_2)$_2$Cu.
M. Tamura, H. Sawa, S. Aonuma, R. Kato and M. Kinoshita
J. Phys. Soc. Jpn., **63**(2), 429-432 (1994)
38. Magnetic Structure of the 4,4,4´,4´,5,5,5´,5´-Octamethyl-2,2´-*m*-phenylenebis(4,5-dihydroimidazol-1-oxyl 3-Oxide) Biradical: Quantum Spin Effect of S=1 Species Associated with Structral Change.

D. Shiomi, M. Tamura, H. Aruga Katori, T. Goto, A. Hayashi, Y. Ueda, H. Sawa, R. Kato and M. Kinoshita
J. Mater. Chem., **4**(6), 1915-1920 (1994).

39. Three-dimensional Fermi Surface in θ-(BEDT-TTF)$_2$I$_3$.
T. Terashima, S. Uji, H. Aoki, M. Tamura, M. Kinoshita and M. Tokumoto
Solid State Commun., **91**(8), 595-598 (1994).
40. Magnetic Properties and Crystal Structure of the *p*-Fluorophenyl Nitronyl Nitroxide Radical Crystal: Ferromagnetic Intermolecular Interactions leading to a Three dimensional Network of Ground Triplet Dimeric Molecules.
Y. Hosokoshi, M. Tamura, M. Kinoshita, H. Sawa, R. Kato, Y. Fujiwara and Y. Ueda
J. Mater. Chem., **4**(8), 1219-1226 (1994).
41. Organic Radical Crystals, α-Nitronyl Nitroxide Family: High-field Magnetization Study
Y. Hosokoshi, M. Tamura, D. Shiomi, N. Iwasawa, K. Nozawa, M. Kinoshita, H. Aruga Katori and T. Goto
Physica B, **201**, 497-499 (1994).
42. Two-dimensional Ferromagnetic Intermolecular Interactions in Crystals of the *p*-Cyanophenyl Nitronyl Nitroxide Radical.
Y. Hosokoshi, M. Tamura, H. Sawa, R. Kato and M. Kinoshita
J. Mater. Chem., in press.
43. Coexistence of One- and Three-dimensional Fermi Surfaces and Heavy Cyclotron Mass in Molecular Conductor (DMe-DCNQI)$_2$Cu.
S. Uji, T. Terashima, H. Aoki, J. S. Brooks, R. Kato, H. Sawa, S. Aonuma, M. Tamura and M. Kinoshita
Phys. Rev. B, in press.
44. Magnetic Properties and Crystal Structures of 2-Hydro and 2-Halo Nitronyl Nitroxide Radical Crystals.
Y. Hosokoshi, M. Tamura, K. Nozawa, S. Suzuki, M. Kinoshita, H. Sawa and R. Kato
Synth. Metals, in press.
45. Ferromagnetic Resonance and Nonlinear Absorption in *p*-NPNN.
K. Oshima, H. Kawanoue, Y. Haibara, H. Yamazaki, K. Awaga, M. Tamura and M. Kinoshita
Synth Metals, in press.
46. Fermi Surface and Cyclotron Mass in (DMe-DCNQI)$_2$Cu System.
S. Uji, T. Terashima, H. Aoki, J. S. Brooks, R. Kato, H. Sawa, S. Aonuma, M. Tamura and M. Kinoshita
Synth. Metals, in press.
47. Charge Transfer and Reentrant Phenomenon in Deuterated (DMe-DCNQI)$_2$Cu.
H. Sawa, M. Tamura, S. Aonuma, M. Kinoshita and R. Kato

Synth. Metals, in press.

48. Crystal Structure and Physical Properties of Molecular Metal (DI-DCNQI)$_2$Cu (DI-DCNQI=2,5-Diiodo-*N*,*N*'-dicyanoquinonediimine).
R. Kato, Y. Kashimura, H. Sawa, S. Aonuma, M. Tamura, M. Kinoshita, H. Takahashi and N. Môri
Synth. Metals, in press.
49. Magnetic Properties of DCNQI-Cu Systems.
M. Tamura, H. Sawa, Y. Kashimura, S. Aonuma, R. Kato, M. Kinoshita and H. Kobayashi
Synth. Metals, in press.
50. The Shubnikov-de Haas Oscillations and a Small Closed Orbit in θ-(BEDT-TTF)$_2$I$_3$.
T. Terashima, S. Uji, H. Aoki, M. Tamura, M. Kinoshita and M. Tokumoto
Synth. Metals, in press.
51. Reexamination of Angle Dependent Magnetoresistance Oscillation in θ-(BEDT-TTF)$_2$I$_3$.
T. Terashima, S. Uji, H. Aoki, M. Tamura, M. Kinoshita and M. Tokumoto
Synth. Metals, in press.
52. Angular Magnetoresistance Oscillations and Magnetic Break-down in θ-(BEDT-TTF)$_2$I$_3$.
S. J. Klepper, G. J. Athas, J. S. Brooks, M. Tokumoto, T. Kinoshita, M. Tamura and M. Kinoshita
Synth. Metals, in press.
53. Coexistence of Superconductivity with CDW (or SDW): Ambient-pressure Superconductivity Based on [Ni(dmit)$_2$], α-EDT-TTF[Ni(dmit)$_2$]
H. Tajima, M. Inokuchi, S. Ikeda, M. Arifuku, T. Naito, M. Tamura, T. Ohta, A. Kobayashi, R. Kato, H. Kobayashi and H. Kuroda
Synth. Metals, in press.
54. Charge Transfer Controlled Phase Transition in a Molecular Conductor, (DMe-DCNQI)$_2$Cu – Doping Effect –.
H. Sawa, M. Tamura, S. Aonuma, M. Kinoshita and R. Kato
J. Phys. Soc. Jpn.., in press.
55. Fermi Surface and Absence of Additional Mass Enhancement near the Insulating Phase in (DMe-DCNQI)$_2$Cu.
S. Uji, T. Terashima, H. Aoki, R. Kato, H. Sawa, S. Aonuma, M. Tamura and M. Kinoshita
Solid State Commun., in press.
56. Magnetism of the β-Phase *p*-Nitrophenyl Nitronyl Nitroxide Crystal.
K. Takeda, K. Konishi, M. Tamura and M. Kinoshita
Mol. Cryst. Liq. Cryst., in press.
57. (DCNQI)$_2$Cu: Variety of Magnetism Arising from pπ-d Interactions.
M. Tamura, H. Sawa, Y. Kashimura, S. Aonuma, R. Kato and M. Kinoshita

Mol. Cryst. Liq. Cryst., in press.
58. Magnetic Interactions in the Crystals of α- and β-Phases of 2-Hydro Nitronyl Nitroxide and Related Compounds.
Y. Hosokoshi, M. Tamura, K. Nozawa, S. Suzuki, H. Sawa, R. Kato and M. Kinoshita
Mol. Cryst. Liq. Cryst., in press.
59. Ferromagnetic Resonance in *p*-NPNN below 1 K.
K. Oshima, Y. Haibara, H. Yamazaki, K. Awaga, M. Tamura and M. Kinoshita
Mol. Cryst. Liq. Cryst., in press.
60. Enhanced Magnetic Susceptibility of $(DI\text{-}DCNQI)_2Cu$.
M. Tamura, Y. Kashimura, H. Sawa, S. Aonuma, R. Kato and M. Kinoshita
Solid State Commun., **93** (1995) 585-588.